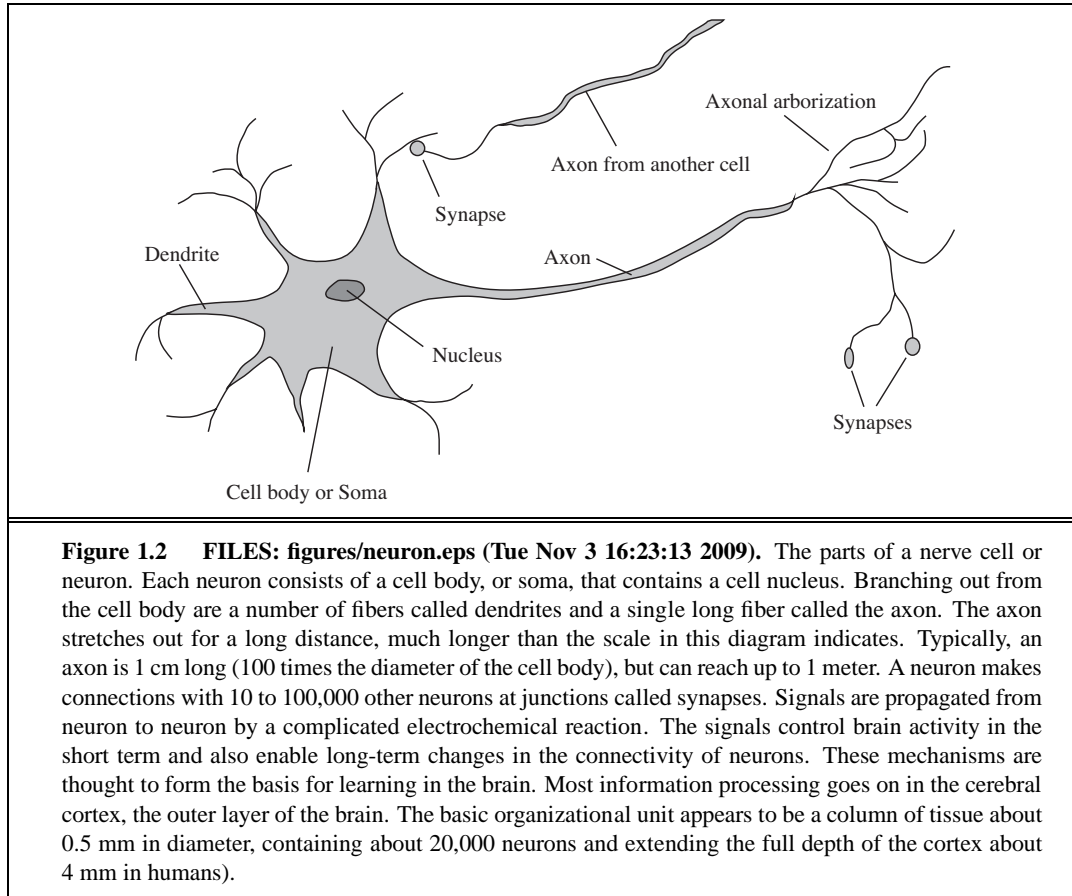
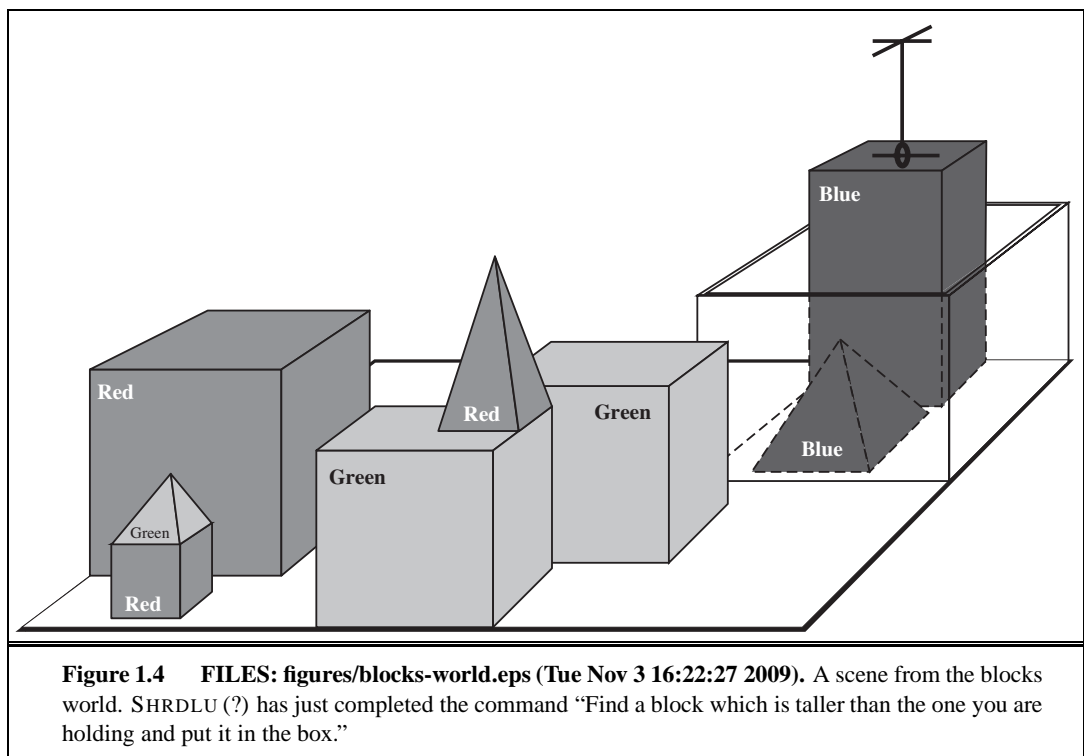


1

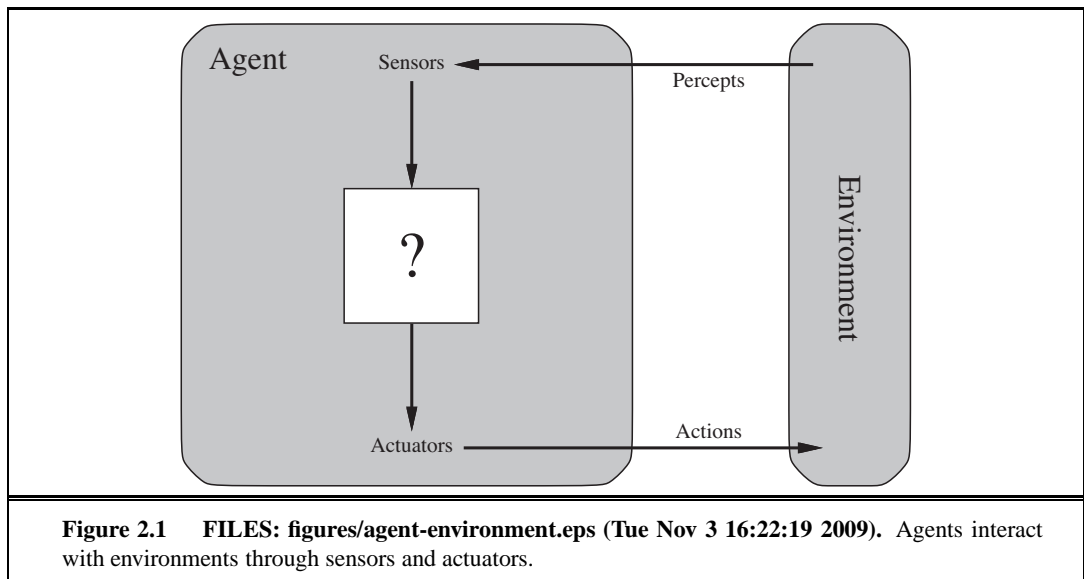
INTRODUCTION

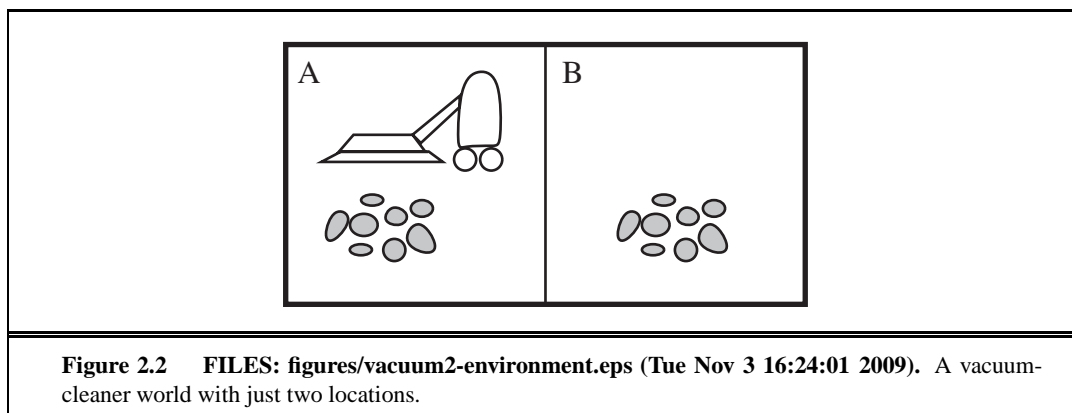


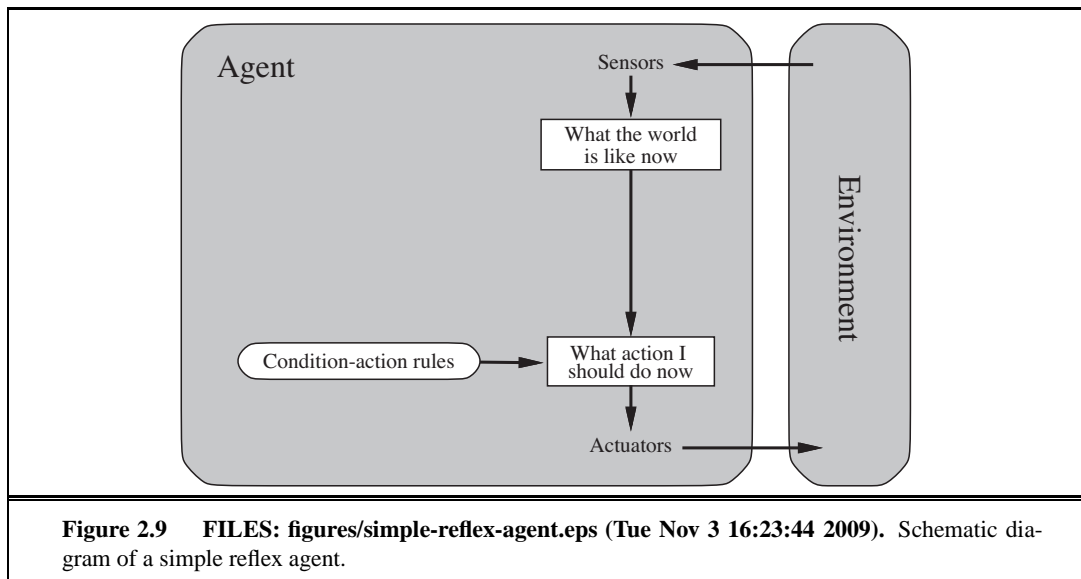


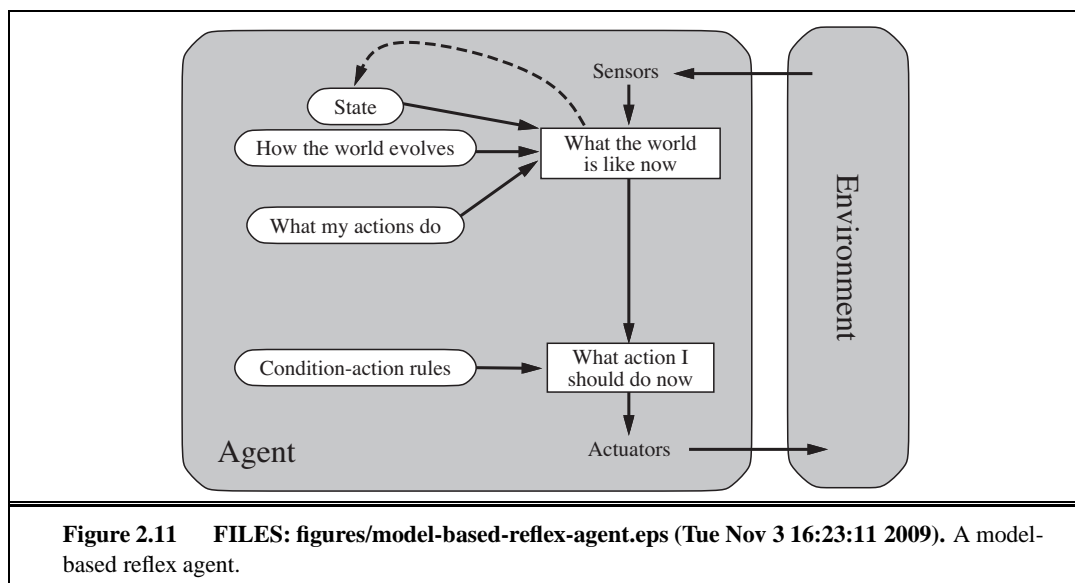
2

INTELLIGENT AGENTS









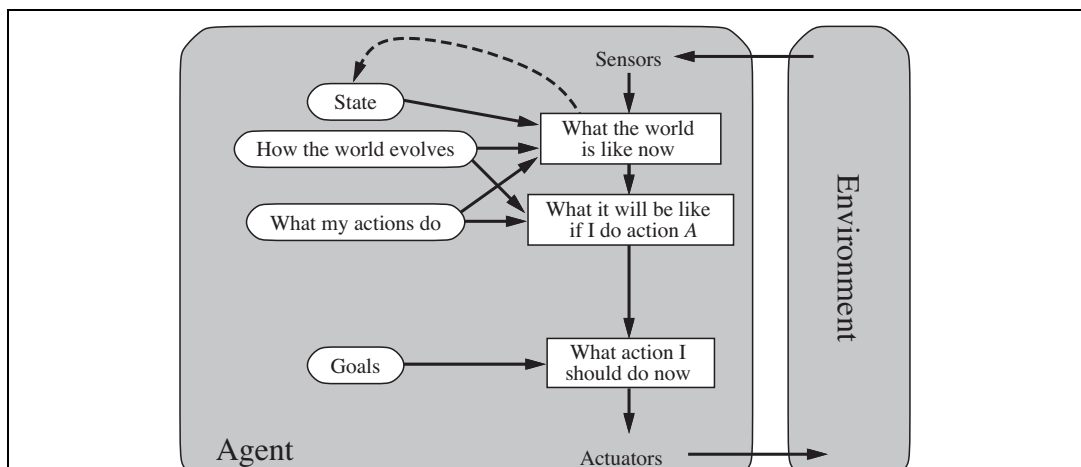
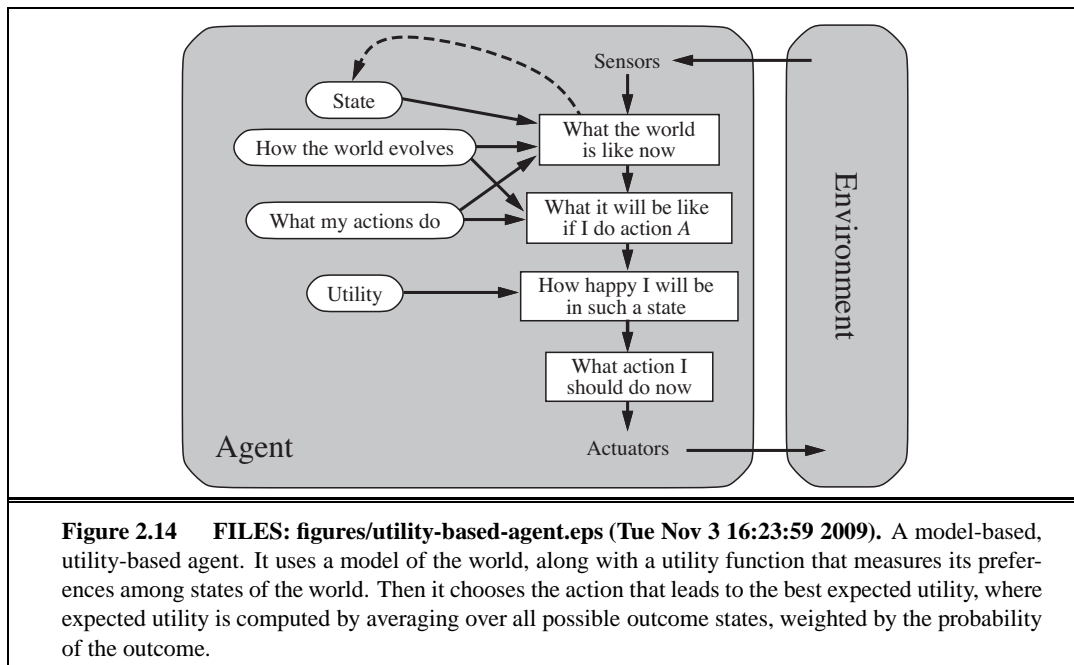
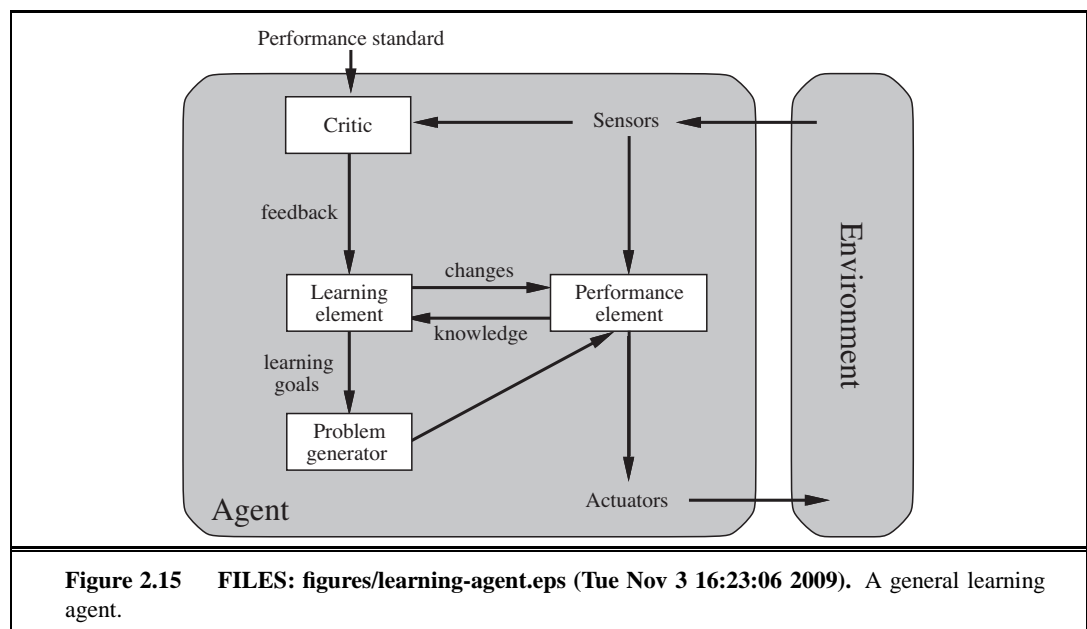
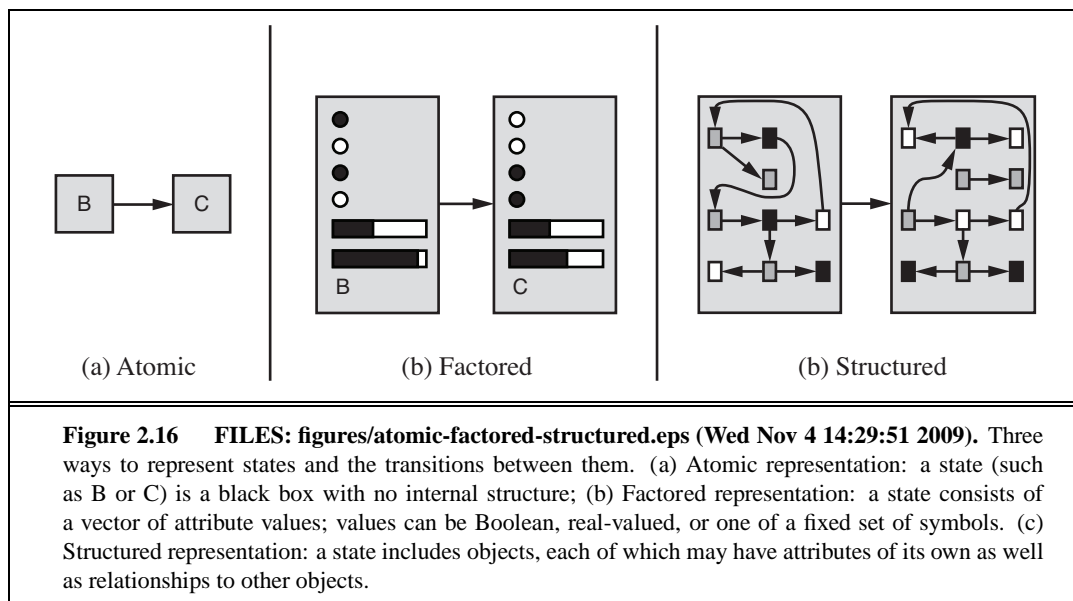


Figure 2.13 FILES: figures/goal-based-agent.eps (Tue Nov 3 16:22:54 2009). A model-based, goal-based agent. It keeps track of the world state as well as a set of goals it is trying to achieve, and chooses an action that will (eventually) lead to the achievement of its goals.

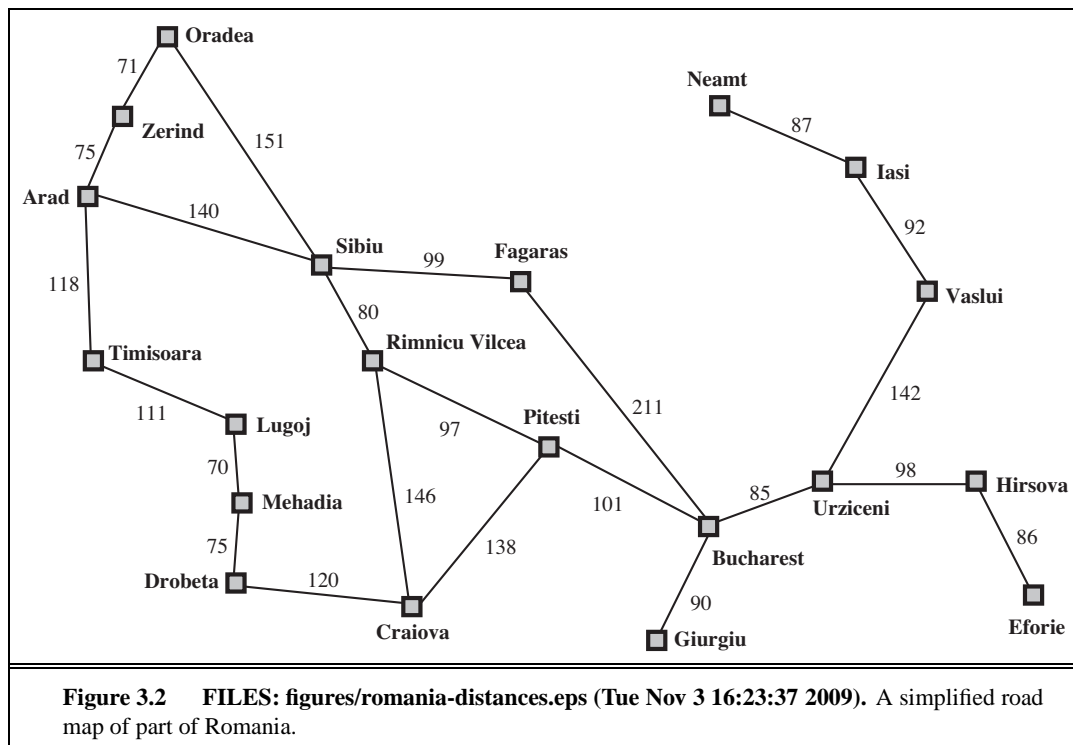


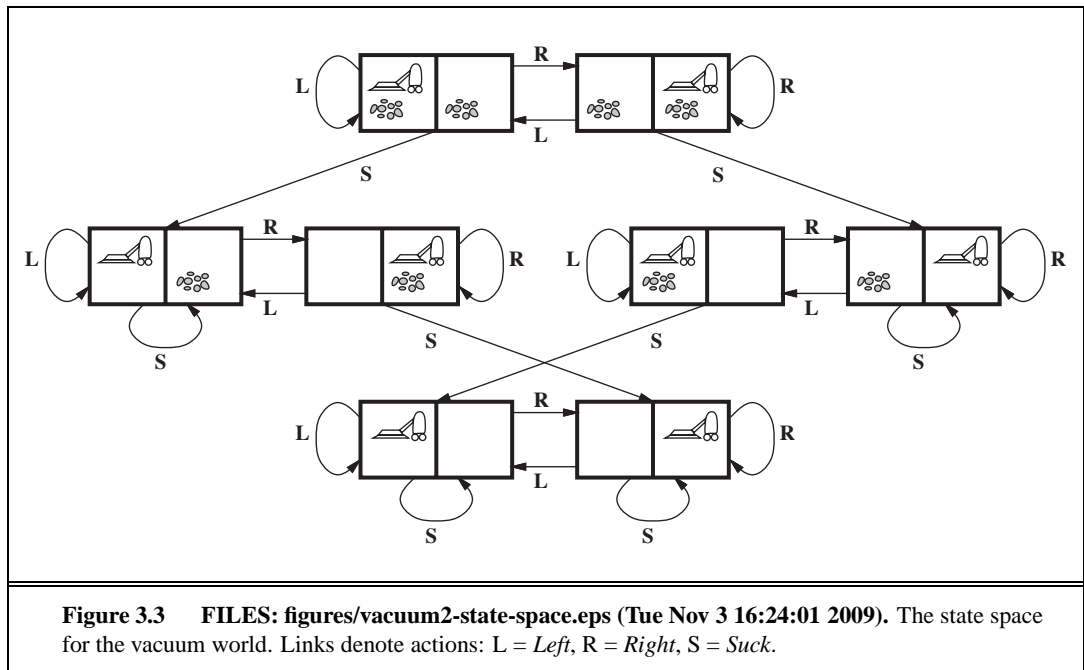


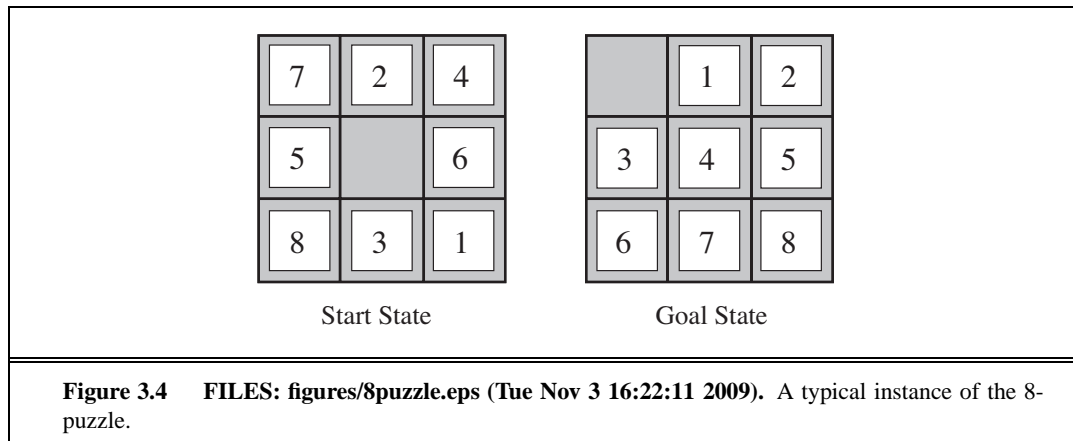


3

SOLVING PROBLEMS BY SEARCHING







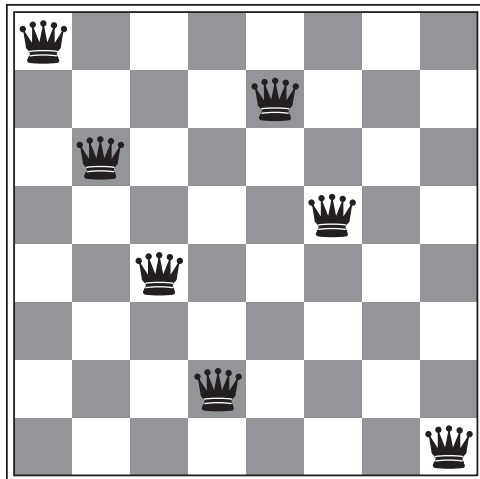
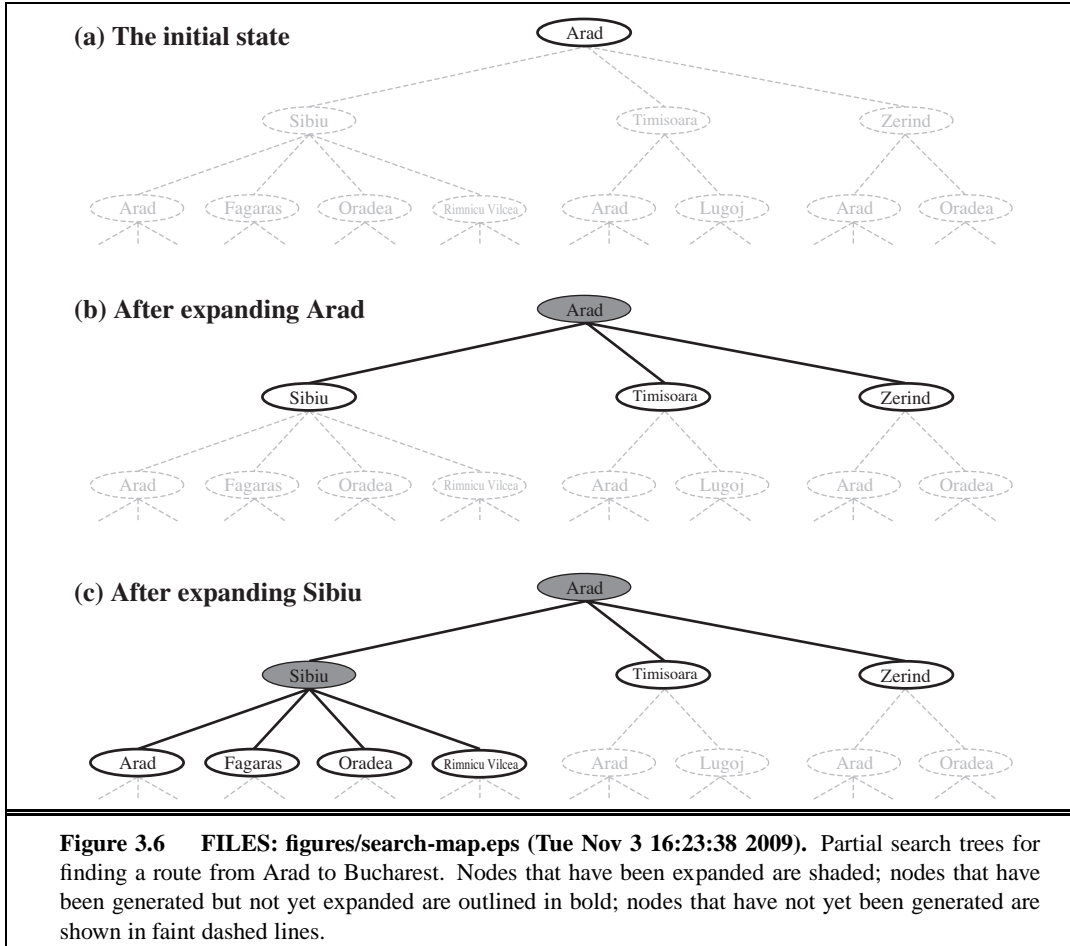


Figure 3.5 FILES: figures/8queens.eps (Wed Nov 4 16:21:52 2009). Almost a solution to the 8-queens problem. (Solution is left as an exercise.)



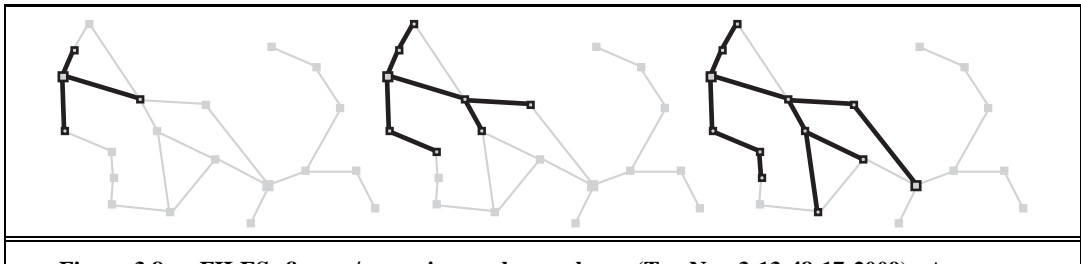


Figure 3.8 FILES: figures/romania-graph-search.eps (Tue Nov 3 13:48:17 2009). A sequence of search trees generated by a graph search on the Romania problem of Figure 3.2. At each stage, we have extended each path by one step. Notice that at the third stage, the northernmost city (Oradea) has become a dead end: both of its successors are already explored via other paths.

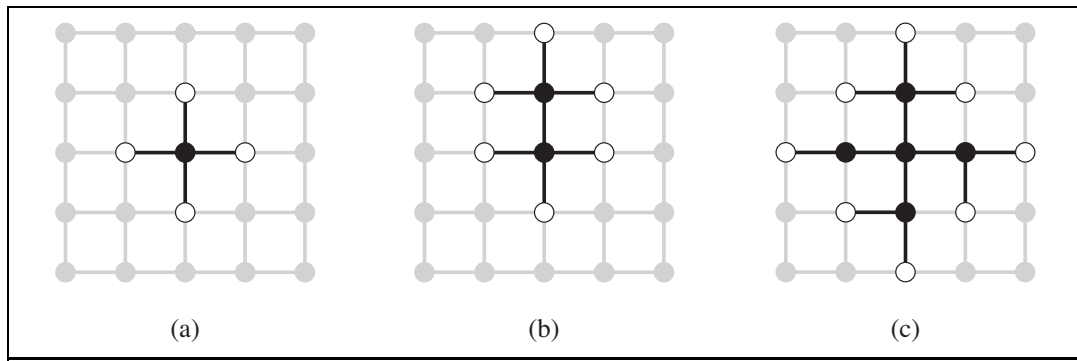
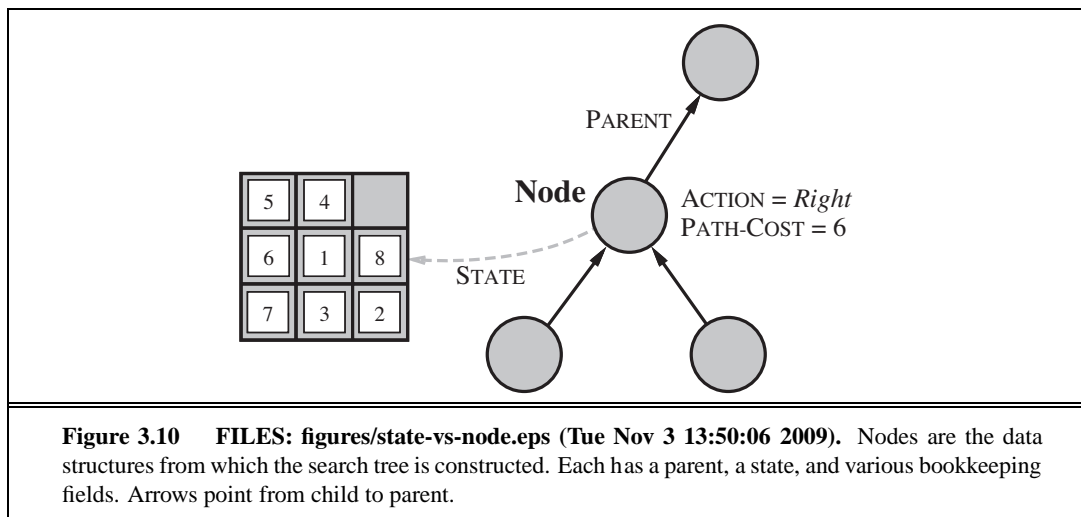
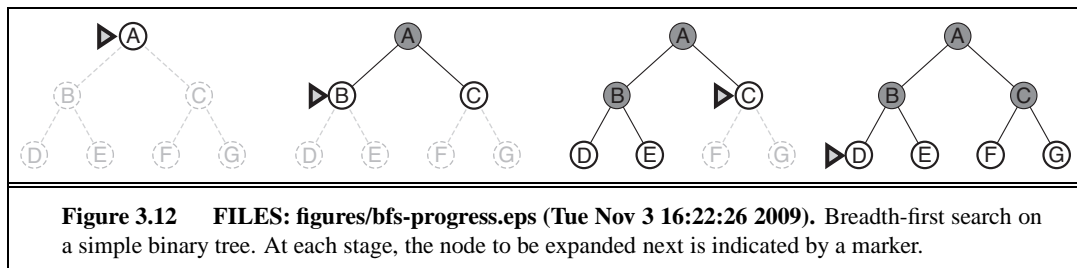
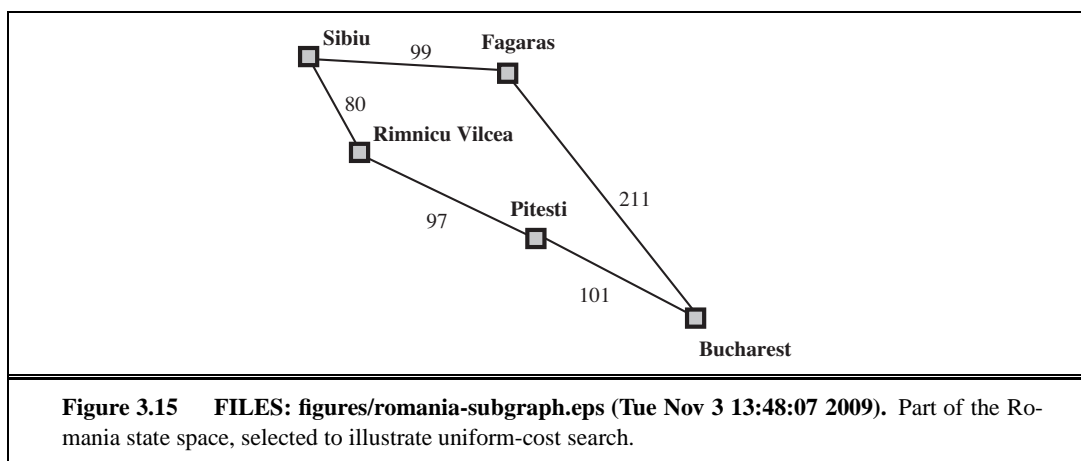
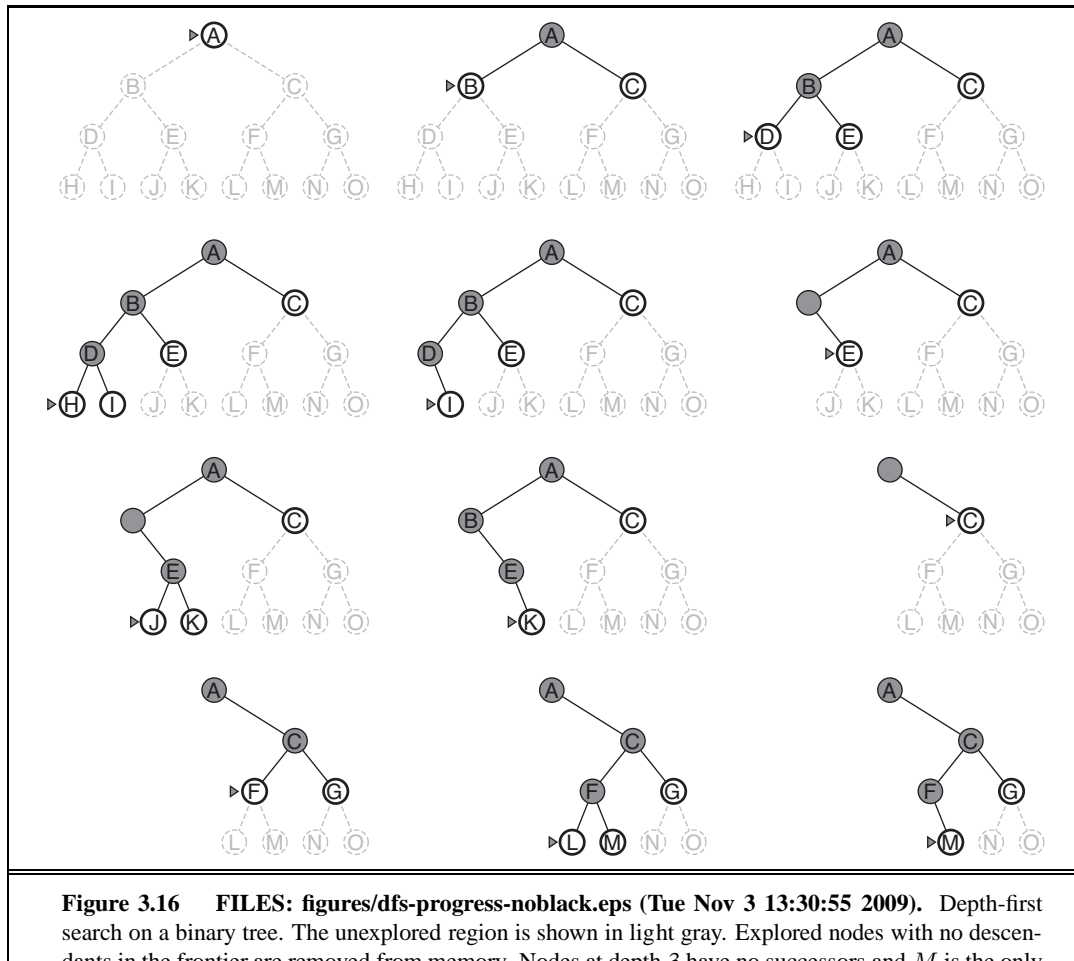


Figure 3.9 FILES: figures/graph-separation.eps (Tue Nov 3 13:36:17 2009). The separation property of GRAPH-SEARCH, illustrated on a rectangular-grid problem. The frontier (white nodes) always separates the explored region of the state space (black nodes) from the unexplored region (gray nodes). In (a), just the root has been expanded. In (b), one leaf node has been expanded. In (c), the remaining successors of the root have been expanded in clockwise order.









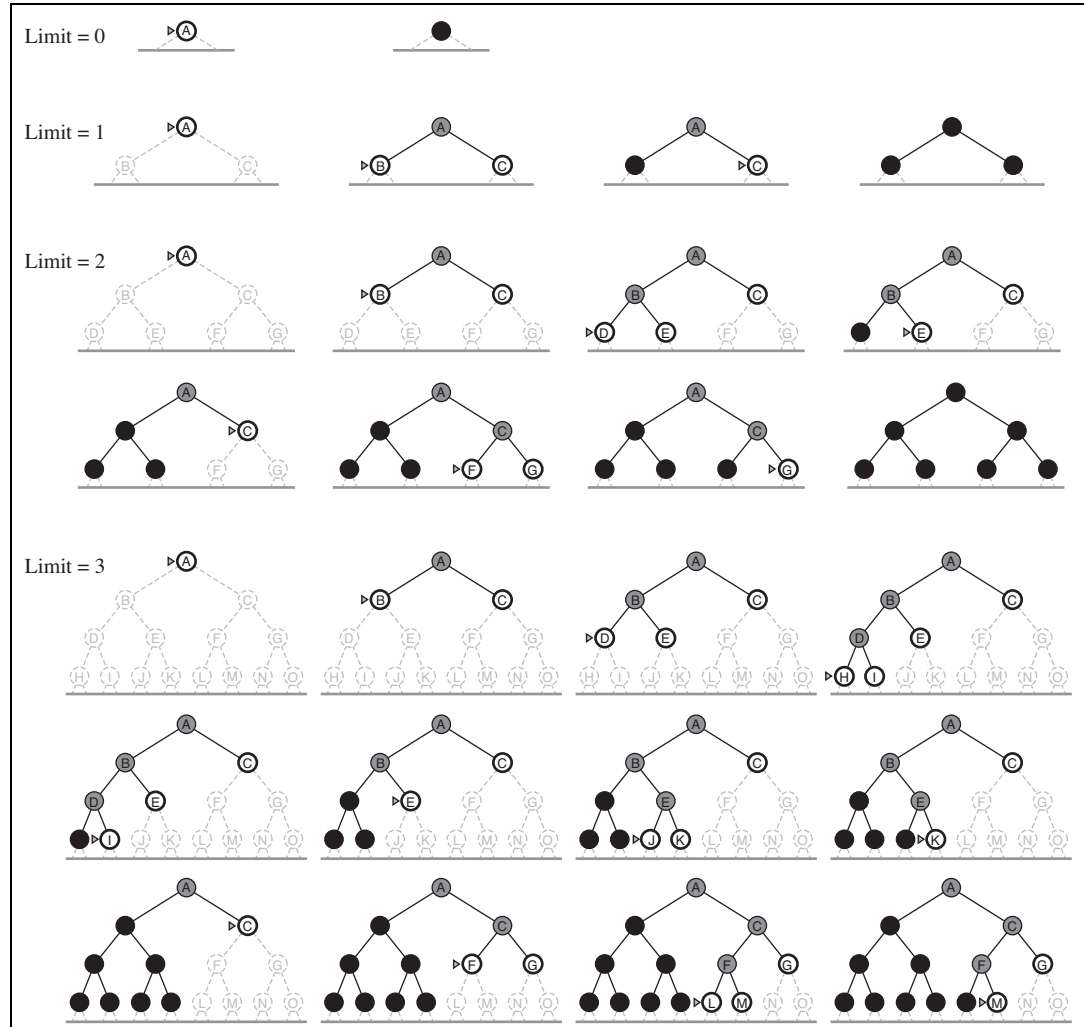
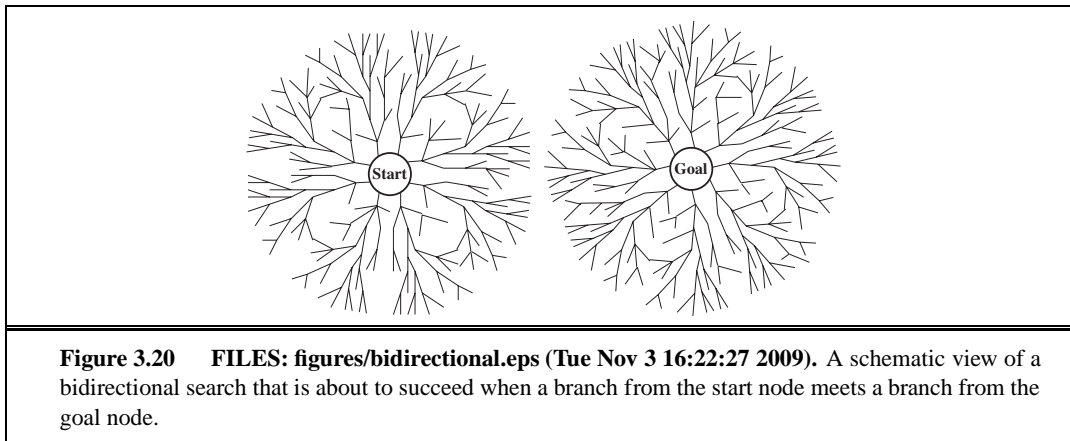
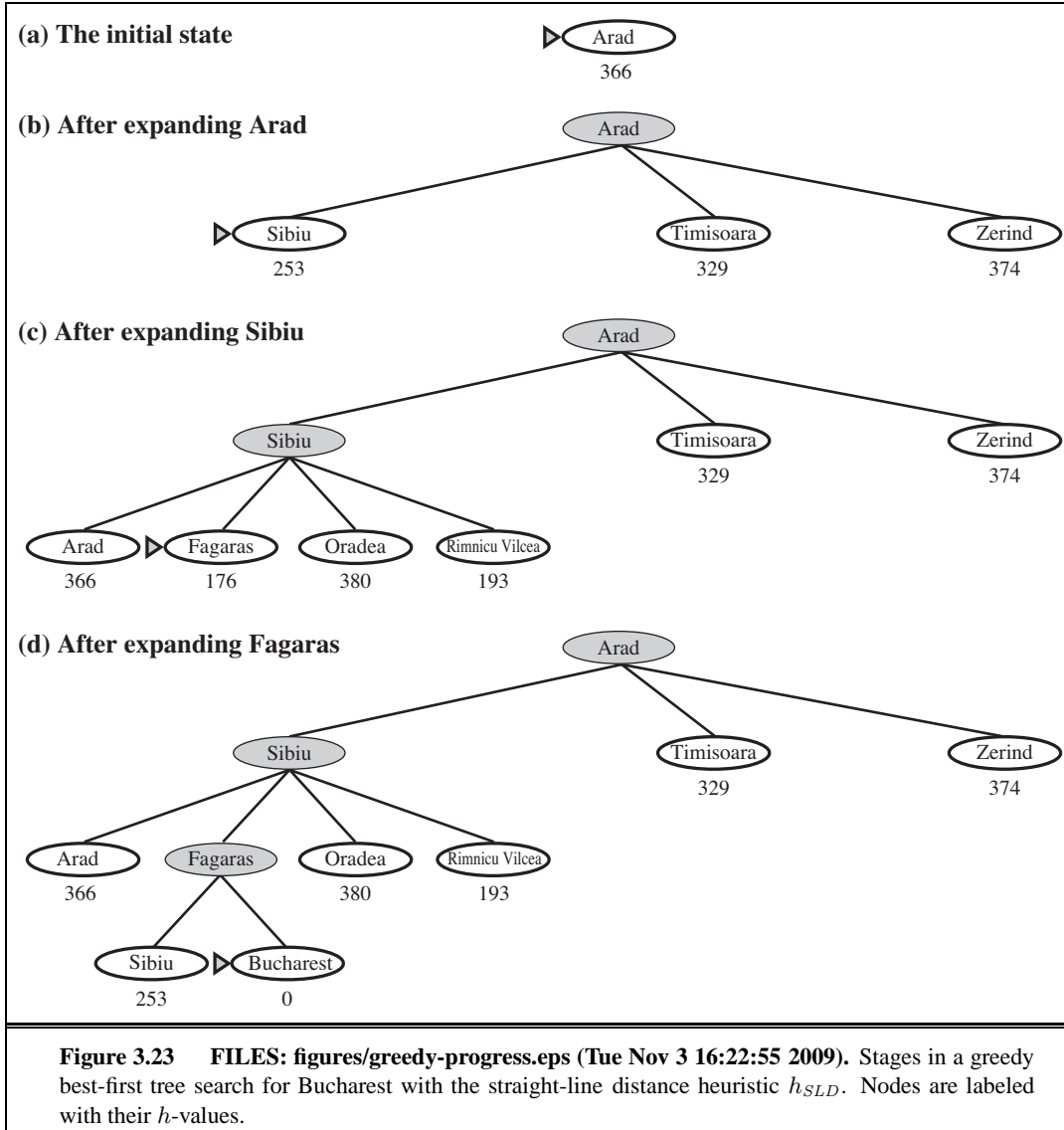


Figure 3.19 FILES: figures/ids-progress.eps (Tue Nov 3 16:23:04 2009). Four iterations of iterative deepening search on a binary tree.



Arad	366	Mehadia	241
Bucharest	0	Neamt	234
Craiova	160	Oradea	380
Drobeta	242	Pitesti	100
Eforie	161	Rimnicu Vilcea	193
Fagaras	176	Sibiu	253
Giurgiu	77	Timisoara	329
Hirsova	151	Urziceni	80
Iasi	226	Vaslui	199
Lugoj	244	Zerind	374

Figure 3.22 FILES: figures/romania-sld.eps (Tue Nov 3 16:23:37 2009). Values of h_{SLD} —straight-line distances to Bucharest.



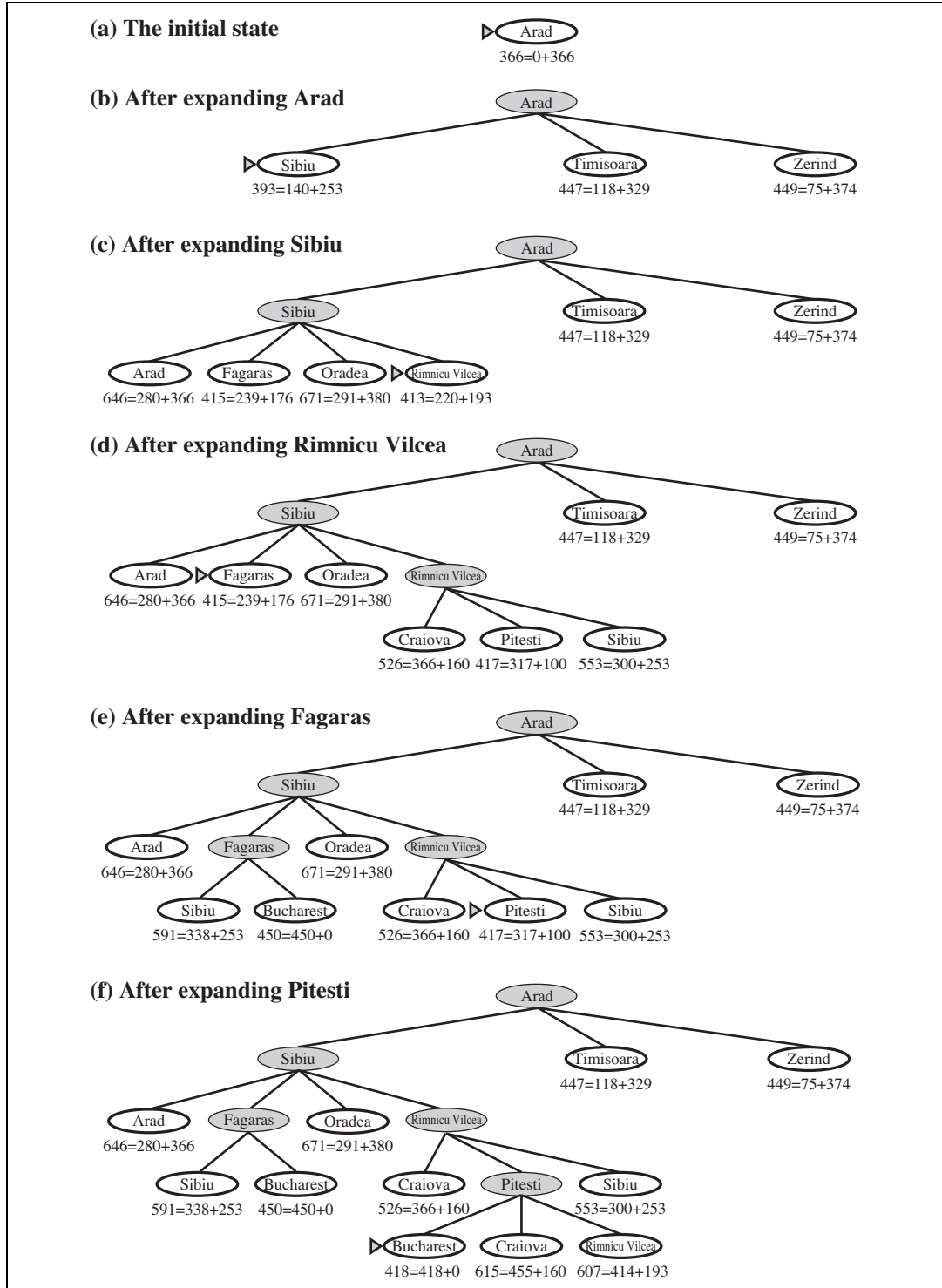
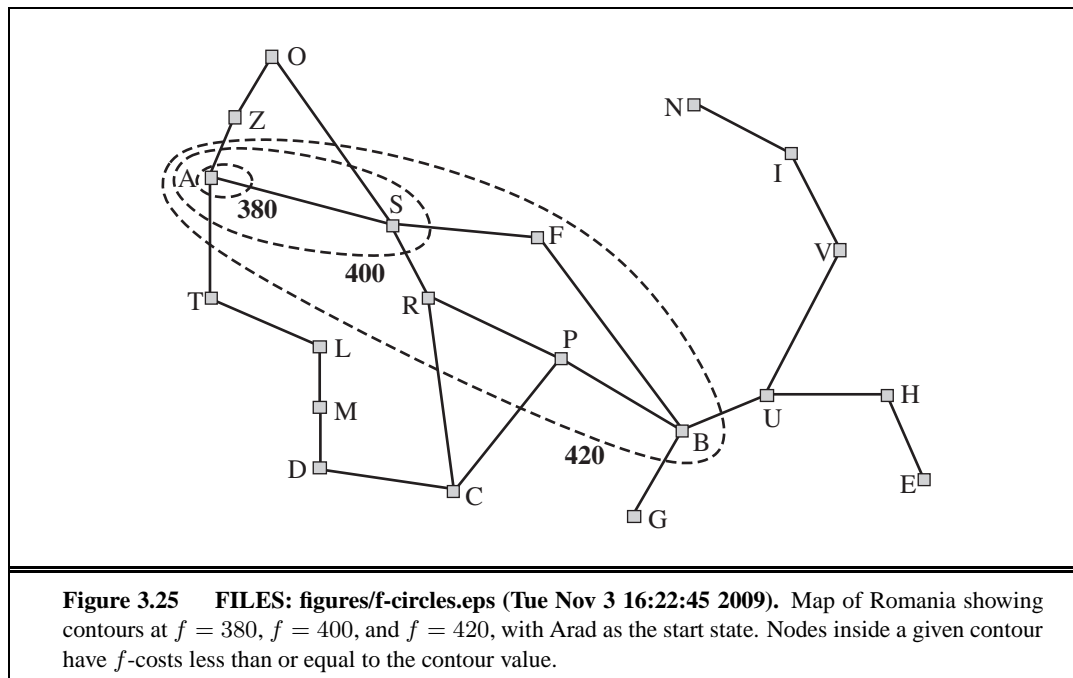


Figure 3.24 FILES: figures/astar-progress.eps (Tue Nov 3 16:22:24 2009). Stages in an A* search for Bucharest. Nodes are labeled with $f = g + h$. The h values are the straight-line distances to Bucharest taken from Figure 3.20.



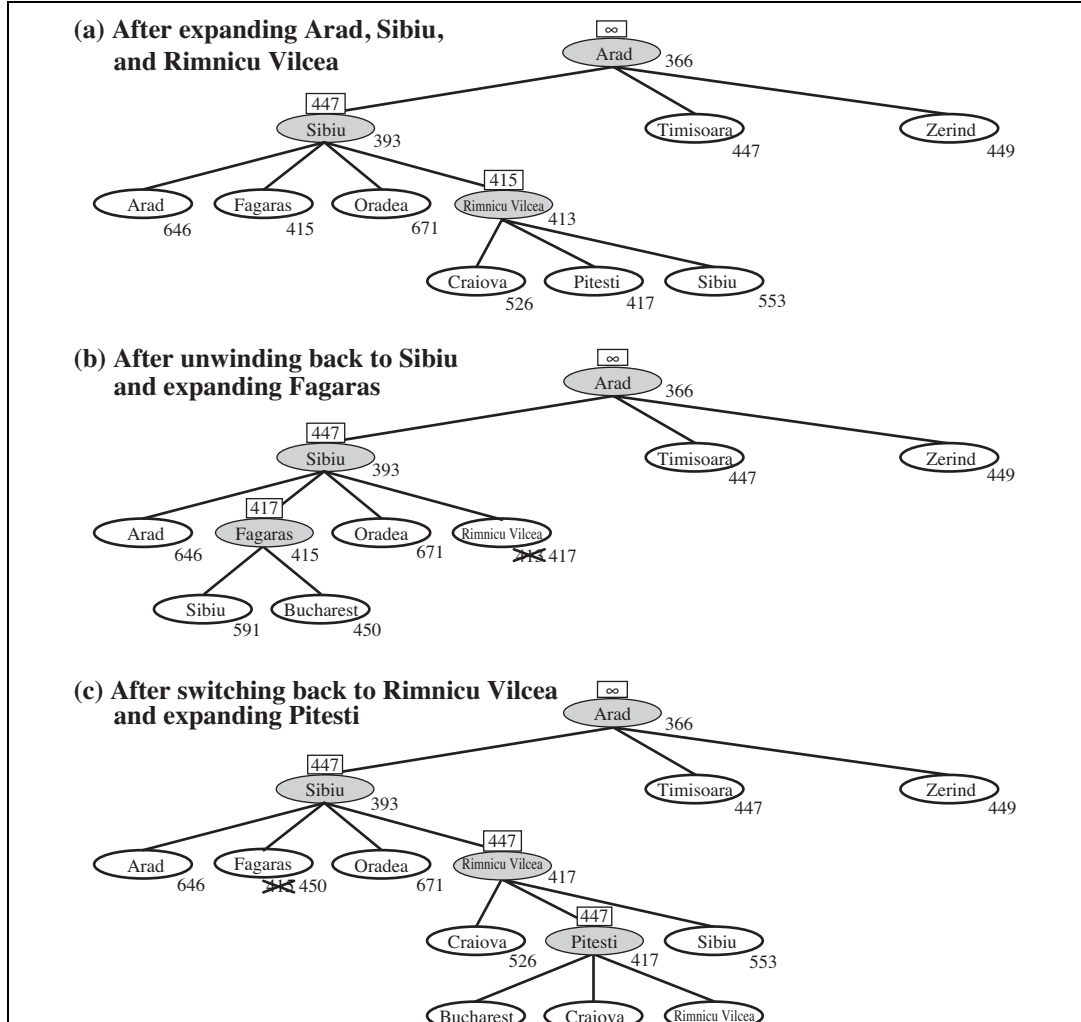
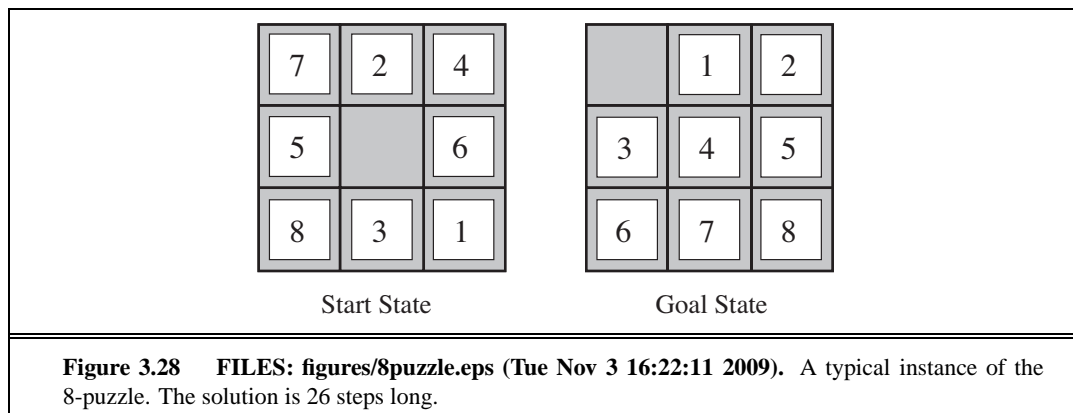
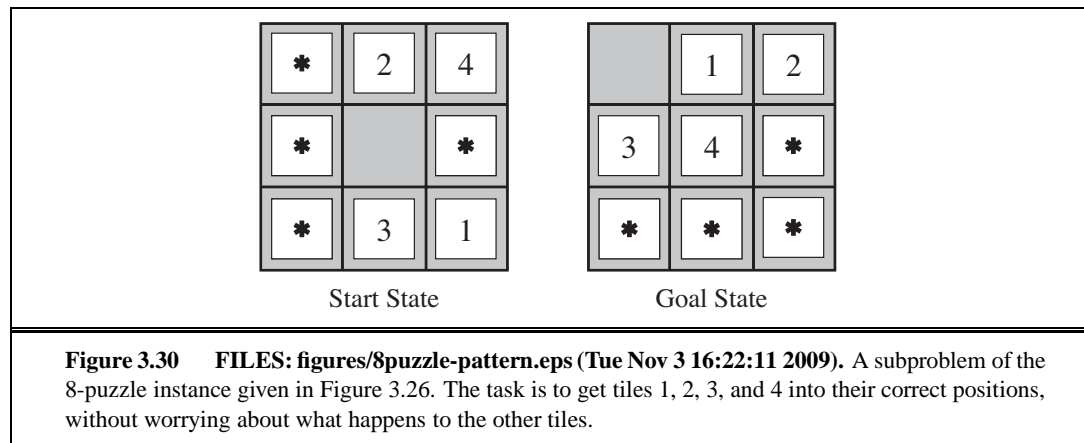
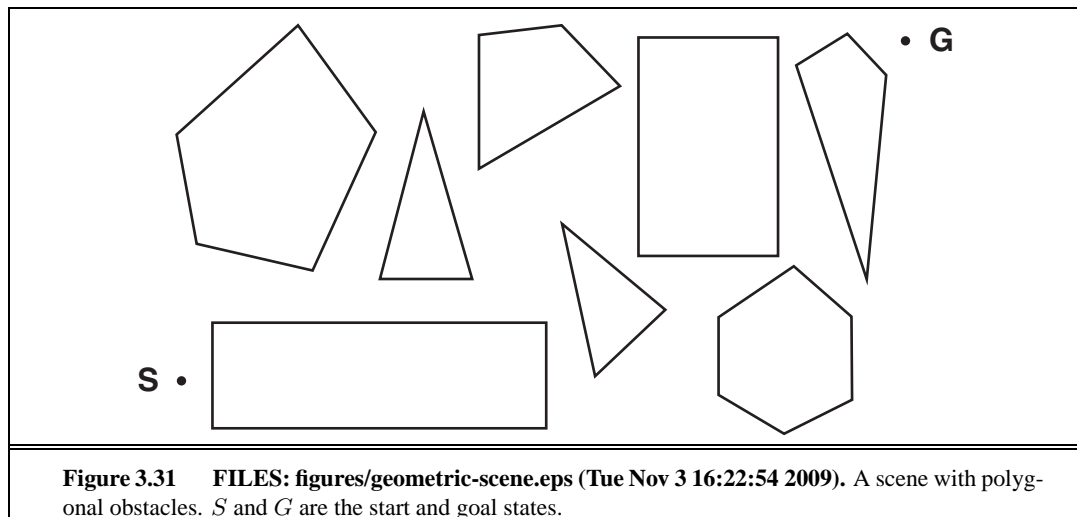
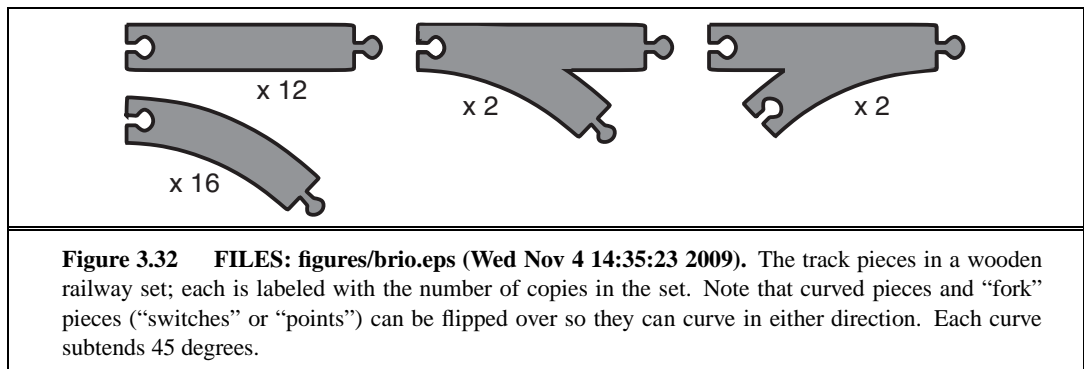


Figure 3.27 FILES: figures/rbfs-progress.eps (Tue Nov 3 16:23:27 2009). Stages in an RBFS search for the shortest route to Bucharest. The f -limit value for each recursive call is shown on top of each current node, and every node is labeled with its f -cost. (a) The path via Rimnicu Vilcea is followed until the current best leaf (Pitesti) has a value that is worse than the best alternative path (Fagaras). (b) The recursion unwinds and the best leaf value of the forgotten subtree (417) is backed up to Rimnicu Vilcea; then Fagaras is expanded, revealing a best leaf value of 450. (c) The recursion unwinds and the best leaf value of the forgotten subtree (450) is backed up to Fagaras; then Rimnicu Vilcea is expanded. This time, because the best alternative path (through Timisoara) costs at least 447, the expansion continues to Bucharest.



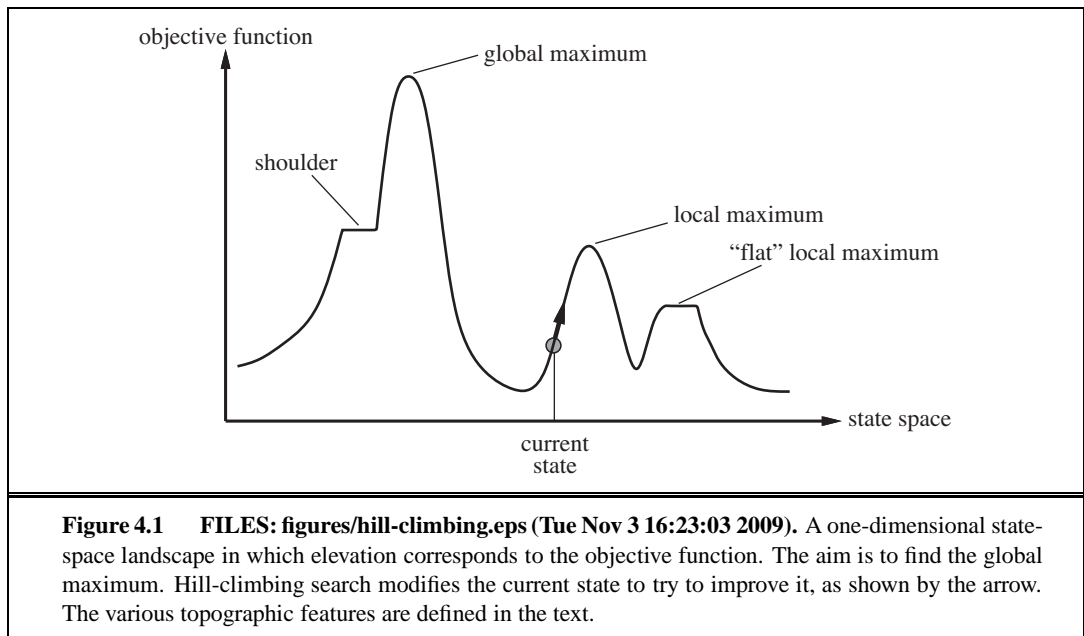






4

BEYOND CLASSICAL SEARCH



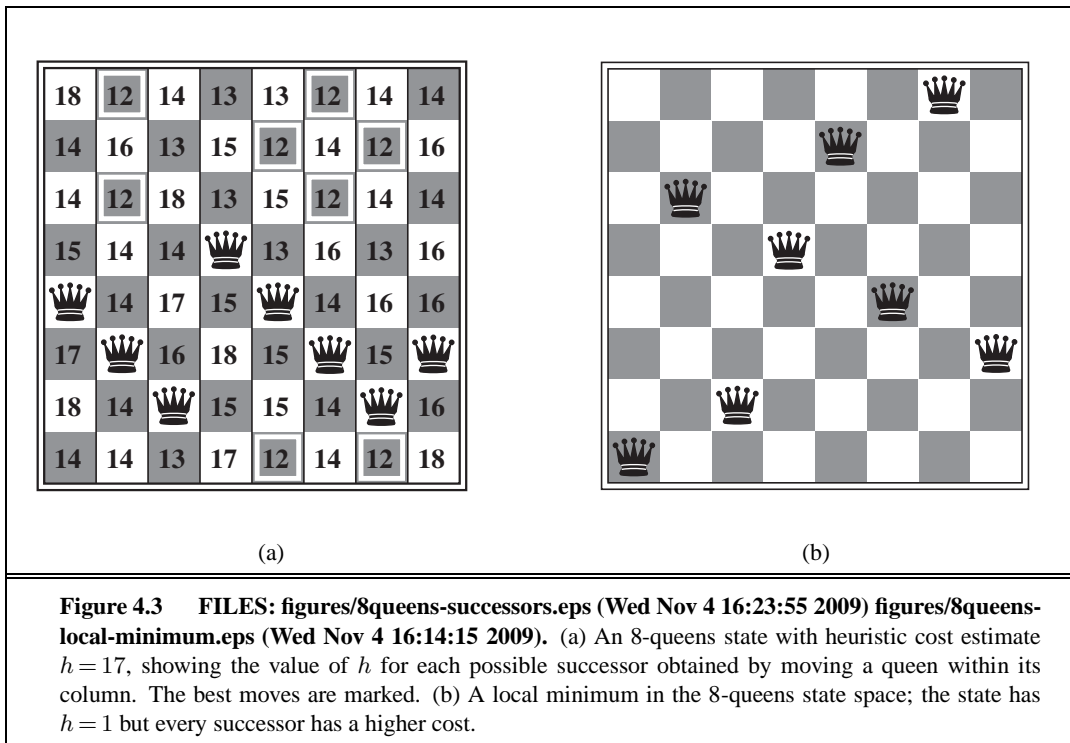


Figure 4.3 FILES: figures/8queens-successors.eps (Wed Nov 4 16:23:55 2009) figures/8queens-local-minimum.eps (Wed Nov 4 16:14:15 2009). (a) An 8-queens state with heuristic cost estimate $h = 17$, showing the value of h for each possible successor obtained by moving a queen within its column. The best moves are marked. (b) A local minimum in the 8-queens state space; the state has $h = 1$ but every successor has a higher cost.

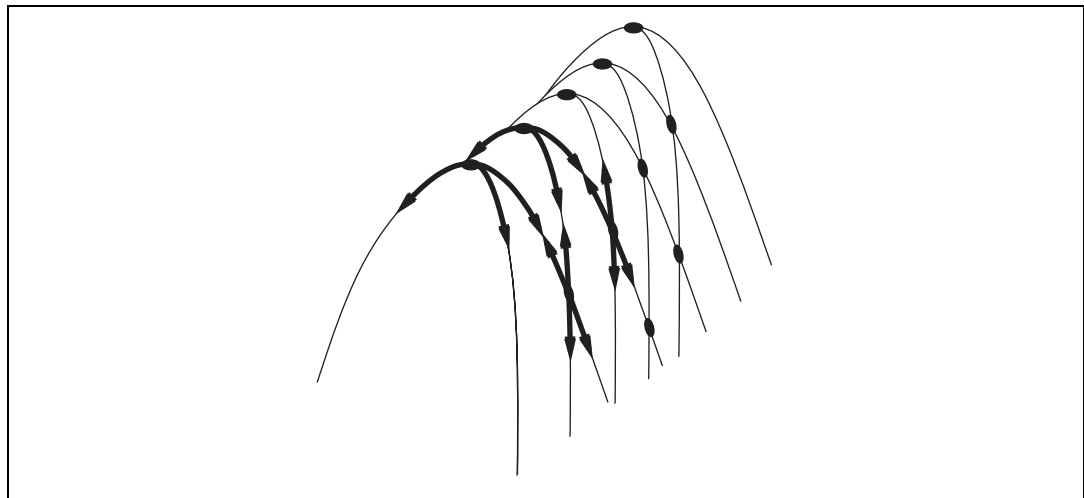
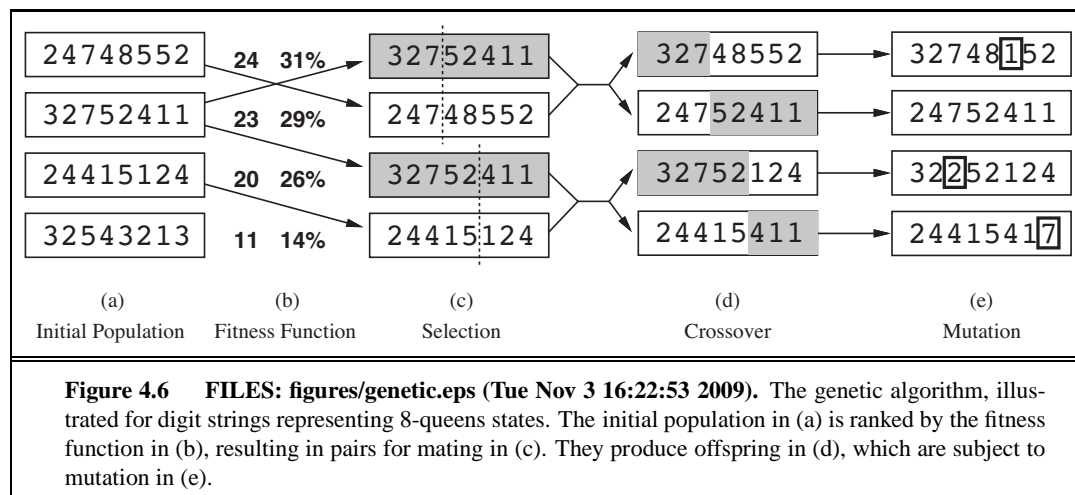
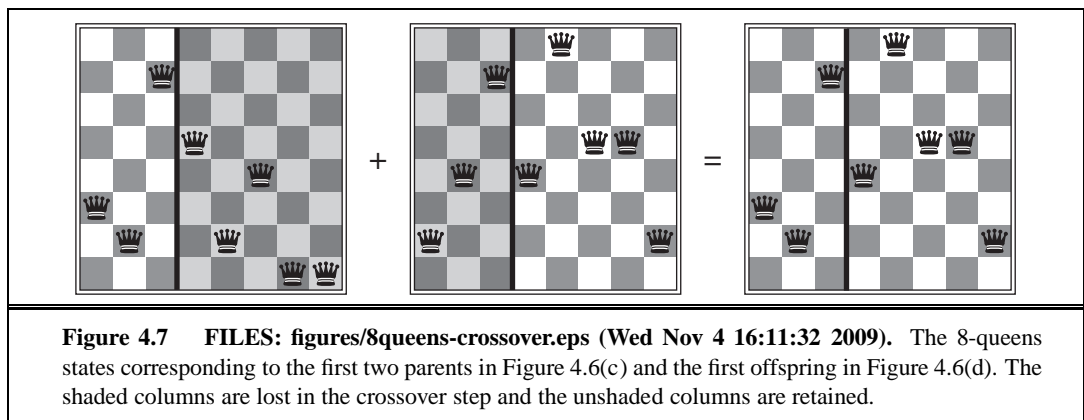
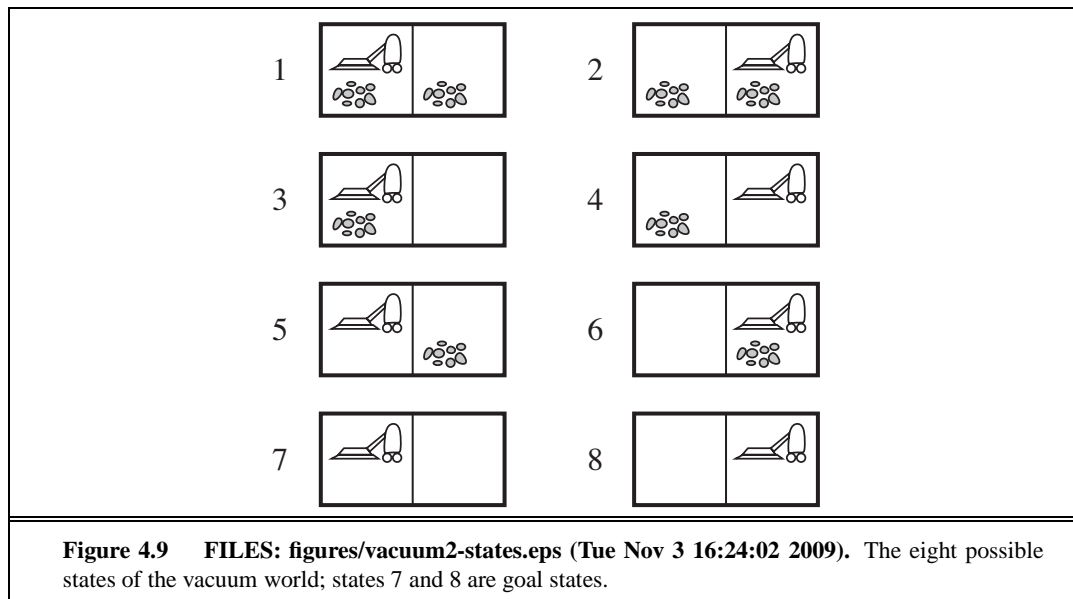
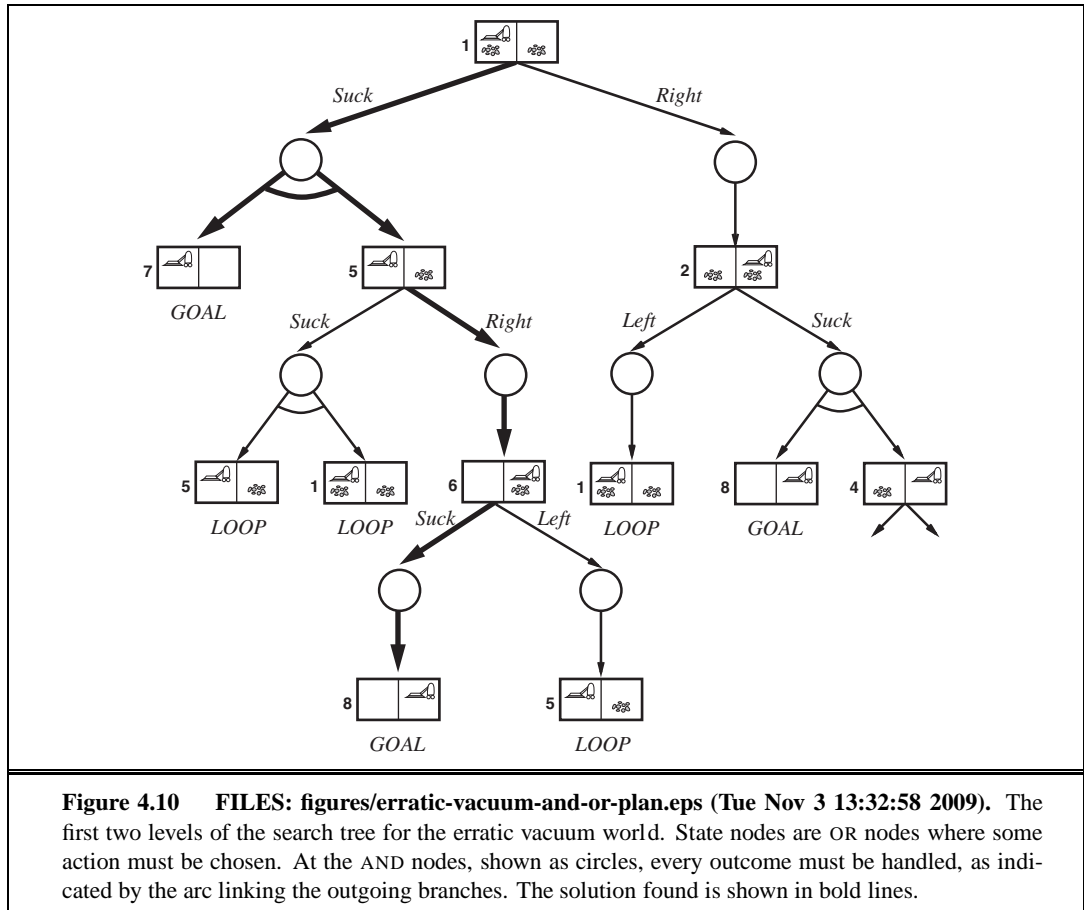


Figure 4.4 FILES: figures/ridge.eps (Tue Nov 3 16:23:29 2009). Illustration of why ridges cause difficulties for hill climbing. The grid of states (dark circles) is superimposed on a ridge rising from left to right, creating a sequence of local maxima that are not directly connected to each other. From each local maximum, all the available actions point downhill.









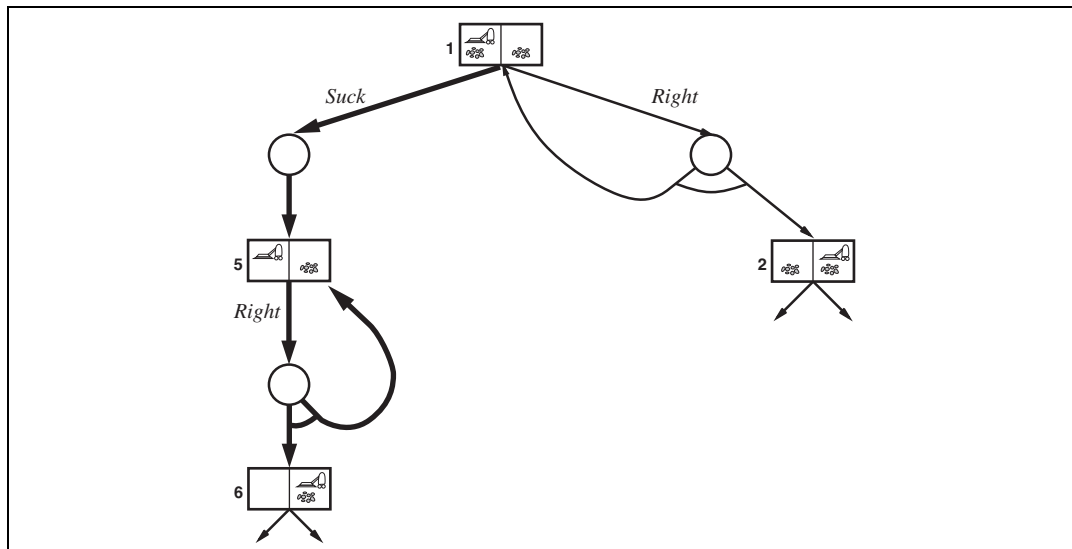
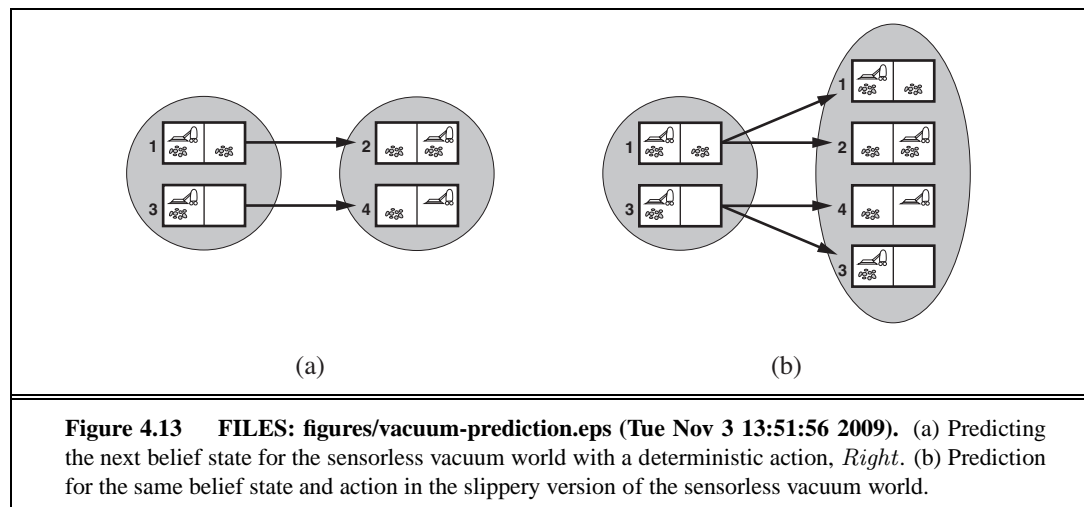


Figure 4.12 FILES: `figures/slippery-vacuum-loop-plan.eps` (Tue Nov 3 13:48:56 2009). Part of the search graph for the slippery vacuum world, where we have shown (some) cycles explicitly. All solutions for this problem are cyclic plans because there is no way to move reliably.



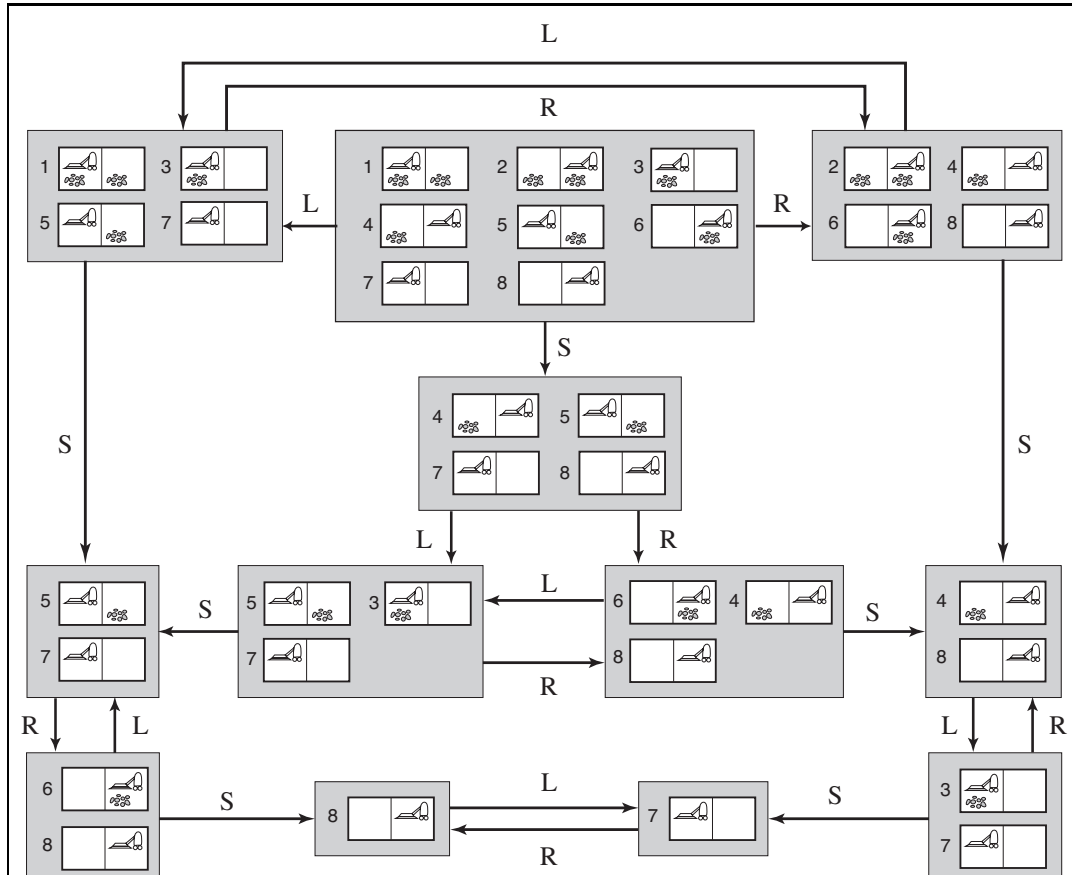


Figure 4.14 FILES: figures/vacuum2-sets.eps (Tue Nov 3 16:24:01 2009). The reachable portion of the belief-state space for the deterministic, sensorless vacuum world. Each shaded box corresponds to a single belief state. At any given point, the agent is in a particular belief state but does not know which physical state it is in. The initial belief state (complete ignorance) is the top center box. Actions are represented by labeled links. Self-loops are omitted for clarity.

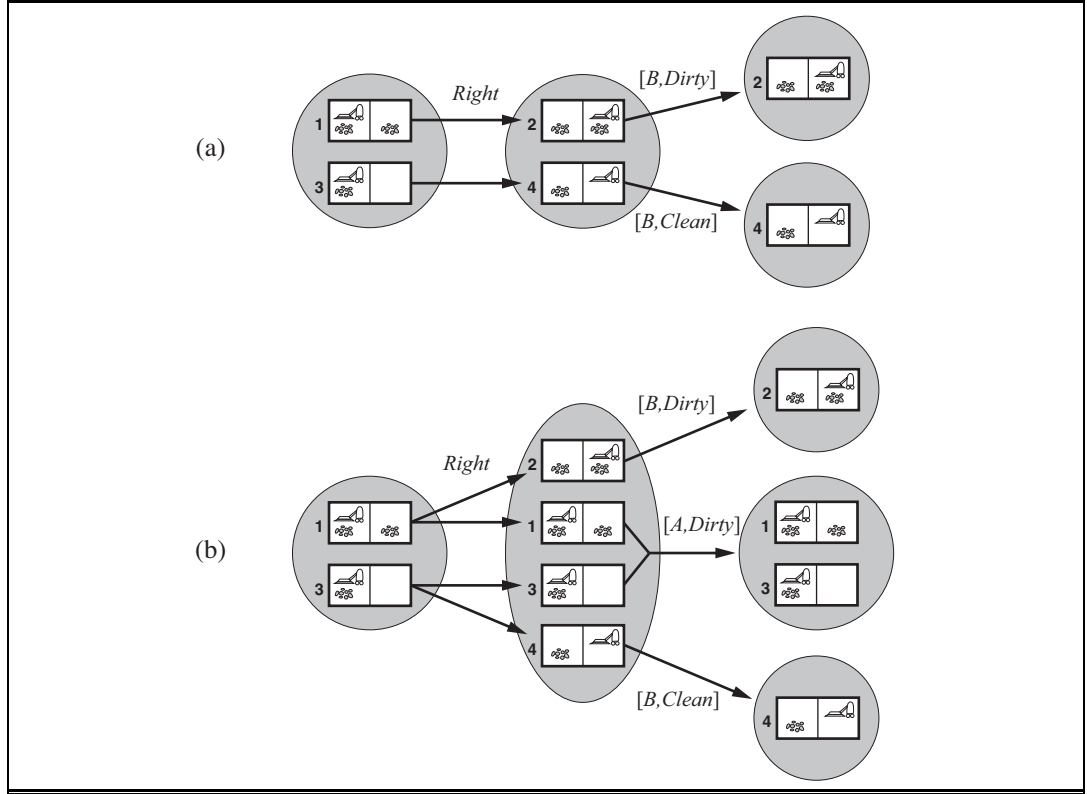
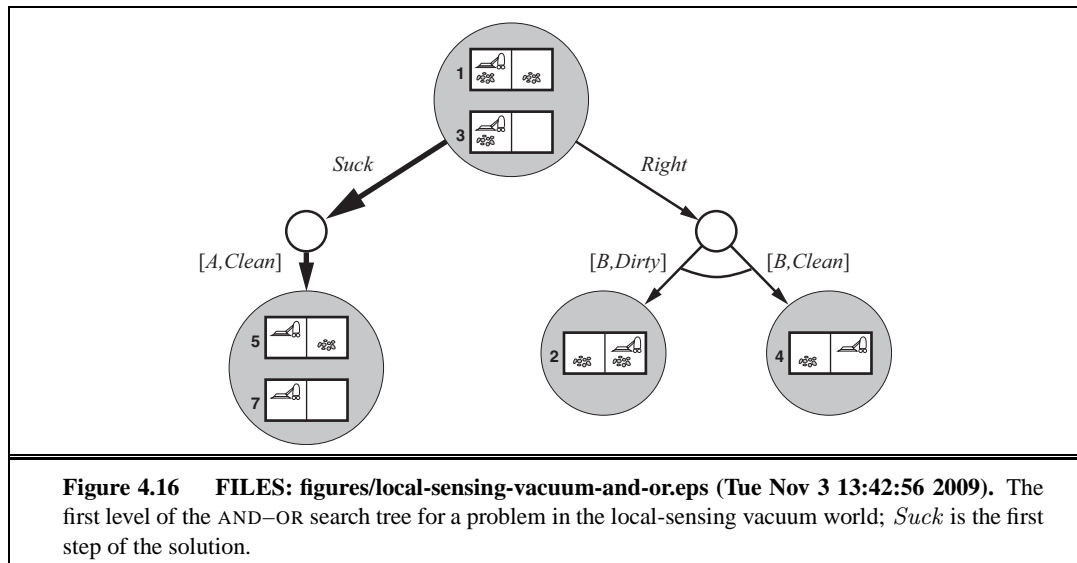
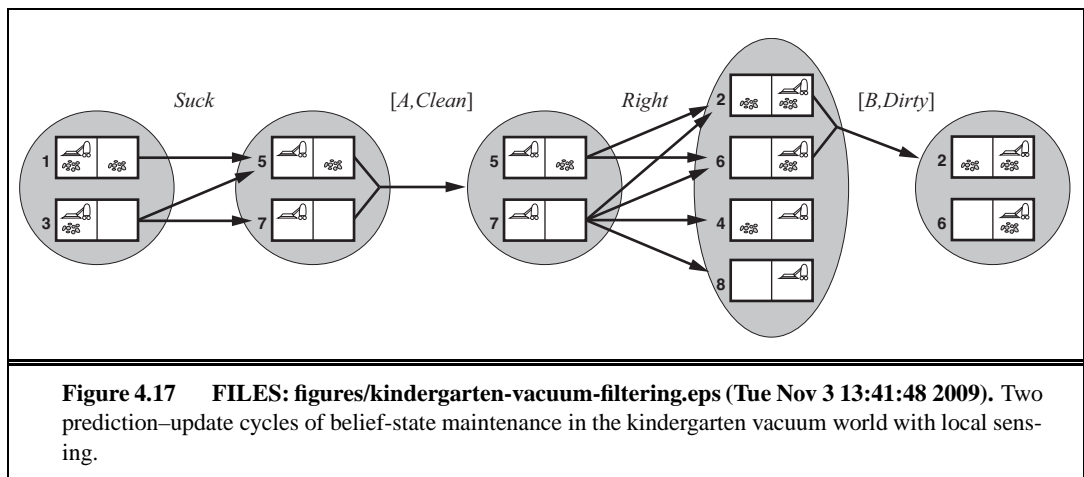
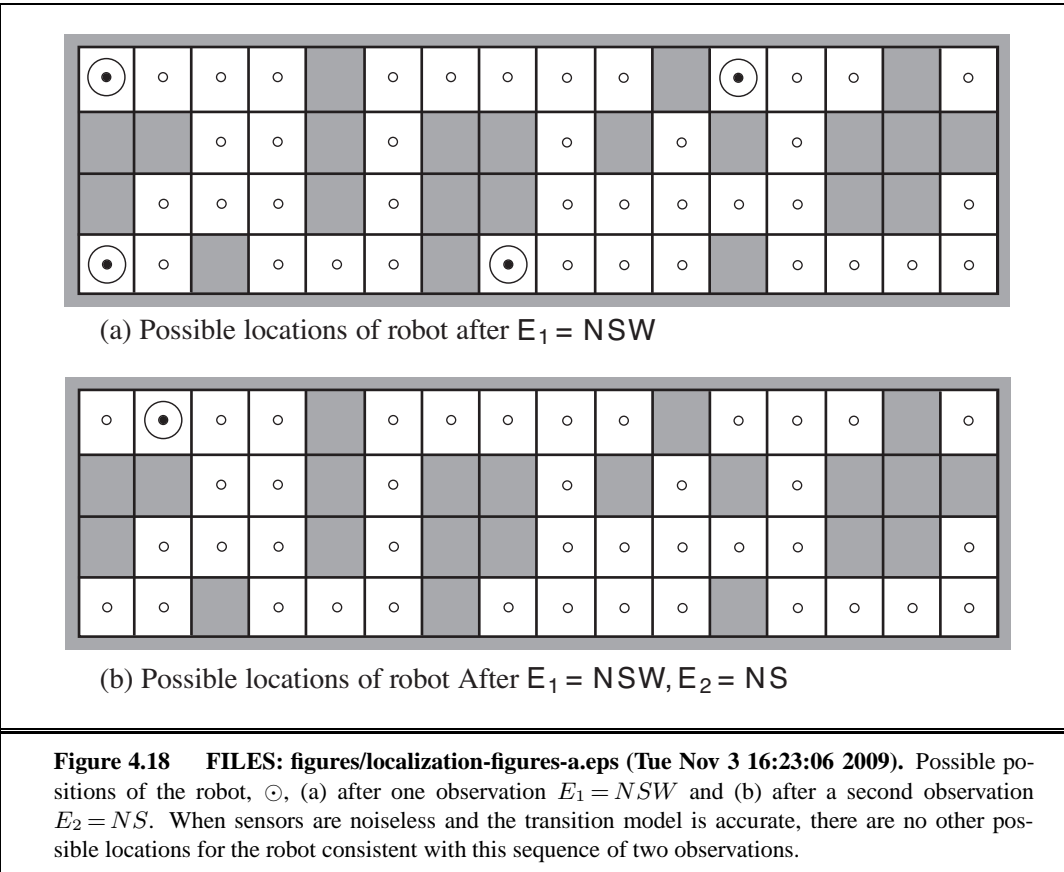
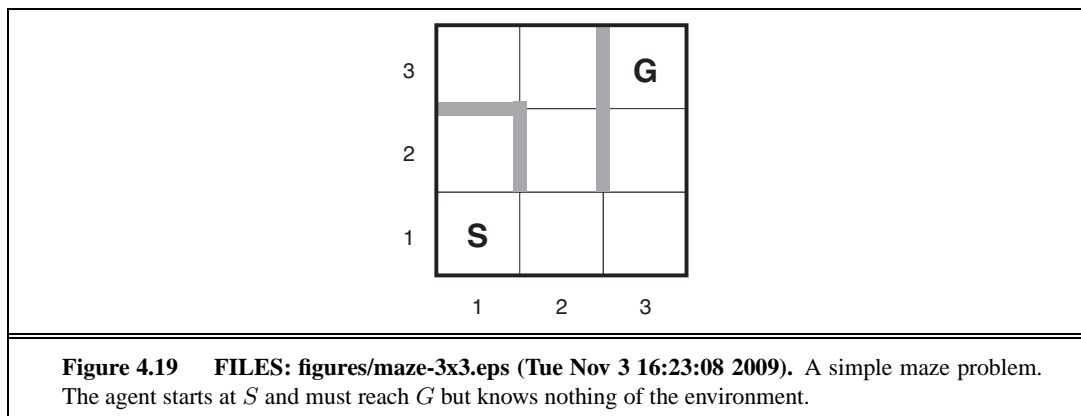


Figure 4.15 FILES: figures/vacuum-prediction-update.eps (Tue Nov 3 13:52:01 2009). Two examples of transitions in local-sensing vacuum worlds. (a) In the deterministic world, *Right* is applied in the initial belief state, resulting in a new belief state with two possible physical states; for those states, the possible percepts are $[B, \text{Dirty}]$ and $[B, \text{Clean}]$, leading to two belief states, each of which is a singleton. (b) In the slippery world, *Right* is applied in the initial belief state, giving a new belief state with four physical states; for those states, the possible percepts are $[A, \text{Dirty}]$, $[B, \text{Dirty}]$, and $[B, \text{Clean}]$, leading to three belief states as shown.









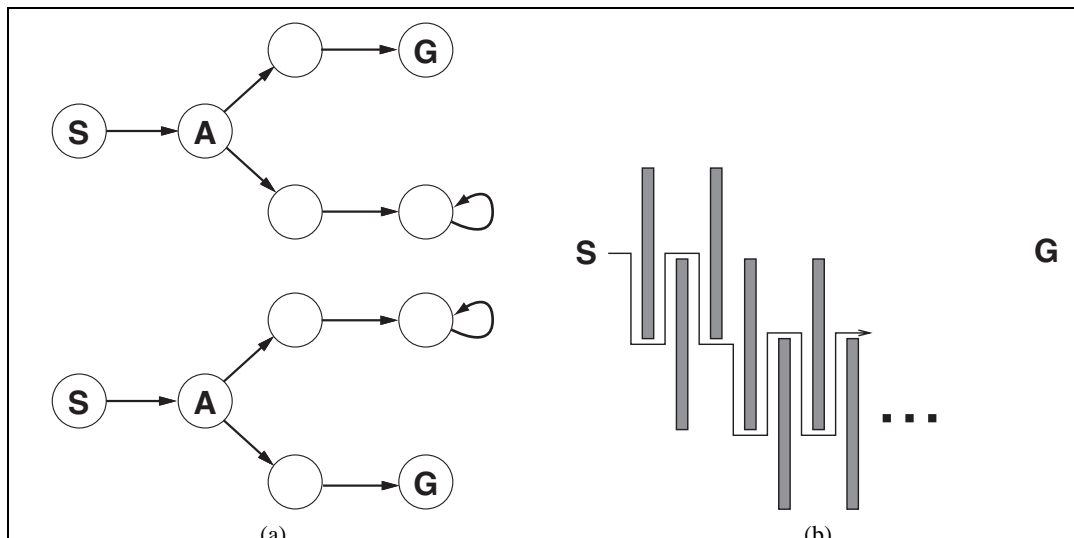
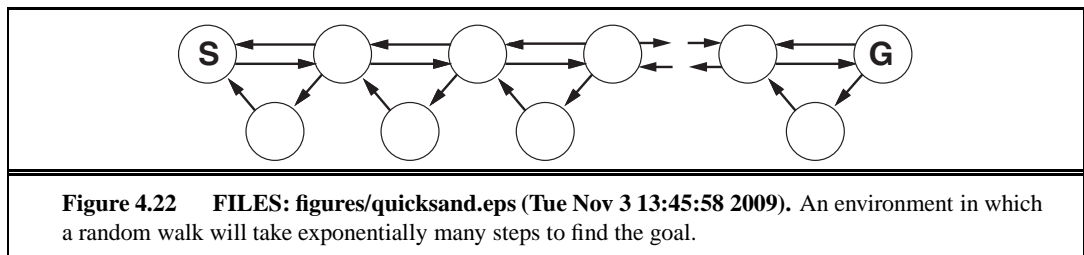


Figure 4.20 FILES: figures/adversary-spaces.eps (Tue Nov 3 16:22:18 2009) figures/adversary-blocks.eps (Sun Oct 25 01:08:26 2009). (a) Two state spaces that might lead an online search agent into a dead end. Any given agent will fail in at least one of these spaces. (b) A two-dimensional environment that can cause an online search agent to follow an arbitrarily inefficient route to the goal. Whichever choice the agent makes, the adversary blocks that route with another long, thin wall, so that the path followed is much longer than the best possible path.



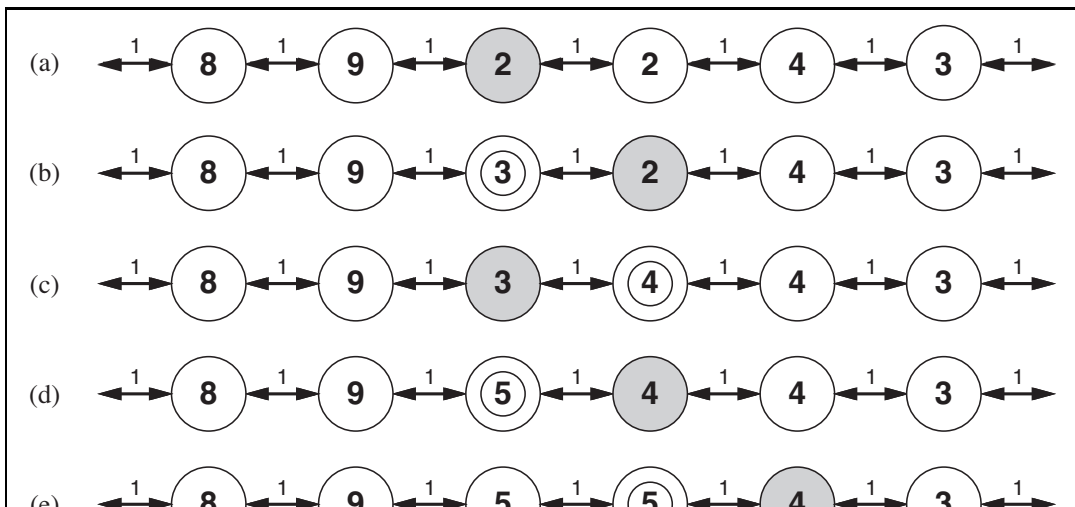
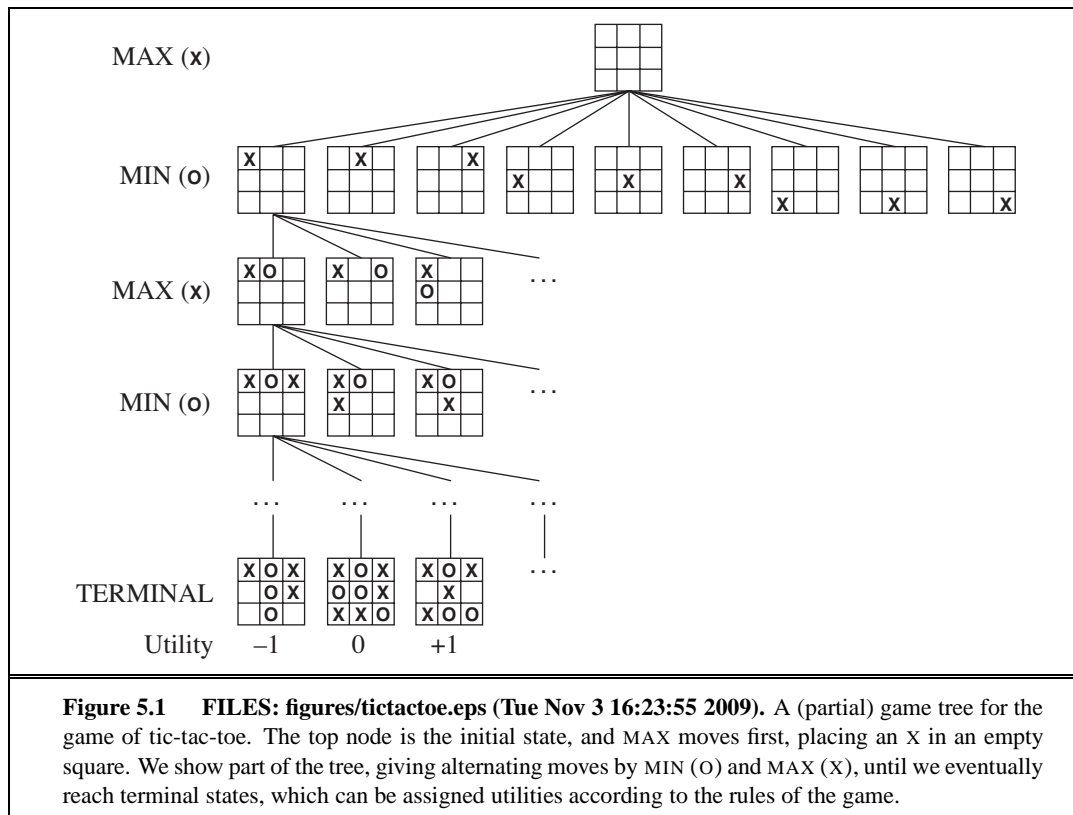


Figure 4.23 FILES: figures/lrta-progress.eps (Tue Nov 3 16:23:08 2009). Five iterations of LRTA* on a one-dimensional state space. Each state is labeled with $H(s)$, the current cost estimate to reach a goal, and each link is labeled with its step cost. The shaded state marks the location of the agent, and the updated cost estimates at each iteration are circled.

5

ADVERSARIAL SEARCH



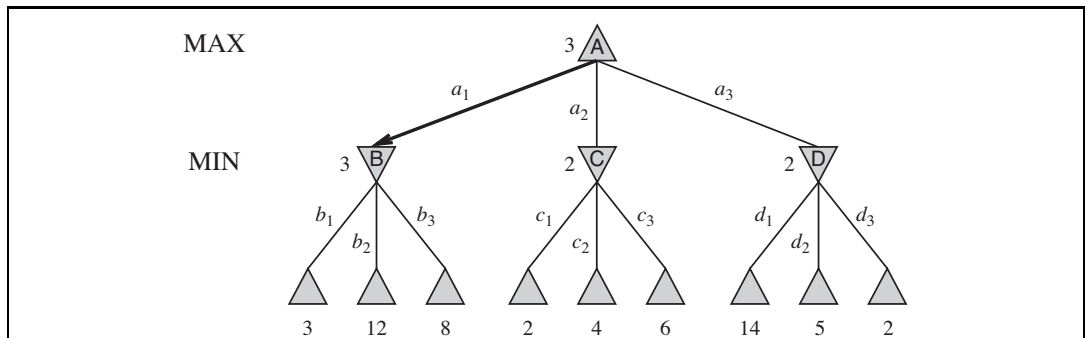
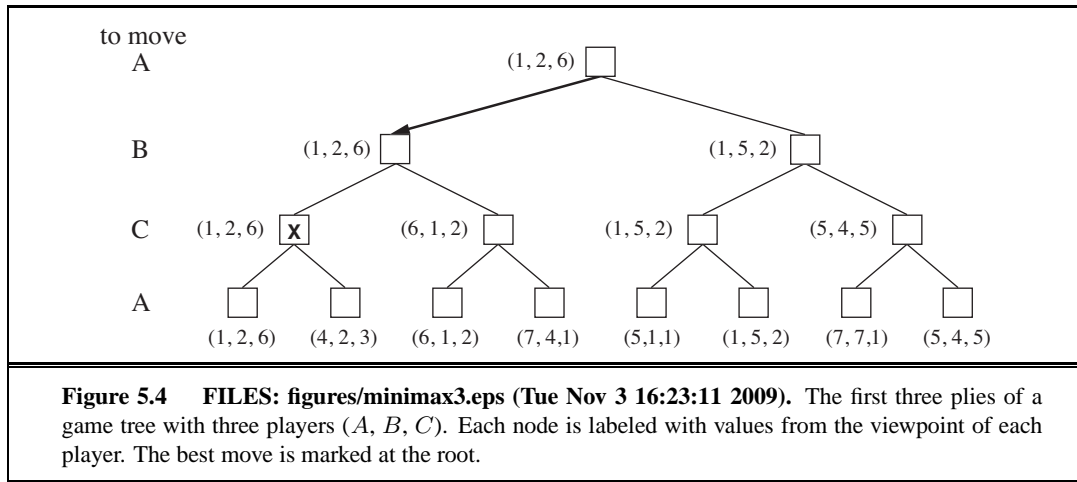


Figure 5.2 FILES: figures/minimax.eps (Tue Nov 3 16:23:11 2009). A two-ply game tree. The \triangle nodes are “MAX nodes,” in which it is MAX’s turn to move, and the ∇ nodes are “MIN nodes.” The terminal nodes show the utility values for MAX; the other nodes are labeled with their minimax values. MAX’s best move at the root is a_1 , because it leads to the state with the highest minimax value, and MIN’s best reply is b_1 , because it leads to the state with the lowest minimax value.



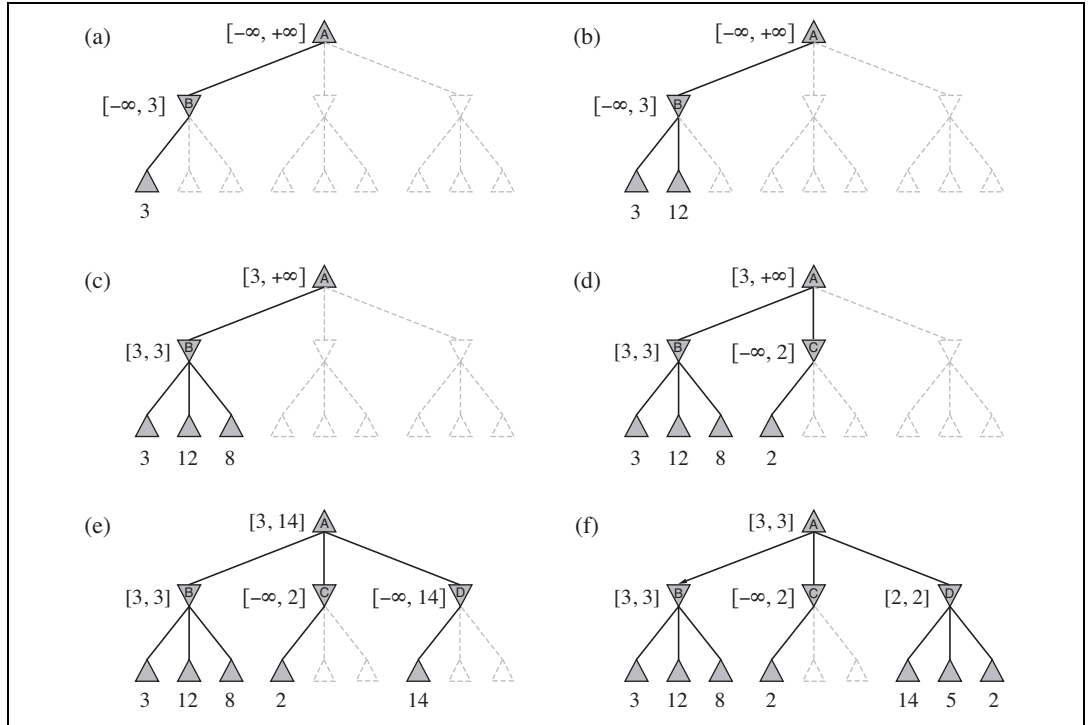
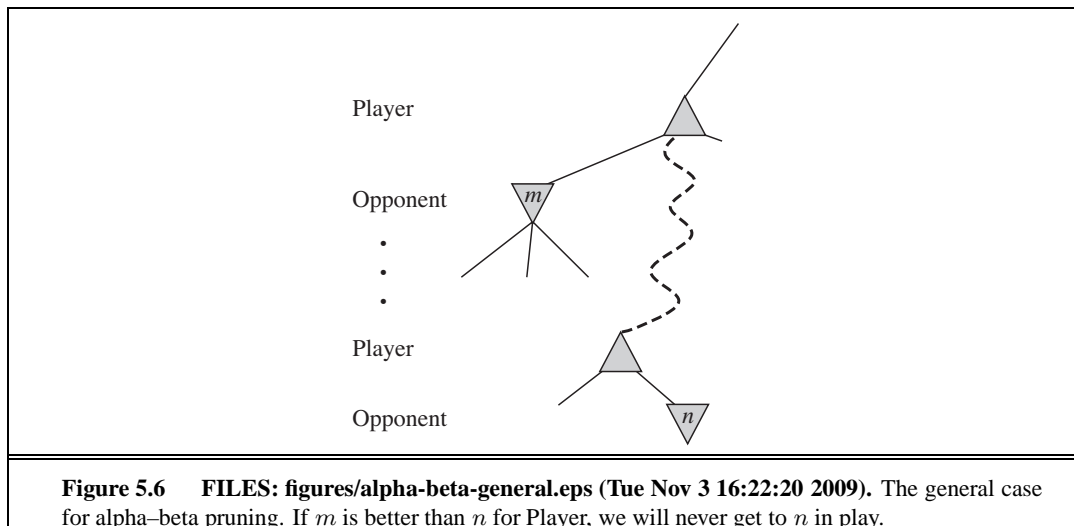


Figure 5.5 FILES: figures/alpha-beta-progress.eps (Tue Nov 3 16:22:20 2009). Stages in the calculation of the optimal decision for the game tree in Figure 5.2. At each point, we show the range of possible values for each node. (a) The first leaf below B has the value 3. Hence, B, which is a MIN node, has a value of *at most* 3. (b) The second leaf below B has a value of 12; MIN would avoid this move, so the value of B is still at most 3. (c) The third leaf below B has a value of 8; we have seen all B's successor states, so the value of B is exactly 3. Now, we can infer that the value of the root is *at least* 3, because MAX has a choice worth 3 at the root. (d) The first leaf below C has the value 2. Hence, C, which is a MIN node, has a value of *at most* 2. But we know that B is worth 3, so MAX would never choose C. Therefore, there is no point in looking at the other successor states of C. This is an example of alpha-beta pruning. (e) The first leaf below D has the value 14, so D is worth *at most* 14. This is still higher than MAX's best alternative (i.e., 3), so we need to keep exploring D's successor states. Notice also that we now have bounds on all of the successors of the root, so the root's value is also at most 14. (f) The second successor of D is worth 5, so again we need to keep exploring. The third successor is worth 2, so now D is worth exactly 2. MAX's decision at the root is to move to B, giving a value of 3.



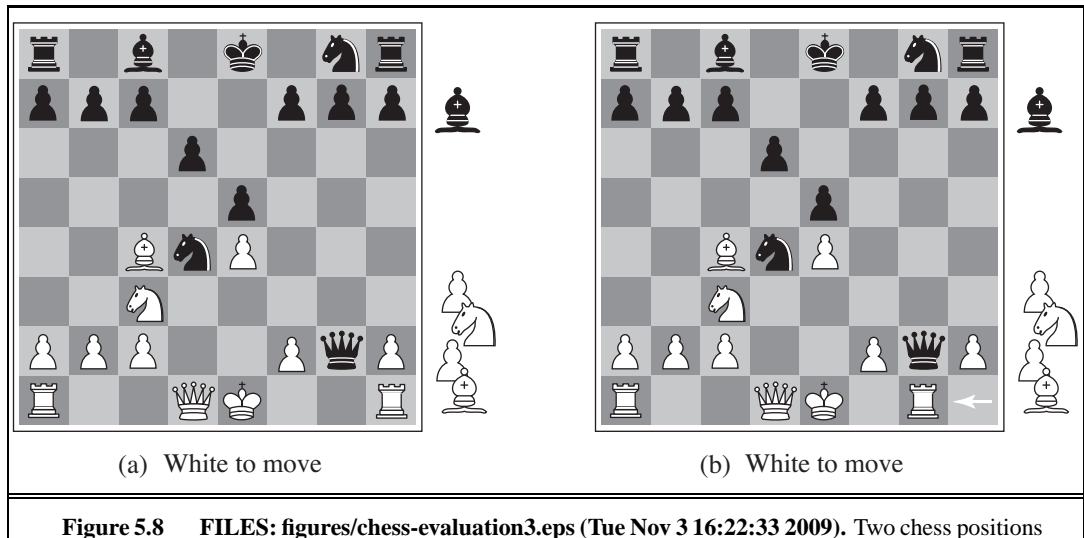


Figure 5.8 FILES: figures/chess-evaluation3.eps (Tue Nov 3 16:22:33 2009). Two chess positions that differ only in the position of the rook at lower right. In (a), Black has an advantage of a knight and two pawns, which should be enough to win the game. In (b), White will capture the queen, giving it an advantage that should be strong enough to win.

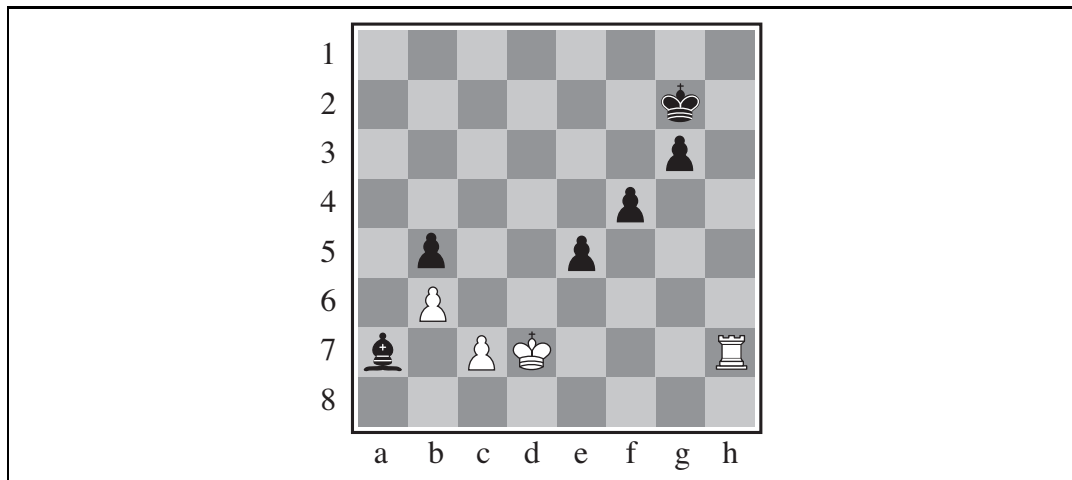


Figure 5.9 FILES: figures/horizon.eps (Tue Nov 3 16:23:03 2009). The horizon effect. With Black to move, the black bishop is surely doomed. But Black can forestall that event by checking the white king with its pawns, forcing the king to capture the pawns. This pushes the inevitable loss of the bishop over the horizon, and thus the pawn sacrifices are seen by the search algorithm as good moves rather than bad ones.

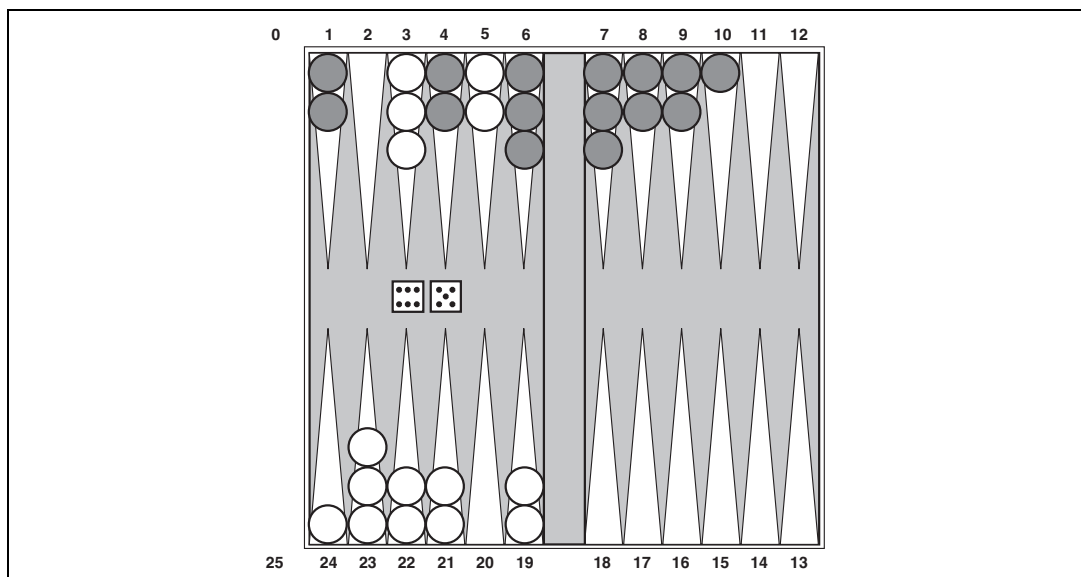
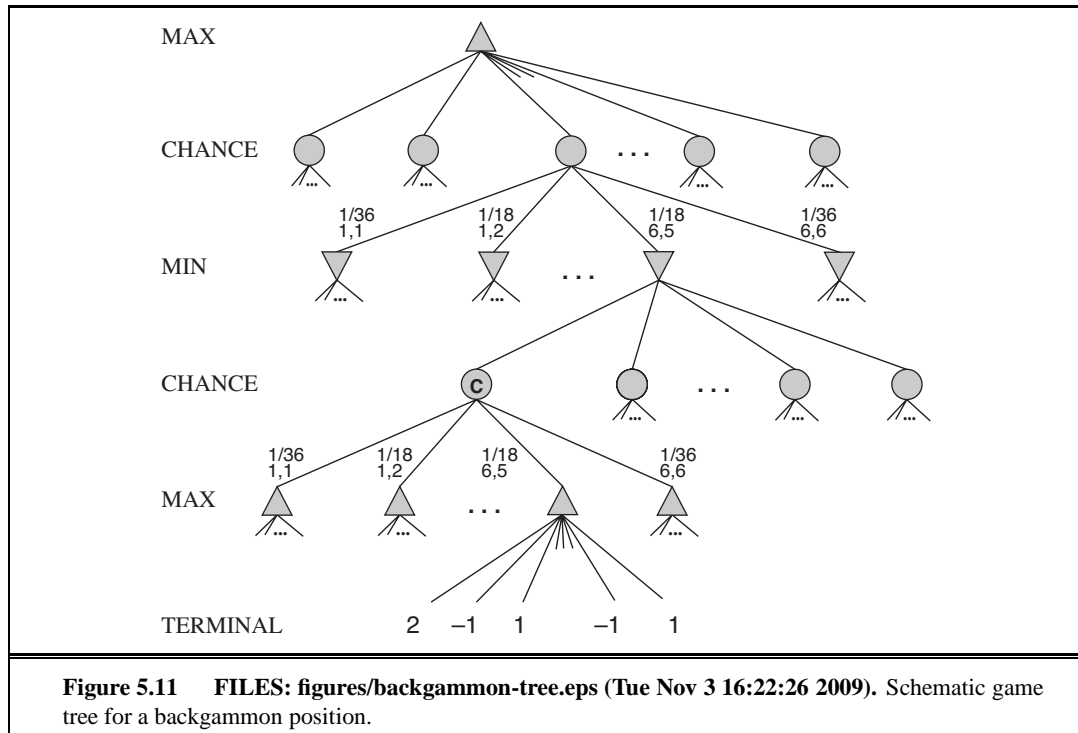


Figure 5.10 FILES: figures/backgammon-position.eps (Tue Nov 3 16:22:26 2009). A typical backgammon position. The goal of the game is to move all one's pieces off the board. White moves clockwise toward 25, and Black moves counterclockwise toward 0. A piece can move to any position unless multiple opponent pieces are there; if there is one opponent, it is captured and must start over. In the position shown, White has rolled 6–5 and must choose among four legal moves: (5–10,5–11), (5–11,19–24), (5–10,10–16), and (5–11,11–16), where the notation (5–11,11–16) means move one piece from position 5 to 11, and then move a piece from 11 to 16.



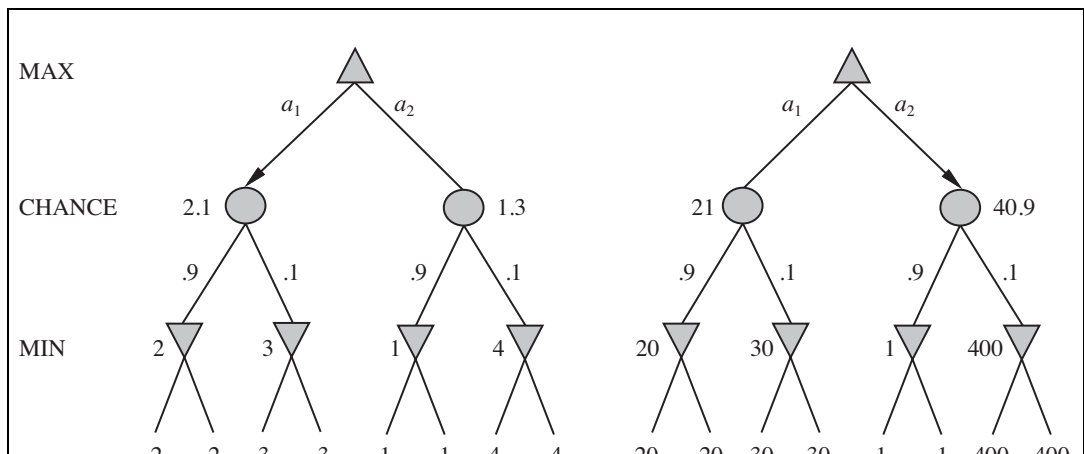
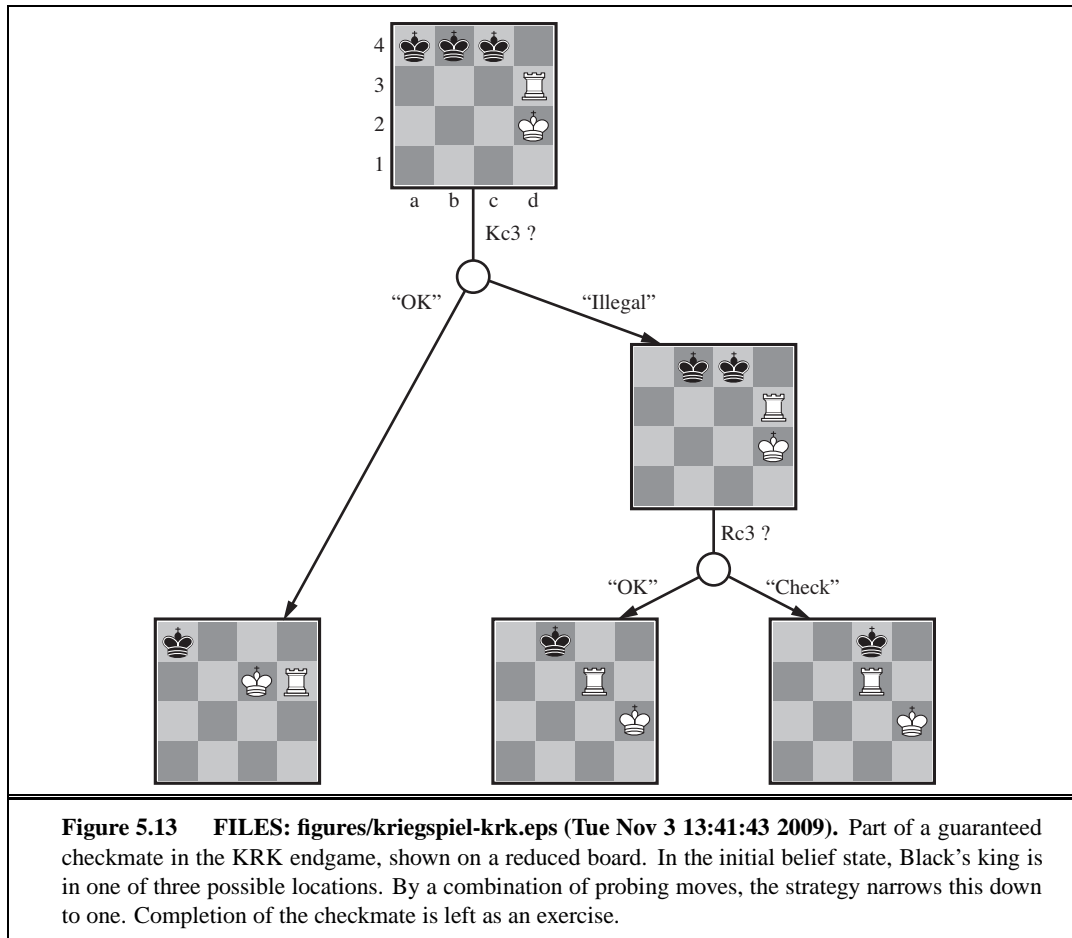
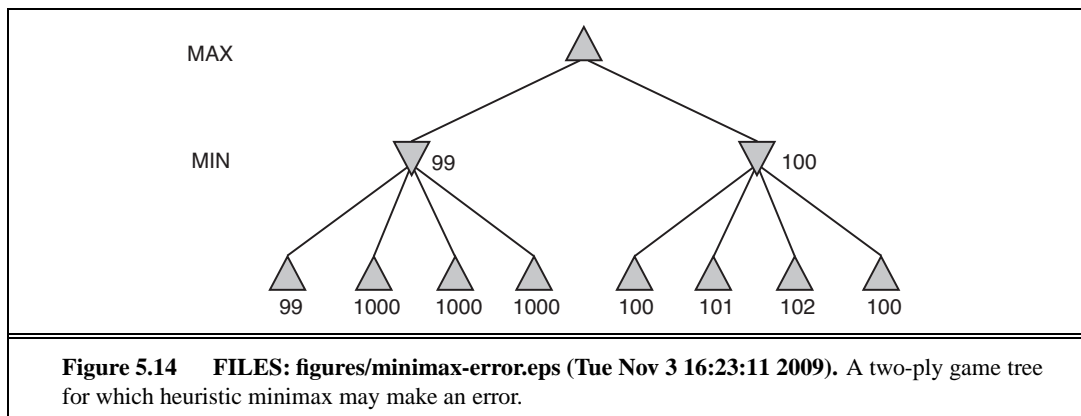
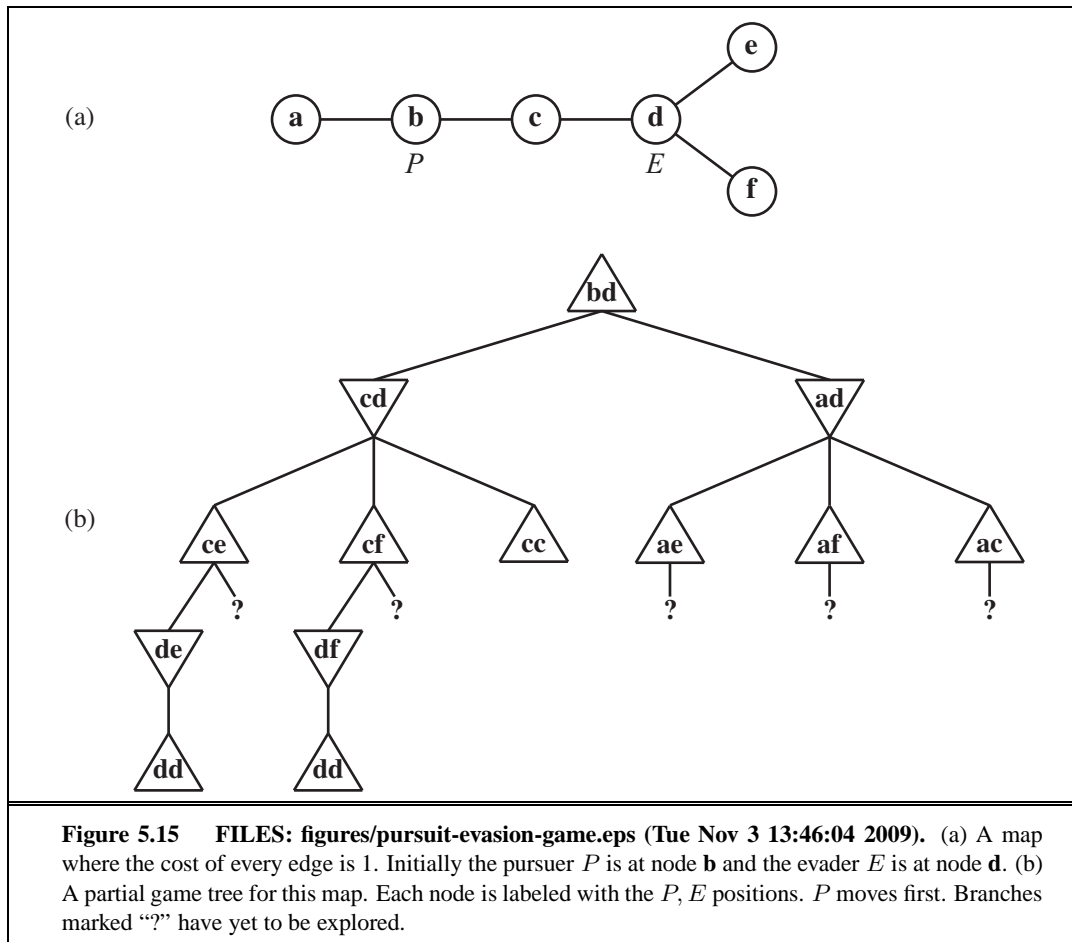
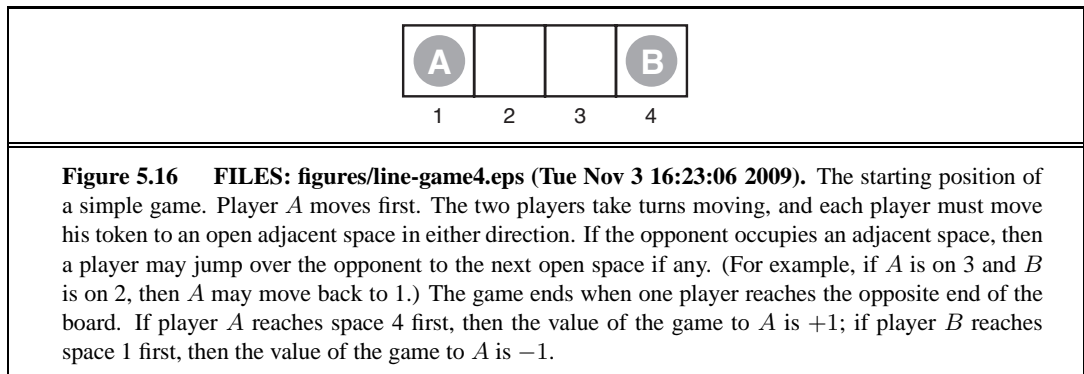


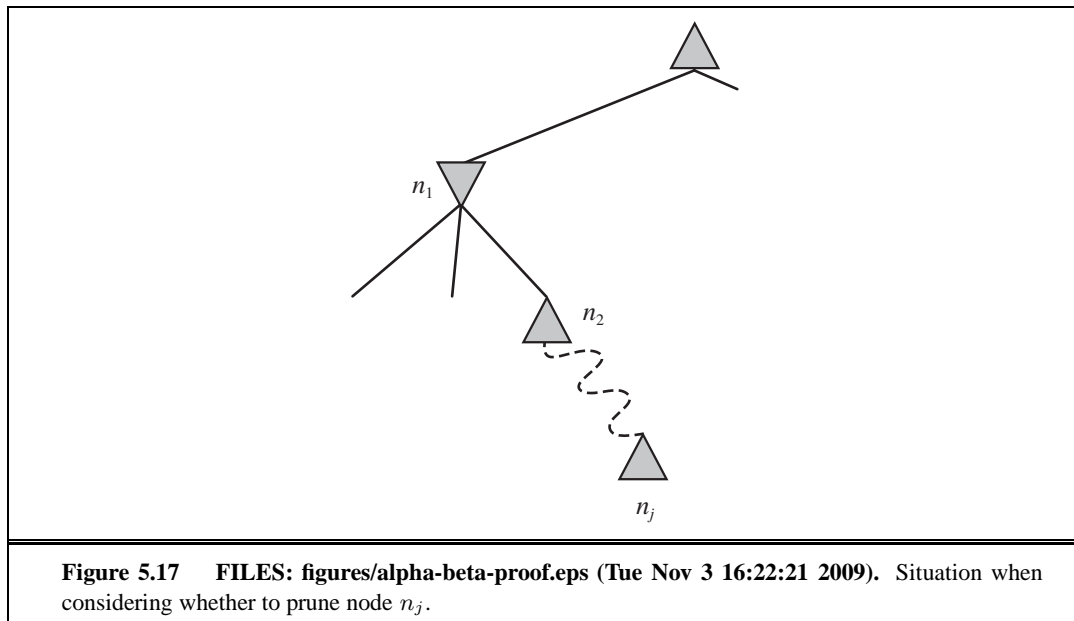
Figure 5.12 FILES: figures/chance-evaluation.eps (Tue Nov 3 16:22:32 2009). An order-preserving transformation on leaf values changes the best move.

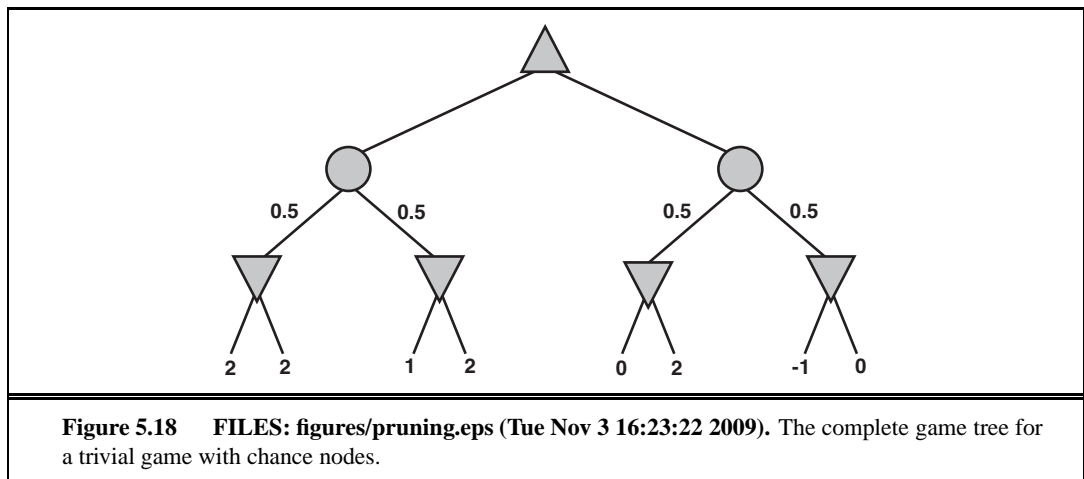








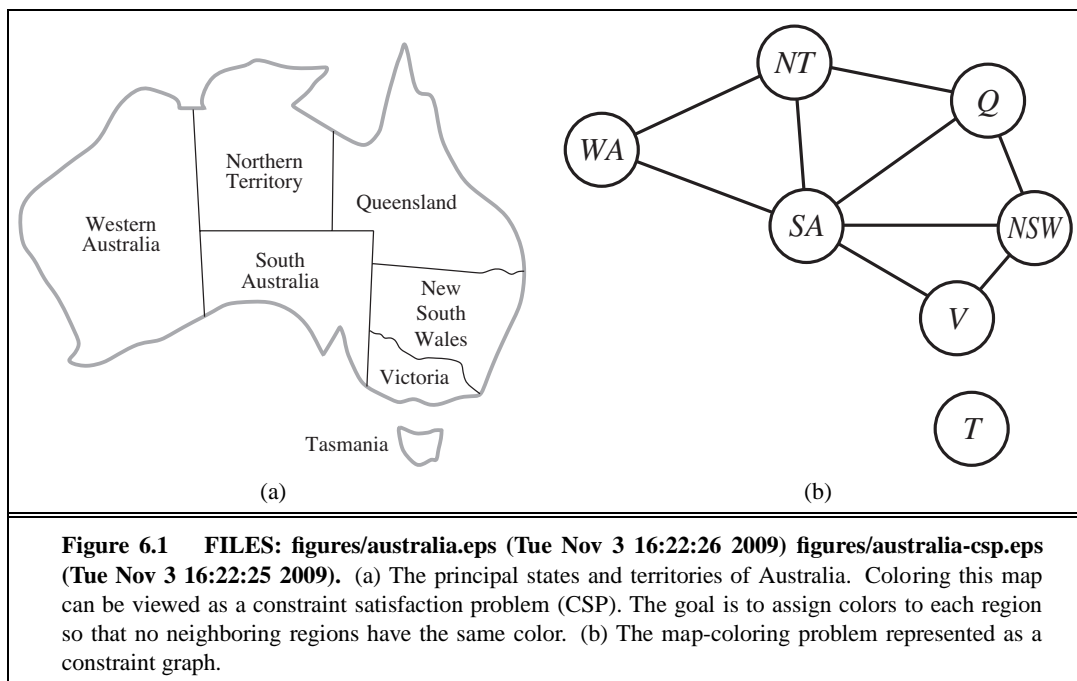


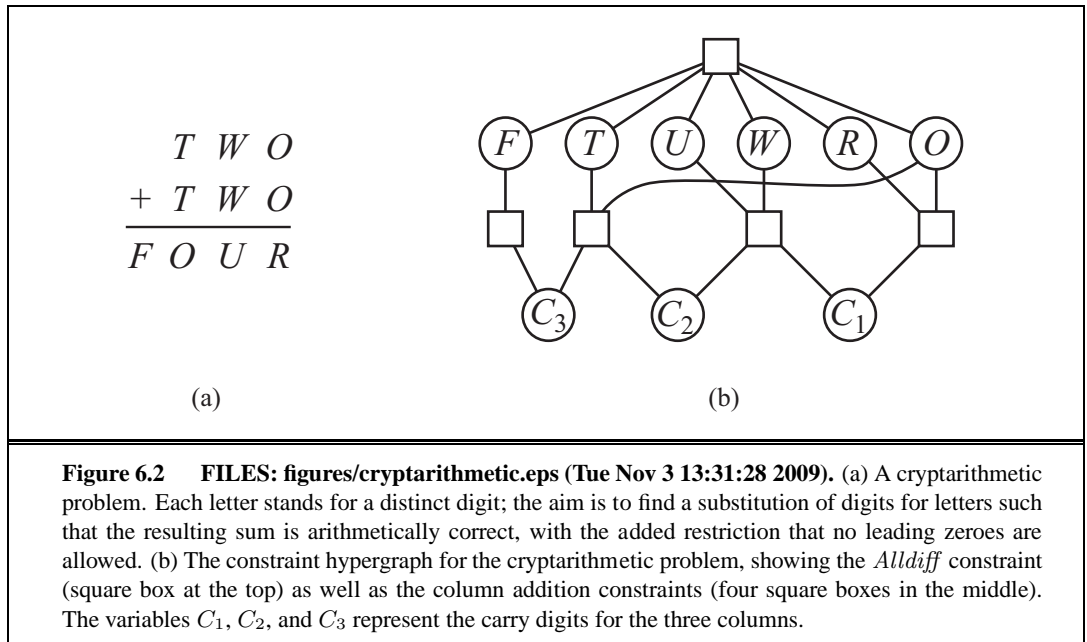




6

CONSTRAINT SATISFACTION PROBLEMS





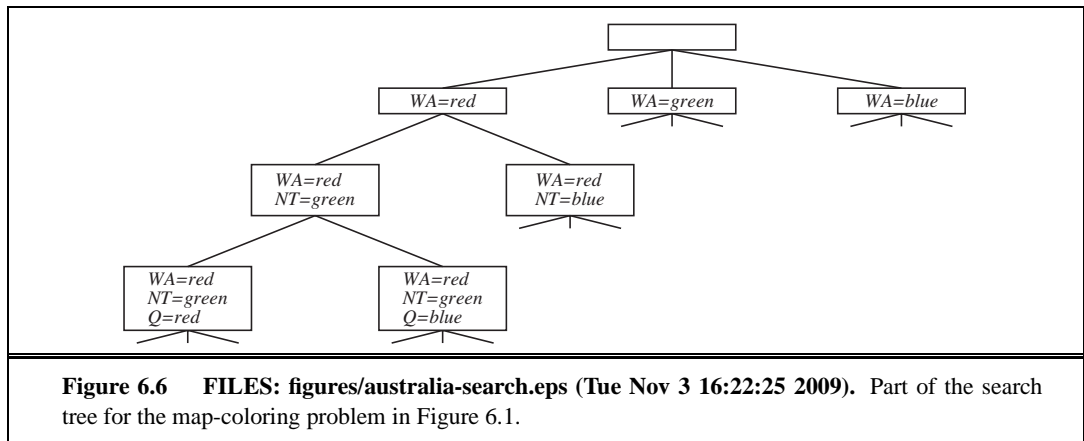
	1	2	3	4	5	6	7	8	9
A			3	2		6			
B	9			3	5				1
C			1	8		6	4		
D			8	1		2	9		
E	7								8
F			6	7		8	2		
G			2	6		9	5		
H	8			2	3				9
I			5		1		3		

(a)

	1	2	3	4	5	6	7	8	9
A	4	8	3	9	2	1	6	5	7
B	9	6	7	3	4	5	8	2	1
C	2	5	1	8	7	6	4	9	3
D	5	4	8	1	3	2	9	7	6
E	7	2	9	5	6	4	1	3	8
F	1	3	6	7	9	8	2	4	5
G	3	7	2	6	8	9	5	1	4
H	8	1	4	2	5	3	7	6	9
I	6	9	5	4	1	7	3	8	2

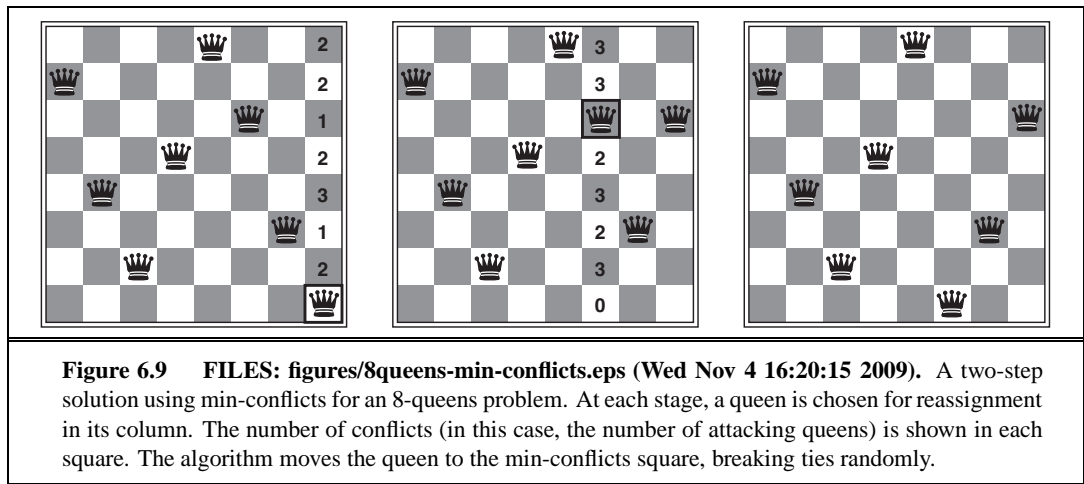
(b)

Figure 6.4 FILES: figures/sudoku.eps (Tue Nov 3 13:49:46 2009). (a) A Sudoku puzzle and (b) its solution.



	WA	NT	Q	NSW	V	SA	T
Initial domains	R G B	R G B	R G B	R G B	R G B	R G B	R G B
After $WA=red$	(R)	G B	R G B	R G B	R G B	G B	R G B
After $Q=green$	(R)	B	(G)	R B	R G B	B	R G B
After $V=blue$	(R)	B	(G)	R	(B)		R G B

Figure 6.7 FILES: figures/australia-fc.eps (Tue Nov 3 16:22:25 2009). The progress of a map-coloring search with forward checking. $WA = red$ is assigned first; then forward checking deletes *red* from the domains of the neighboring variables *NT* and *SA*. After $Q = green$ is assigned, *green* is deleted from the domains of *NT*, *SA*, and *NSW*. After $V = blue$ is assigned, *blue* is deleted from the domains of *NSW* and *SA*, leaving *SA* with no legal values.



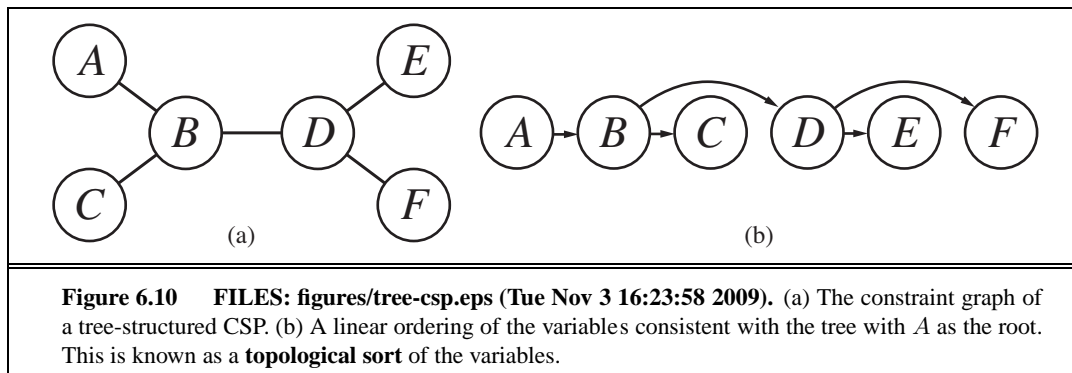


Figure 6.10 FILES: figures/tree-csp.eps (Tue Nov 3 16:23:58 2009). (a) The constraint graph of a tree-structured CSP. (b) A linear ordering of the variables consistent with the tree with A as the root. This is known as a **topological sort** of the variables.

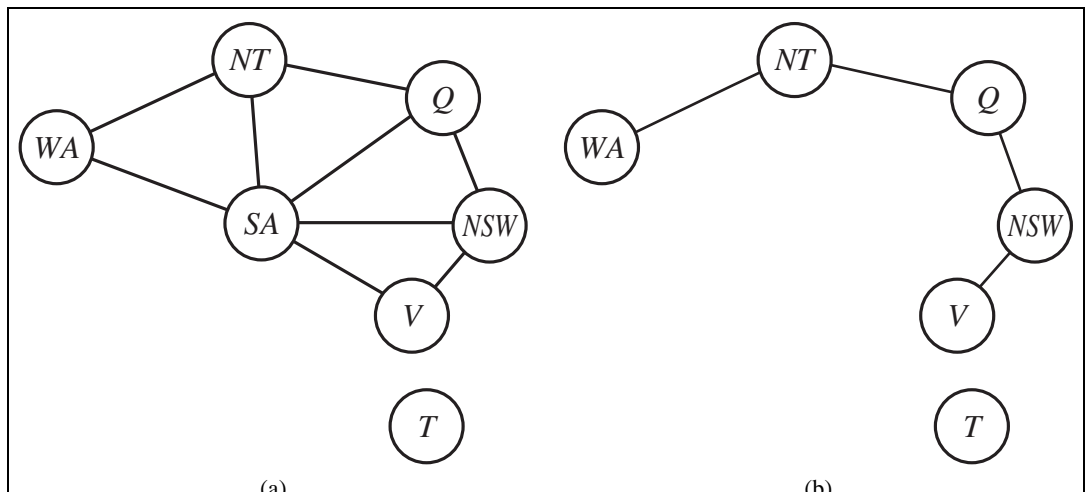
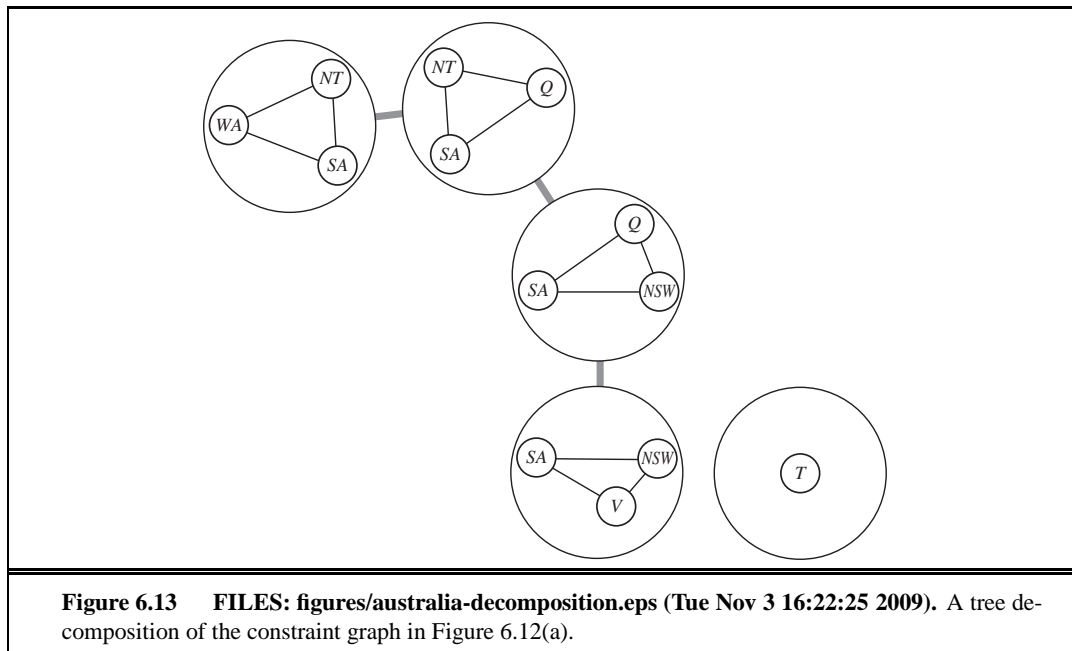


Figure 6.12 FILES: figures/australia-csp.eps (Tue Nov 3 16:22:25 2009) figures/australia-tree.eps (Tue Nov 3 16:22:26 2009). (a) The original constraint graph from Figure 6.1. (b) The constraint graph after the removal of *SA*.



7

LOGICAL AGENTS

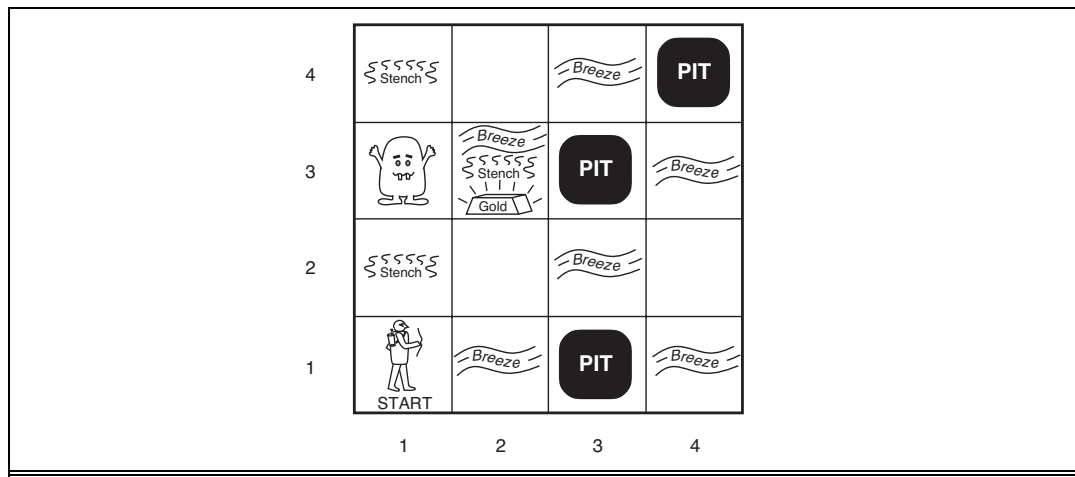
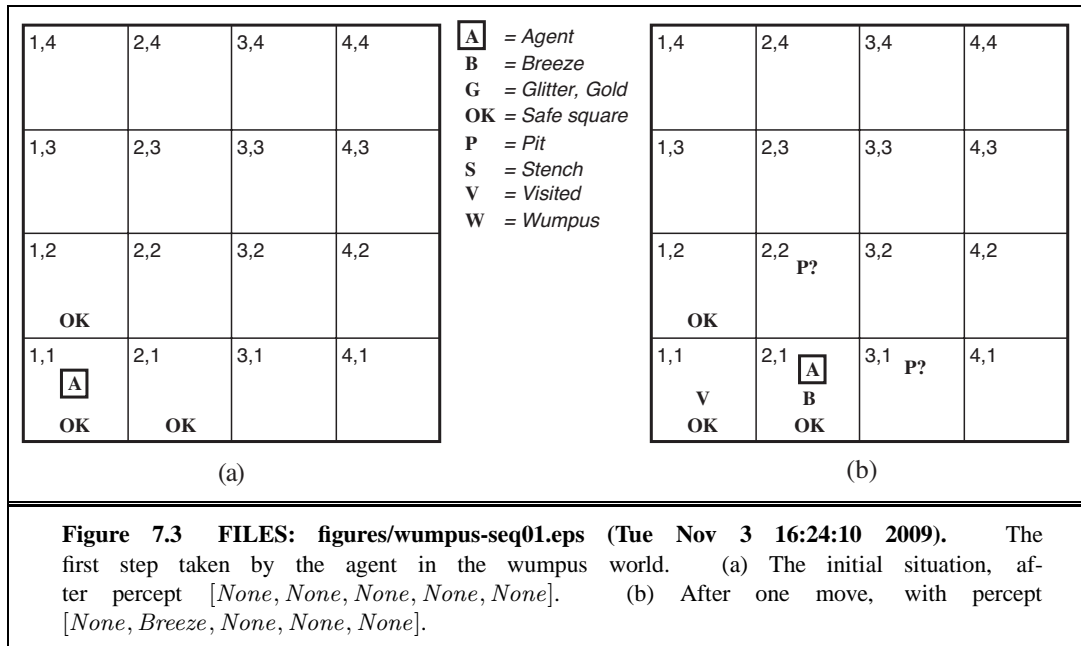
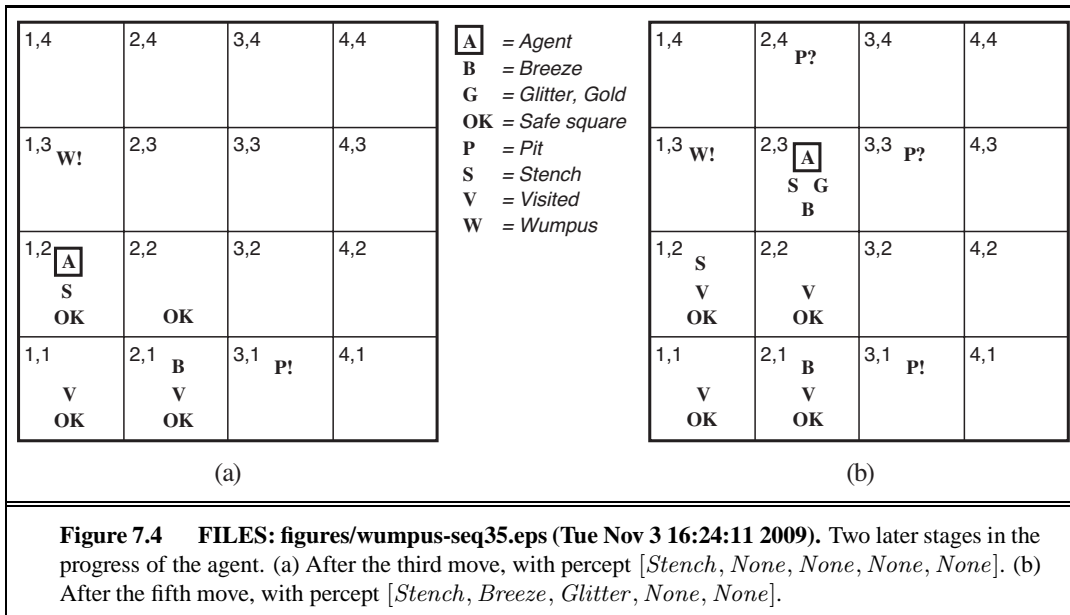


Figure 7.2 FILES: figures/wumpus-world.eps (Tue Nov 3 16:24:13 2009). A typical wumpus world. The agent is in the bottom left corner, facing right.





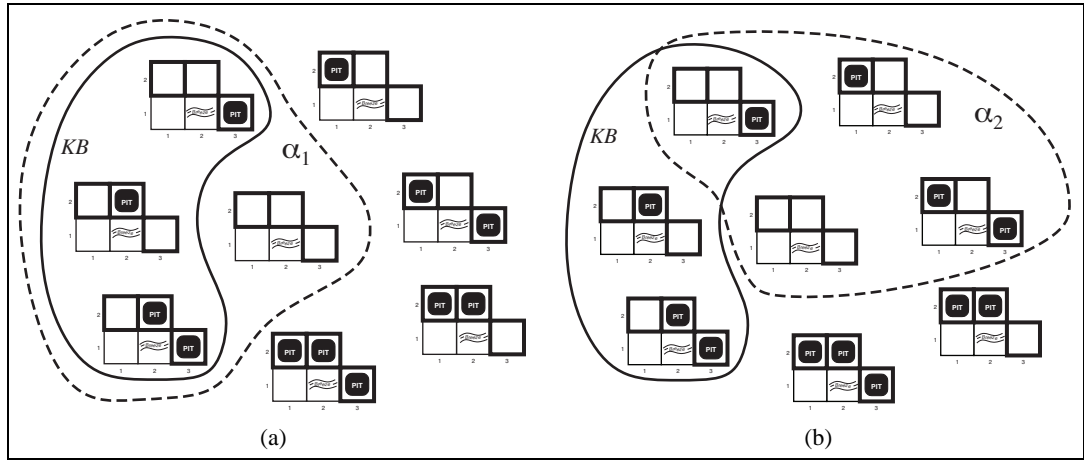
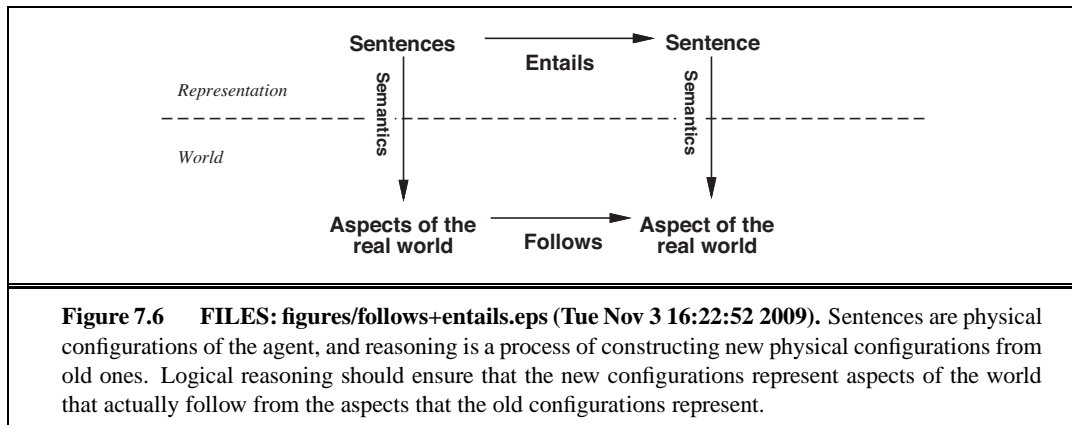
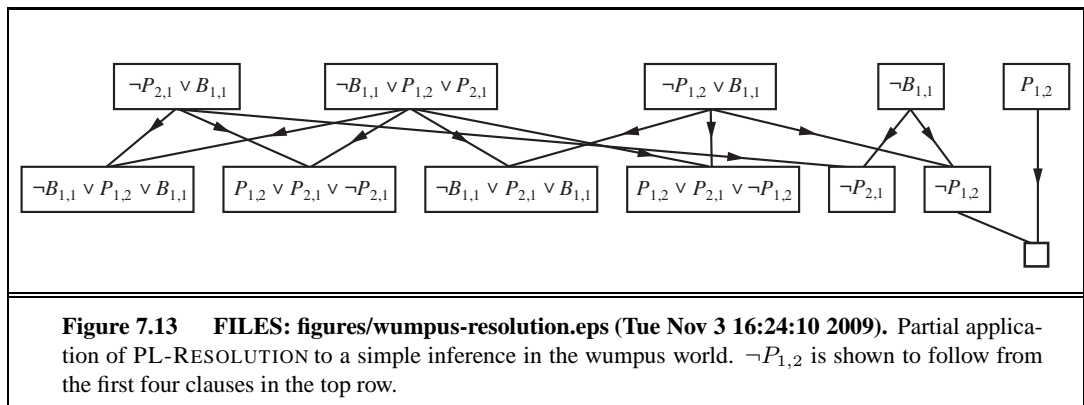
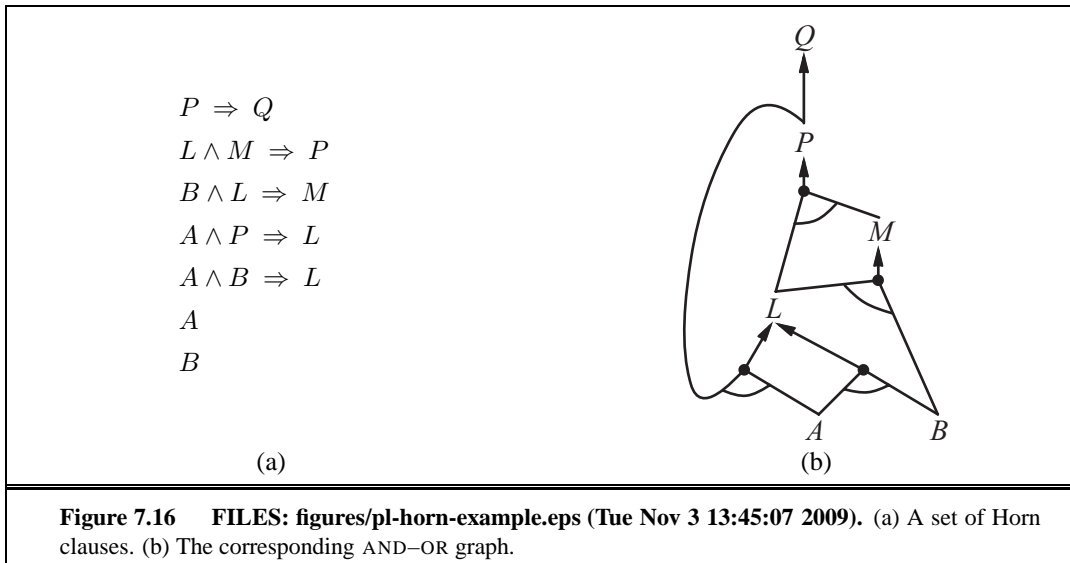


Figure 7.5 FILES: figures/wumpus-entailment.eps (Tue Nov 3 16:24:09 2009) figures/wumpus-nonen entailment.eps (Tue Nov 3 16:24:10 2009). Possible models for the presence of pits in squares [1,2], [2,2], and [3,1]. The KB corresponding to the observations of nothing in [1,1] and a breeze in [2,1] is shown by the solid line. (a) Dotted line shows models of α_1 (no pit in [1,2]). (b) Dotted line shows models of α_2 (no pit in [2,2]).







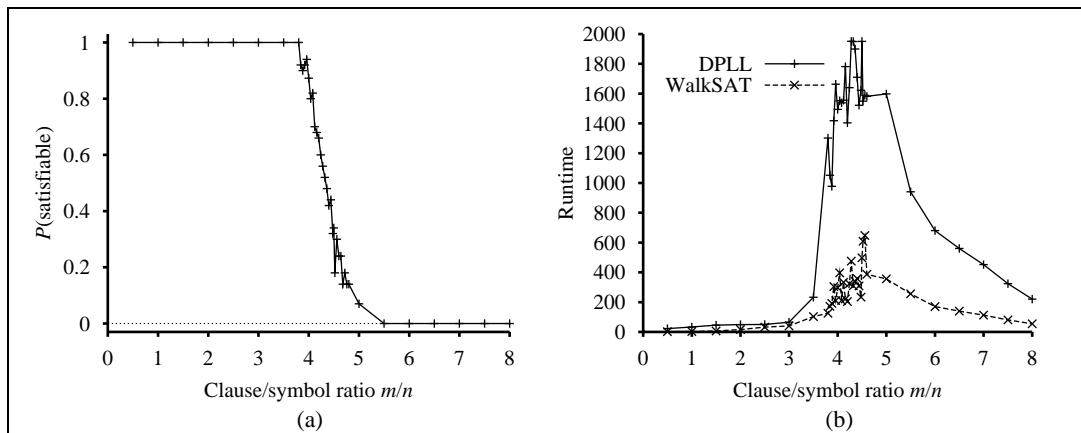


Figure 7.19 FILES: . (a) Graph showing the probability that a random 3-CNF sentence with $n = 50$ symbols is satisfiable, as a function of the clause/symbol ratio m/n . (b) Graph of the median run time (measured in number of recursive calls to DPLL, a good proxy) on random 3-CNF sentences. The most difficult problems have a clause/symbol ratio of about 4.3.

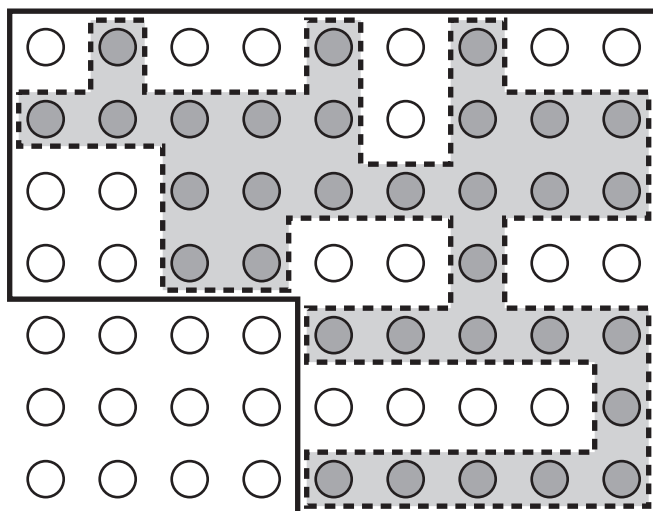
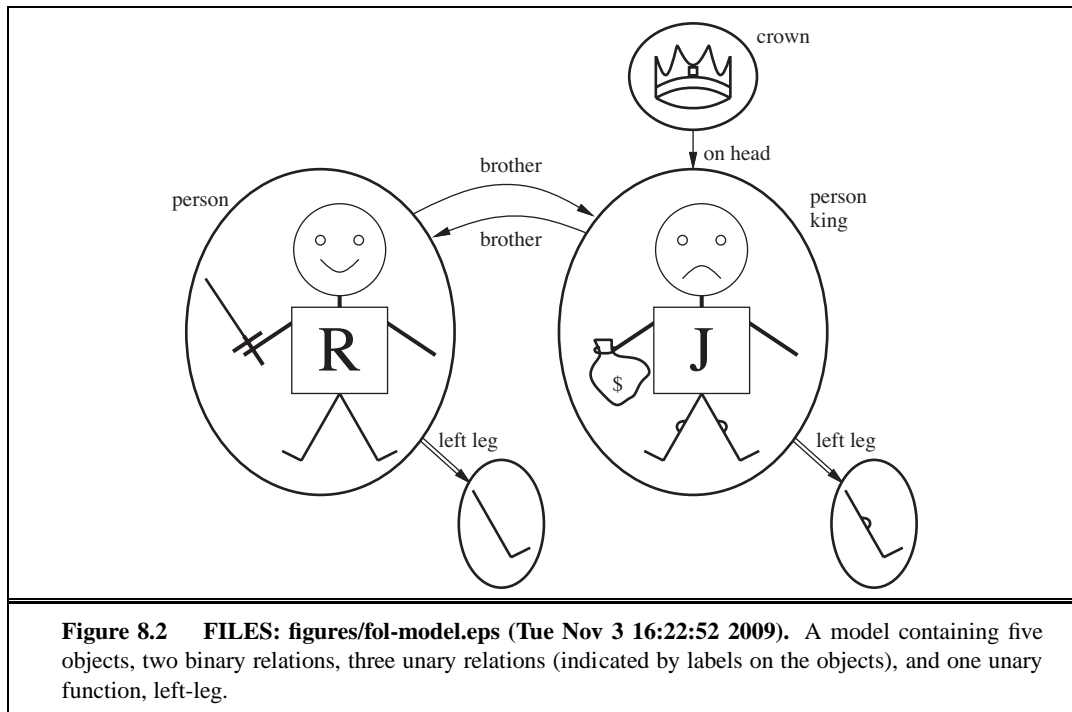


Figure 7.21 FILES: figures/wiggly-belief-state.eps (Tue Nov 3 13:53:12 2009). Depiction of a 1-CNF belief state (bold outline) as a simply representable, conservative approximation to the exact (wiggly) belief state (shaded region with dashed outline). Each possible world is shown as a circle; the shaded ones are consistent with all the percepts.

8

FIRST-ORDER LOGIC



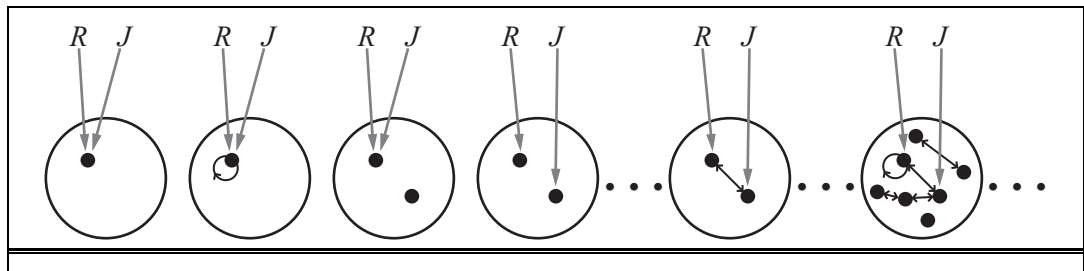
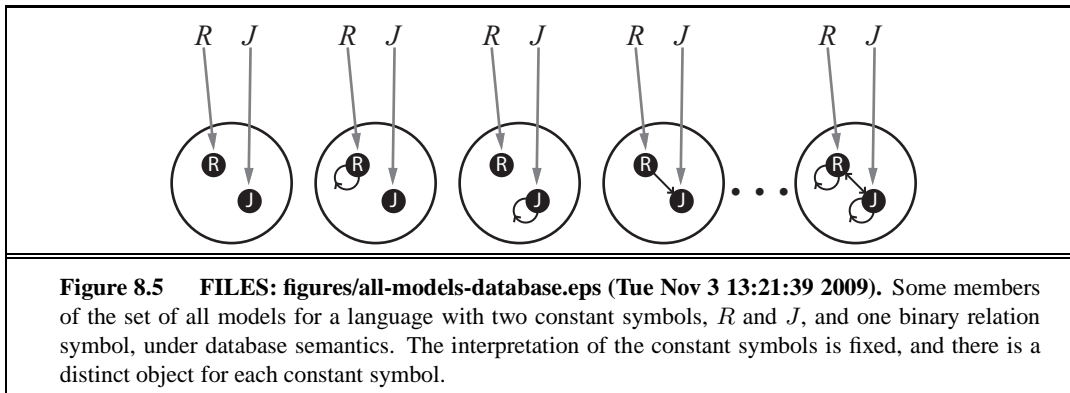


Figure 8.4 FILES: figures/all-models-standard.eps (Tue Nov 3 13:21:28 2009). Some members of the set of all models for a language with two constant symbols, R and J , and one binary relation symbol. The interpretation of each constant symbol is shown by a gray arrow. Within each model, the related objects are connected by arrows.



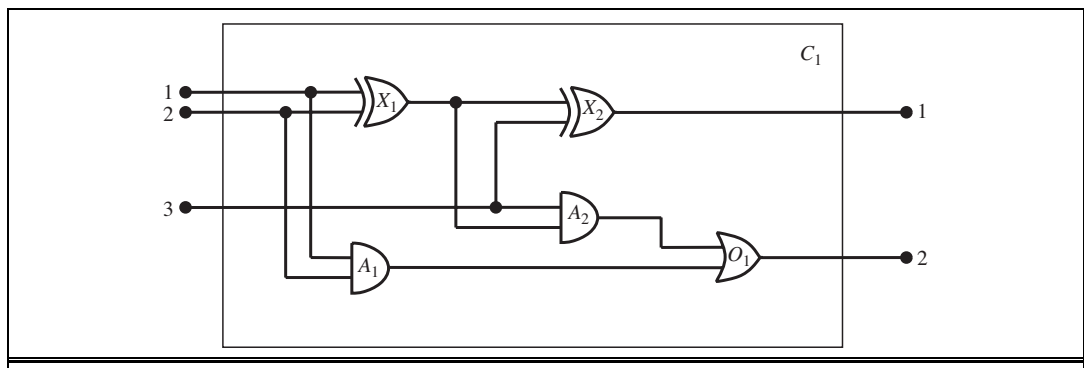
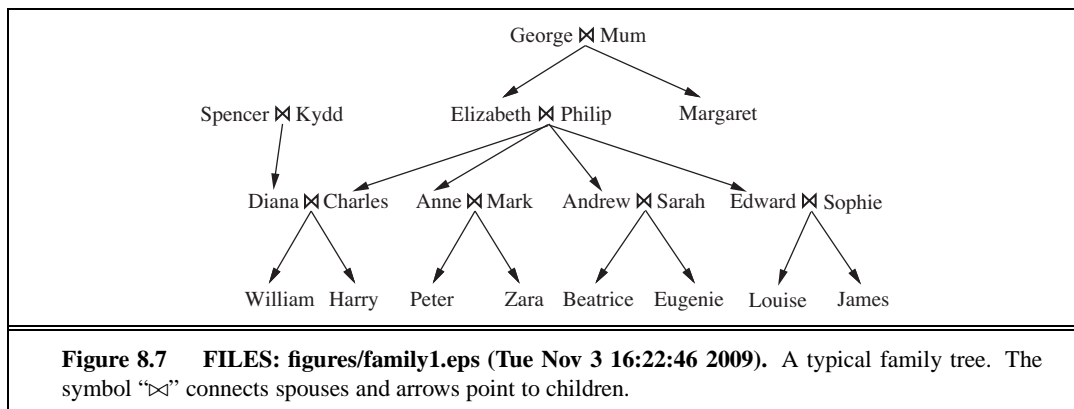
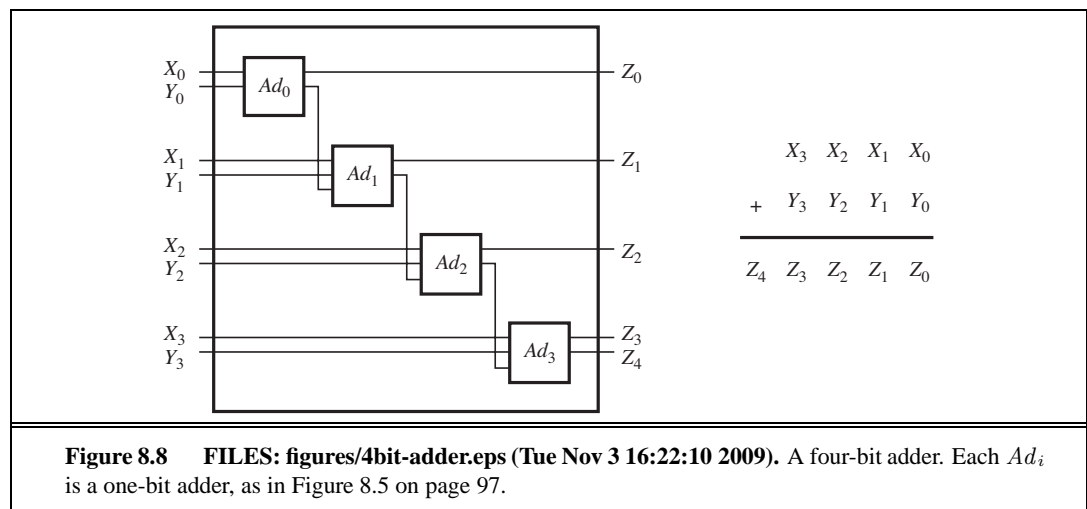


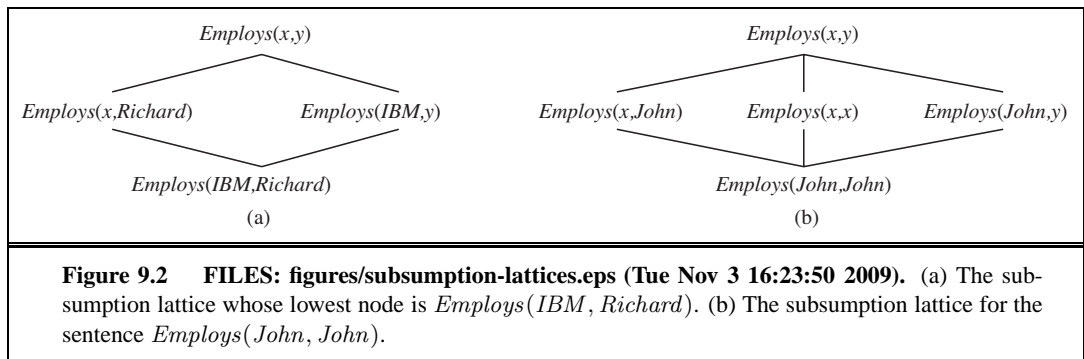
Figure 8.6 FILES: figures/adder.eps (Tue Nov 3 16:22:18 2009). A digital circuit C1, purporting to be a one-bit full adder. The first two inputs are the two bits to be added, and the third input is a carry bit. The first output is the sum, and the second output is a carry bit for the next adder. The circuit contains two XOR gates, two AND gates, and one OR gate.

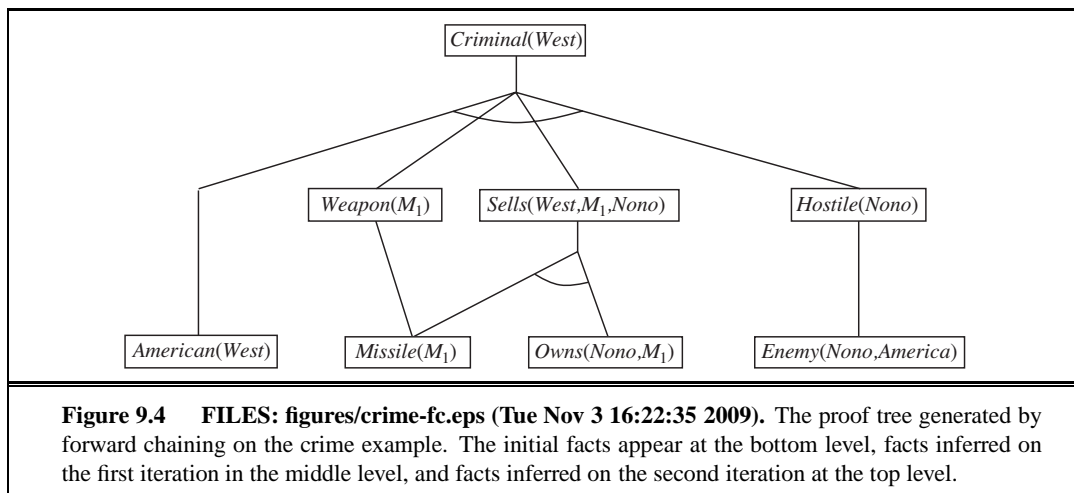


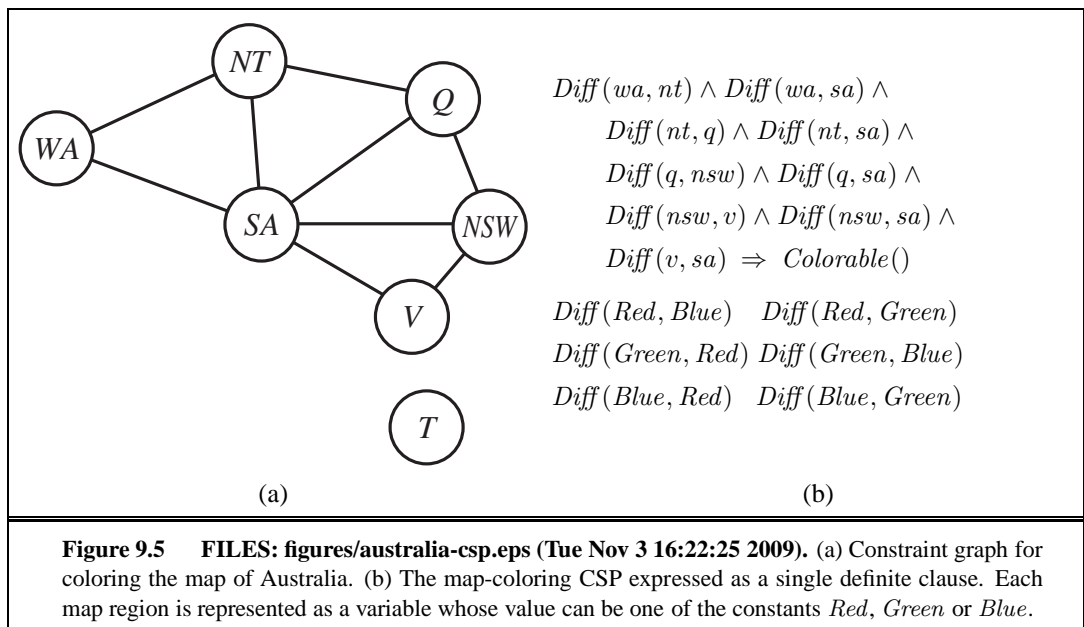


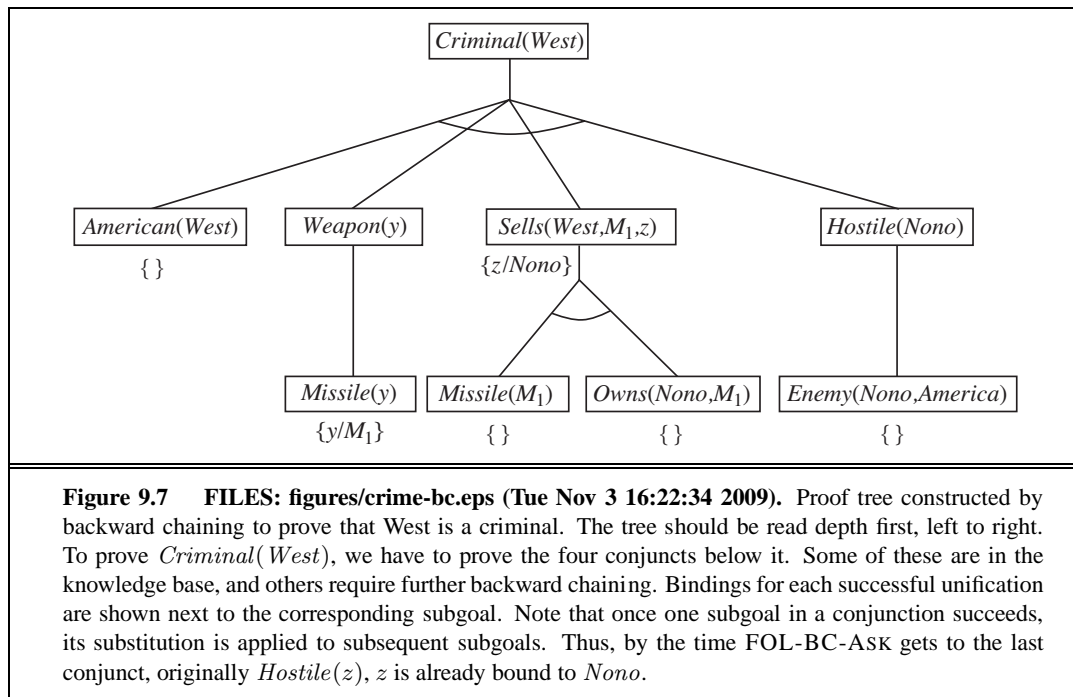
9

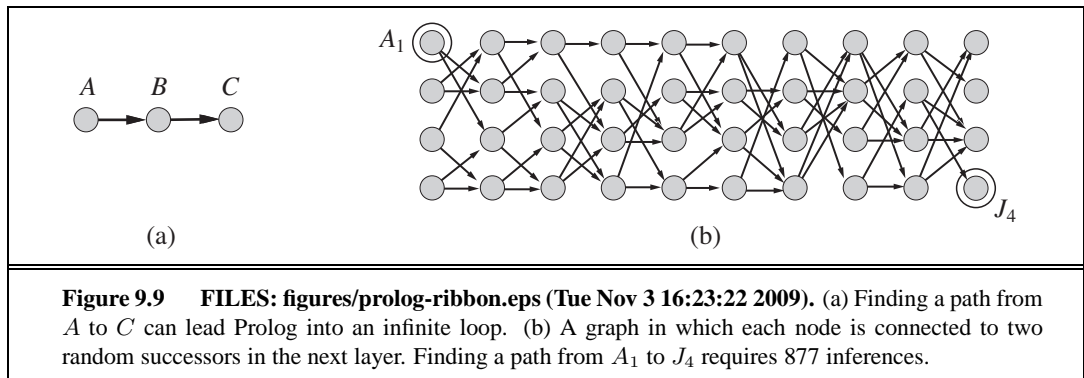
INFERENCE IN FIRST-ORDER LOGIC











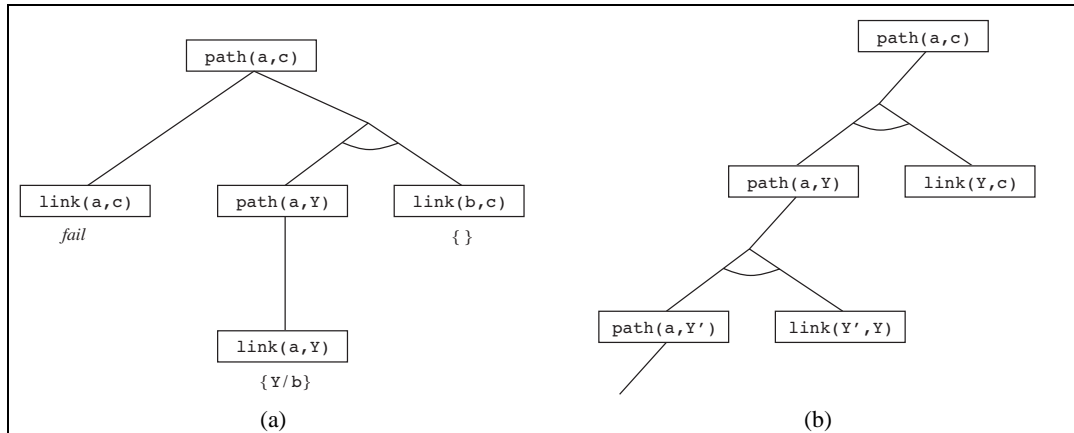
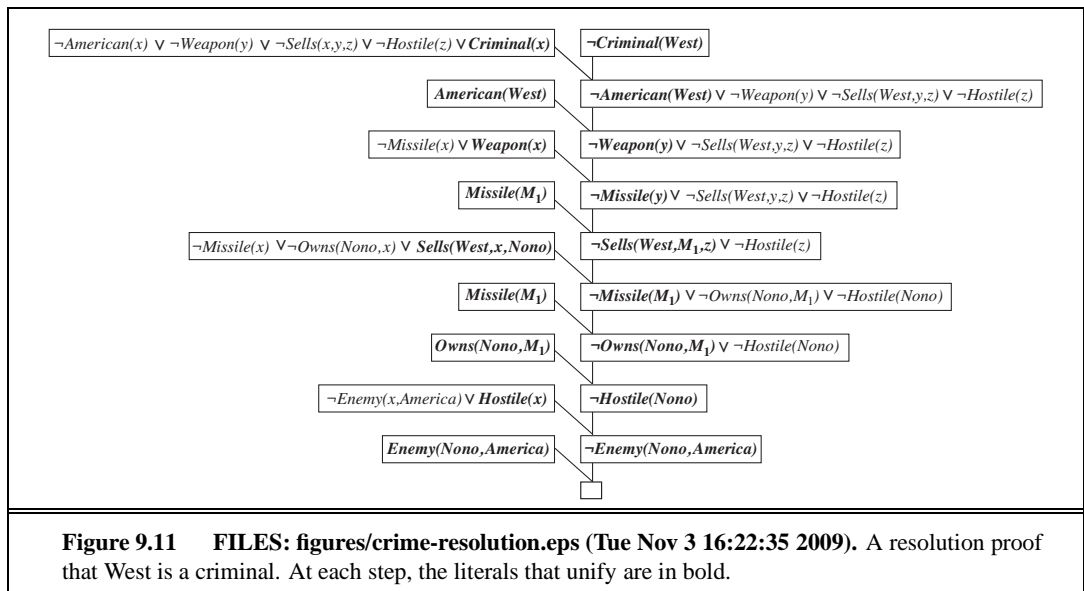
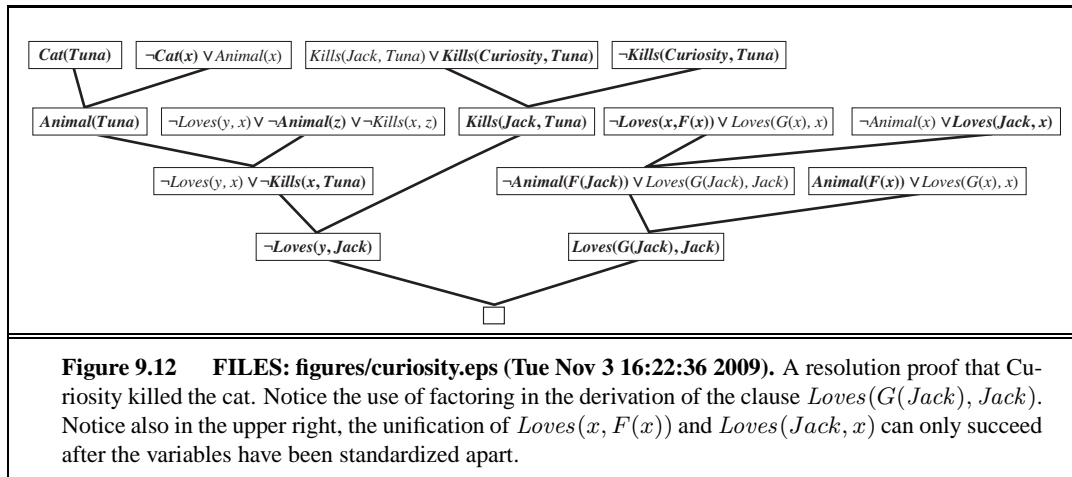
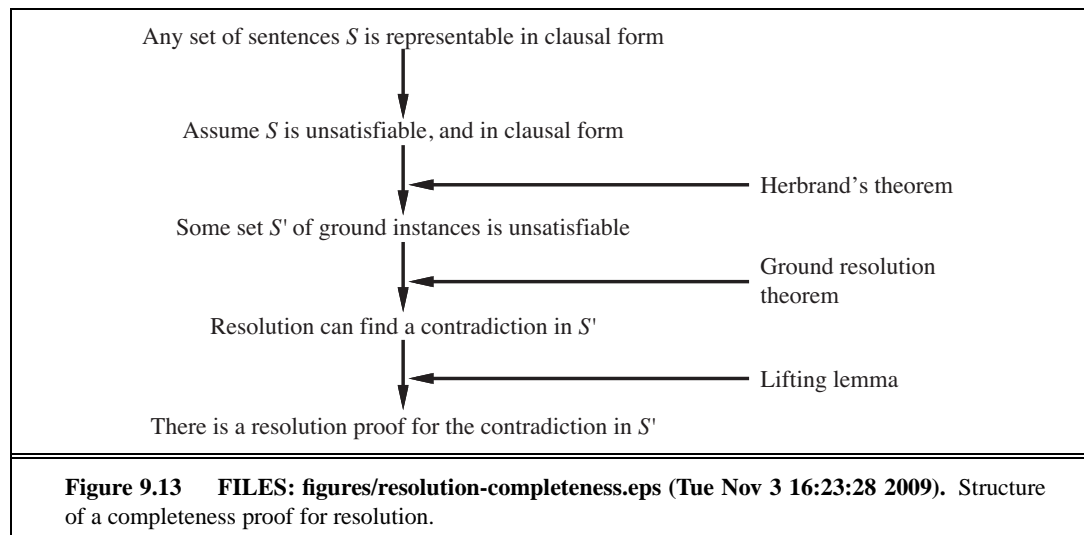


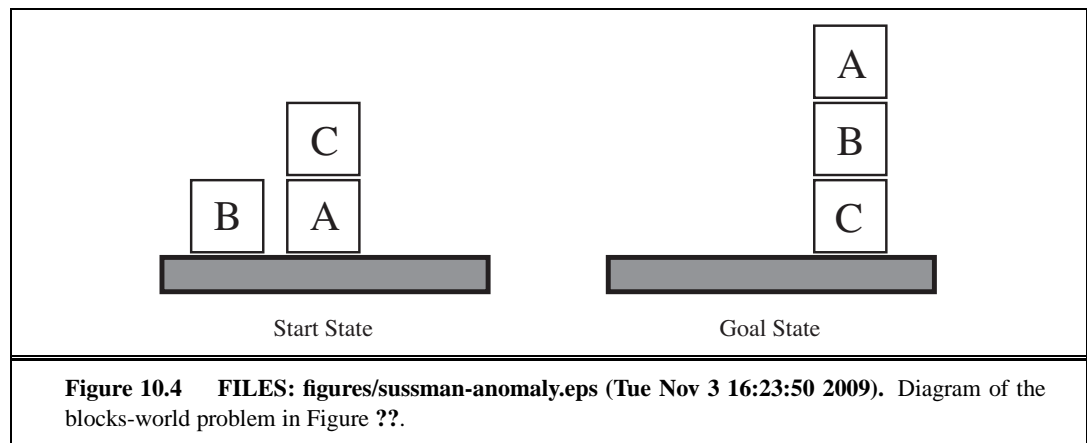
Figure 9.10 FILES: figures/proof-abc1.eps (Tue Nov 3 16:23:22 2009) figures/proof-abc2.eps (Tue Nov 3 16:23:22 2009). (a) Proof that a path exists from A to C . (b) Infinite proof tree generated when the clauses are in the “wrong” order.







10 CLASSICAL PLANNING



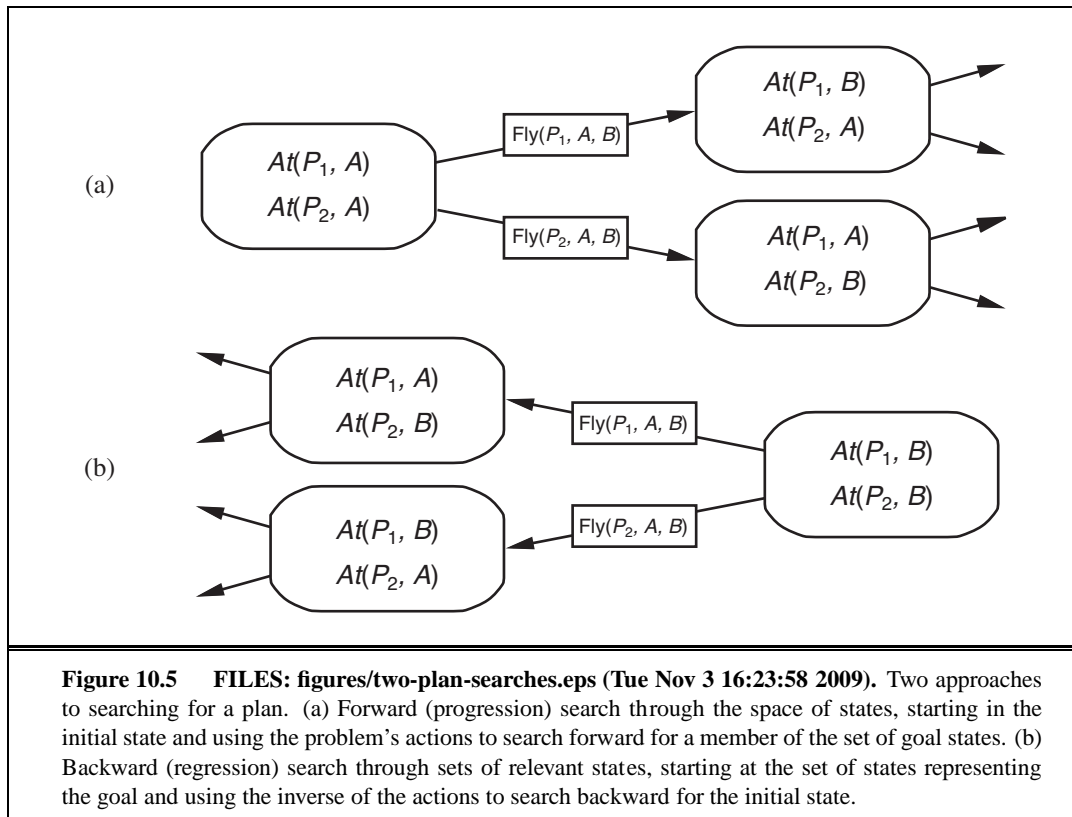


Figure 10.5 FILES: figures/two-plan-searches.eps (Tue Nov 3 16:23:58 2009). Two approaches to searching for a plan. (a) Forward (progression) search through the space of states, starting in the initial state and using the problem's actions to search forward for a member of the set of goal states. (b) Backward (regression) search through sets of relevant states, starting at the set of states representing the goal and using the inverse of the actions to search backward for the initial state.

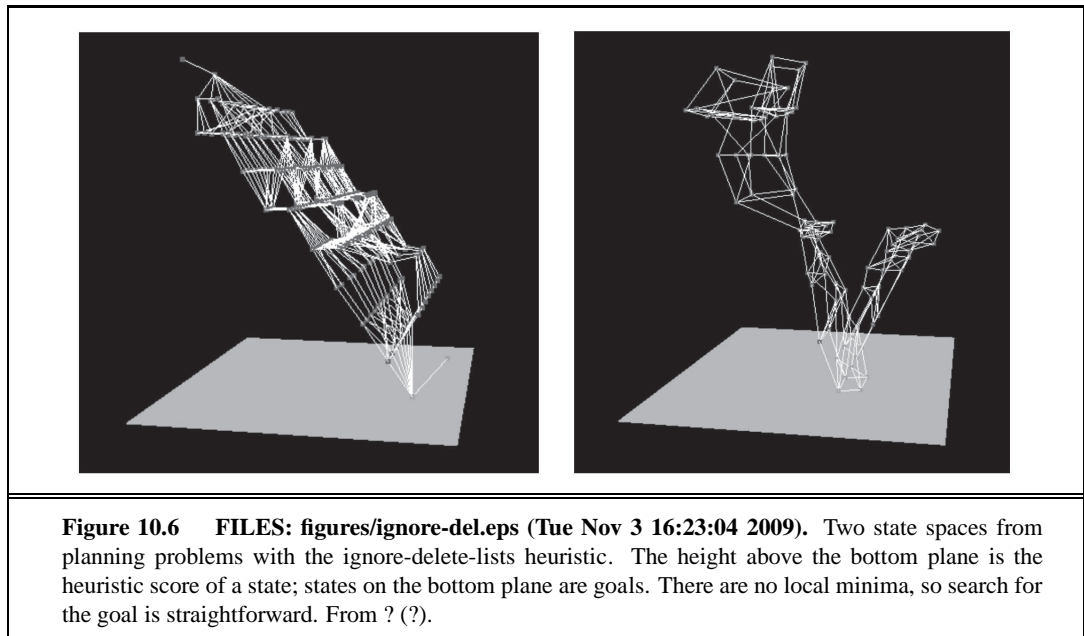
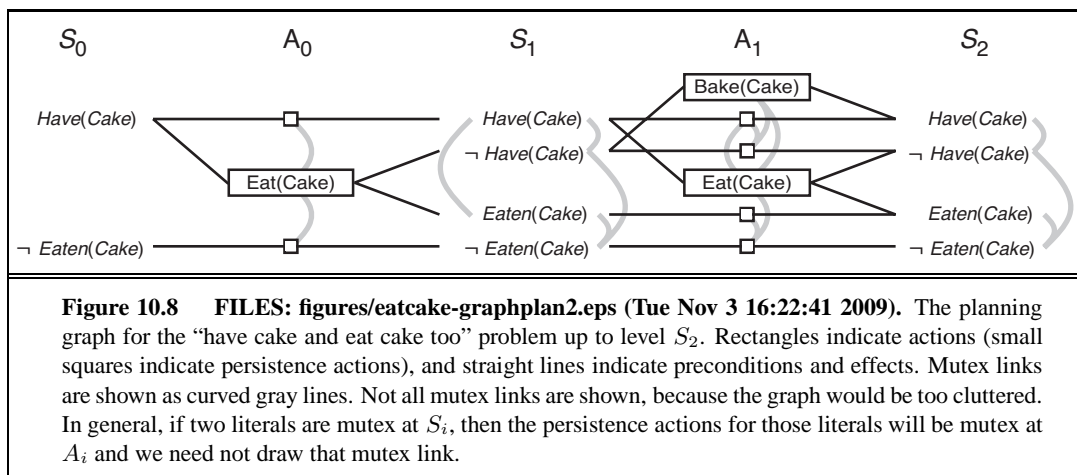


Figure 10.6 FILES: figures/ignore-del.eps (Tue Nov 3 16:23:04 2009). Two state spaces from planning problems with the ignore-delete-lists heuristic. The height above the bottom plane is the heuristic score of a state; states on the bottom plane are goals. There are no local minima, so search for the goal is straightforward. From ? (?).



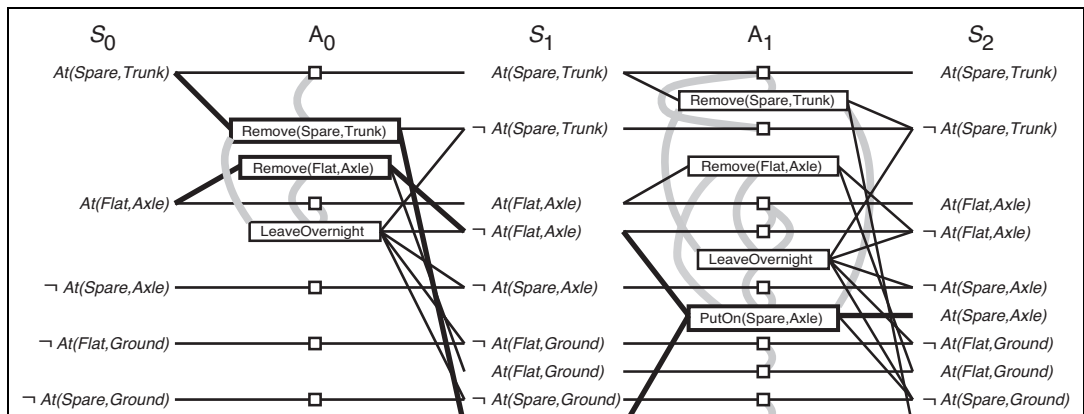


Figure 10.10 FILES: figures/tire-graphplan2.eps (Tue Nov 3 16:23:55 2009). The planning graph for the spare tire problem after expansion to level S_2 . Mutex links are shown as gray lines. Not all links are shown, because the graph would be too cluttered if we showed them all. The solution is indicated by bold lines and outlines.

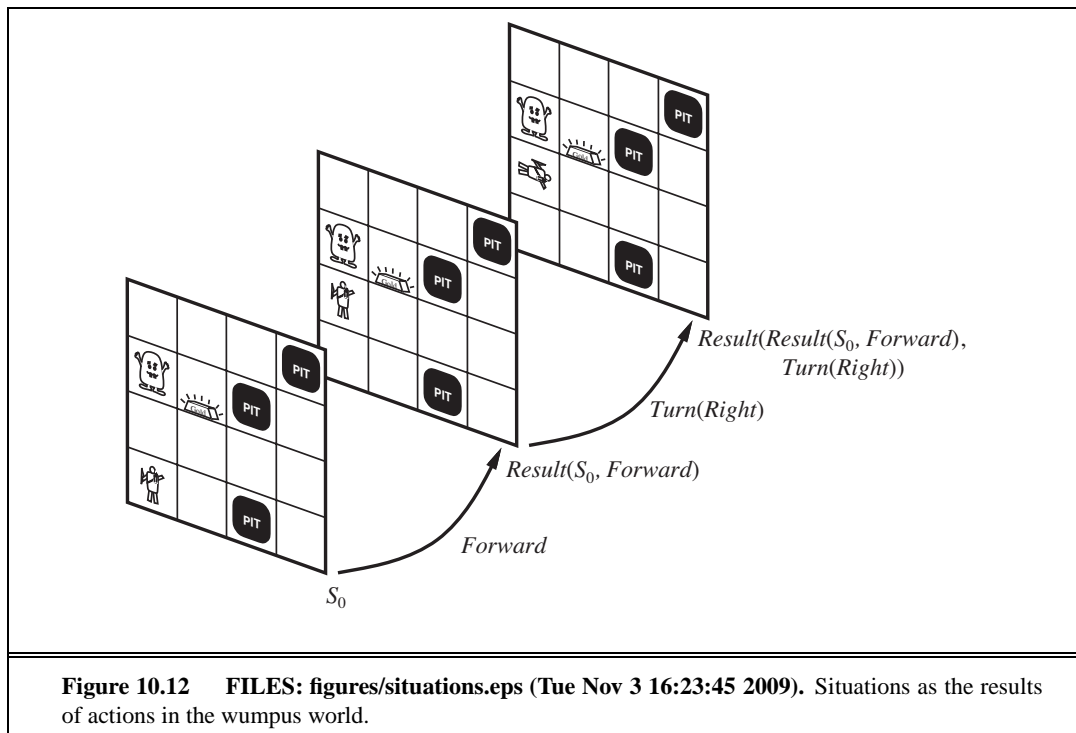
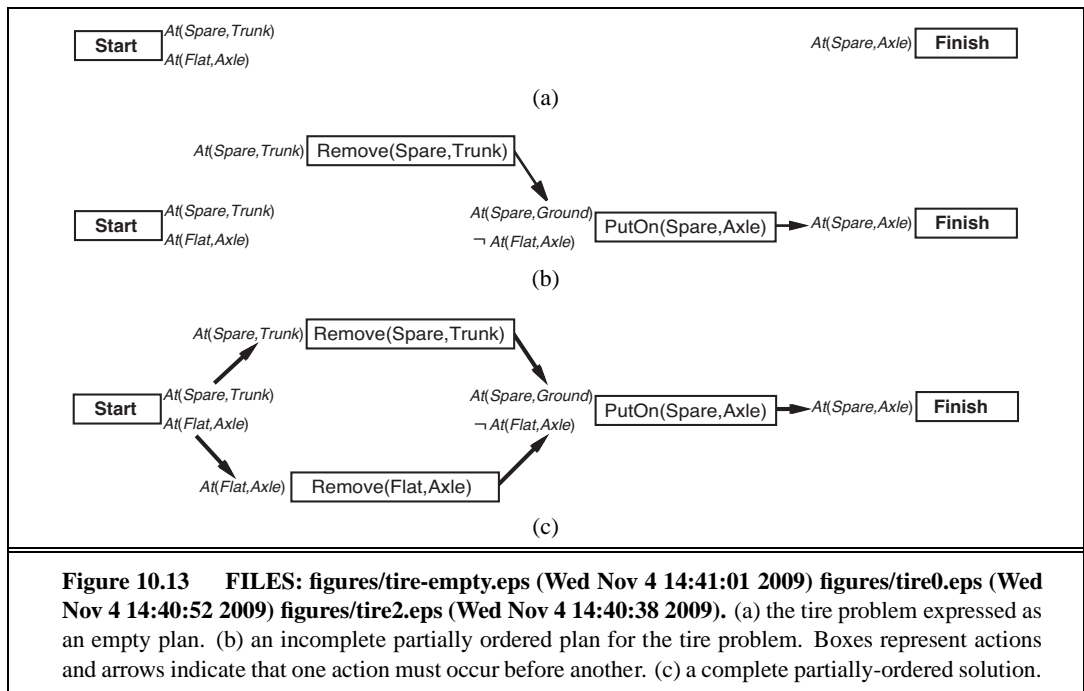


Figure 10.12 FILES: figures/situations.eps (Tue Nov 3 16:23:45 2009). Situations as the results of actions in the wumpus world.



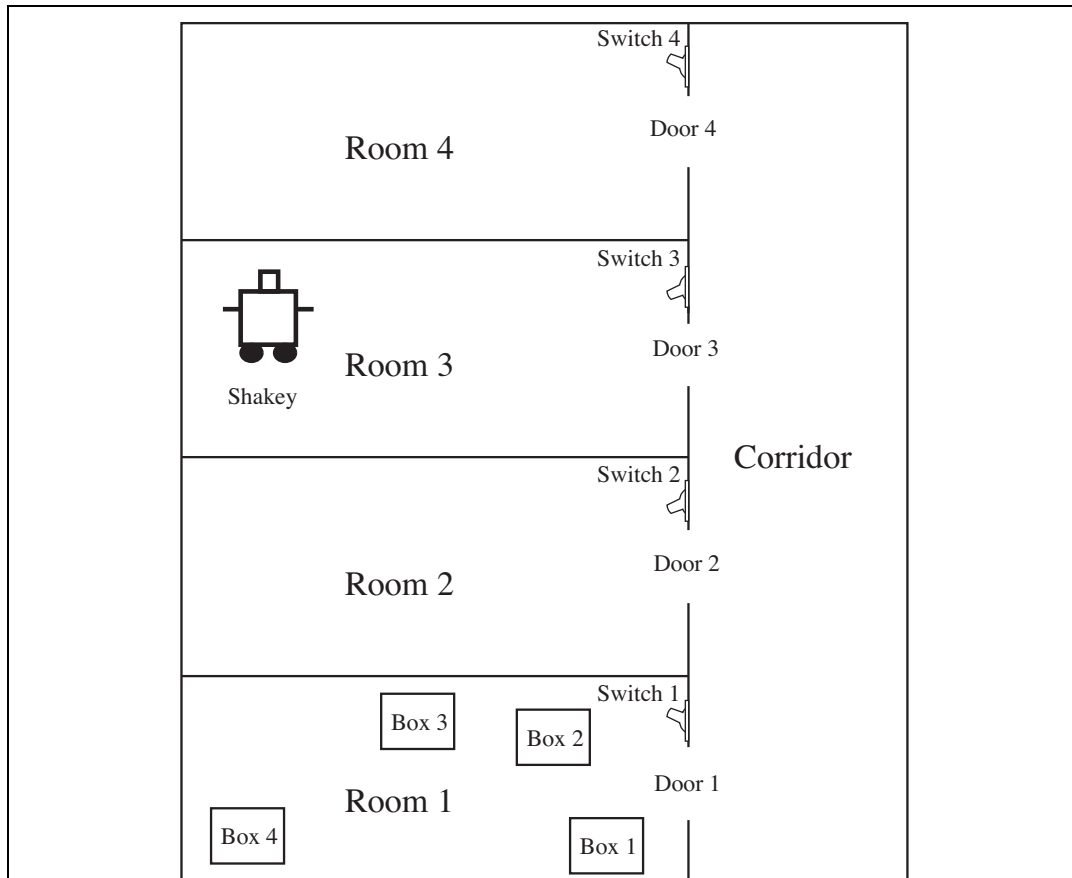
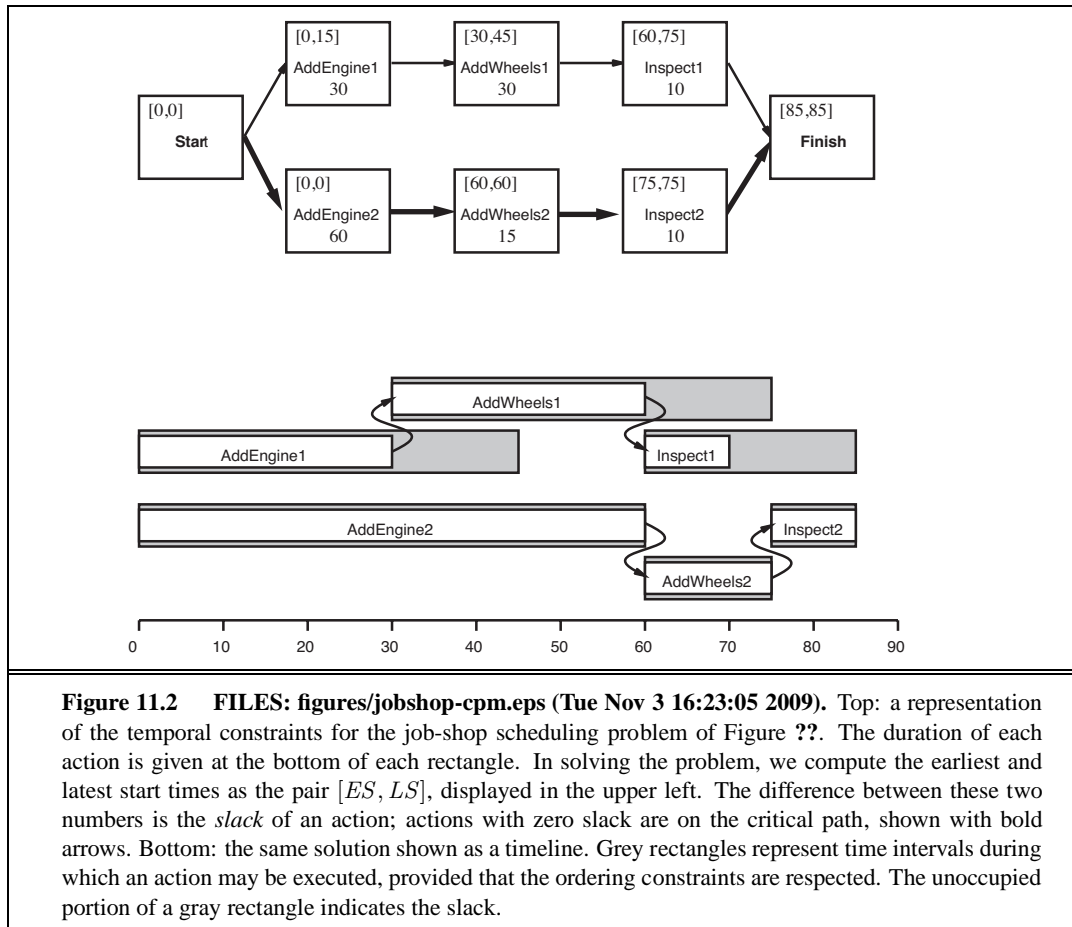
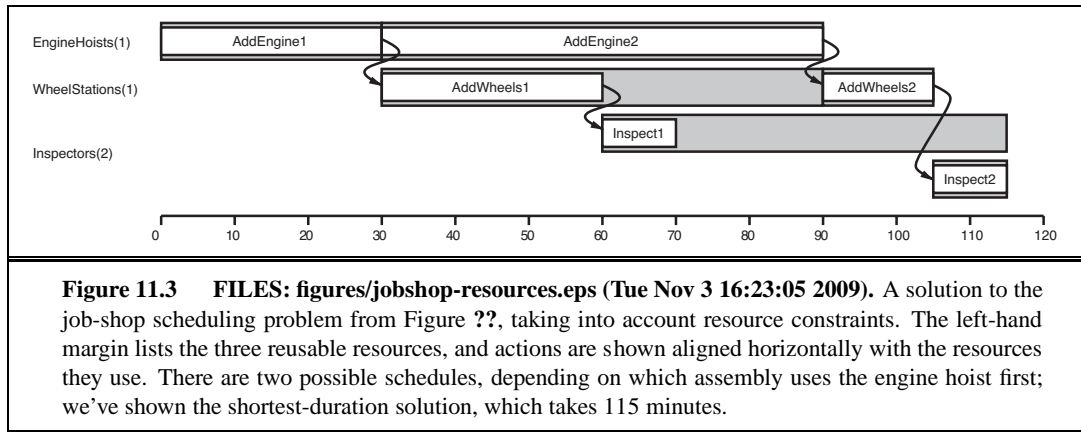
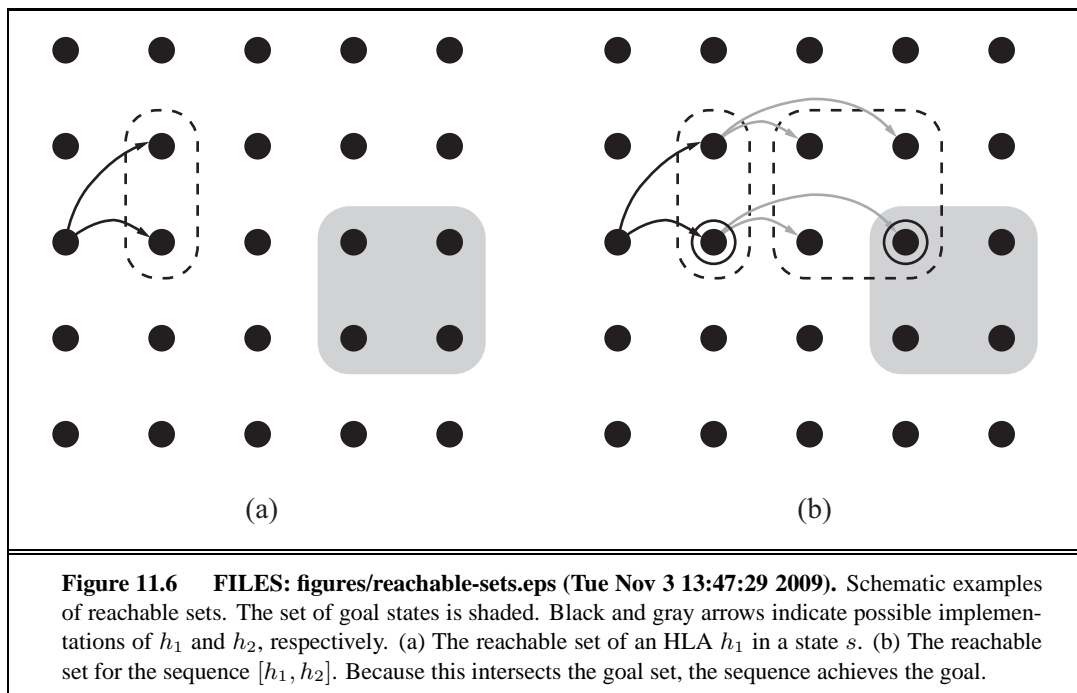


Figure 10.14 FILES: figures/shakey2.eps (Tue Nov 3 16:23:43 2009). Shakey's world. Shakey can move between landmarks within a room, can pass through the door between rooms, can climb climbable objects and push pushable objects, and can flip light switches.

11 PLANNING AND ACTING IN THE REAL WORLD







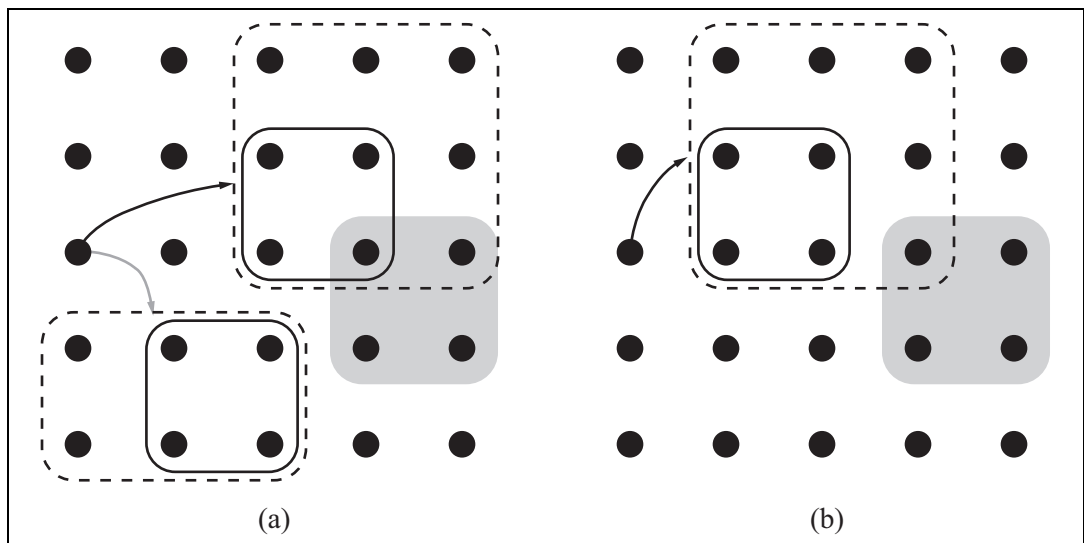
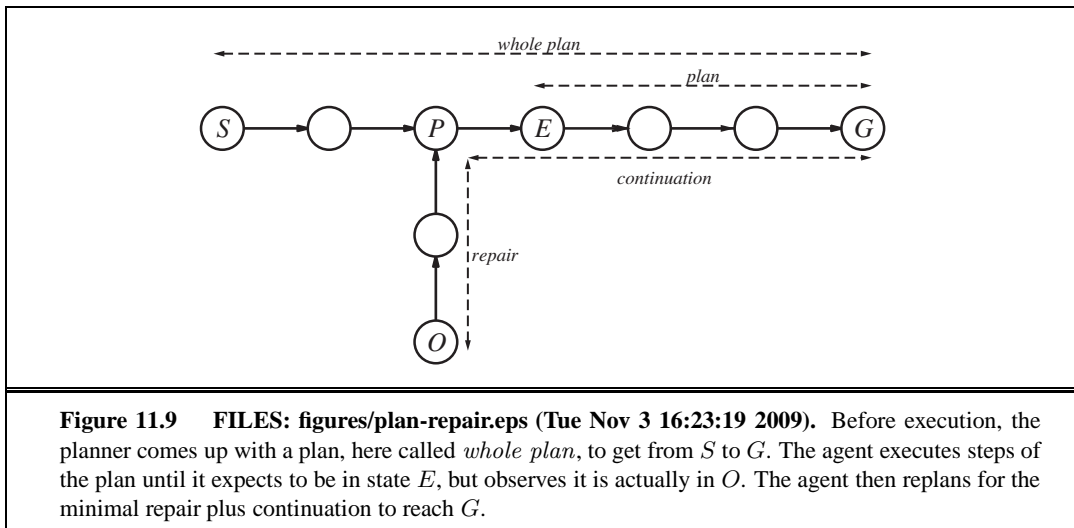


Figure 11.7 FILES: figures/approximate-HLA.eps (Tue Nov 3 13:23:08 2009). Goal achievement for high-level plans with approximate descriptions. The set of goal states is shaded. For each plan, the pessimistic (solid lines) and optimistic (dashed lines) reachable sets are shown. (a) The plan indicated by the black arrow definitely achieves the goal, while the plan indicated by the gray arrow definitely doesn't. (b) A plan that would need to be refined further to determine if it really does achieve the goal.



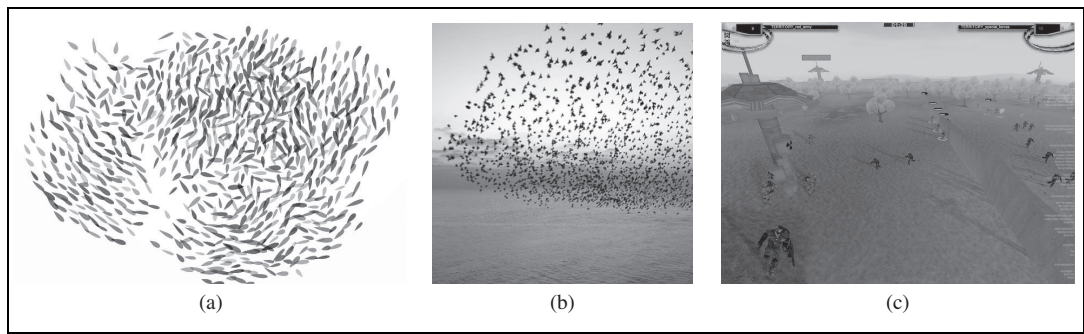


Figure 11.11 FILES: figures/boids-neurogame.eps (Thu Nov 5 22:33:01 2009). (a) A simulated flock of birds, using Reynolds' boids model. Image courtesy Giuseppe Randazzo, novastructura.net. (b) An actual flock of starlings. Image by Eduardo (pastaboy sleeps on flickr). (c) Two competitive teams of agents attempting to capture the towers in the NERO game. Image courtesy Risto Miikkulainen.

12 KNOWLEDGE REPRESENTATION

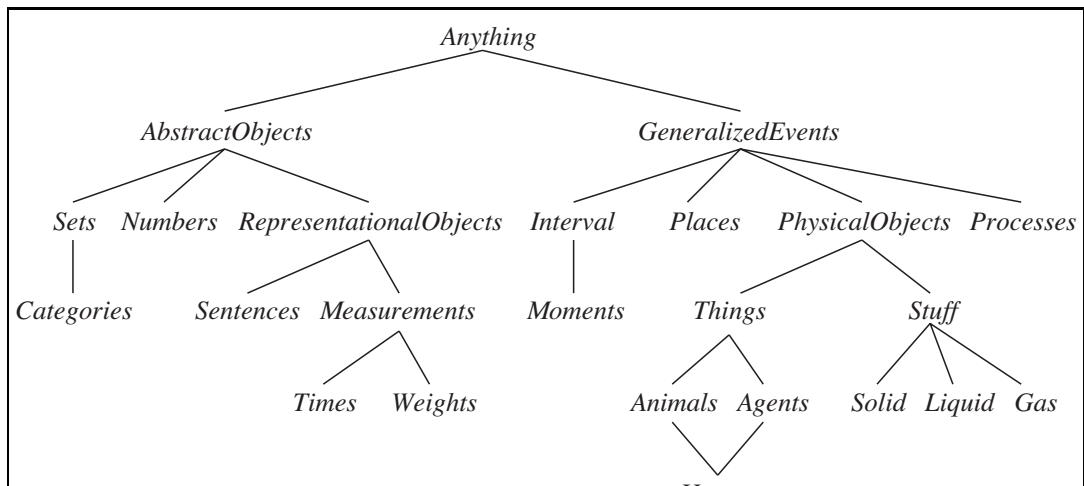
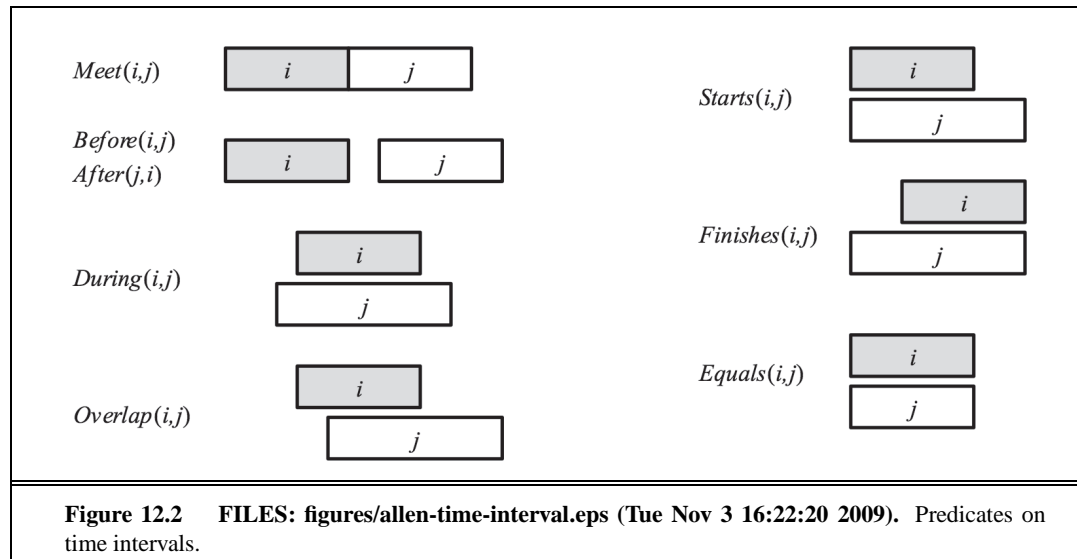


Figure 12.1 FILES: figures/everything.eps (Tue Nov 3 16:22:41 2009). The upper ontology of the world, showing the topics to be covered later in the chapter. Each link indicates that the lower concept is a specialization of the upper one. Specializations are not necessarily disjoint; a human is both an animal and an agent, for example. We will see in Section ?? why physical objects come under generalized events.



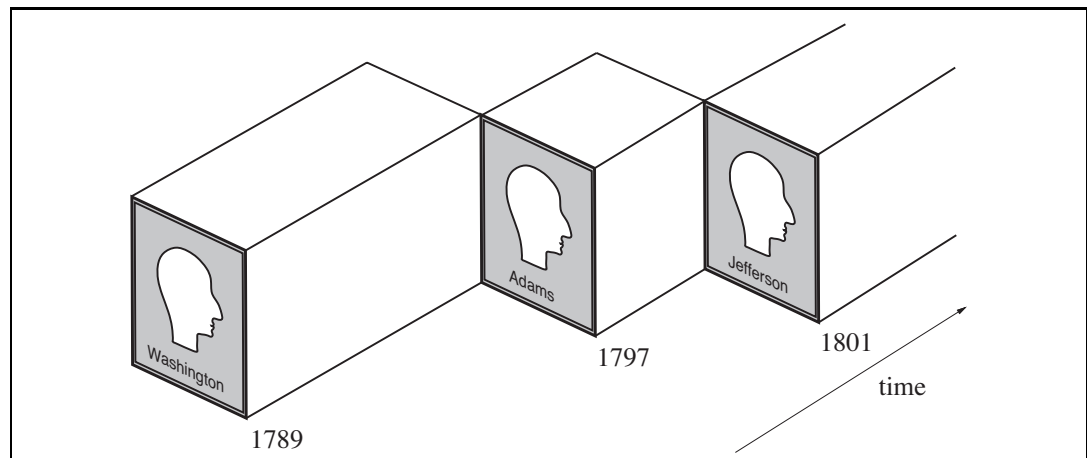
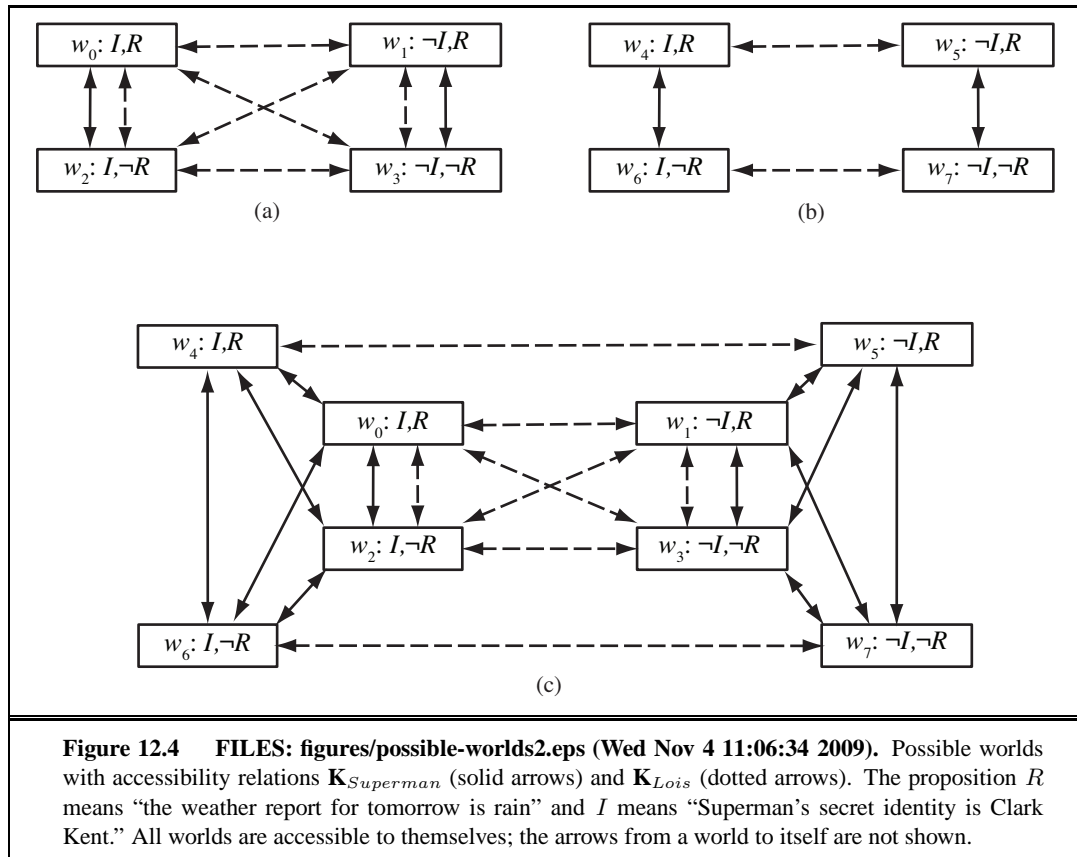
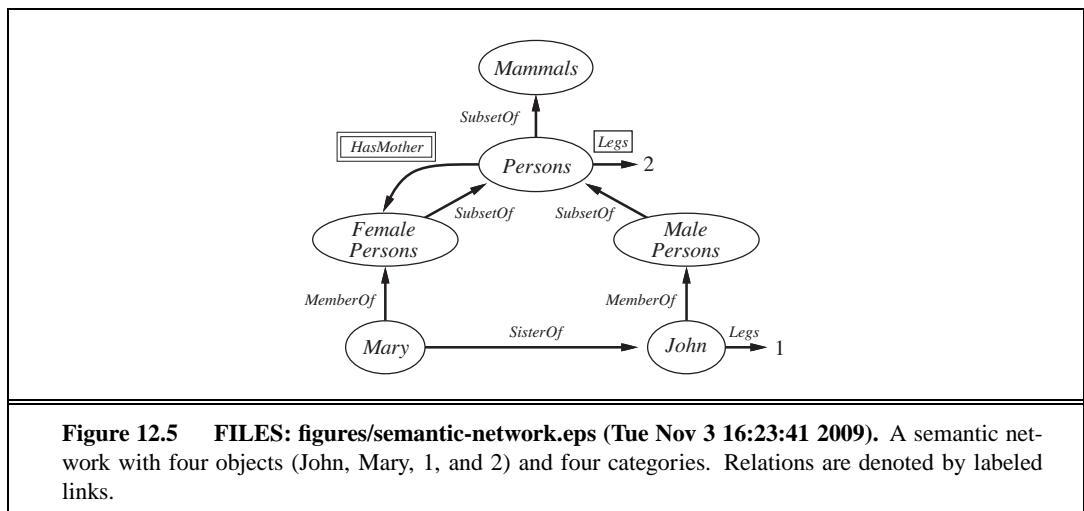
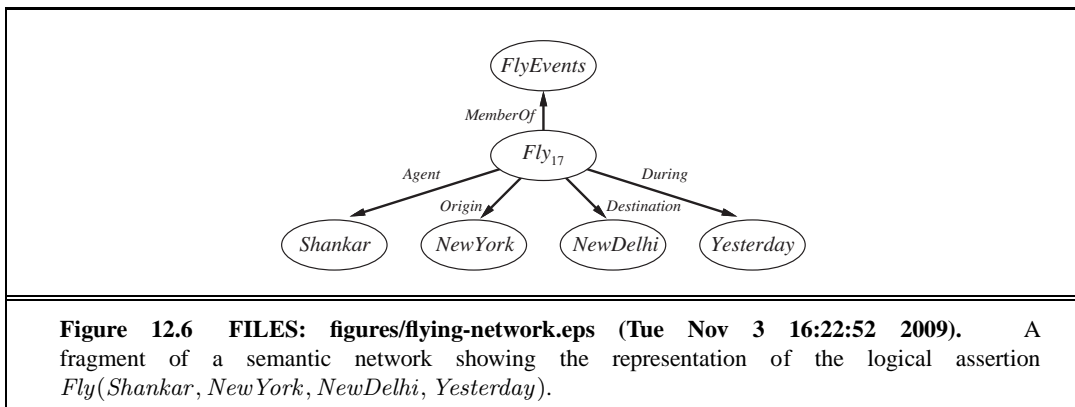


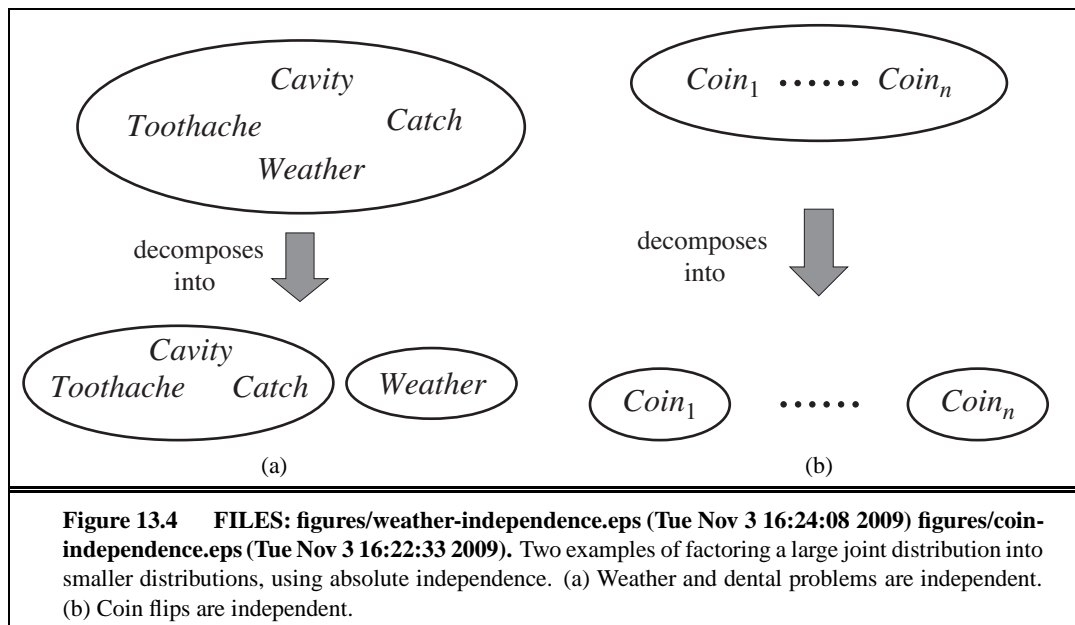
Figure 12.3 FILES: figures/president-usa.eps (Tue Nov 3 16:23:22 2009). A schematic view of the object *President(USA)* for the first 15 years of its existence.







13 QUANTIFYING UNCERTAINTY



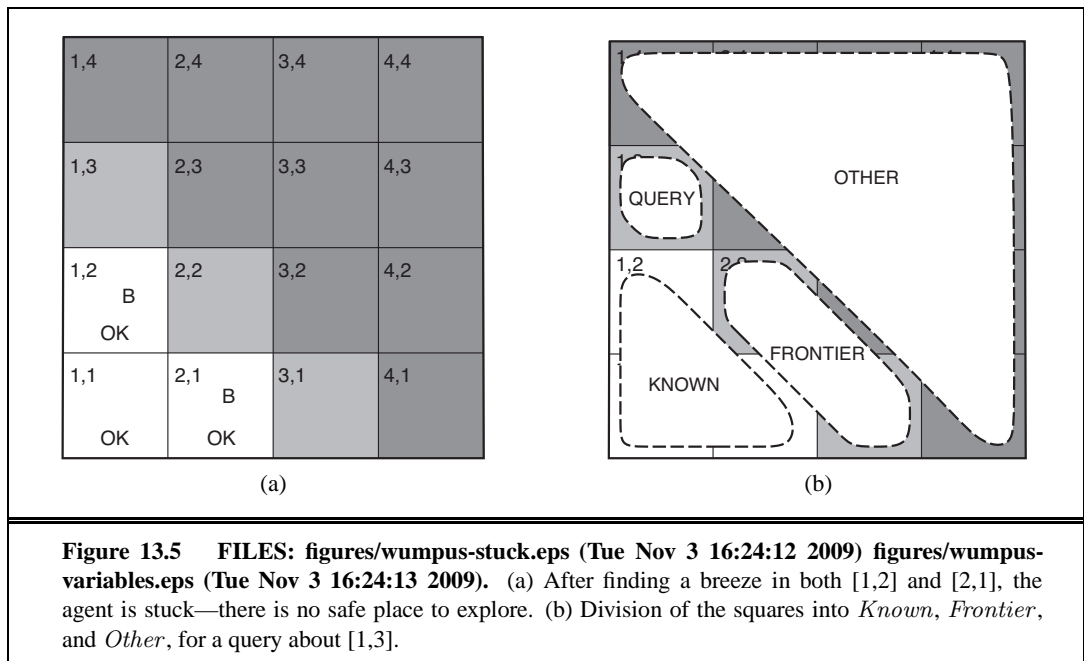
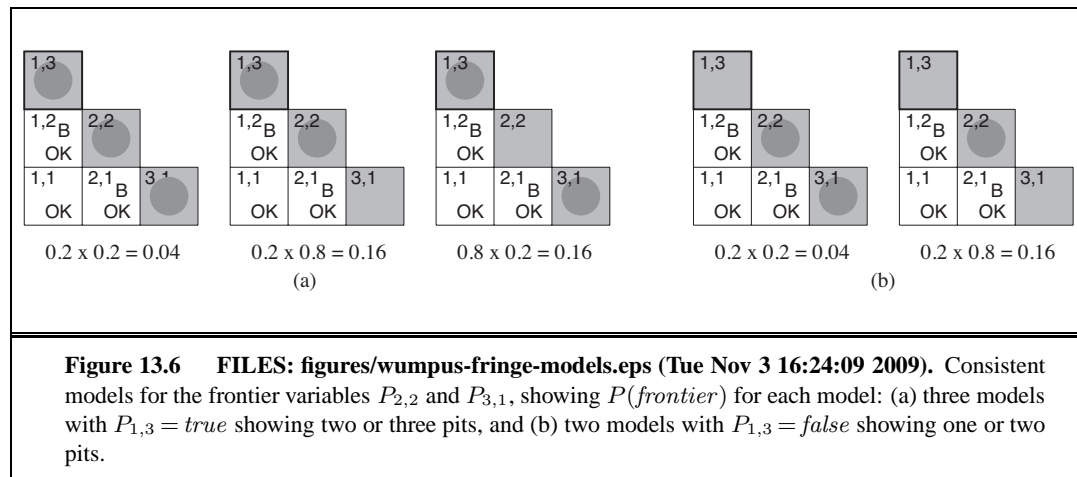
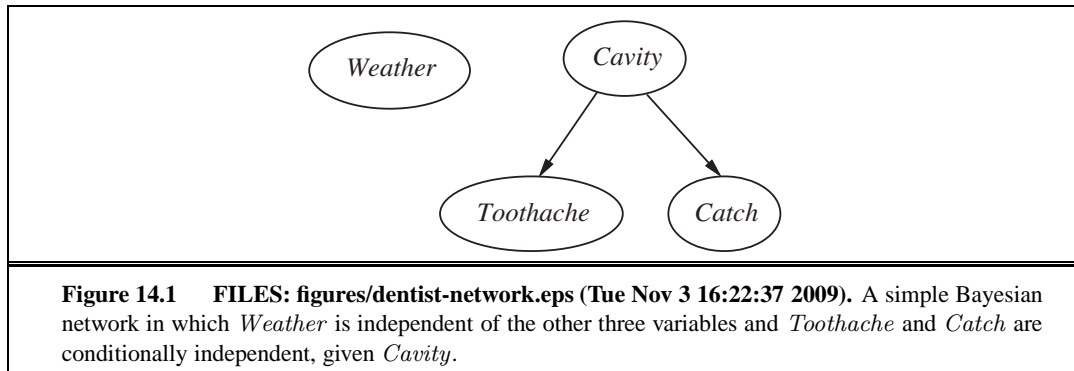


Figure 13.5 FILES: `figures/wumpus-stuck.eps` (Tue Nov 3 16:24:12 2009) `figures/wumpus-variables.eps` (Tue Nov 3 16:24:13 2009). (a) After finding a breeze in both [1,2] and [2,1], the agent is stuck—there is no safe place to explore. (b) Division of the squares into *Known*, *Frontier*, and *Other*, for a query about [1,3].



14 PROBABILISTIC REASONING



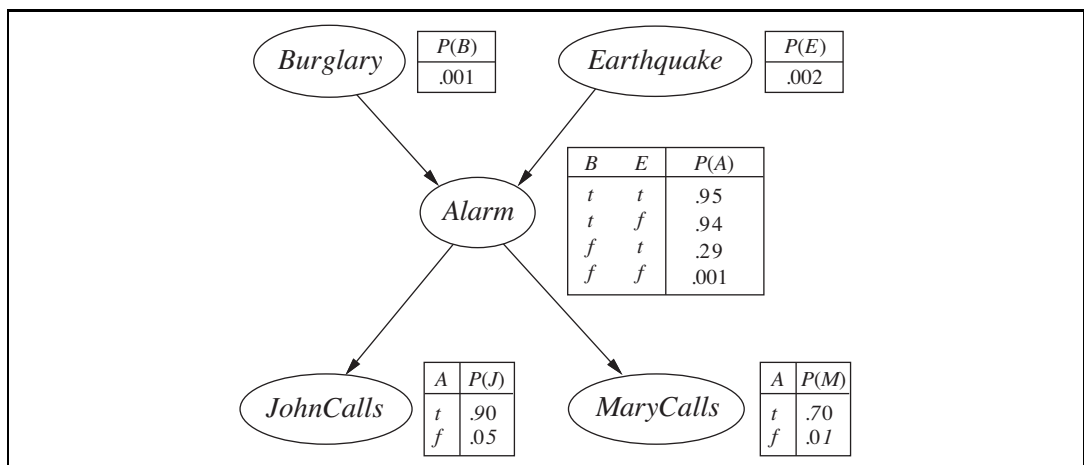


Figure 14.2 FILES: figures/burglary2.eps (Tue Nov 3 16:22:29 2009). A typical Bayesian network, showing both the topology and the conditional probability tables (CPTs). In the CPTs, the letters *B*, *E*, *A*, *J*, and *M* stand for *Burglary*, *Earthquake*, *Alarm*, *JohnCalls*, and *MaryCalls*, respectively.

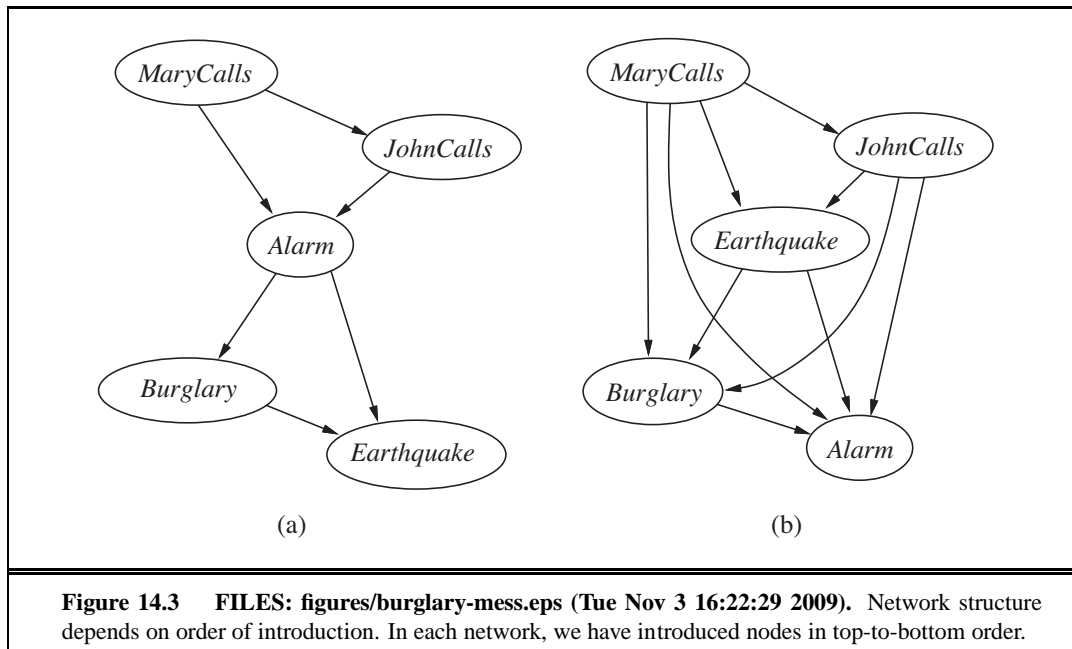


Figure 14.3 FILES: figures/burglary-mess.eps (Tue Nov 3 16:22:29 2009). Network structure depends on order of introduction. In each network, we have introduced nodes in top-to-bottom order.

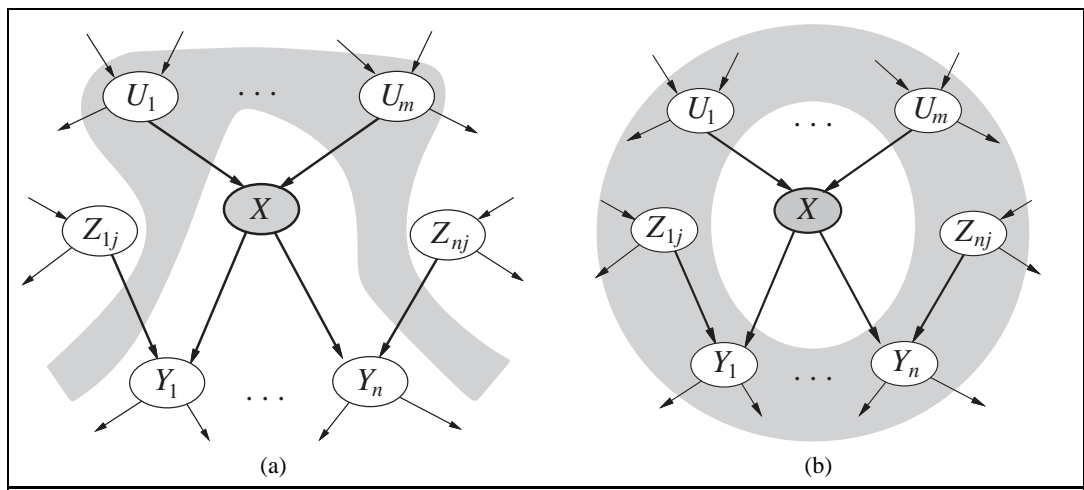


Figure 14.4 FILES: figures/nondescendants.eps (Tue Nov 3 16:23:15 2009) figures/markov-blanket.eps (Tue Nov 3 16:23:08 2009). (a) A node X is conditionally independent of its non-descendants (e.g., the Z_{ij} s) given its parents (the U_i s shown in the gray area). (b) A node X is conditionally independent of all other nodes in the network given its Markov blanket (the gray area).

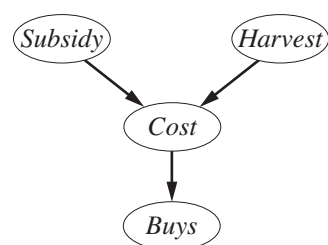


Figure 14.5 FILES: figures/continuous-net.eps (Tue Nov 3 16:22:34 2009). A simple network with discrete variables (*Subsidy* and *Buys*) and continuous variables (*Harvest* and *Cost*).

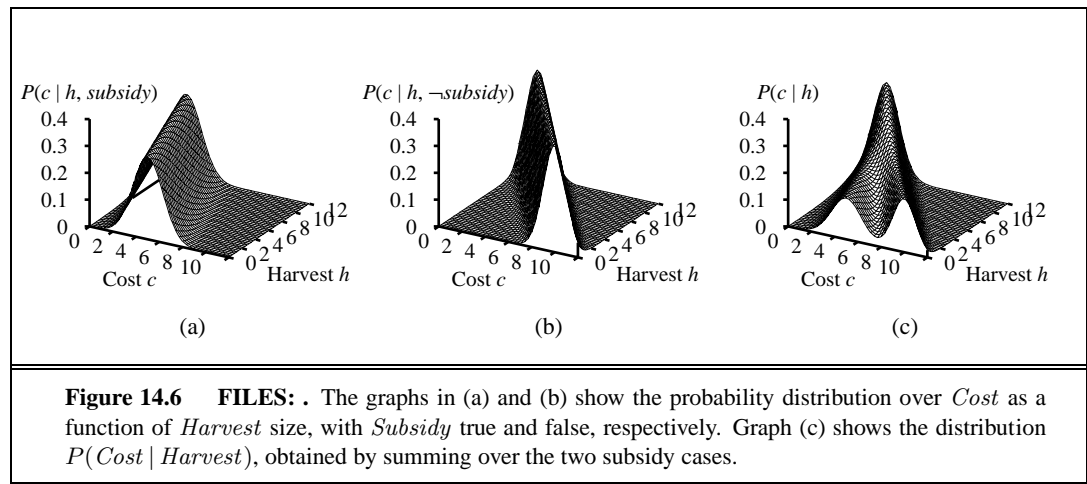


Figure 14.6 FILES: . The graphs in (a) and (b) show the probability distribution over *Cost* as a function of *Harvest* size, with *Subsidy* true and false, respectively. Graph (c) shows the distribution $P(\text{Cost} | \text{Harvest})$, obtained by summing over the two subsidy cases.

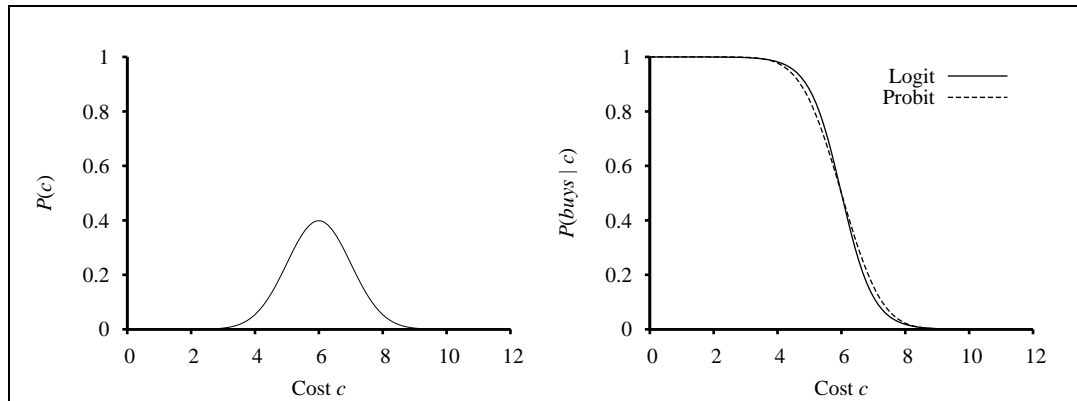


Figure 14.7 FILES: . (a) A normal (Gaussian) distribution for the cost threshold, centered on $\mu = 6.0$ with standard deviation $\sigma = 1.0$. (b) Logit and probit distributions for the probability of $buys$ given $cost$, for the parameters $\mu = 6.0$ and $\sigma = 1.0$.

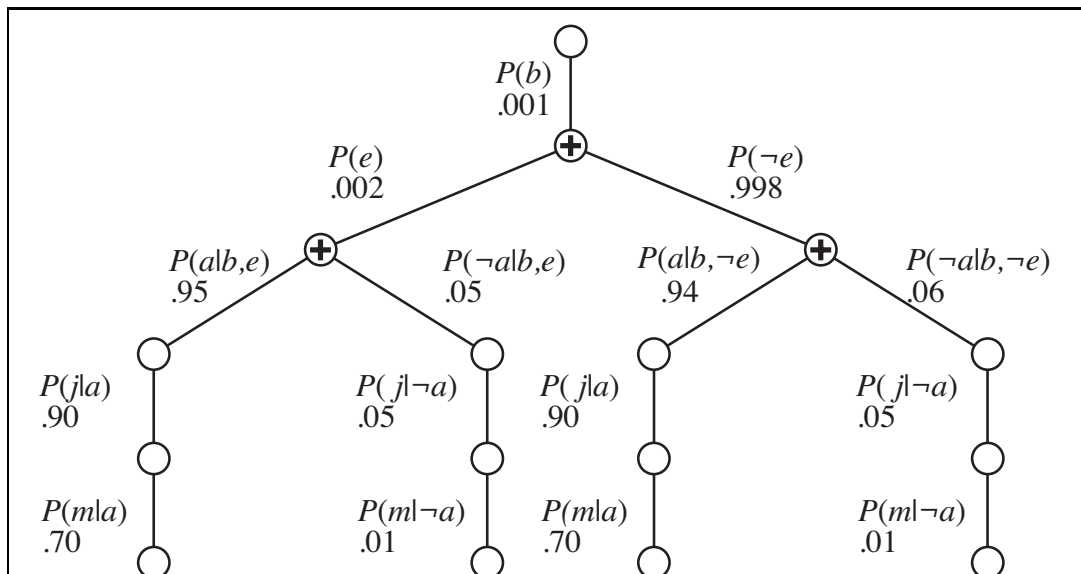
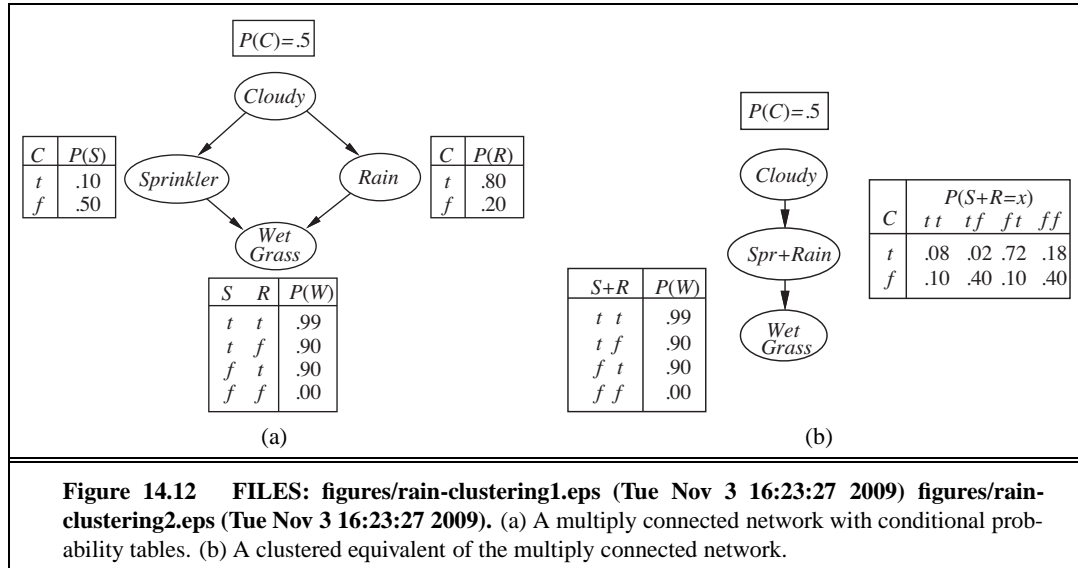


Figure 14.8 FILES: figures/enumeration-tree.eps (Tue Nov 3 16:22:41 2009). The structure of the expression shown in Equation (??). The evaluation proceeds top down, multiplying values along each path and summing at the “+” nodes. Notice the repetition of the paths for j and m .



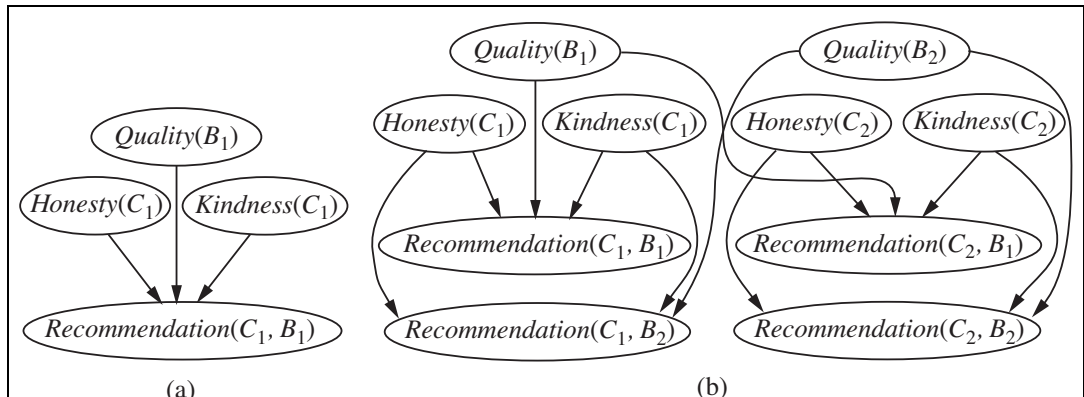


Figure 14.17 FILES: figures/new-14-16-1.eps (Tue Nov 3 16:23:14 2009) figures/new-14-16-2.eps (Tue Nov 3 16:23:14 2009) figures/new-14-16-1.eps (Tue Nov 3 16:23:14 2009). (a) Bayes net for a single customer C_1 recommending a single book B_1 . $Honest(C_1)$ is Boolean, while the other variables have integer values from 1 to 5. (b) Bayes net with two customers and two books.

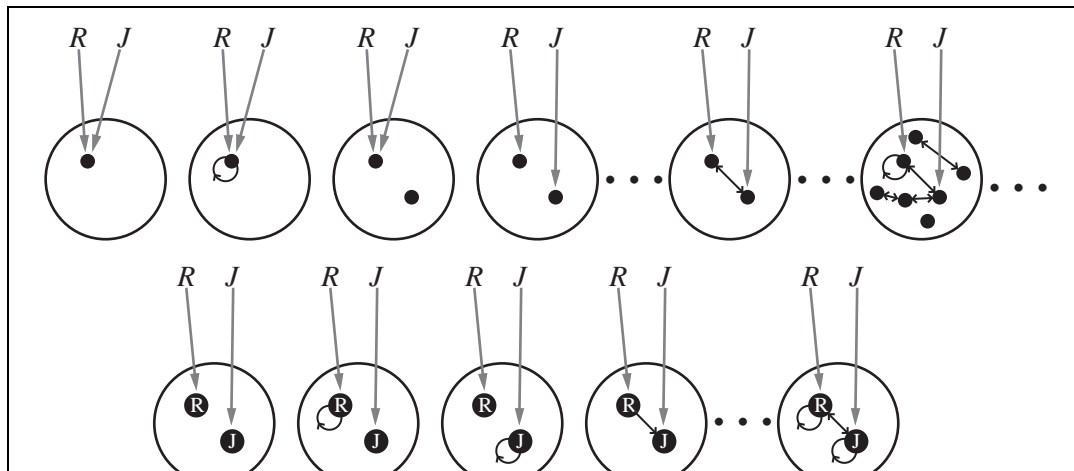
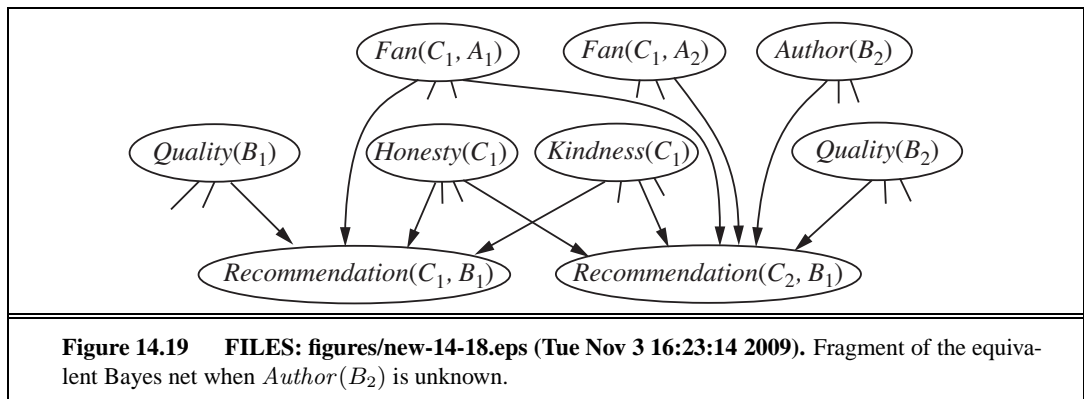
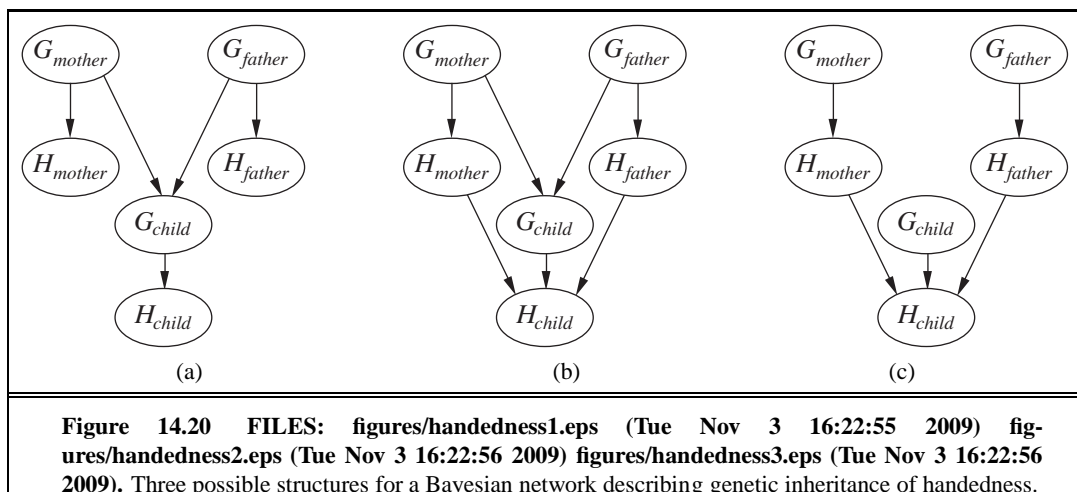


Figure 14.18 FILES: figures/all-models-both.eps (Tue Nov 3 16:22:20 2009). Top: Some members of the set of all possible worlds for a language with two constant symbols, R and J , and one binary relation symbol, under the standard semantics for first-order logic. Bottom: the possible worlds under database semantics. The interpretation of the constant symbols is fixed, and there is a distinct object for each constant symbol.





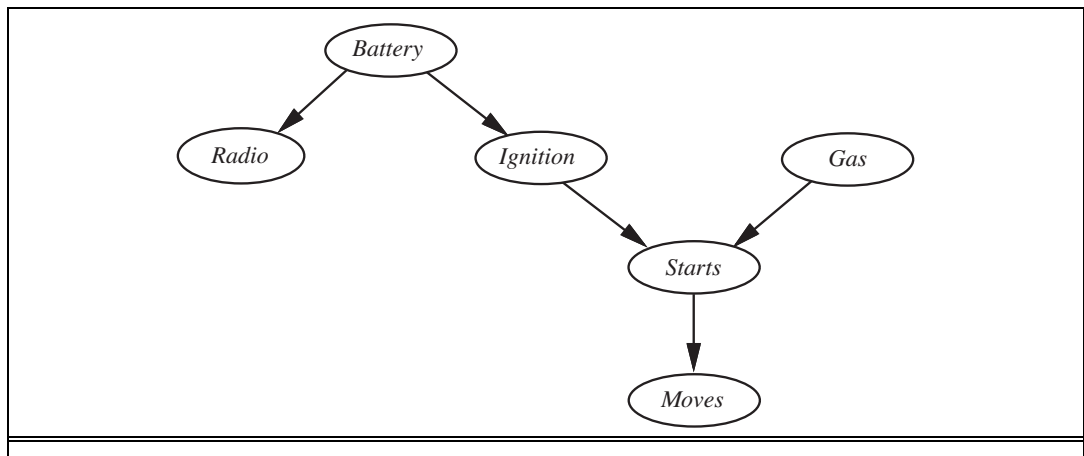
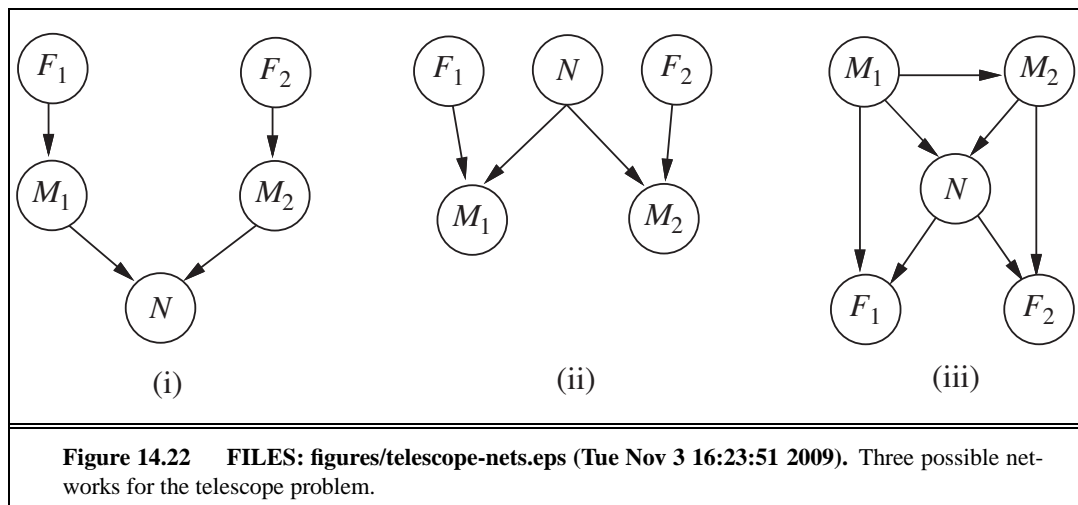
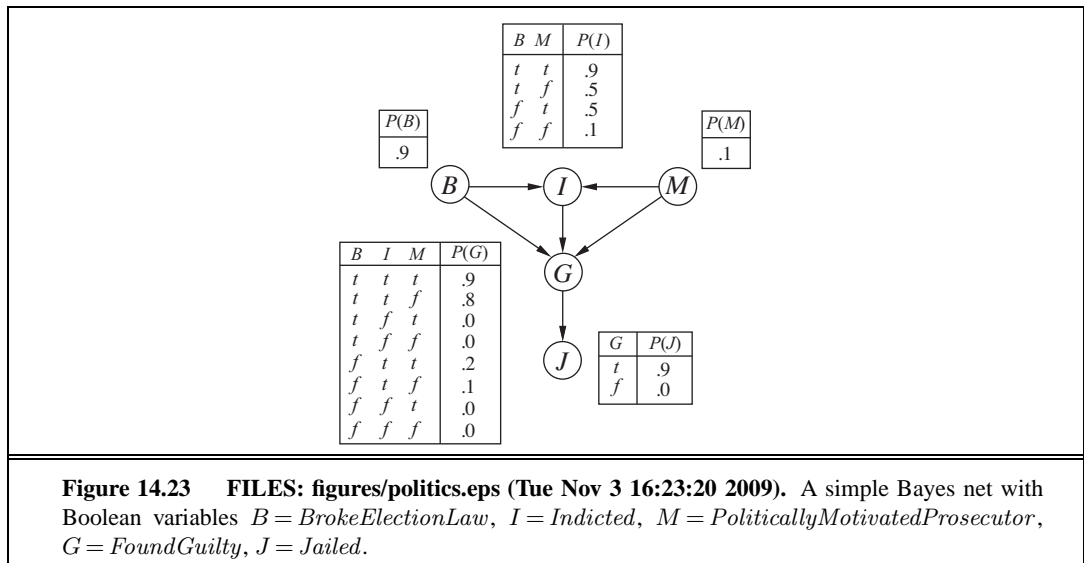
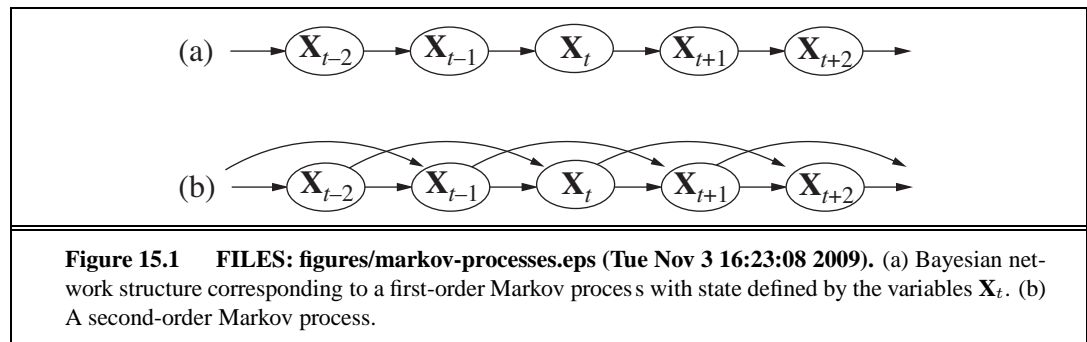


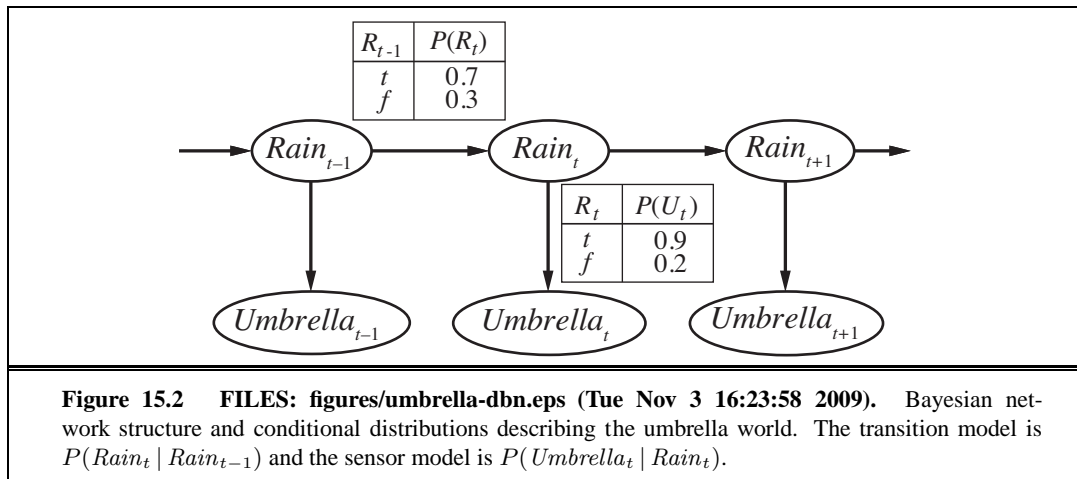
Figure 14.21 FILES: figures/car-starts.eps (Tue Nov 3 16:22:32 2009). A Bayesian network describing some features of a car's electrical system and engine. Each variable is Boolean, and the *true* value indicates that the corresponding aspect of the vehicle is in working order.

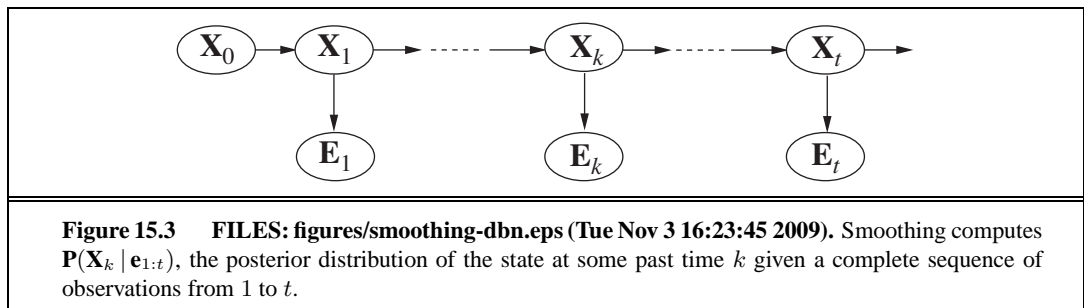




15 PROBABILISTIC REASONING OVER TIME







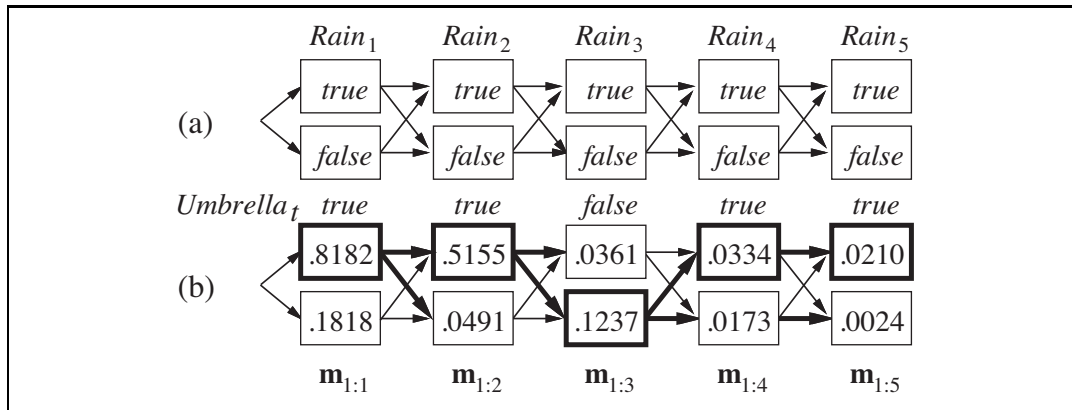
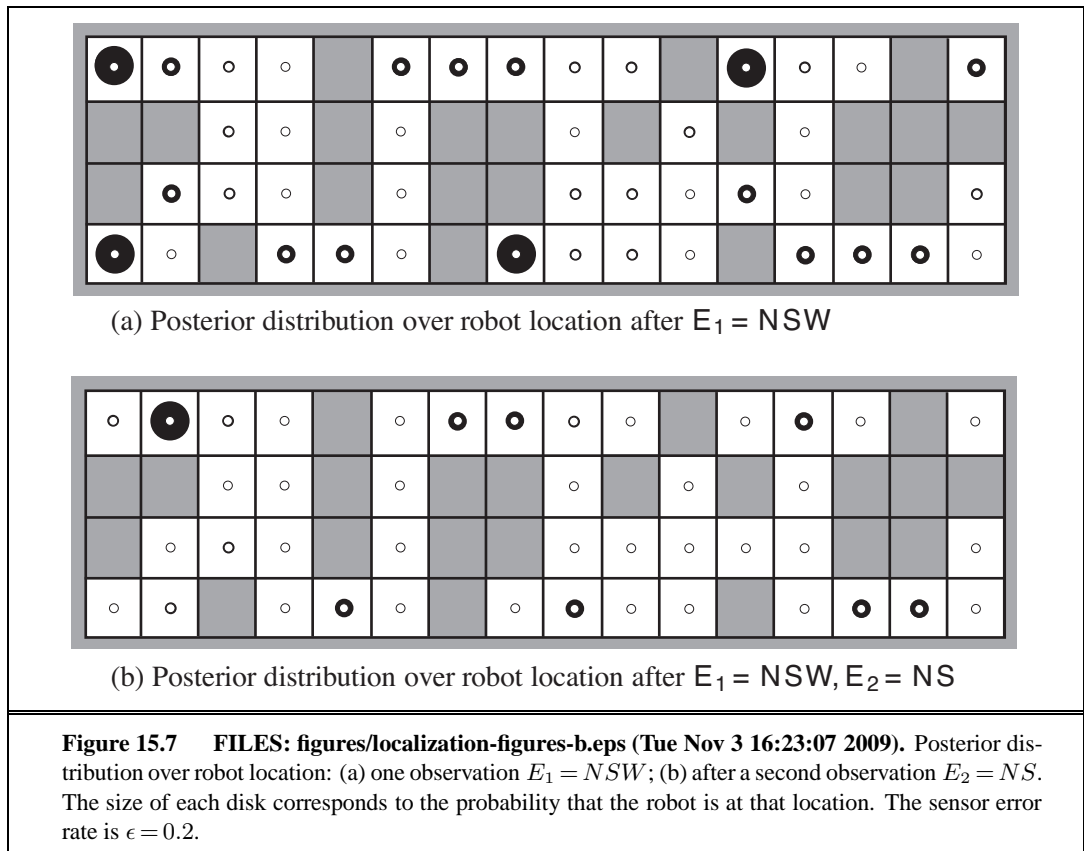


Figure 15.5 FILES: figures/umbrella-paths.eps (Tue Nov 3 16:23:59 2009). (a) Possible state sequences for $Rain_t$ can be viewed as paths through a graph of the possible states at each time step. (States are shown as rectangles to avoid confusion with nodes in a Bayes net.) (b) Operation of the Viterbi algorithm for the umbrella observation sequence $[true, true, false, true, true]$. For each t , we have shown the values of the message $\mathbf{m}_{1:t}$, which gives the probability of the best sequence reaching each state at time t . Also, for each state, the bold arrow leading into it indicates its best predecessor as measured by the product of the preceding sequence probability and the transition probability. Following the bold arrows back from the most likely state in $\mathbf{m}_{1:5}$ gives the most likely sequence.



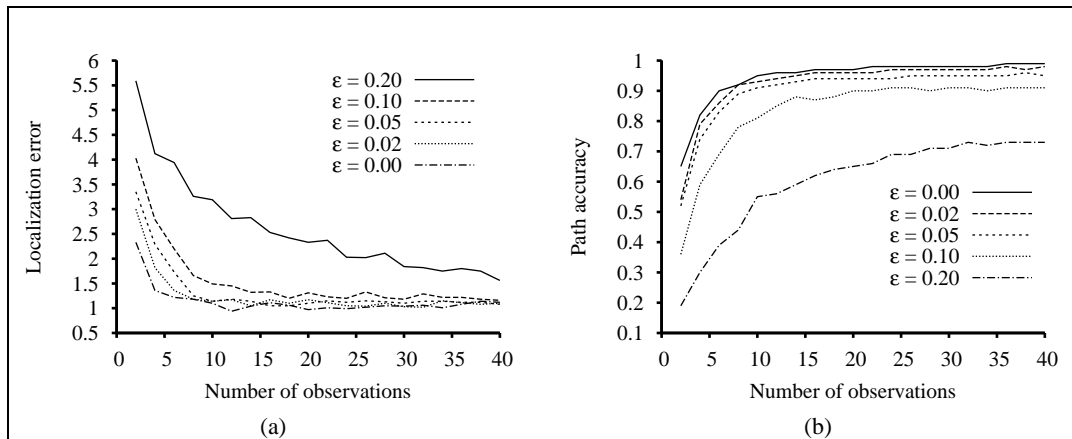
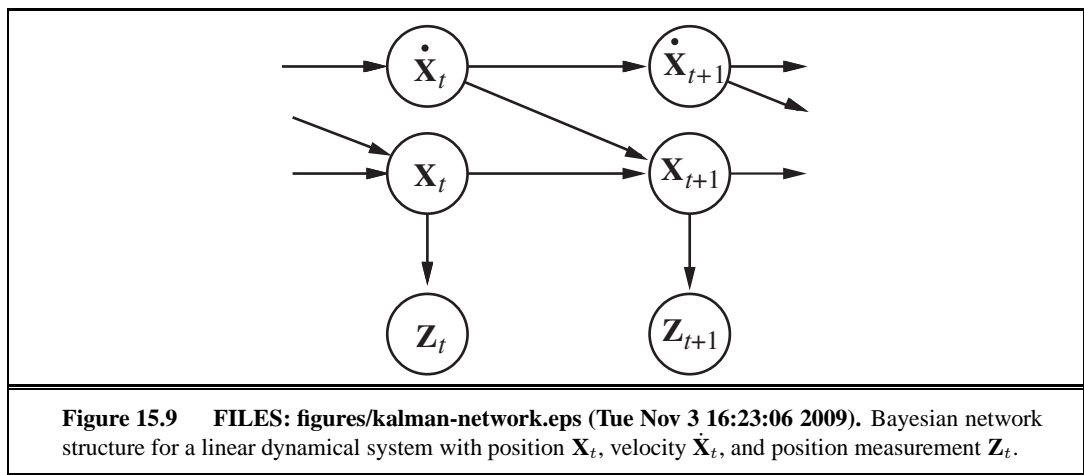


Figure 15.8 FILES: . Performance of HMM localization as a function of the length of the observation sequence for various different values of the sensor error probability ϵ ; data averaged over 400 runs. (a) The localization error, defined as the Manhattan distance from the true location. (b) The Viterbi path accuracy, defined as the fraction of correct states on the Viterbi path.



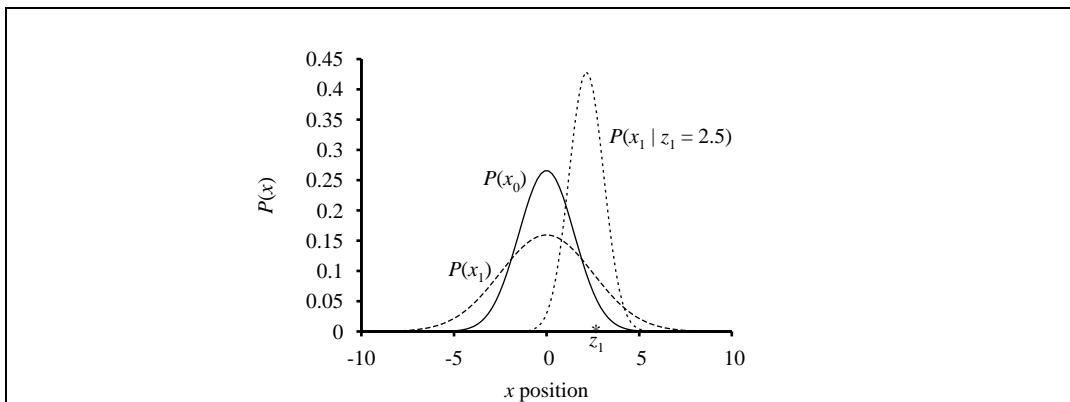


Figure 15.10 FILES: . Stages in the Kalman filter update cycle for a random walk with a prior given by $\mu_0 = 0.0$ and $\sigma_0 = 1.0$, transition noise given by $\sigma_x = 2.0$, sensor noise given by $\sigma_z = 1.0$, and a first observation $z_1 = 2.5$ (marked on the x -axis). Notice how the prediction $P(x_1)$ is flattened out, relative to $P(x_0)$, by the transition noise. Notice also that the mean of the posterior distribution $P(x_1 | z_1)$ is slightly to the left of the observation z_1 because the mean is a weighted average of the prediction and the observation.

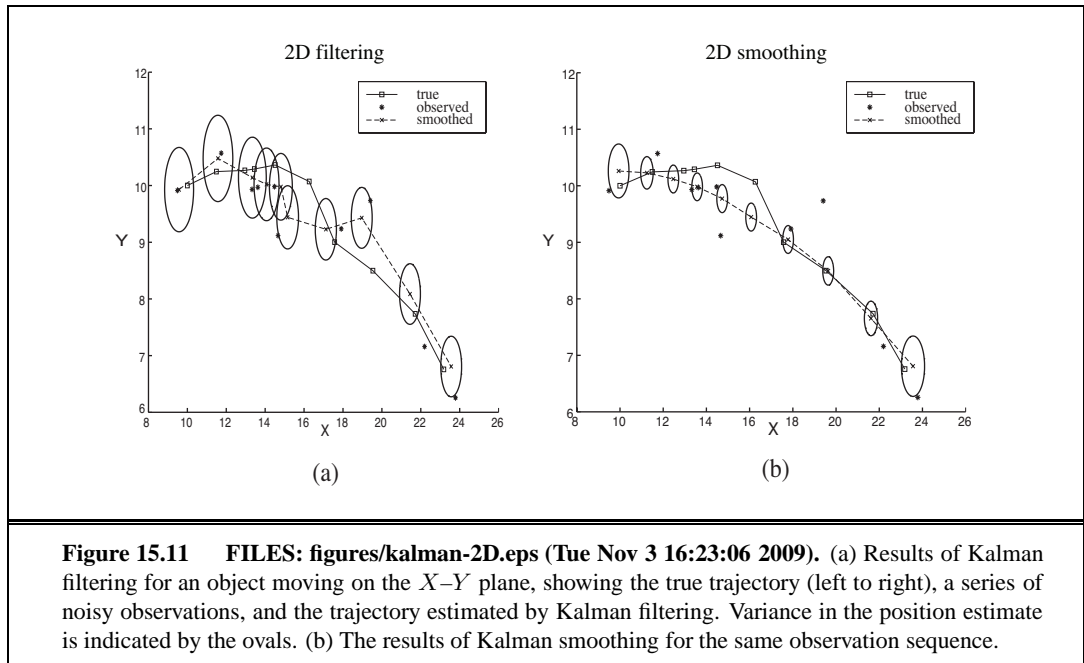


Figure 15.11 FILES: figures/kalman-2D.eps (Tue Nov 3 16:23:06 2009). (a) Results of Kalman filtering for an object moving on the X - Y plane, showing the true trajectory (left to right), a series of noisy observations, and the trajectory estimated by Kalman filtering. Variance in the position estimate is indicated by the ovals. (b) The results of Kalman smoothing for the same observation sequence.

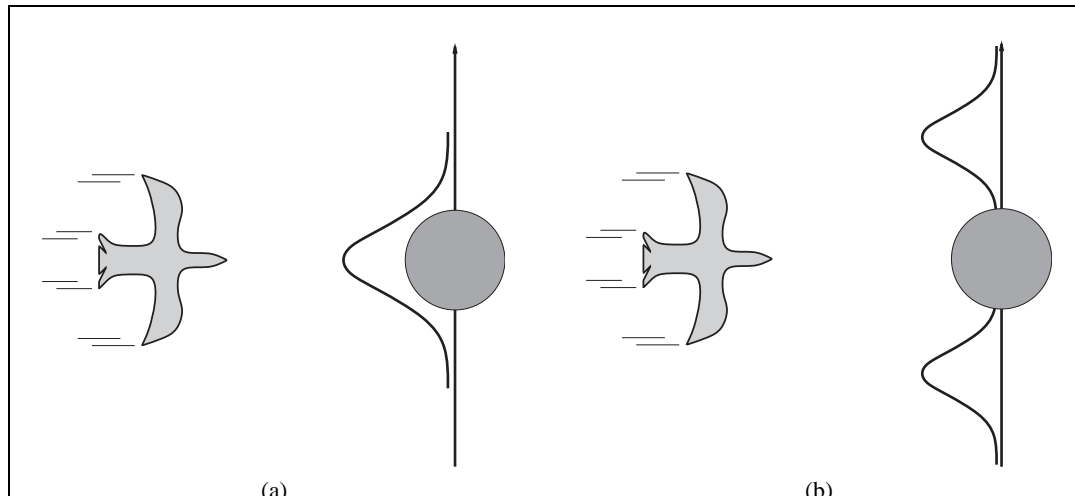


Figure 15.12 FILES: figures/kalman-bird1.eps (Tue Nov 3 16:23:06 2009) figures/kalman-bird2.eps (Tue Nov 3 16:23:06 2009). A bird flying toward a tree (top views). (a) A Kalman filter will predict the location of the bird using a single Gaussian centered on the obstacle. (b) A more realistic model allows for the bird's evasive action, predicting that it will fly to one side or the other.

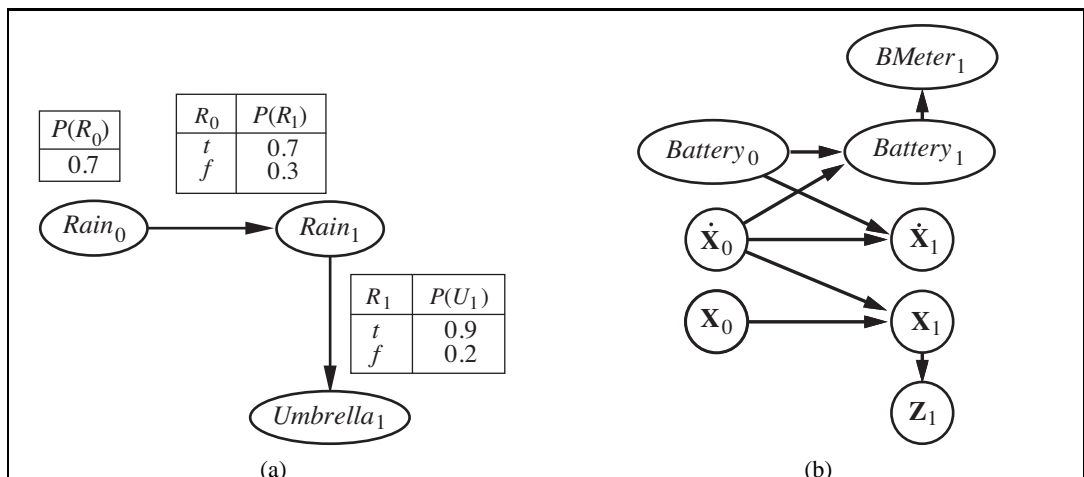


Figure 15.13 FILES: figures/umbrella-1slice.eps (Tue Nov 3 16:23:58 2009) figures/robot-dbn1.eps (Tue Nov 3 16:23:33 2009). (a) Specification of the prior, transition model, and sensor model for the umbrella DBN. All subsequent slices are assumed to be copies of slice 1. (b) A simple DBN for robot motion in the X-Y plane.

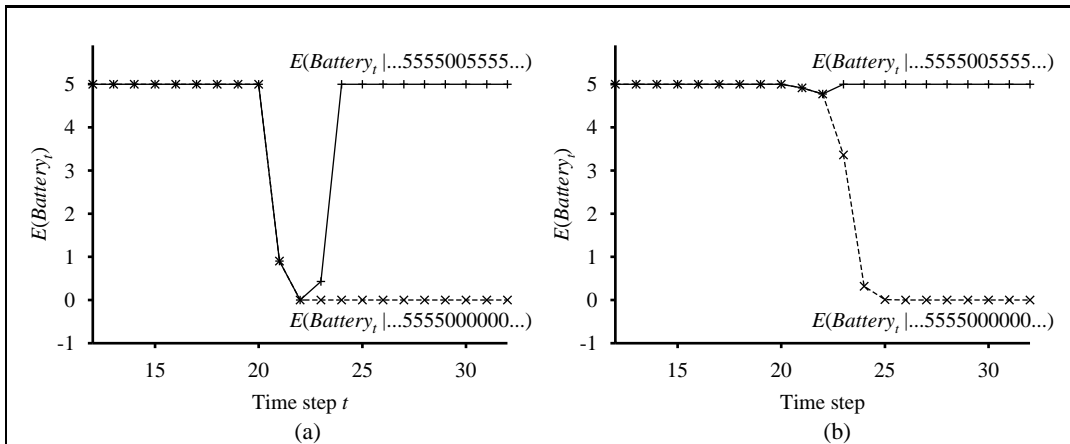


Figure 15.14 FILES: . (a) Upper curve: trajectory of the expected value of $Battery_t$ for an observation sequence consisting of all 5s except for 0s at $t = 21$ and $t = 22$, using a simple Gaussian error model. Lower curve: trajectory when the observation remains at 0 from $t = 21$ onwards. (b) The same experiment run with the transient failure model. Notice that the transient failure is handled well, but the persistent failure results in excessive pessimism about the battery charge.

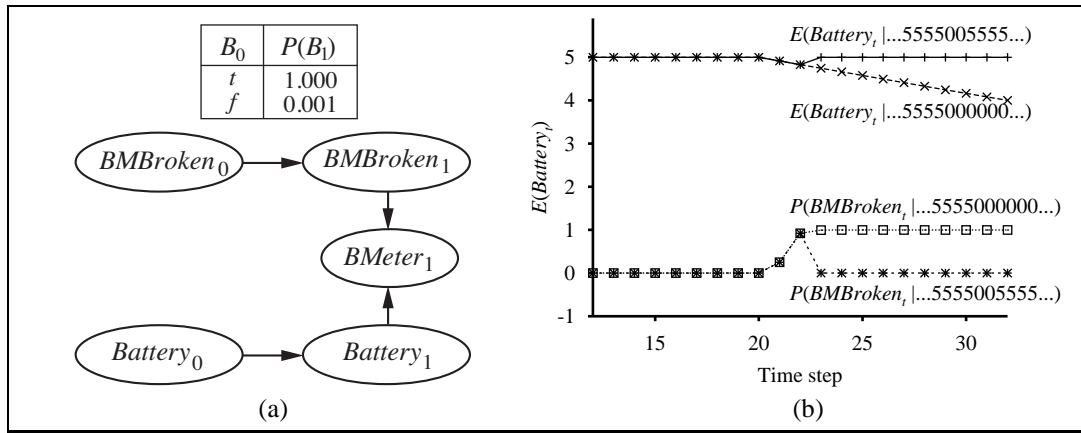
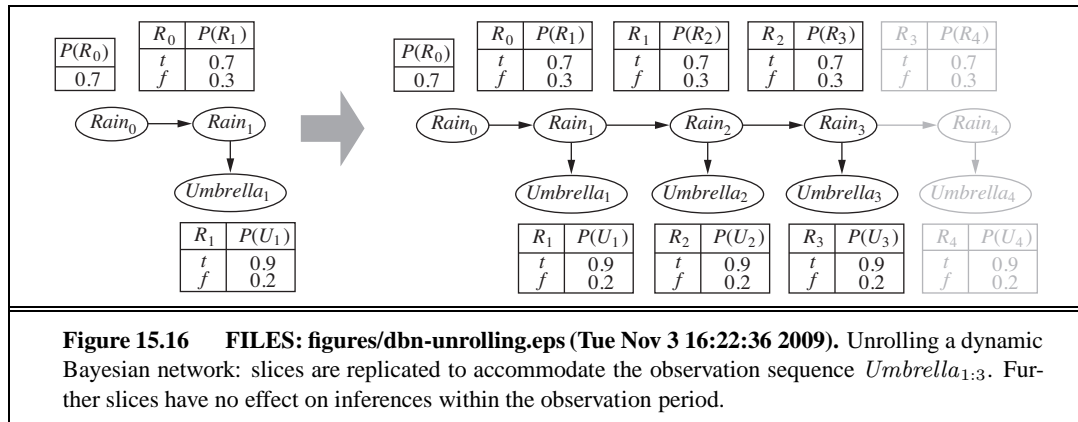


Figure 15.15 FILES: figures/battery-persistence.eps (Tue Nov 3 16:22:26 2009). (a) A DBN fragment showing the sensor status variable required for modeling persistent failure of the battery sensor. (b) Upper curves: trajectories of the expected value of $Battery_t$ for the “transient failure” and “permanent failure” observation sequences. Lower curves: probability trajectories for $BMBroken$ given the two observation sequences.



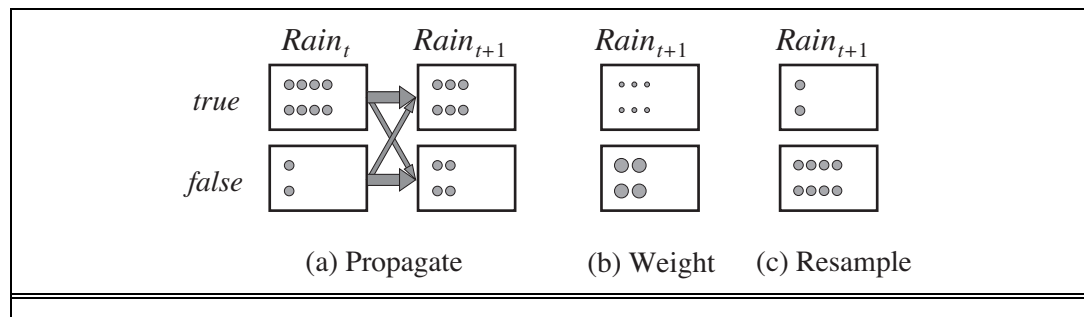
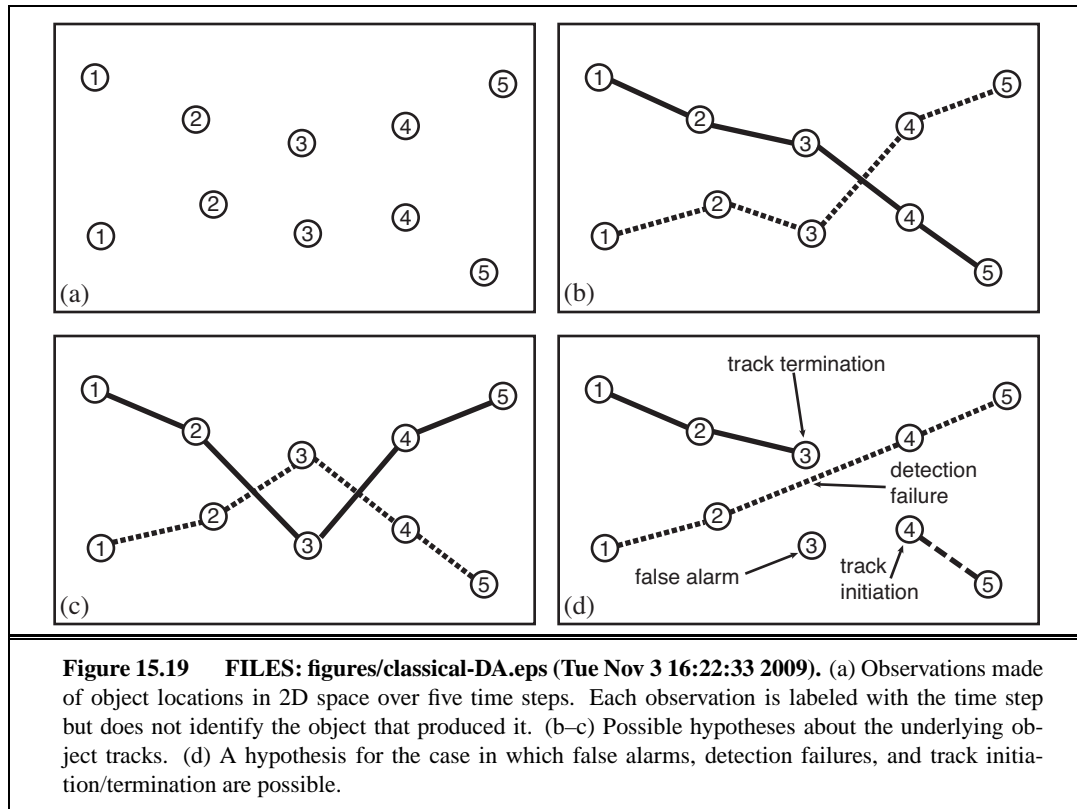


Figure 15.18 FILES: figures/umbrella-particle.eps (Tue Nov 3 16:23:59 2009). The particle filtering update cycle for the umbrella DBN with $N = 10$, showing the sample populations of each state. (a) At time t , 8 samples indicate *rain* and 2 indicate \neg *rain*. Each is propagated forward by sampling the next state through the transition model. At time $t + 1$, 6 samples indicate *rain* and 4 indicate \neg *rain*. (b) \neg *umbrella* is observed at $t + 1$. Each sample is weighted by its likelihood for the observation, as indicated by the size of the circles. (c) A new set of 10 samples is generated by weighted random selection from the current set, resulting in 2 samples that indicate *rain* and 8 that indicate \neg *rain*.



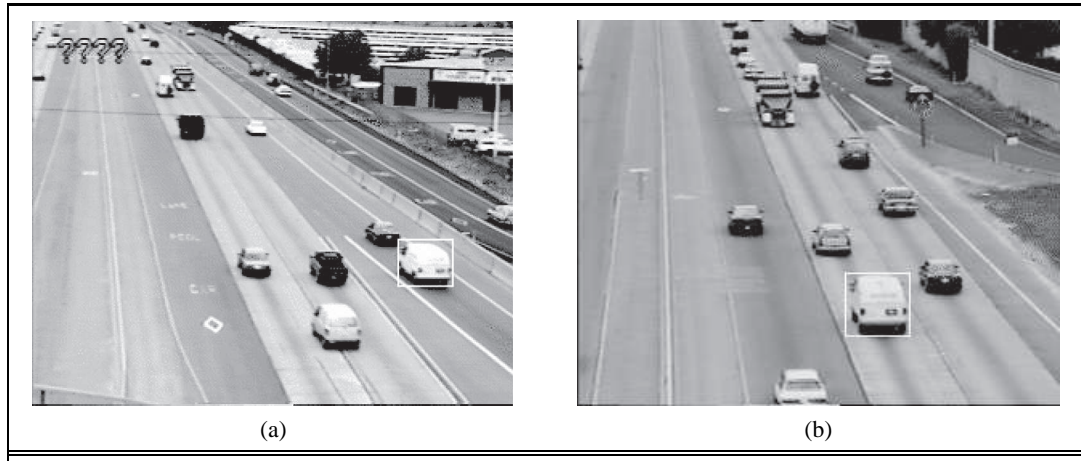
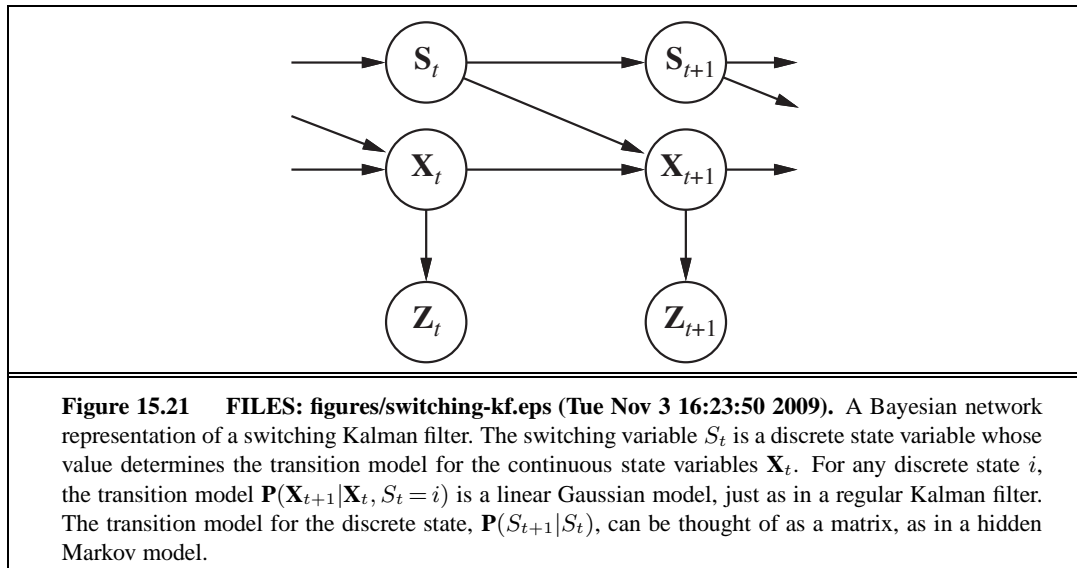
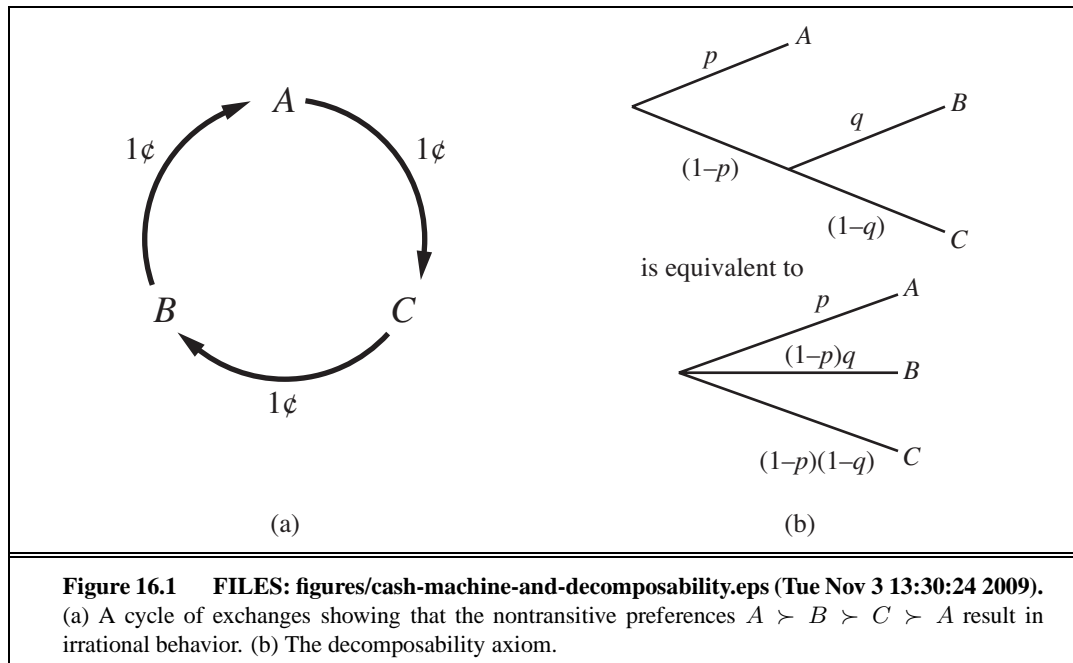


Figure 15.20 FILES: figures/traffic-upstream.eps (Tue Nov 3 16:23:58 2009) figures/traffic-downstream.eps (Tue Nov 3 16:23:57 2009). Images from (a) upstream and (b) downstream surveillance cameras roughly two miles apart on Highway 99 in Sacramento, California. The boxed vehicle has been identified at both cameras.



16 MAKING SIMPLE DECISIONS



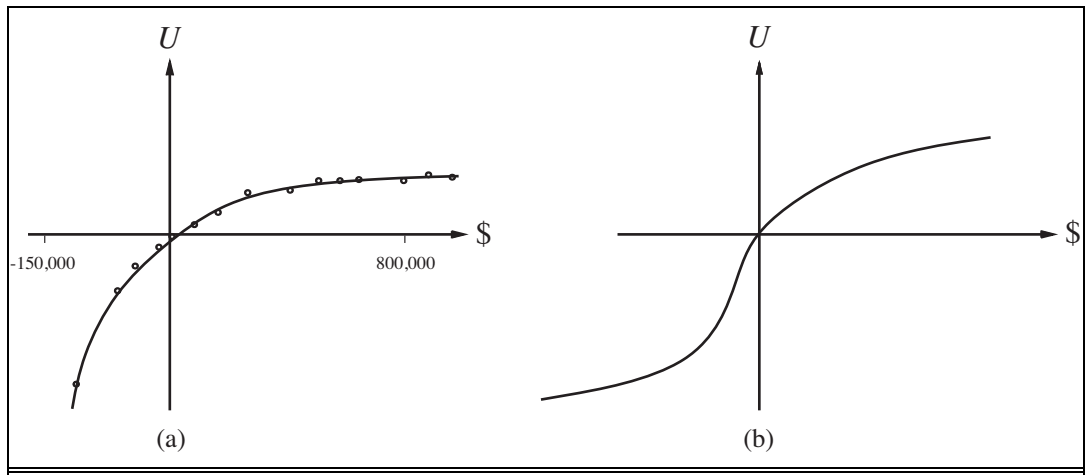
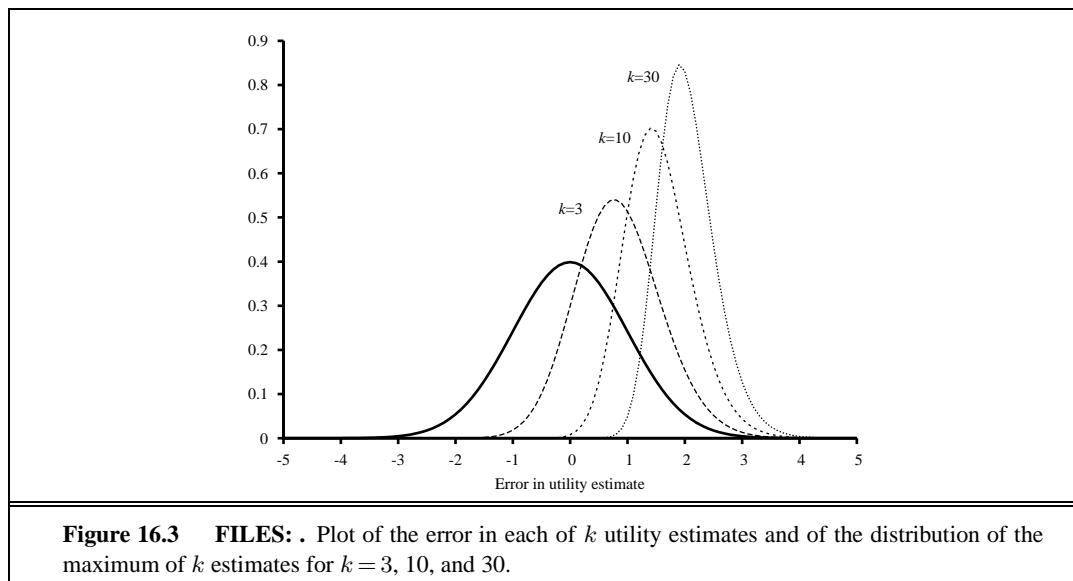
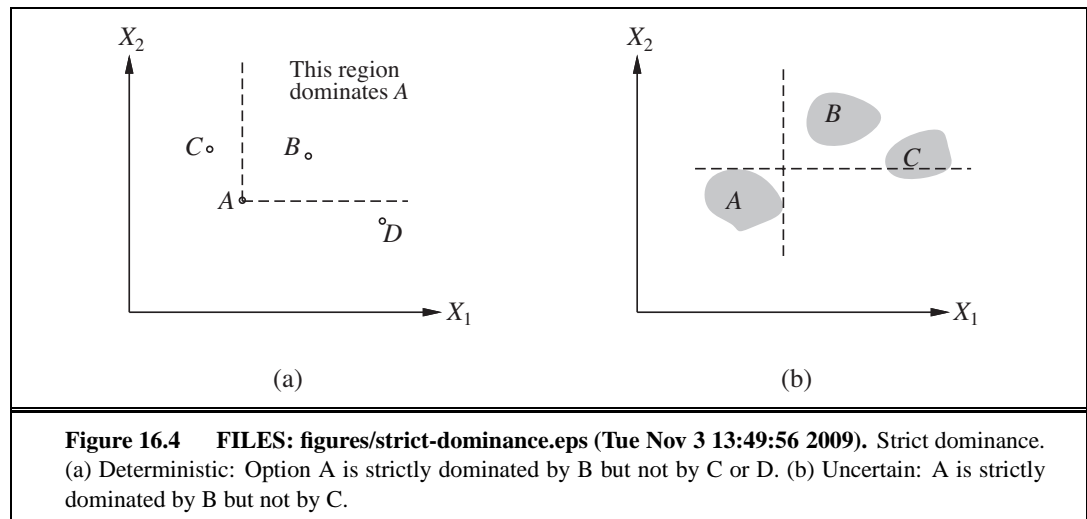
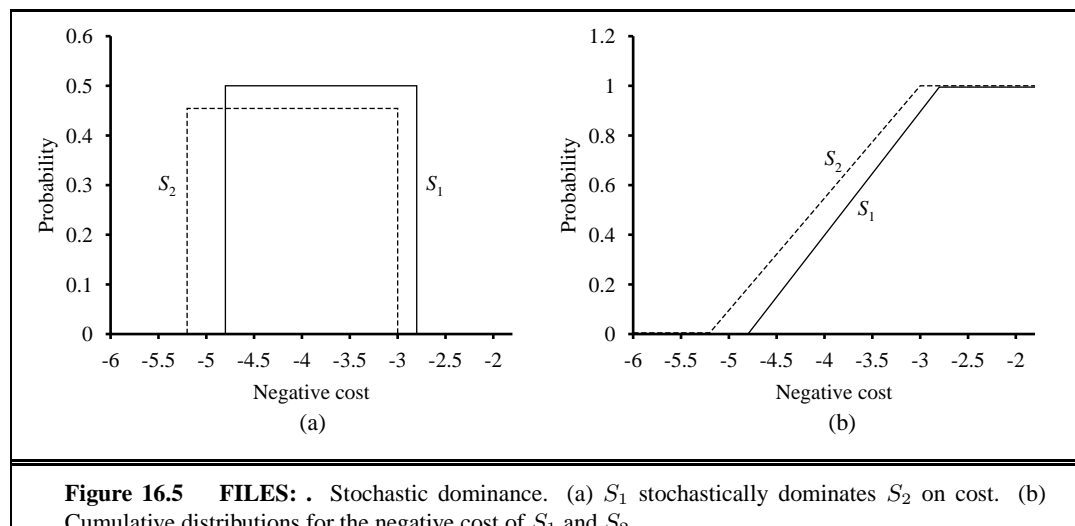
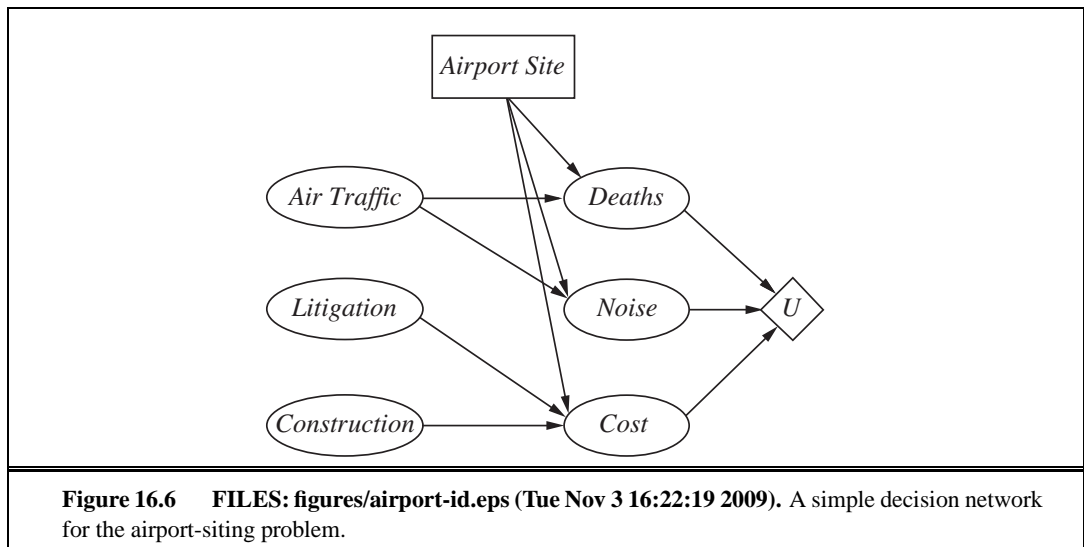


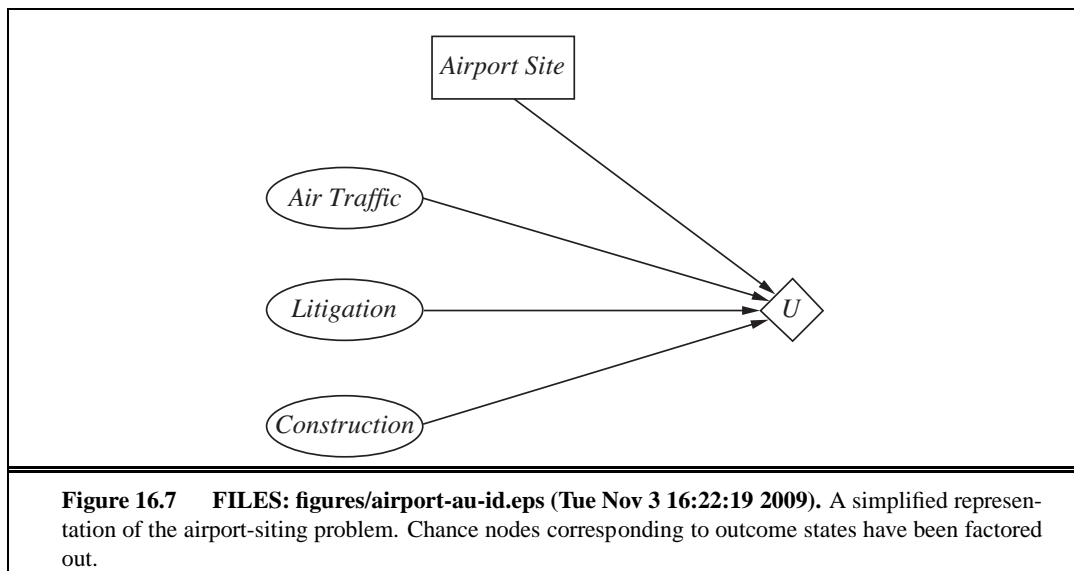
Figure 16.2 FILES: figures/utility-curve.eps (Tue Nov 3 16:24:00 2009). The utility of money.
(a) Empirical data for Mr. Beard over a limited range. (b) A typical curve for the full range.











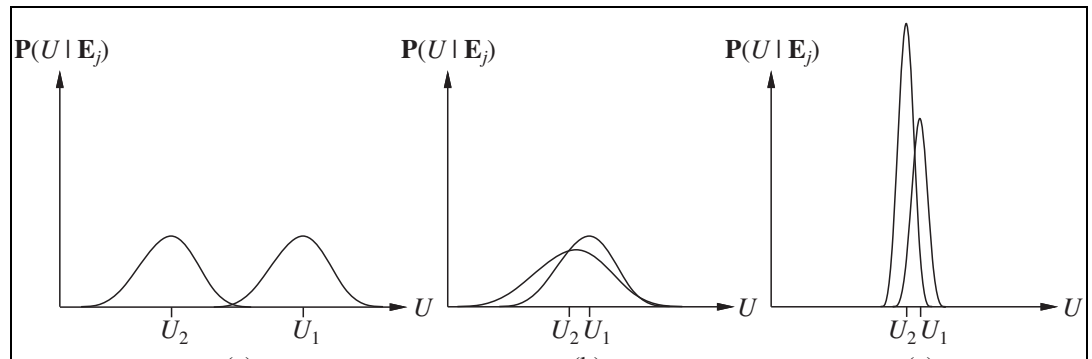
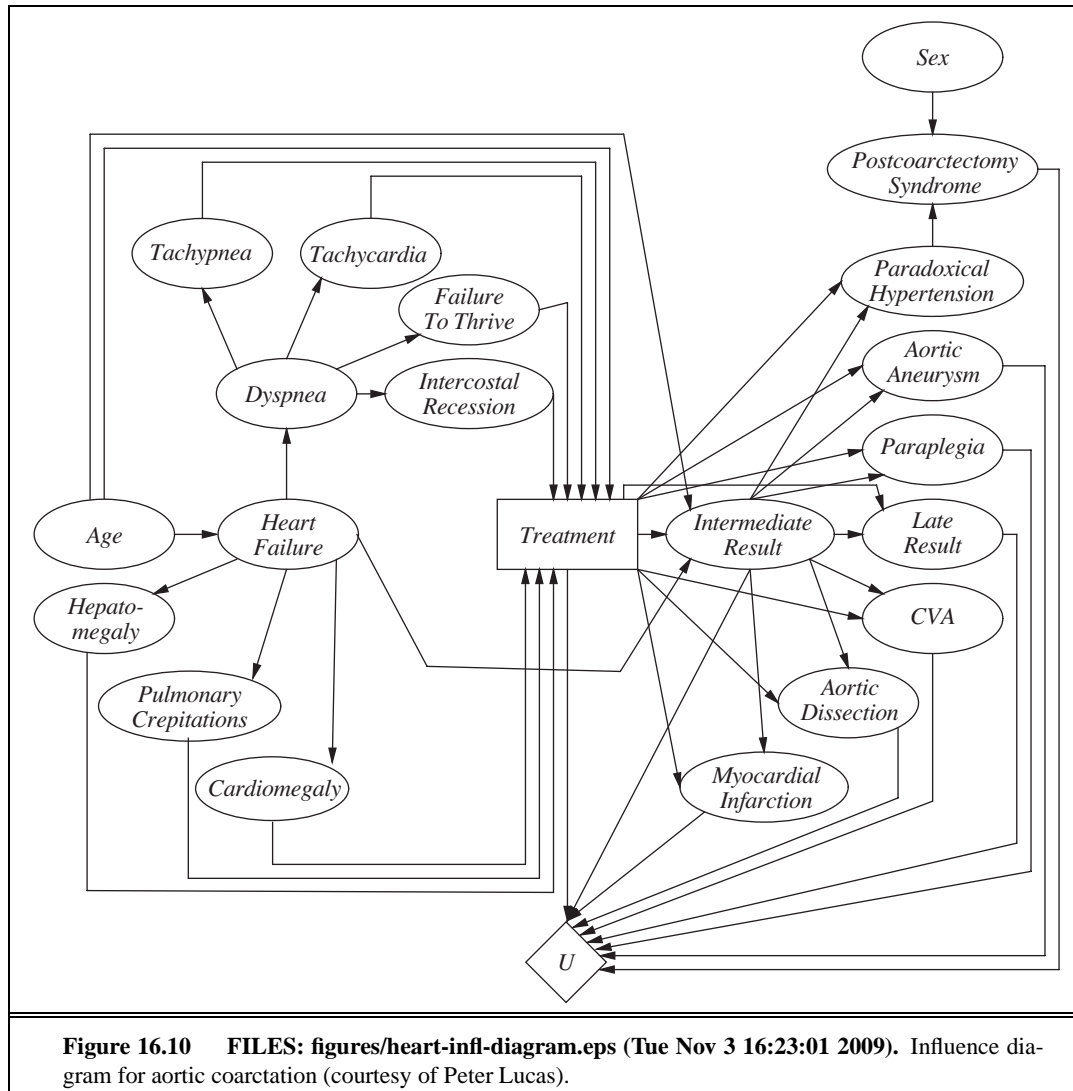
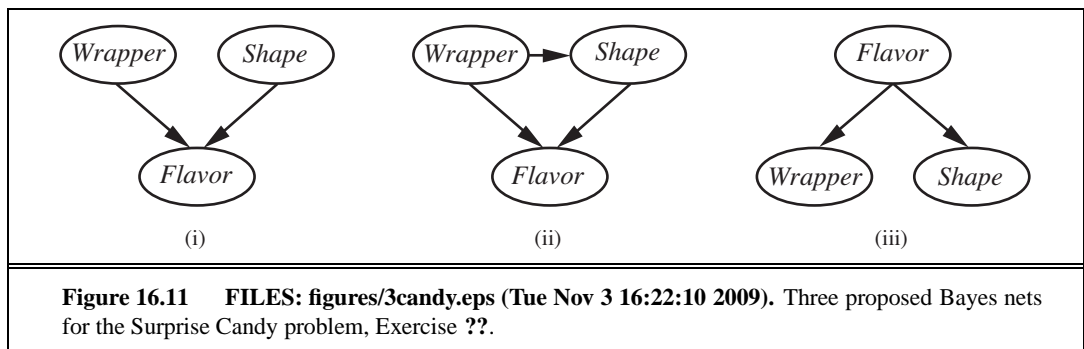
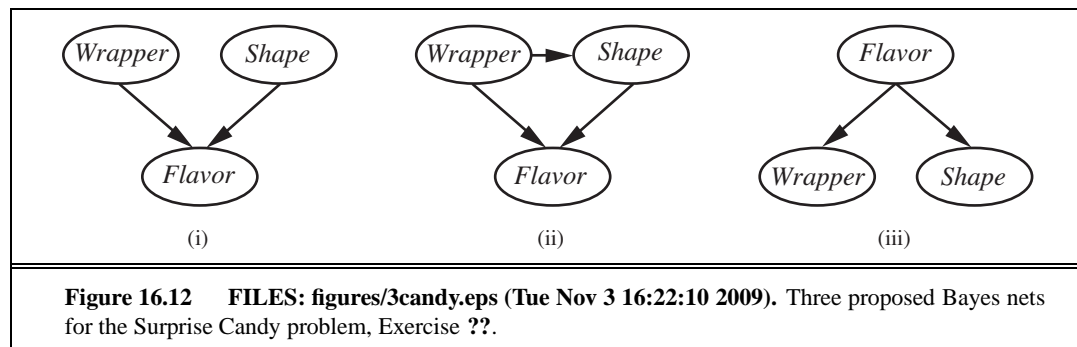


Figure 16.8 FILES: figures/3cases.eps (Tue Nov 3 16:22:10 2009). Three generic cases for the value of information. In (a), a_1 will almost certainly remain superior to a_2 , so the information is not needed. In (b), the choice is unclear and the information is crucial. In (c), the choice is unclear, but because it makes little difference, the information is less valuable. (Note: The fact that U_2 has a high peak in (c) means that its expected value is known with higher certainty than U_1 .)







17 MAKING COMPLEX DECISIONS

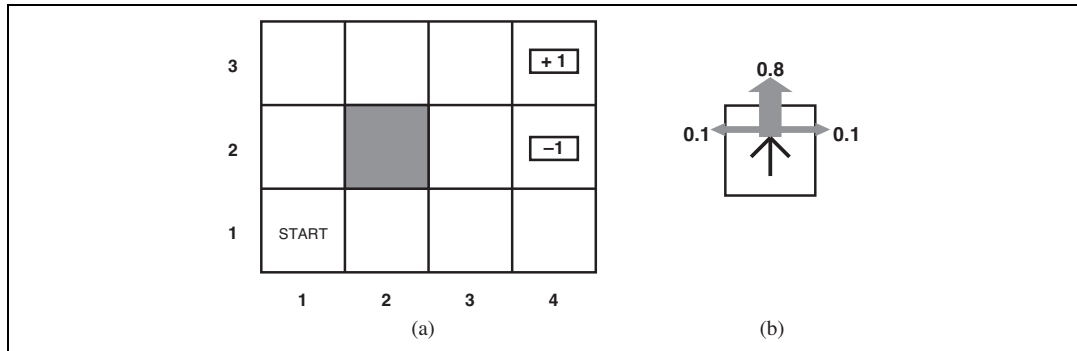
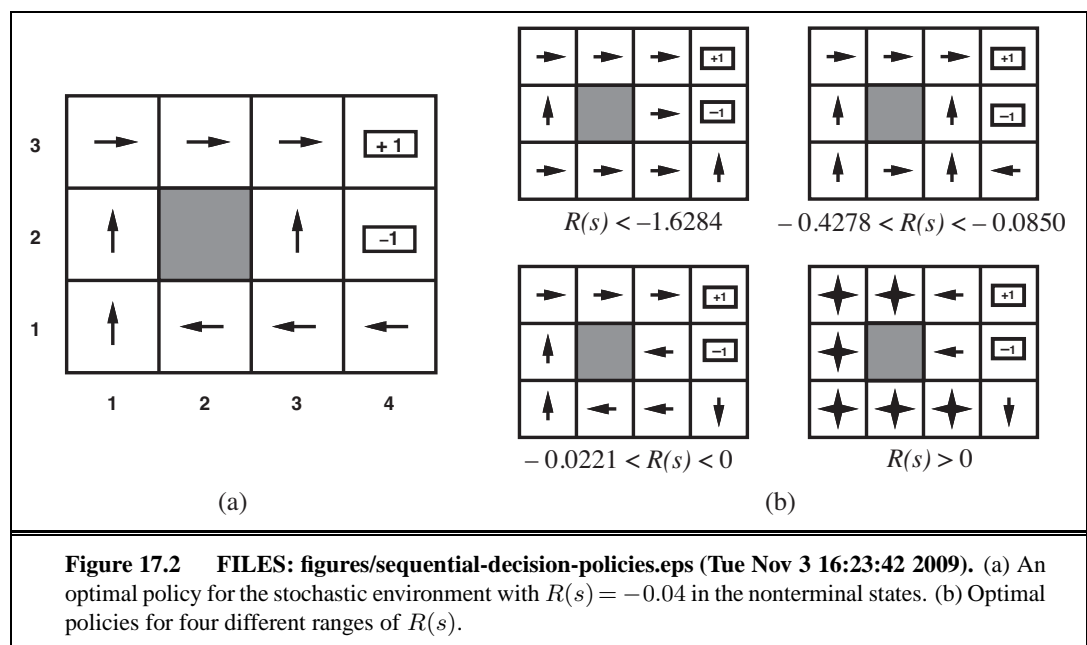
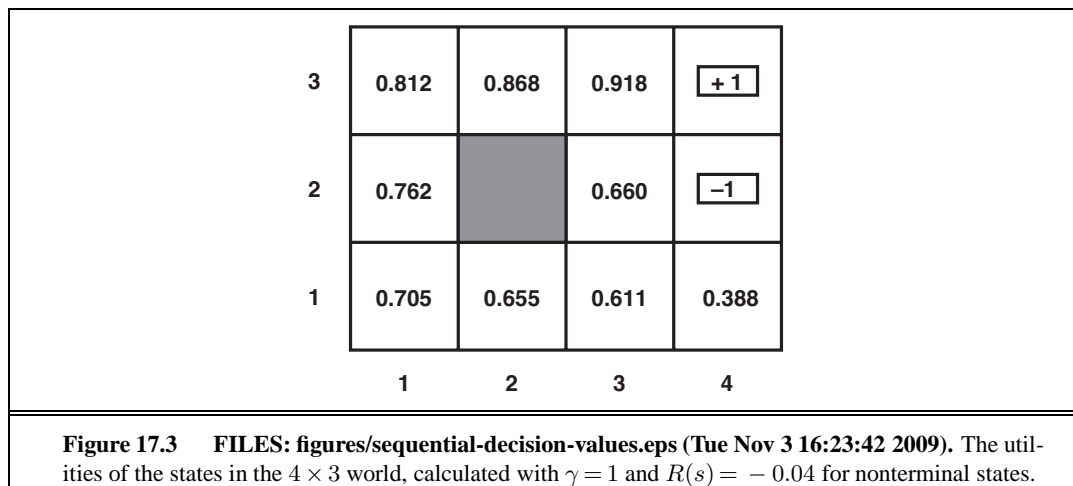


Figure 17.1 FILES: figures/sequential-decision-world.eps (Tue Nov 3 16:23:43 2009). (a) A simple 4×3 environment that presents the agent with a sequential decision problem. (b) Illustration of the transition model of the environment: the “intended” outcome occurs with probability 0.8, but with probability 0.2 the agent moves at right angles to the intended direction. A collision with a wall results in no movement. The two terminal states have reward +1 and -1, respectively, and all other states have a reward of -0.04.





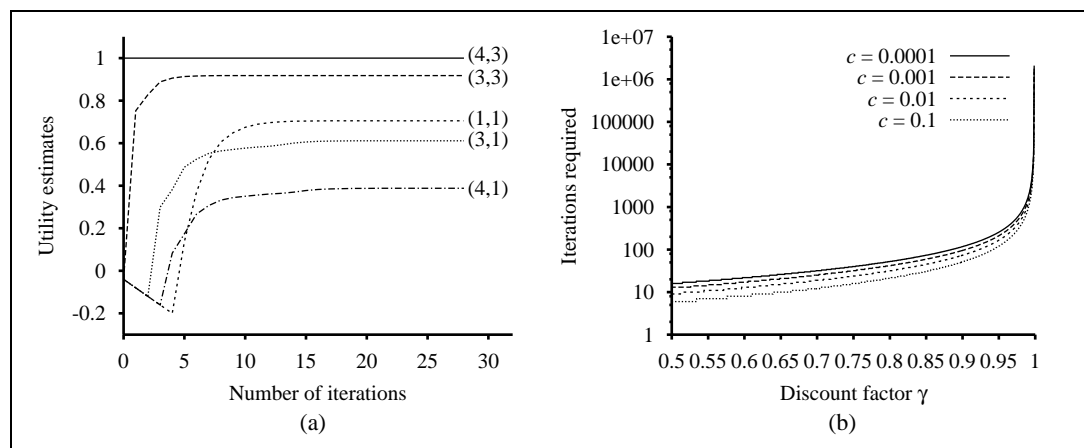
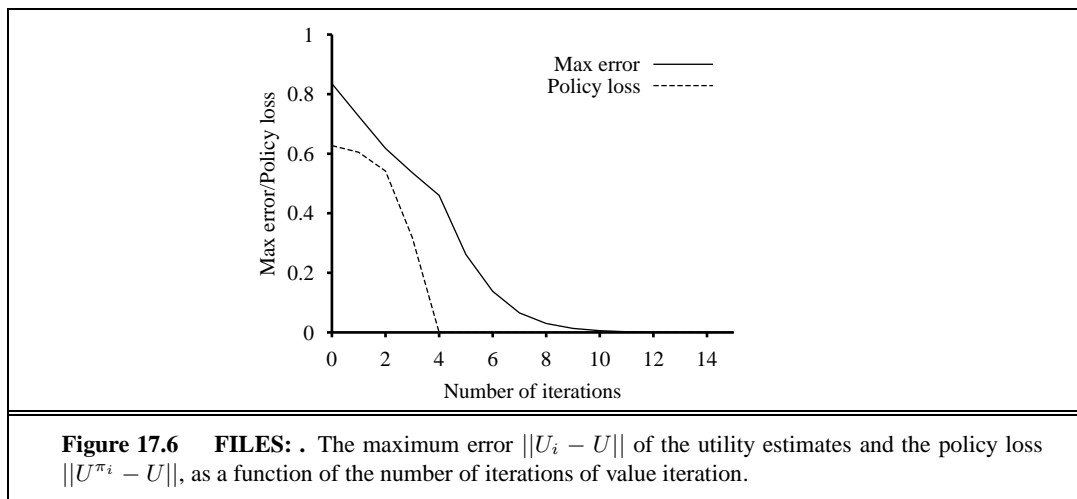


Figure 17.5 FILES: . (a) Graph showing the evolution of the utilities of selected states using value iteration. (b) The number of value iterations k required to guarantee an error of at most $\epsilon = c \cdot R_{\max}$, for different values of c , as a function of the discount factor γ .



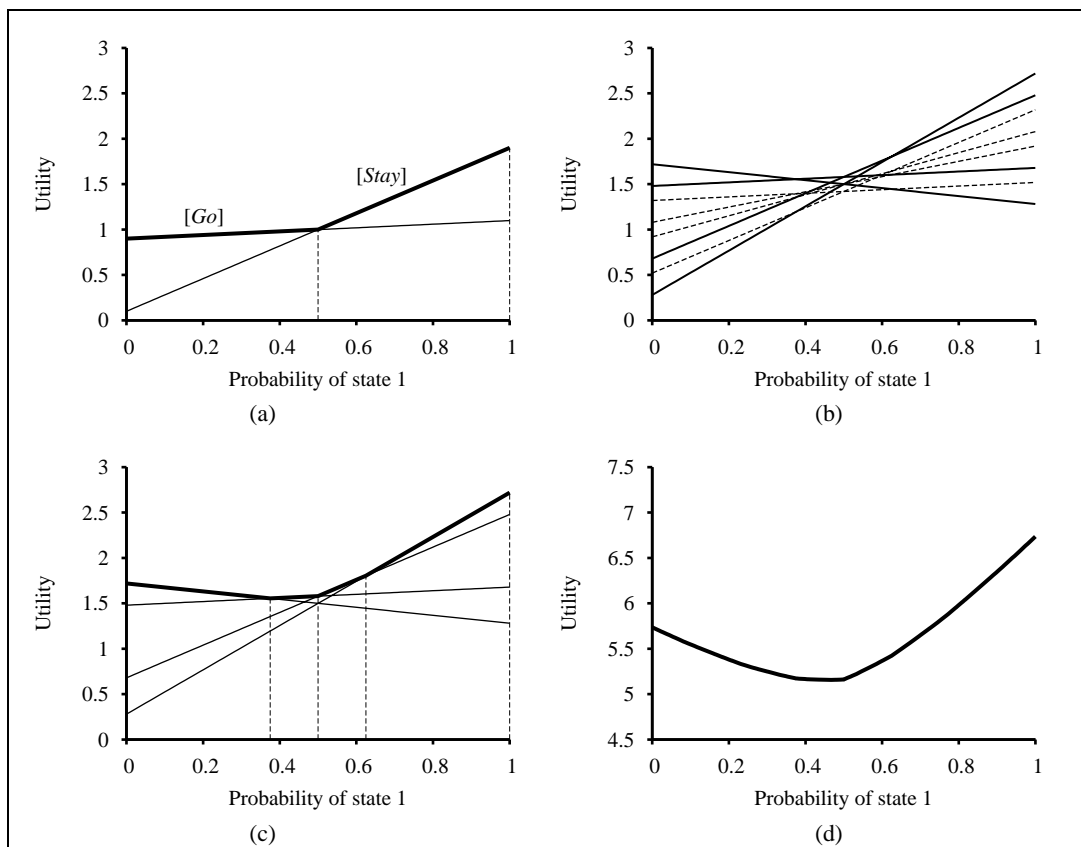
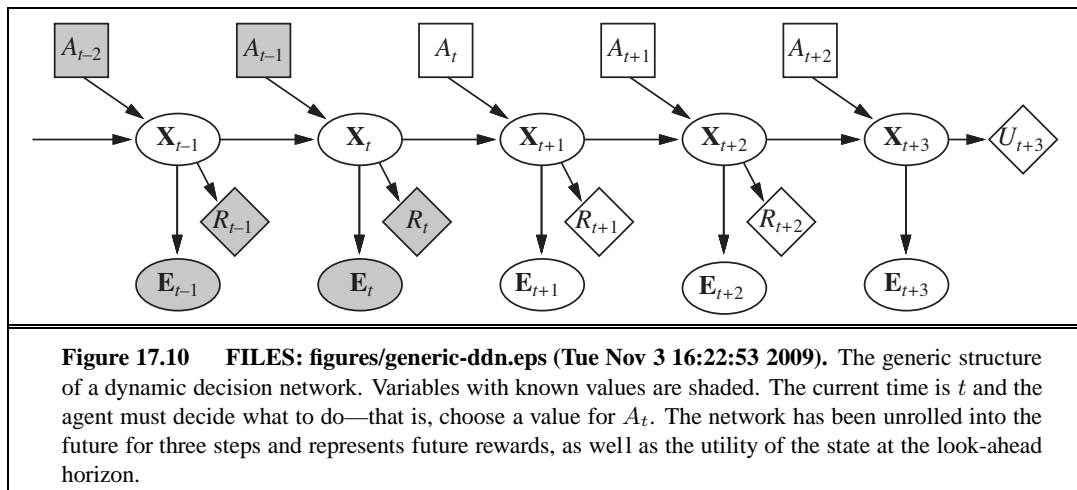
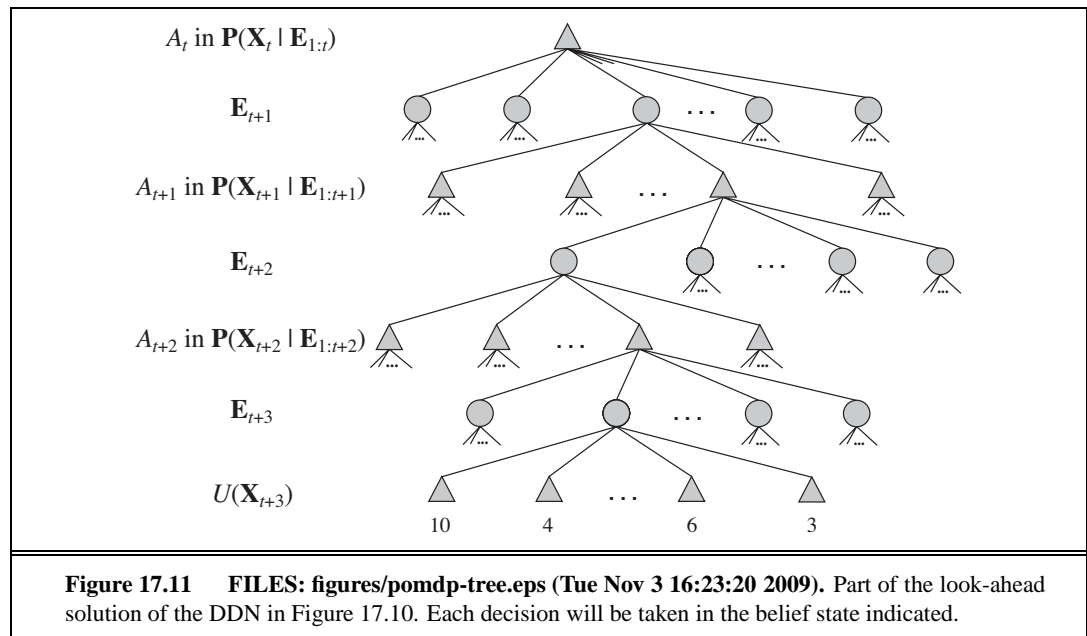
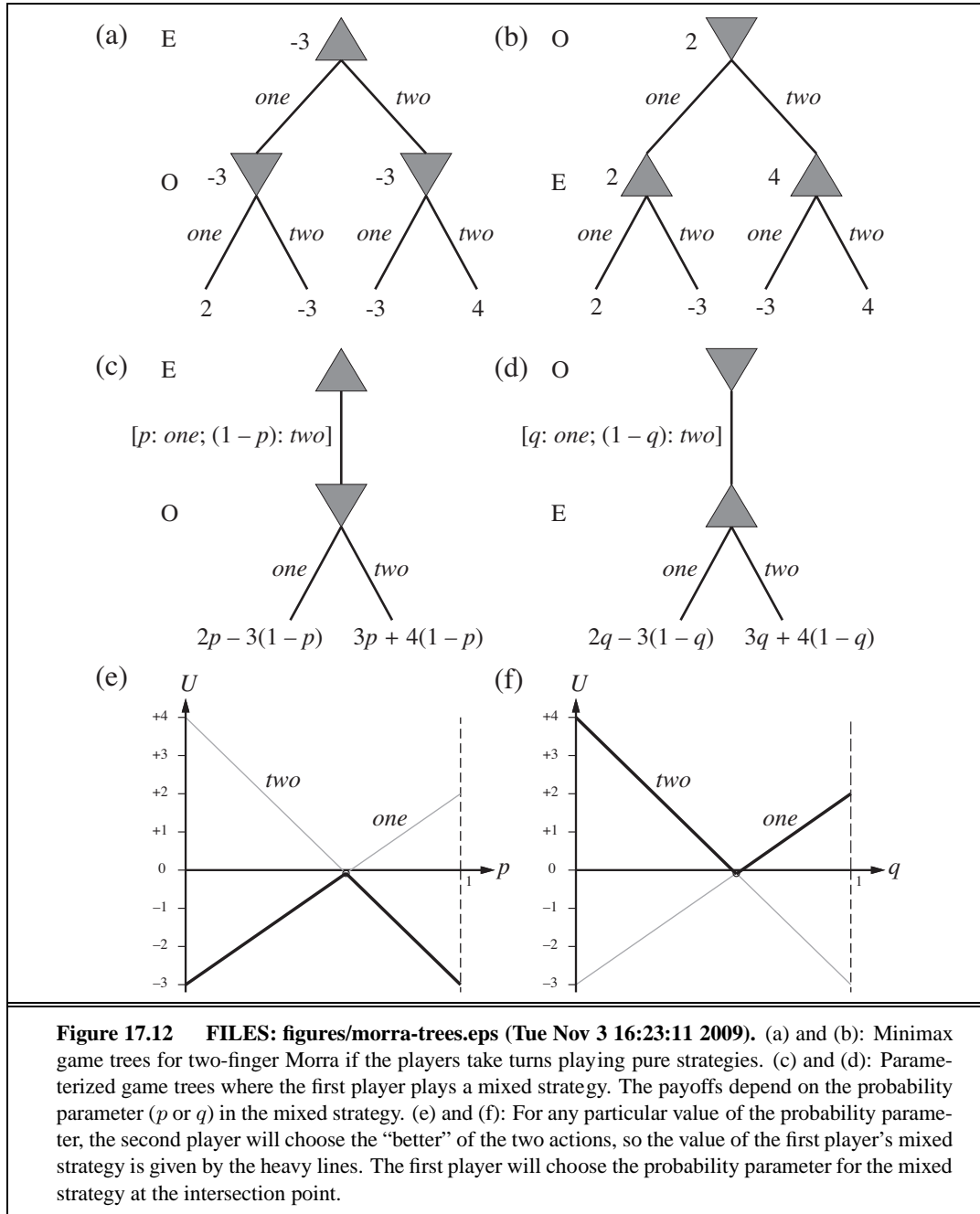
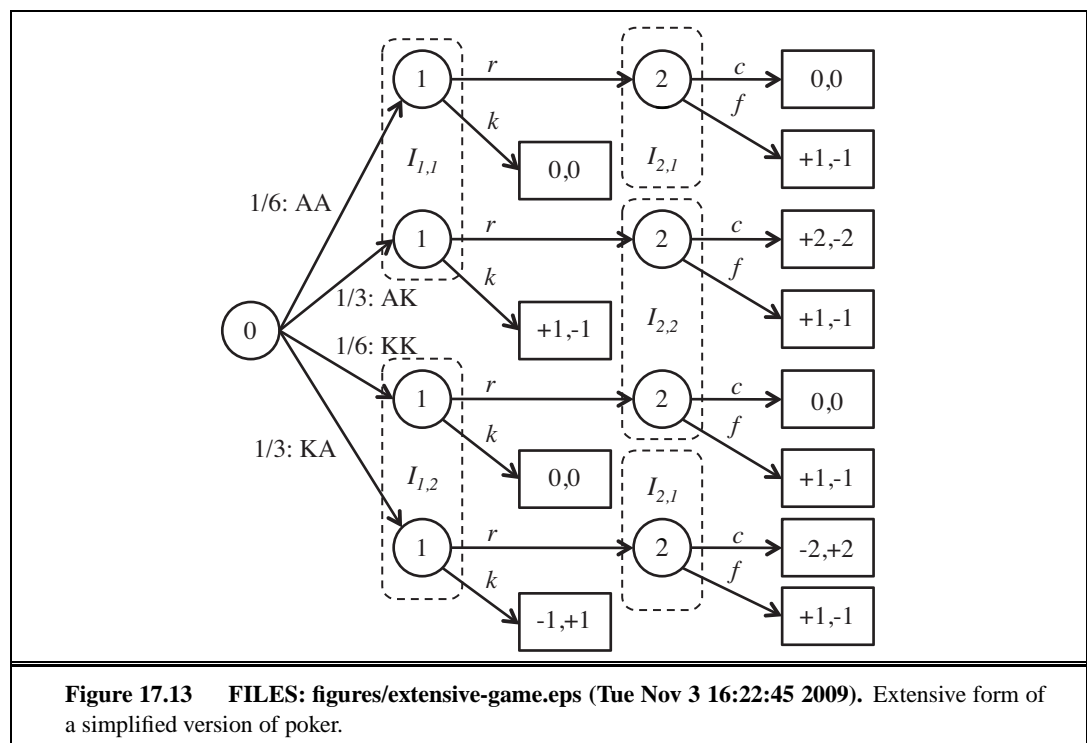


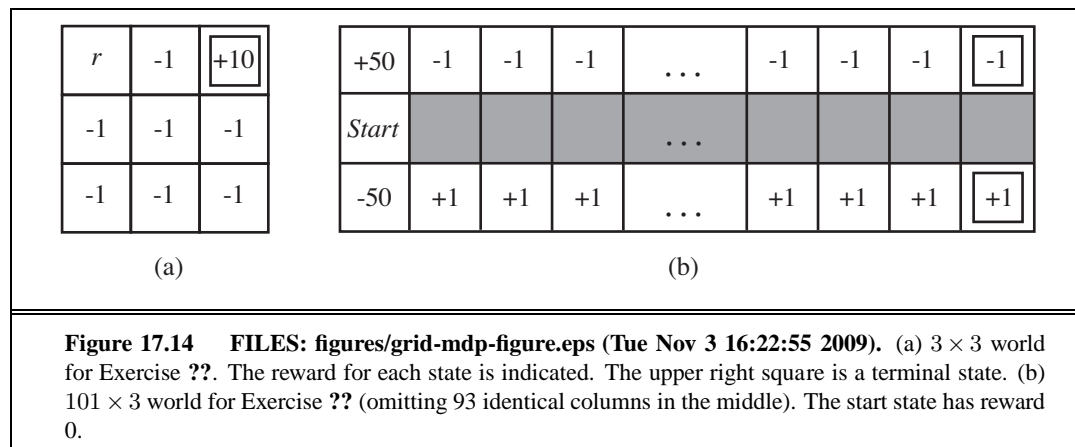
Figure 17.8 FILES: . (a) Utility of two one-step plans as a function of the initial belief state $b(1)$ for the two-state world, with the corresponding utility function shown in bold. (b) Utilities for 8 distinct two-step plans. (c) Utilities for four undominated two-step plans. (d) Utility function for optimal eight-step plans.



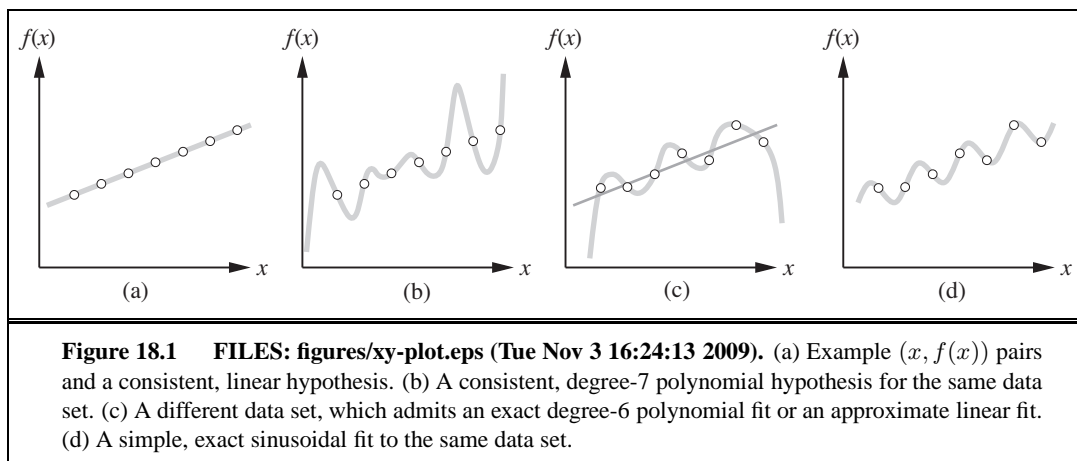


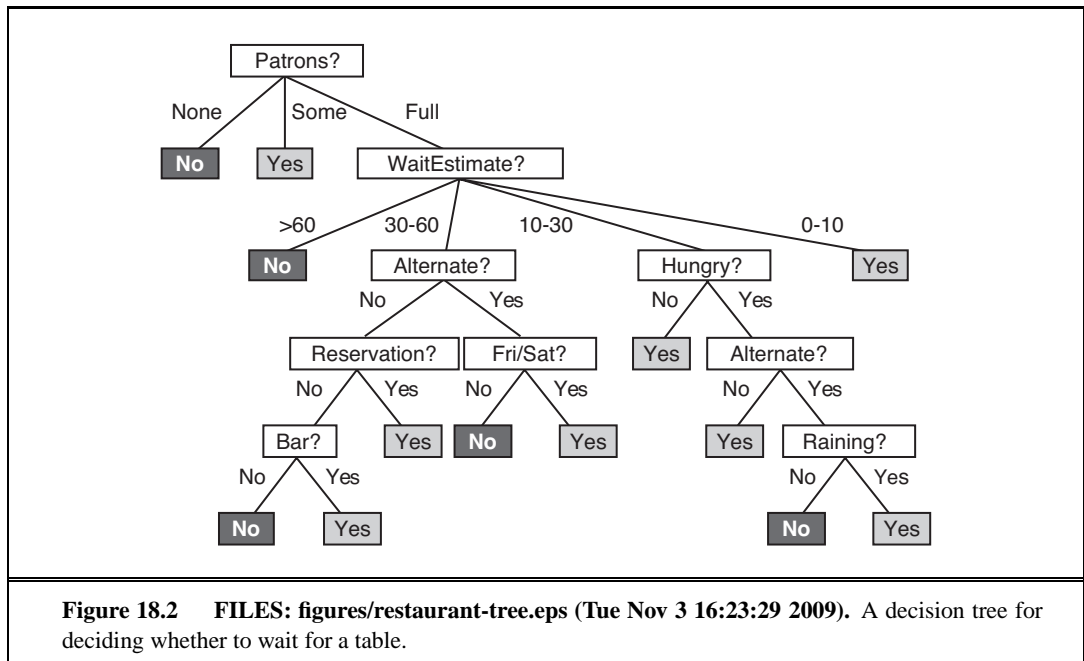


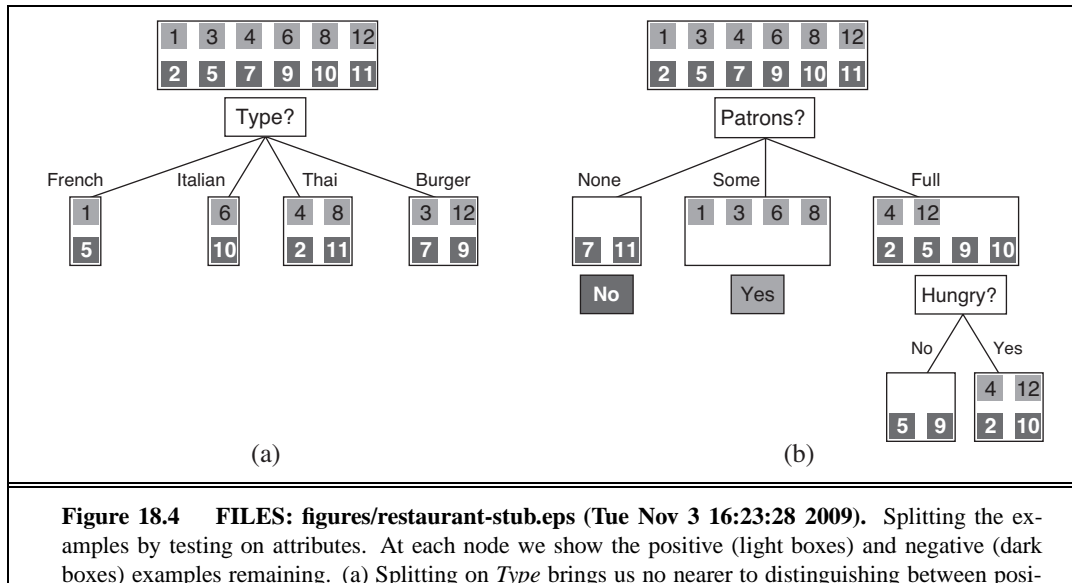


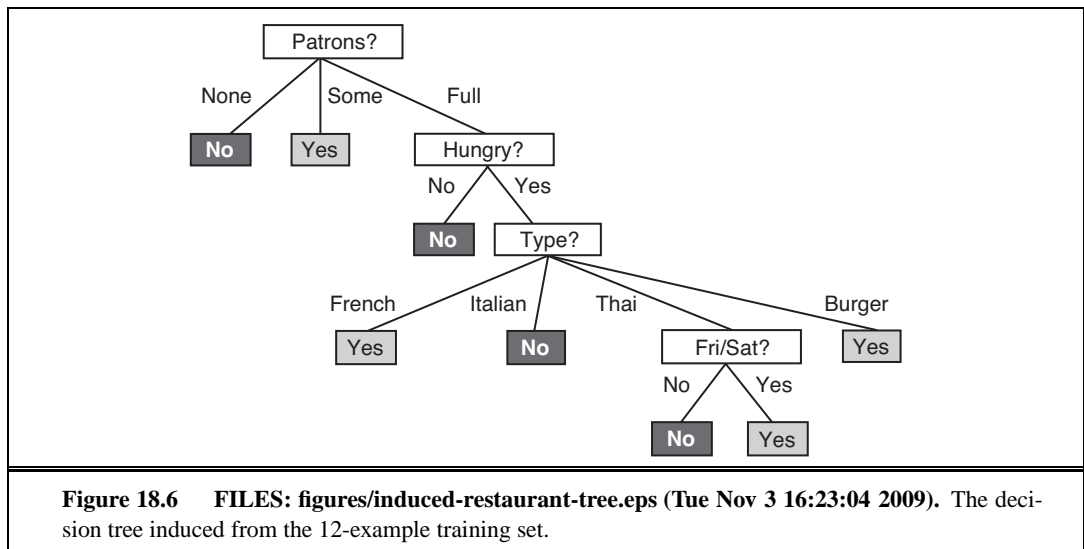


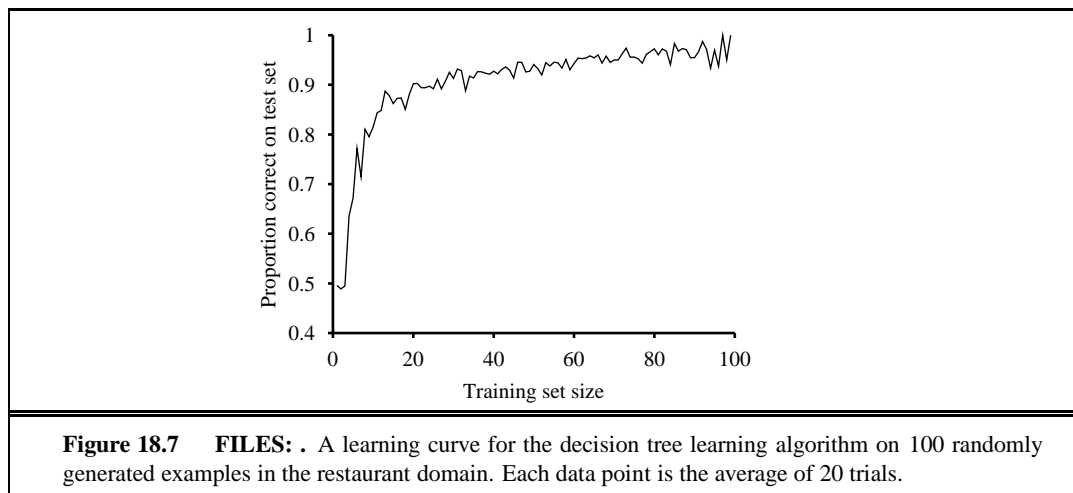
18 LEARNING FROM EXAMPLES

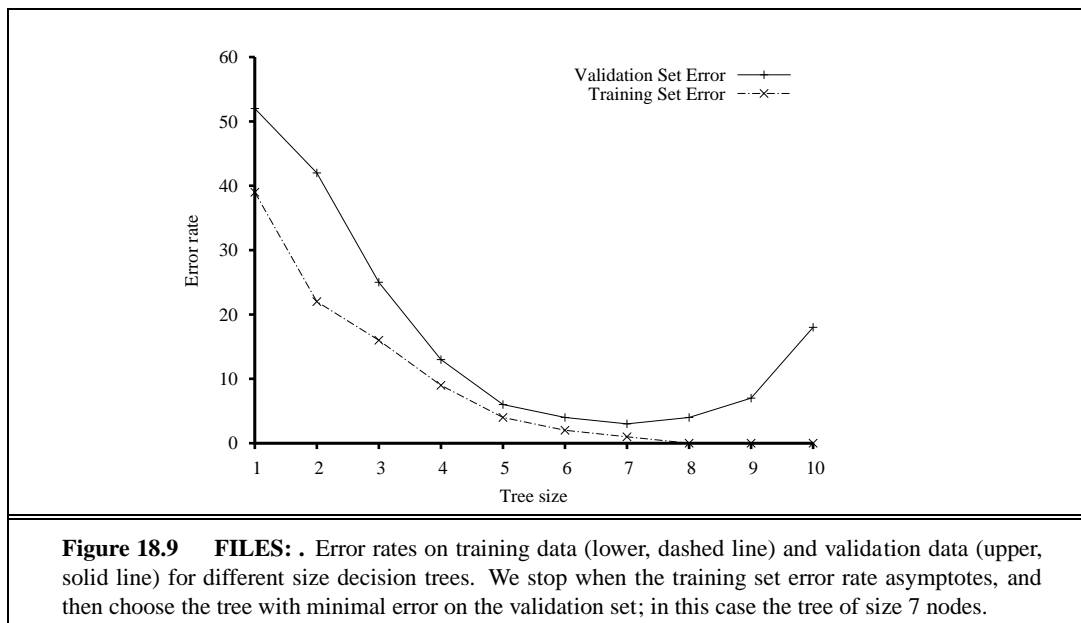


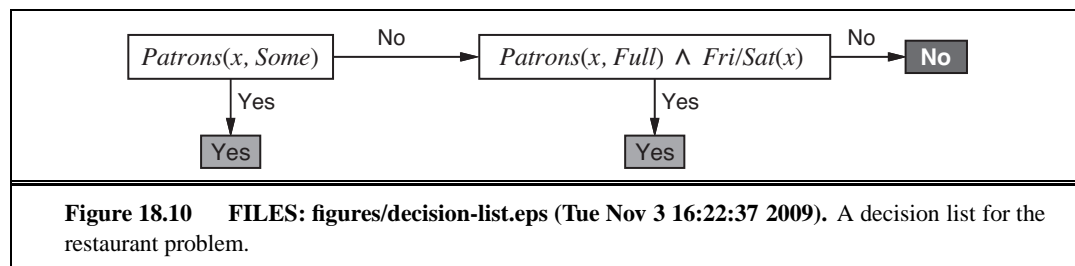


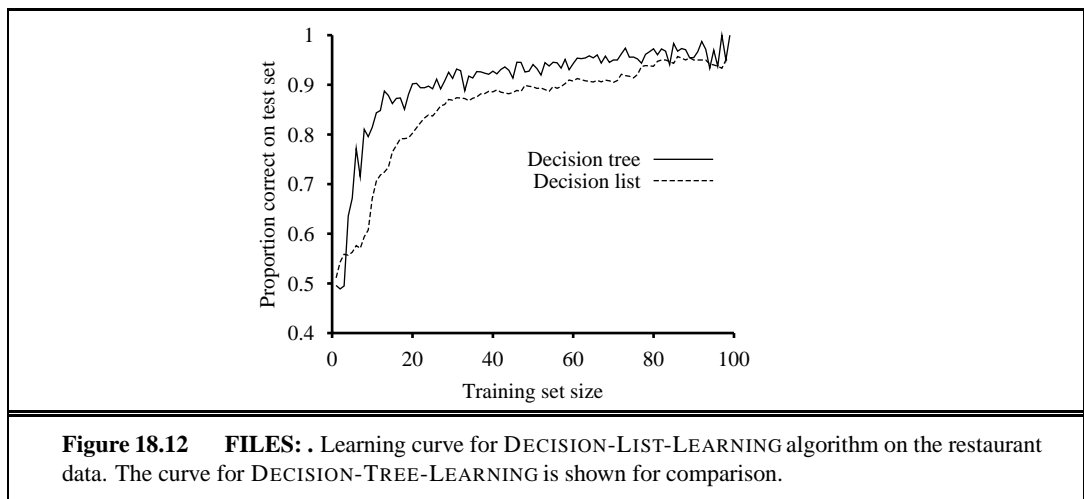


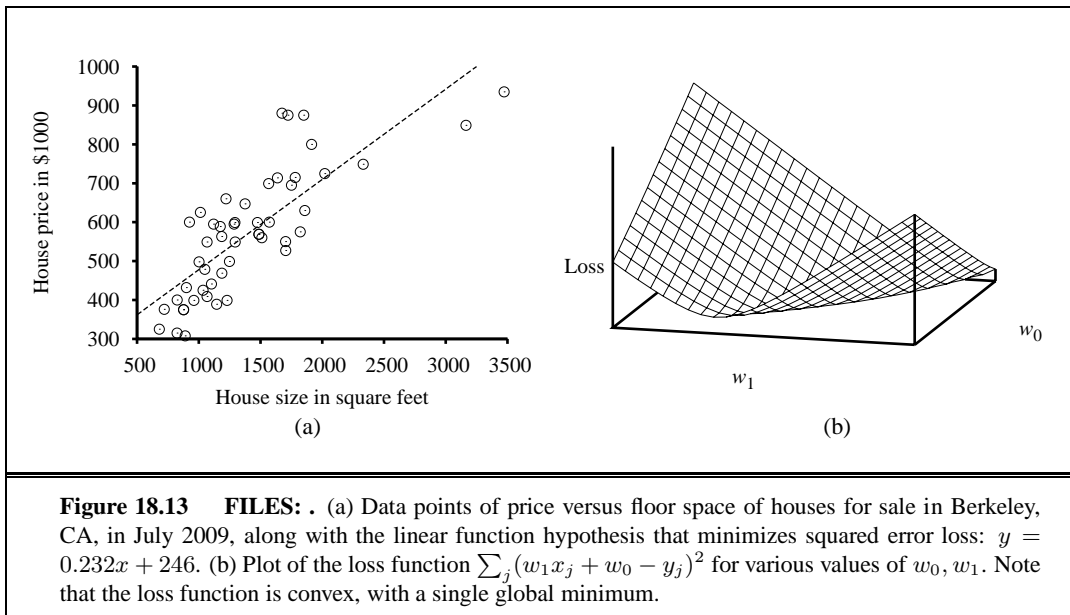












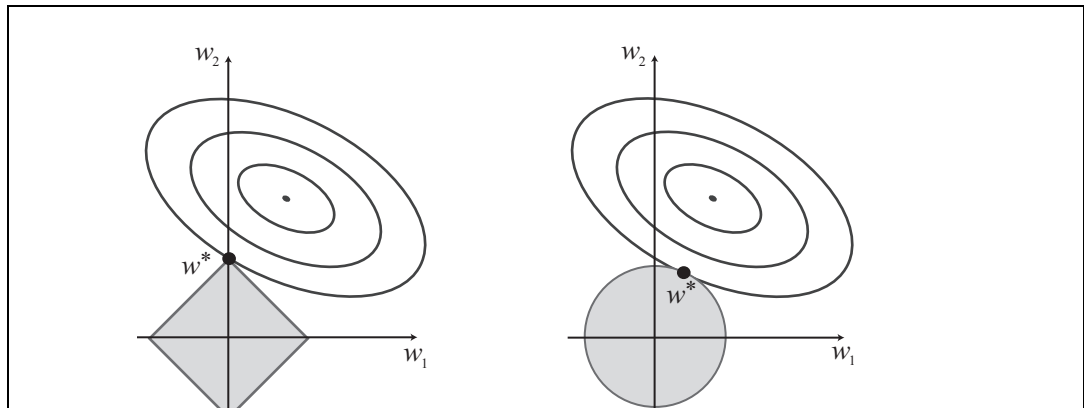


Figure 18.14 FILES: figures/diamond.eps (Wed Nov 4 14:45:53 2009). Why L_1 regularization tends to produce a sparse model. (a) With L_1 regularization (box), the minimal achievable loss (concentric contours) often occurs on an axis, meaning a weight of zero. (b) With L_2 regularization (circle), the minimal loss is likely to occur anywhere on the circle, giving no preference to zero weights.

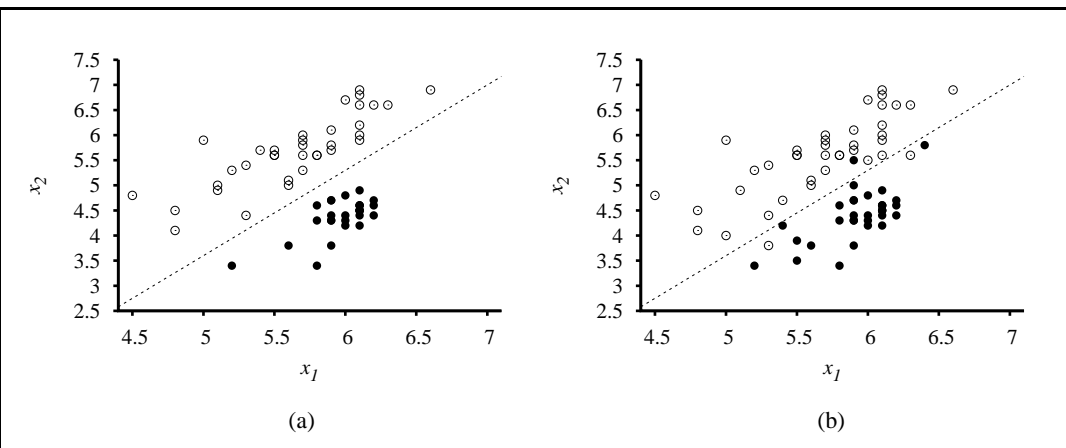


Figure 18.15 FILES: (a) Plot of two seismic data parameters, body wave magnitude x_1 and surface wave magnitude x_2 , for earthquakes (white circles) and nuclear explosions (black circles) occurring between 1982 and 1990 in Asia and the Middle East (?). Also shown is a decision boundary between the classes. (b) The same domain with more data points. The earthquakes and explosions are no longer linearly separable.

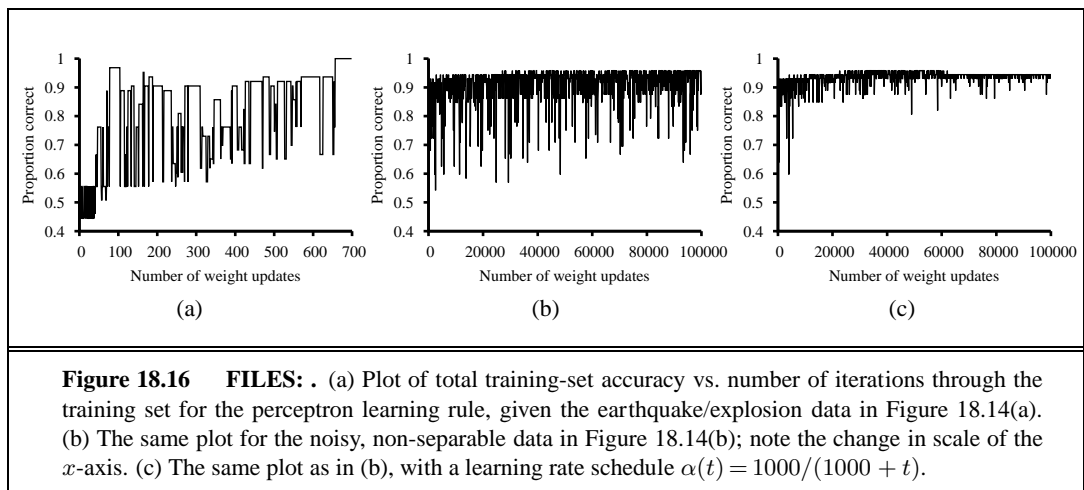
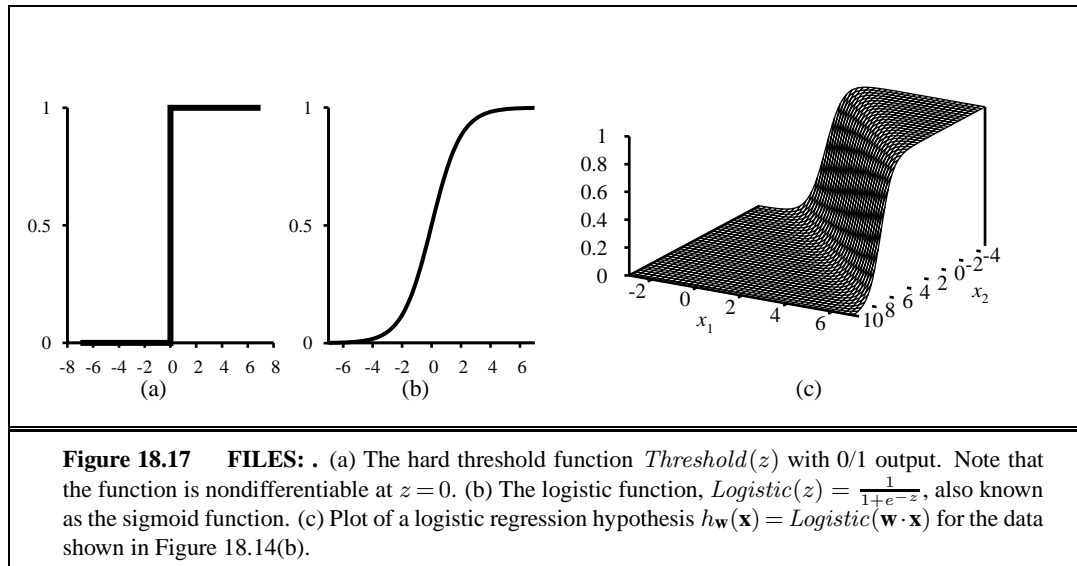
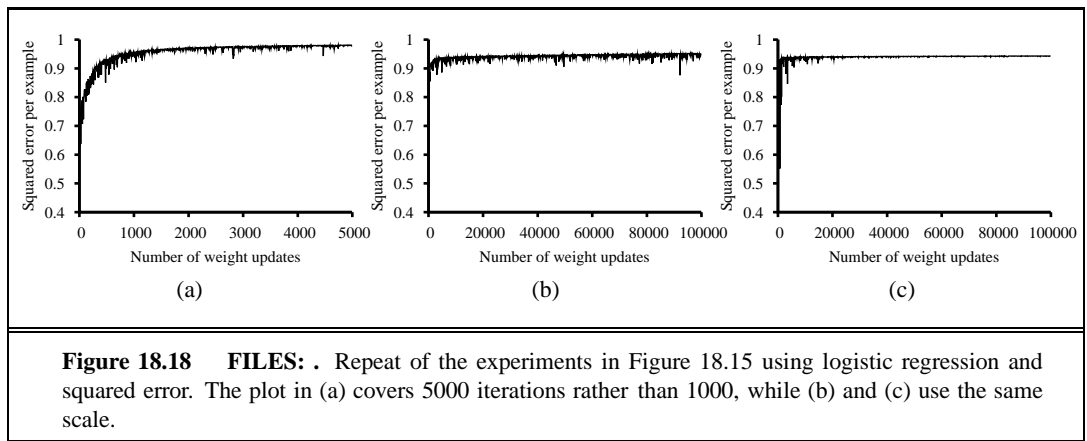
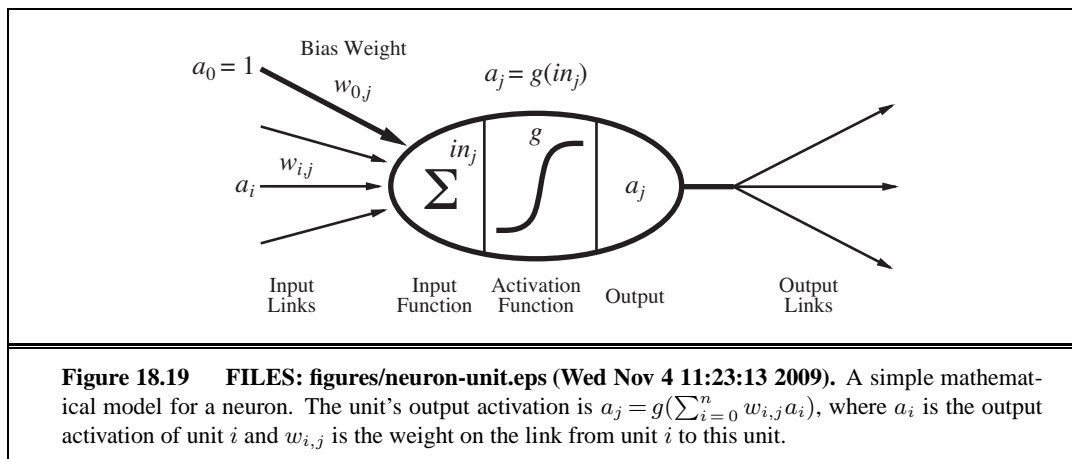


Figure 18.16 FILES: . (a) Plot of total training-set accuracy vs. number of iterations through the training set for the perceptron learning rule, given the earthquake/explosion data in Figure 18.14(a). (b) The same plot for the noisy, non-separable data in Figure 18.14(b); note the change in scale of the x -axis. (c) The same plot as in (b), with a learning rate schedule $\alpha(t) = 1000/(1000 + t)$.







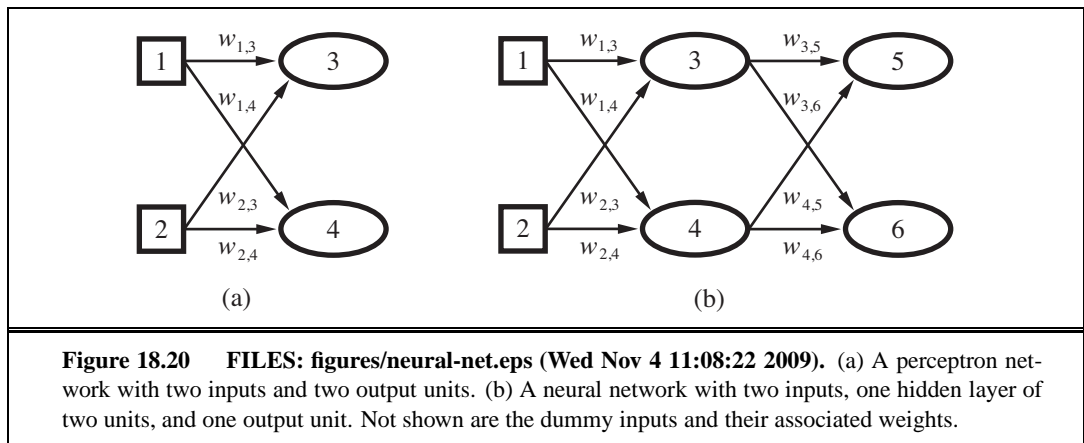
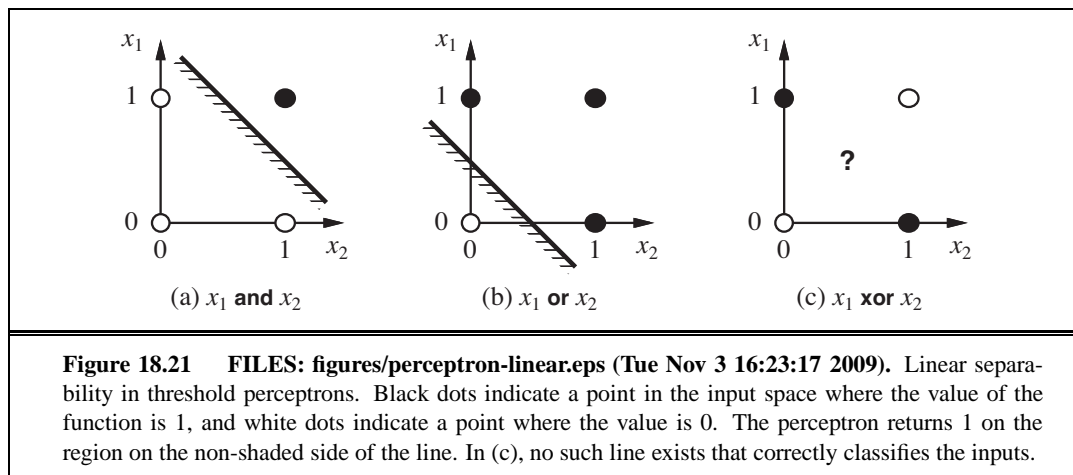


Figure 18.20 FILES: figures/neural-net.eps (Wed Nov 4 11:08:22 2009). (a) A perceptron network with two inputs and two output units. (b) A neural network with two inputs, one hidden layer of two units, and one output unit. Not shown are the dummy inputs and their associated weights.



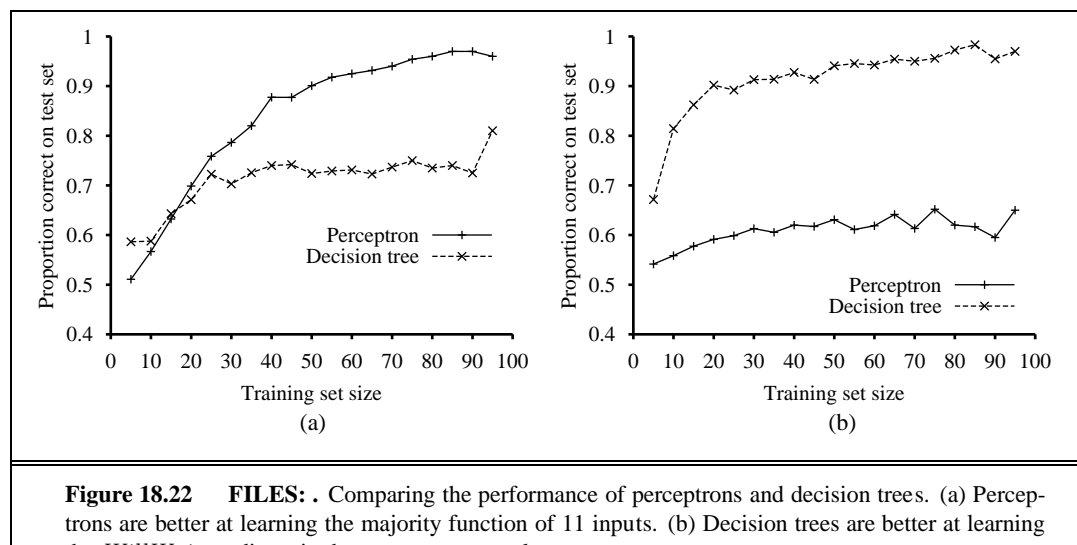


Figure 18.22 FILES: . Comparing the performance of perceptrons and decision trees. (a) Perceptrons are better at learning the majority function of 11 inputs. (b) Decision trees are better at learning the *WillWait* predicate in the restaurant example.

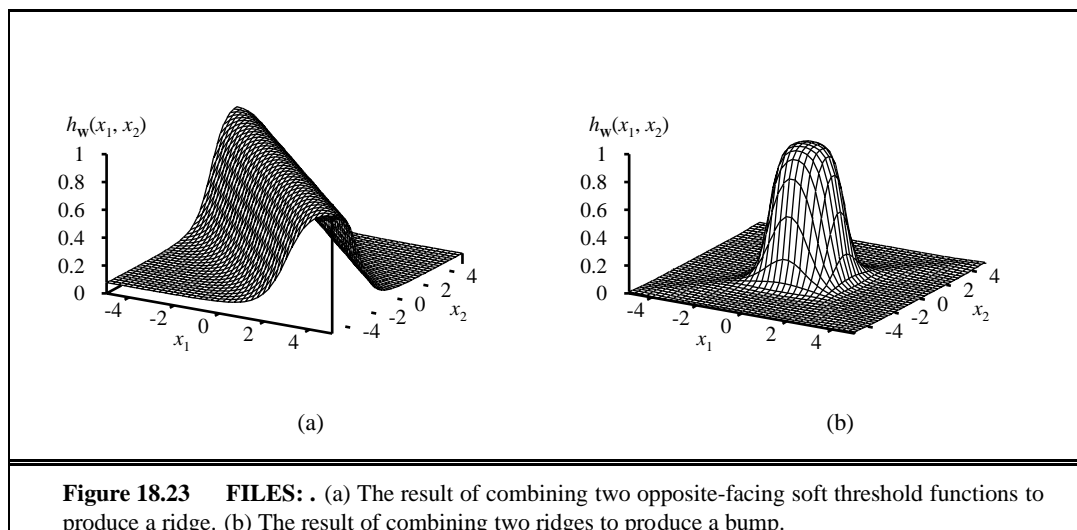


Figure 18.23 FILES: . (a) The result of combining two opposite-facing soft threshold functions to produce a ridge. (b) The result of combining two ridges to produce a bump.

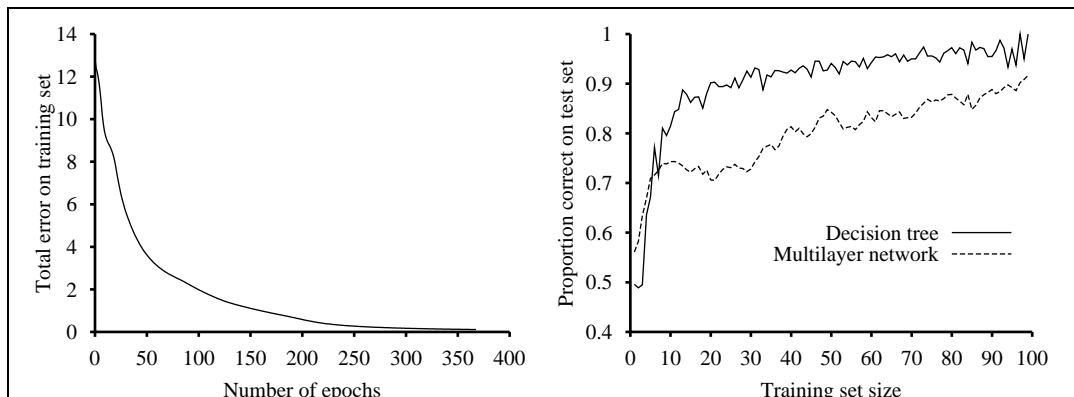
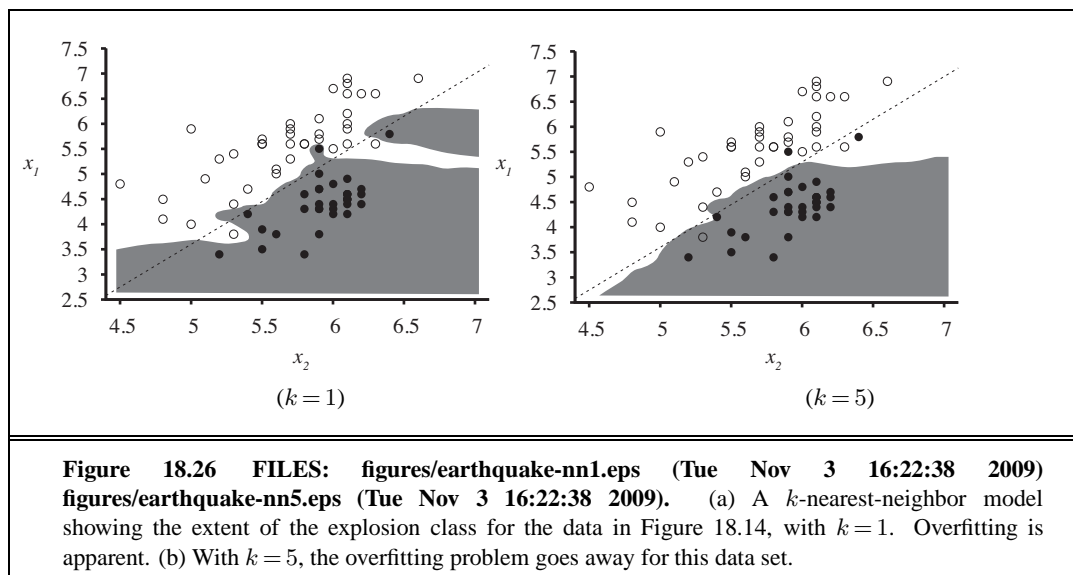


Figure 18.25 FILES: . (a) Training curve showing the gradual reduction in error as weights are modified over several epochs, for a given set of examples in the restaurant domain. (b) Comparative learning curves showing that decision-tree learning does slightly better on the restaurant problem than back-propagation in a multilayer network.



**Figure 18.26 FILES: figures/earthquake-nn1.eps (Tue Nov 3 16:22:38 2009)
figures/earthquake-nn5.eps (Tue Nov 3 16:22:38 2009).** (a) A k -nearest-neighbor model showing the extent of the explosion class for the data in Figure 18.14, with $k = 1$. Overfitting is apparent. (b) With $k = 5$, the overfitting problem goes away for this data set.

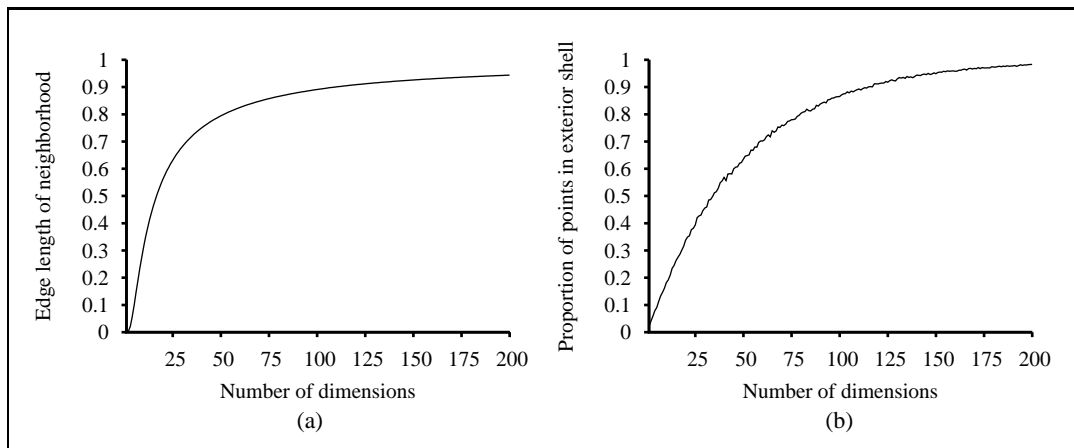
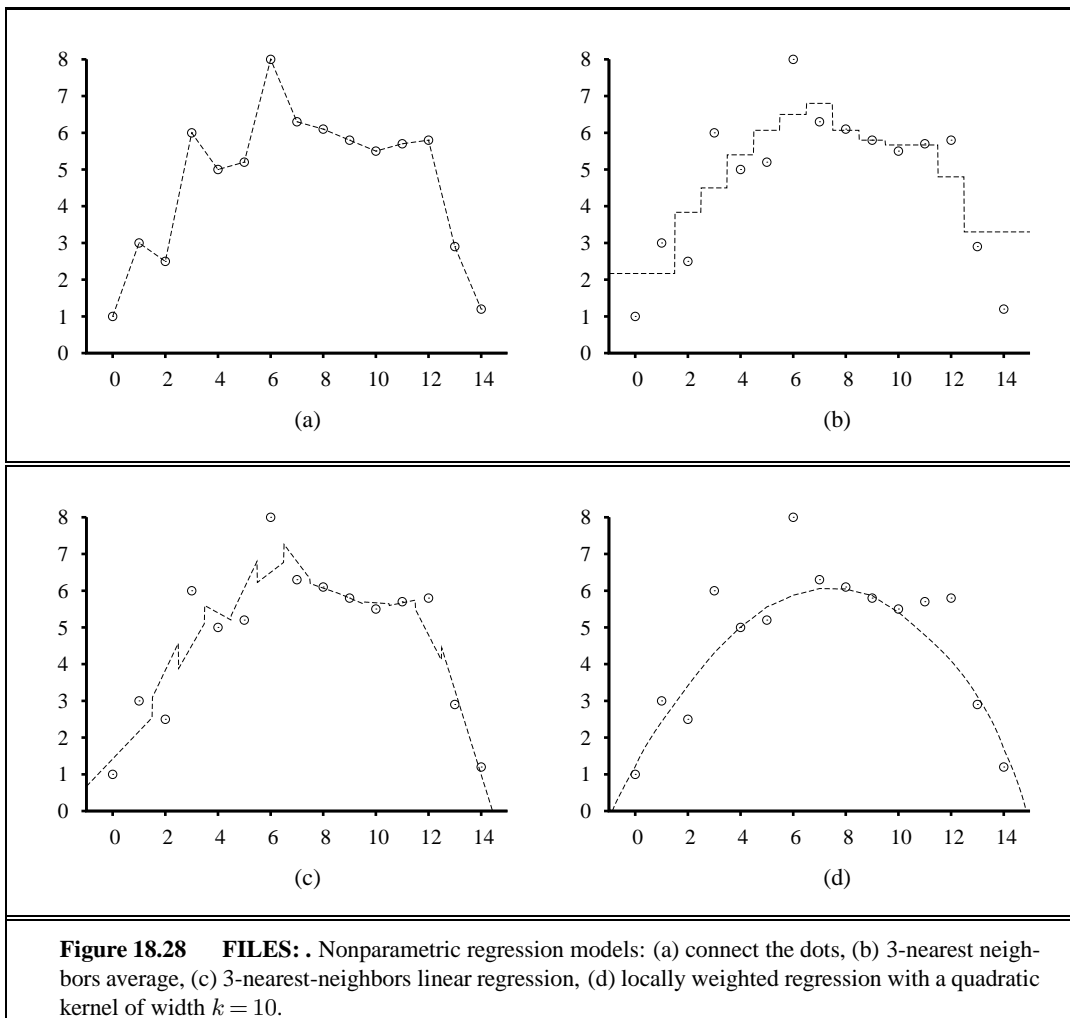
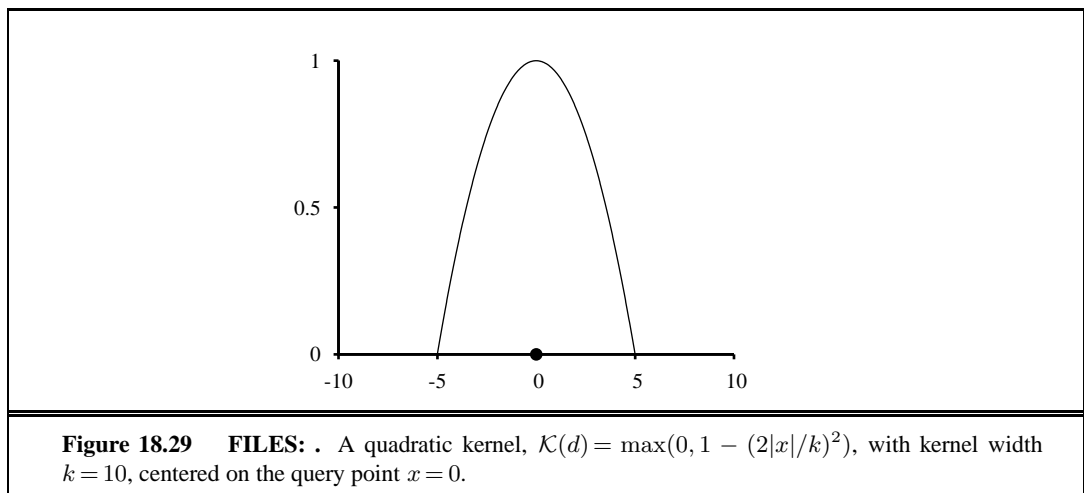
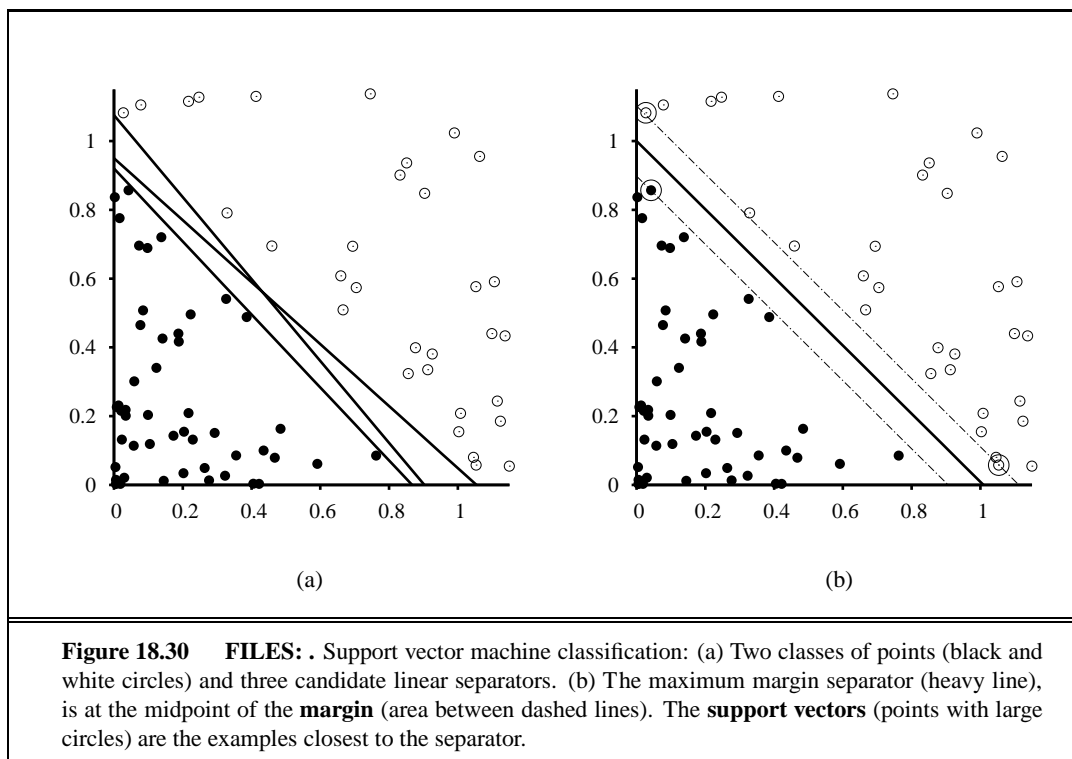
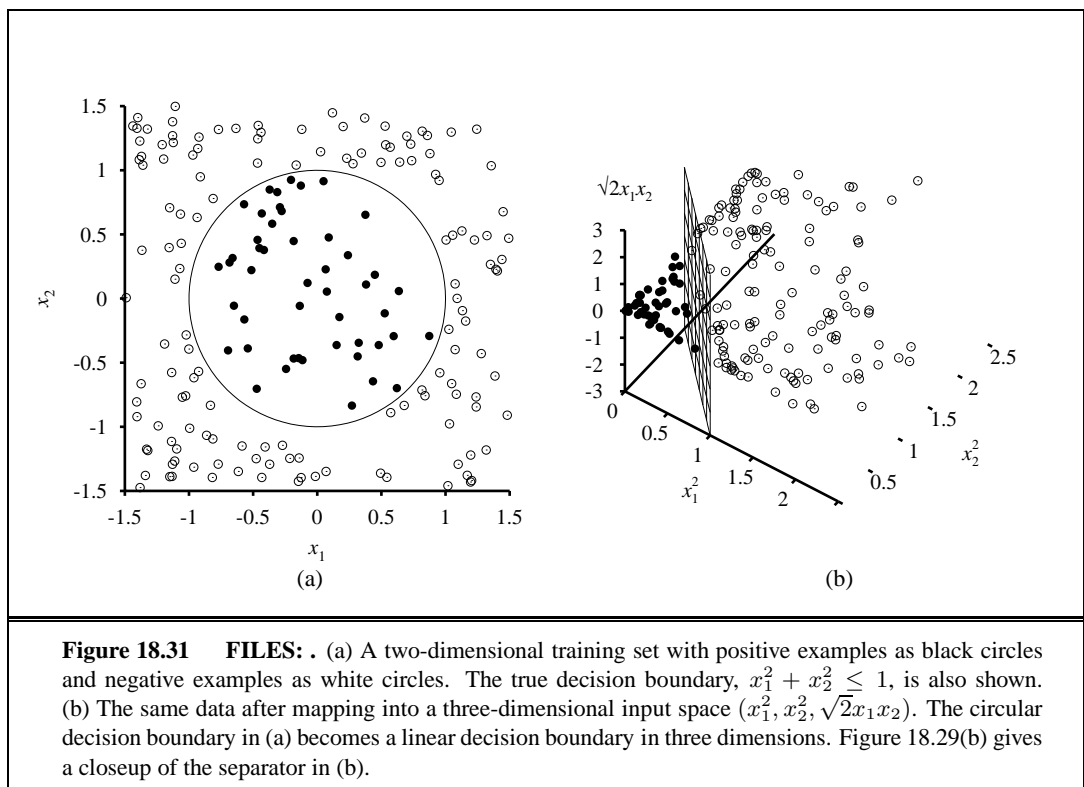


Figure 18.27 FILES: . The curse of dimensionality: (a) The length of the average neighborhood for 10-nearest-neighbors in a unit hypercube with 1,000,000 points, as a function of the number of dimensions. (b) The proportion of points that fall within a thin shell consisting of the outer 1% of the hypercube, as a function of the number of dimensions. Sampled from 10,000 randomly distributed points.









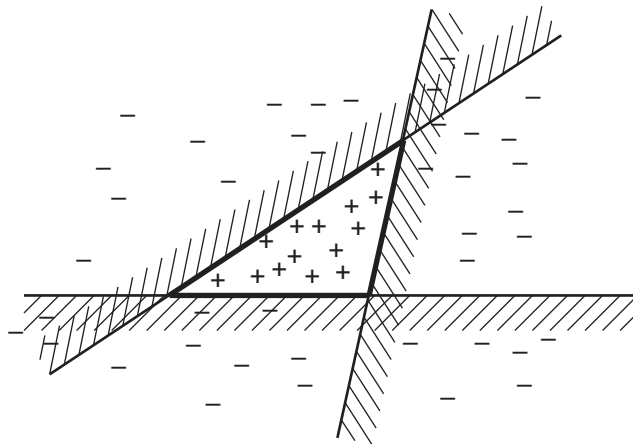
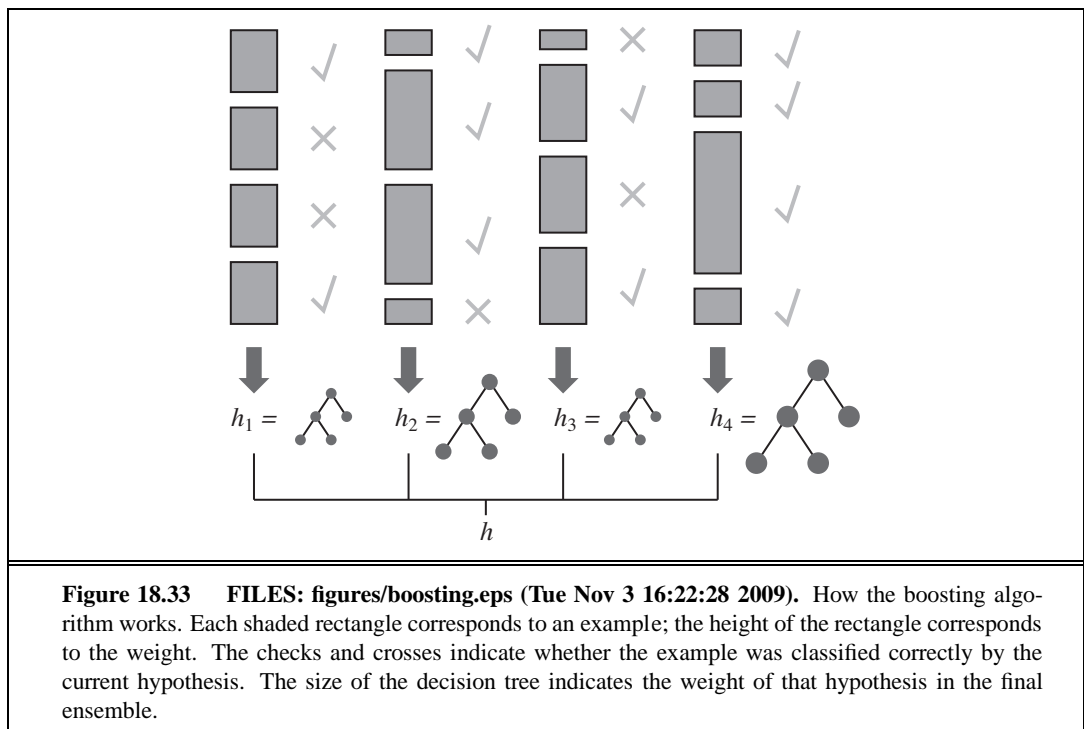


Figure 18.32 FILES: figures/ensemble-expressiveness.eps (Tue Nov 3 16:22:41 2009). Illustration of the increased expressive power obtained by ensemble learning. We take three linear threshold hypotheses, each of which classifies positively on the unshaded side, and classify as positive any example classified positively by all three. The resulting triangular region is a hypothesis not expressible in the original hypothesis space.



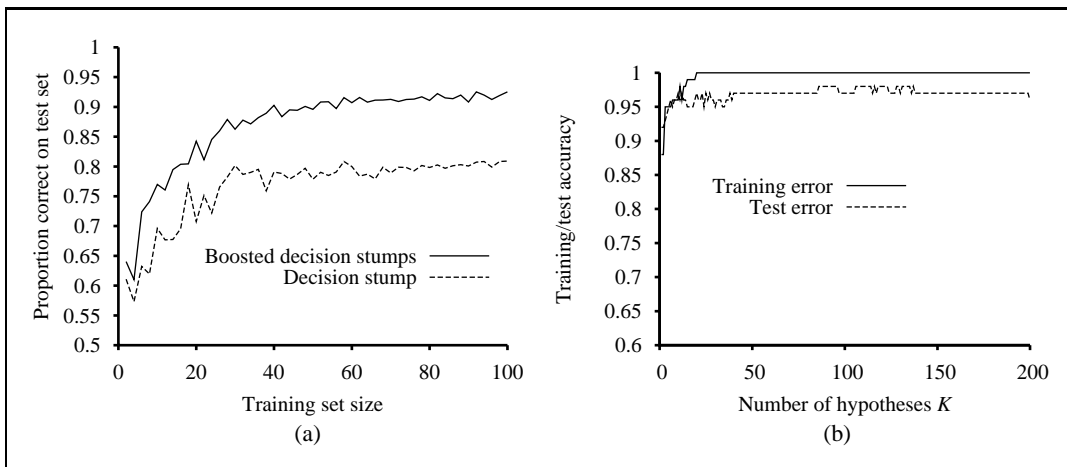
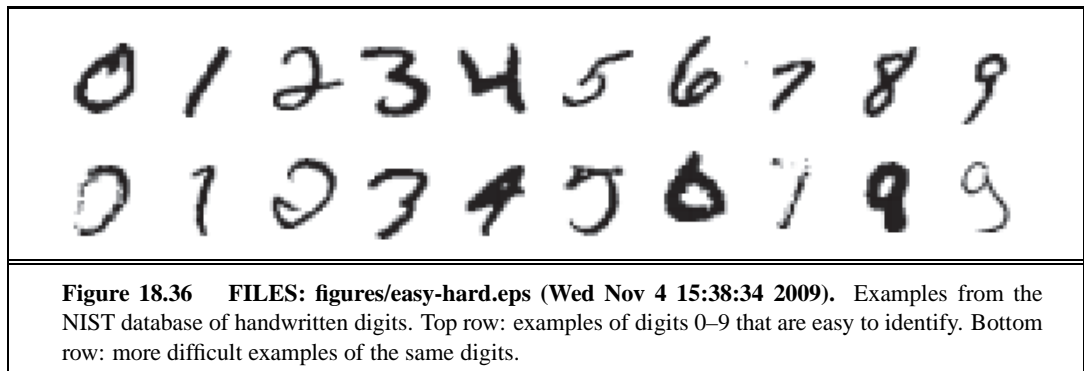


Figure 18.35 FILES: . (a) Graph showing the performance of boosted decision stumps with $K = 5$ versus unboosted decision stumps on the restaurant data. (b) The proportion correct on the training set and the test set as a function of K , the number of hypotheses in the ensemble. Notice that the test set accuracy improves slightly even after the training accuracy reaches 1, i.e., after the ensemble fits the data exactly.



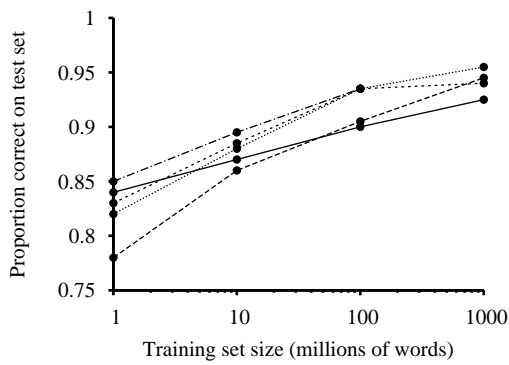
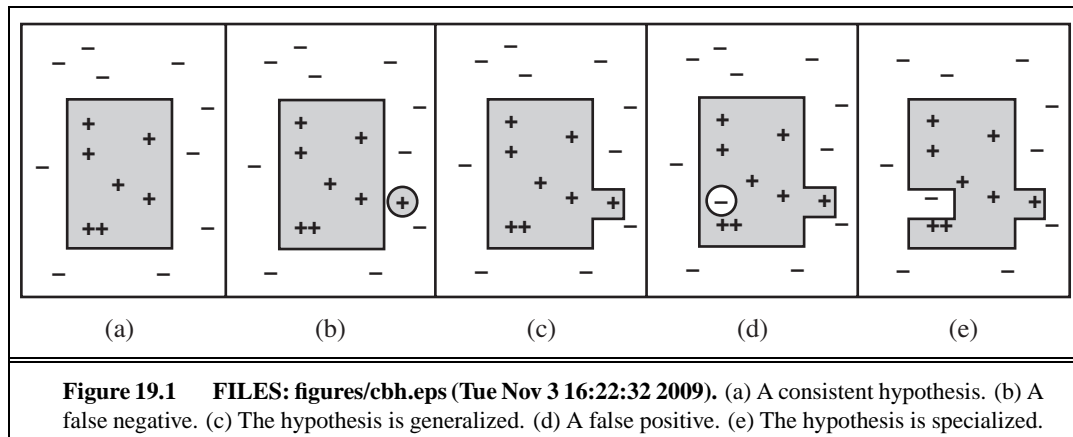
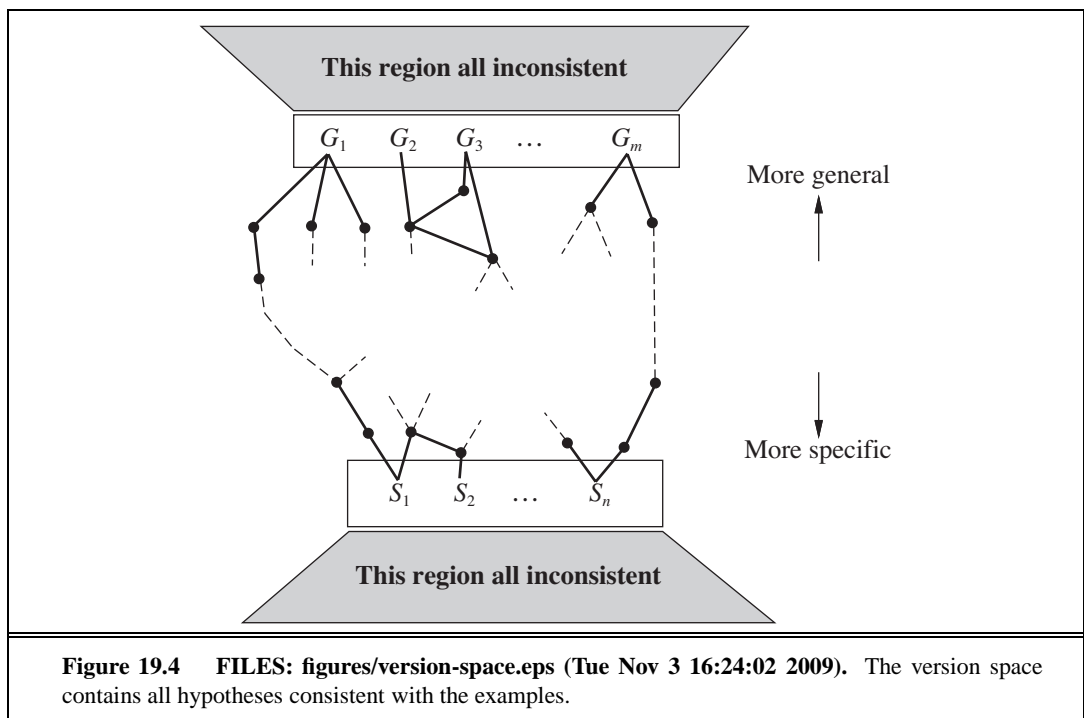
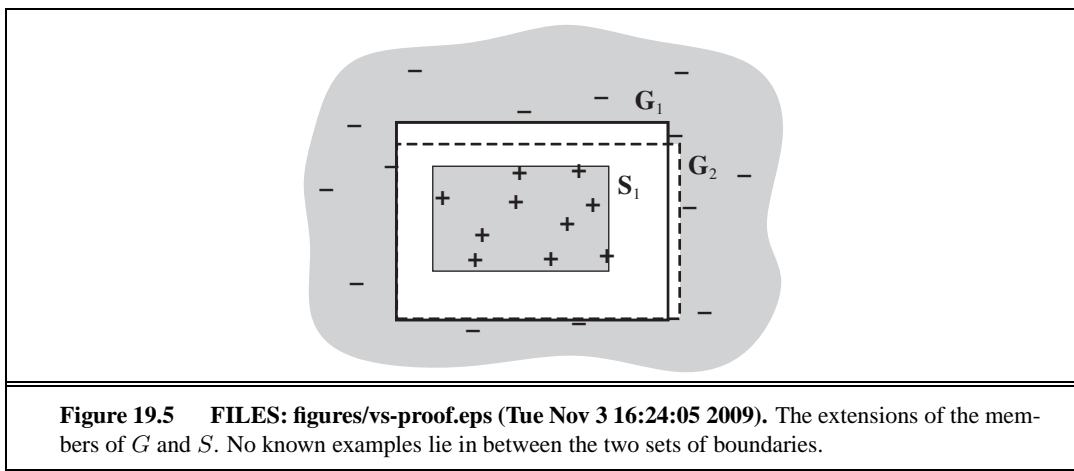


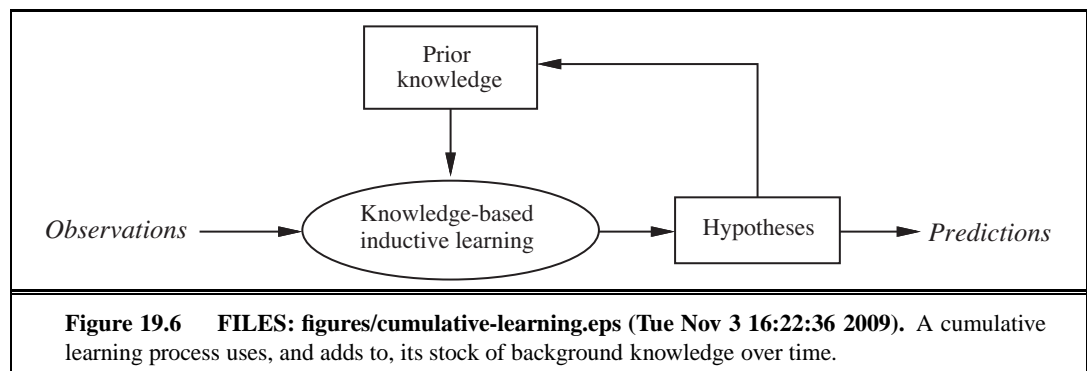
Figure 18.37 FILES: Learning curves for five learning algorithms on a common task. Note that there appears to be more room for improvement in the horizontal direction (more training data) than in the vertical direction (different machine learning algorithm). Adapted from ? (?).

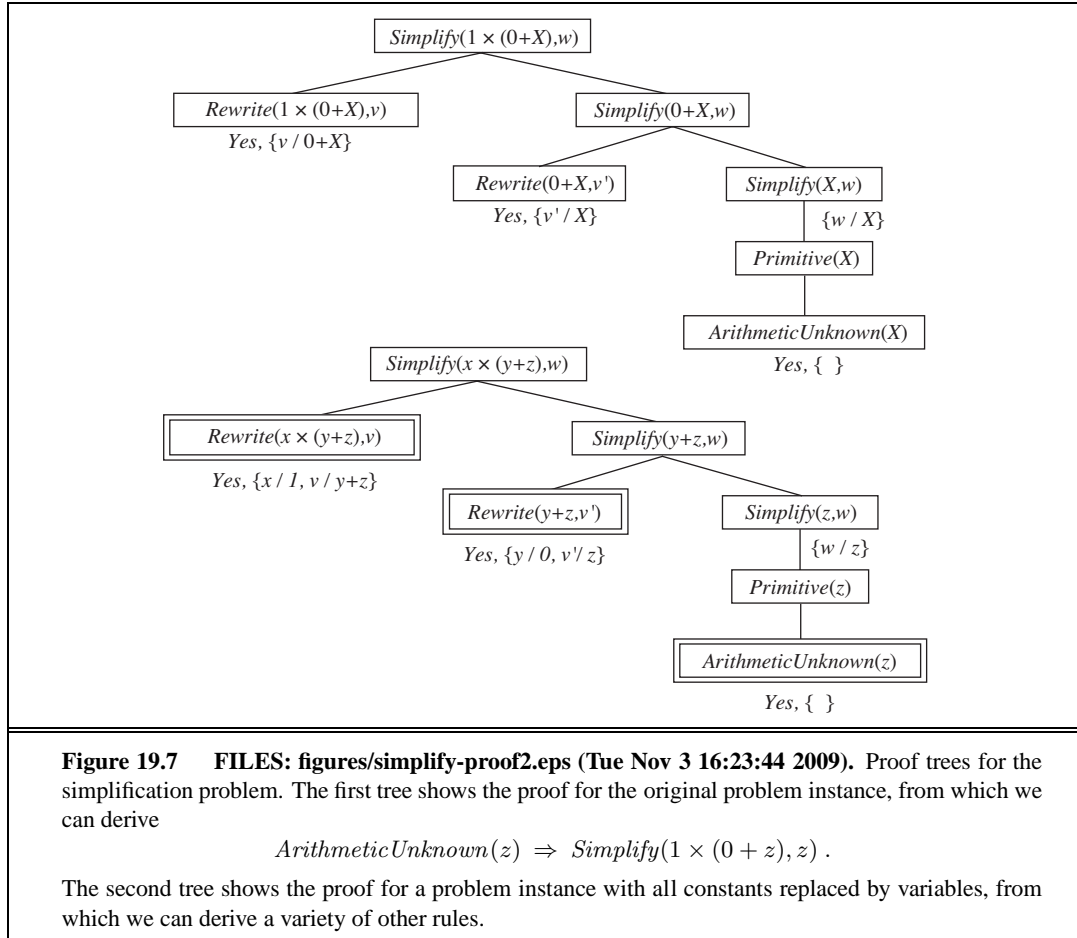
19 KNOWLEDGE IN LEARNING

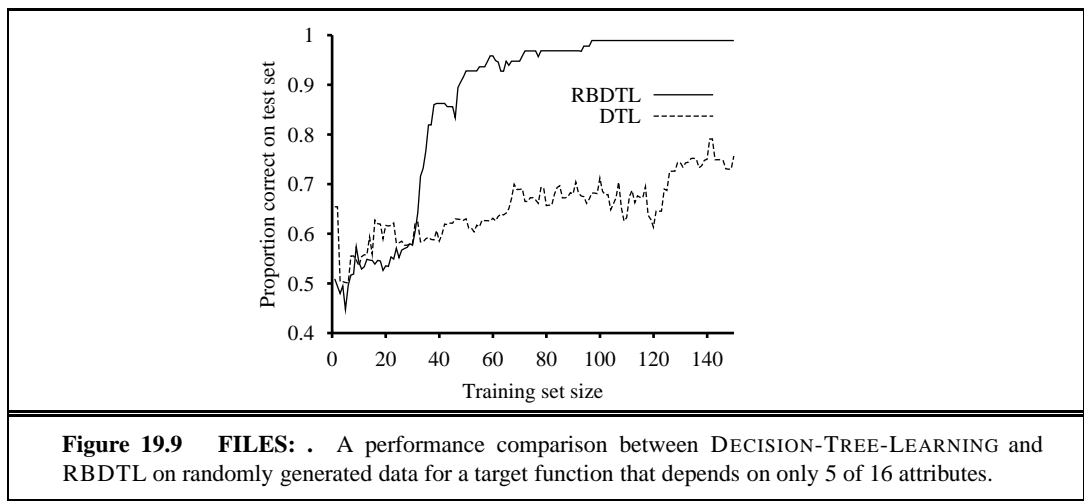












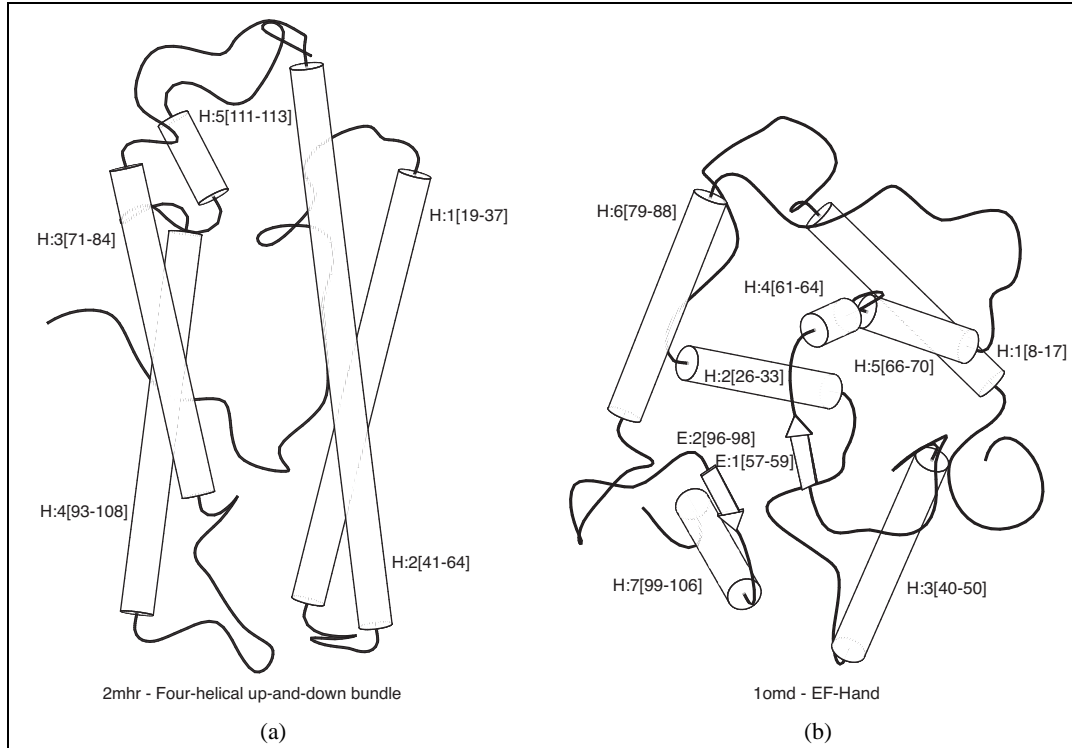
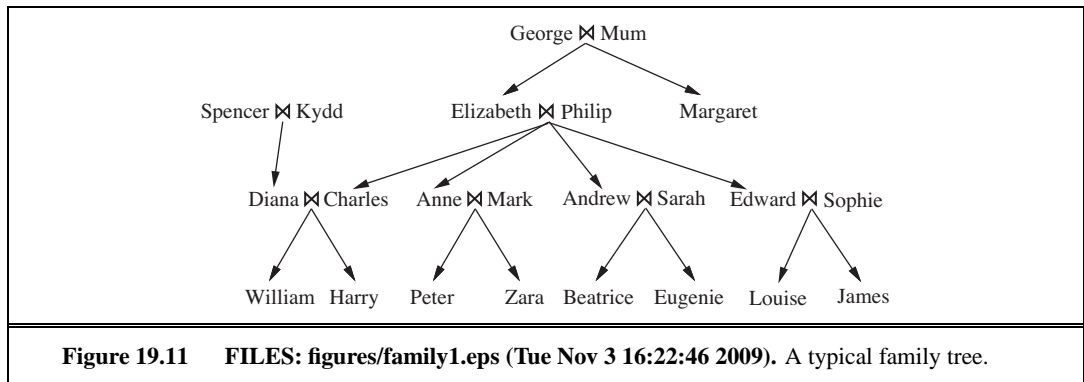
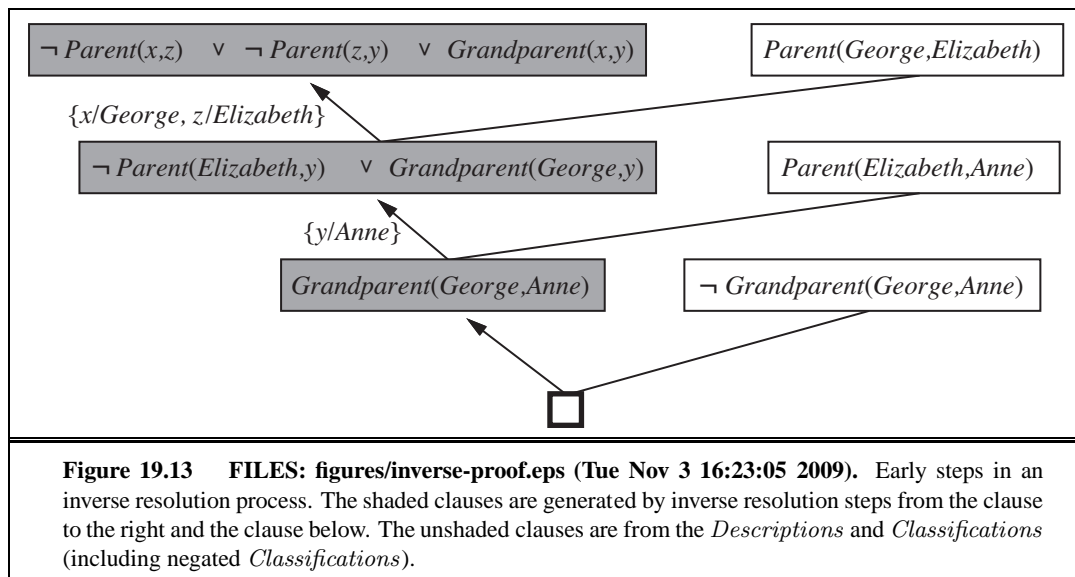


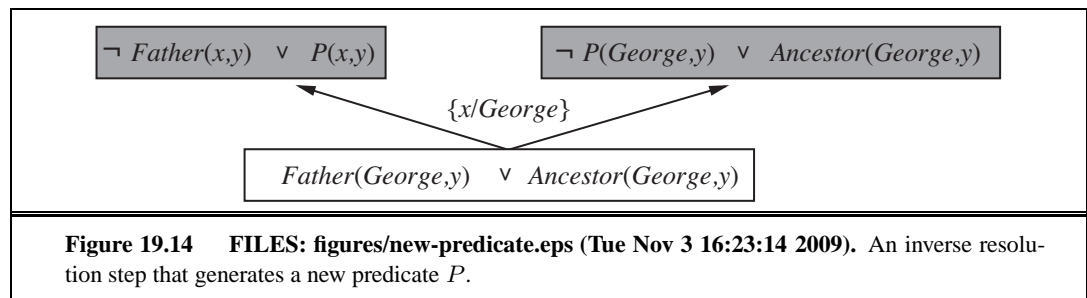
Figure 19.10 FILES: figures/pdb2mhr.eps (Tue Nov 3 16:23:15 2009) figures/pdb1omd.eps (Tue Nov 3 16:23:15 2009). (a) and (b) show positive and negative examples, respectively, of the “four-helical up-and-down bundle” concept in the domain of protein folding. Each example structure is coded into a logical expression of about 100 conjuncts such as $TotalLength(D2mhr, 118) \wedge NumberHelices(D2mhr, 6) \wedge \dots$. From these descriptions and from classifications such as $Fold(FOUR-HELICAL-UP-AND-DOWN-BUNDLE, D2mhr)$, the ILP system PROGOL (?) learned the following rule:

$$\begin{aligned} Fold(\text{FOUR-HELICAL-UP-AND-DOWN-BUNDLE}, p) \Leftarrow \\ \text{Helix}(p, h_1) \wedge Length(h_1, \text{HIGH}) \wedge Position(p, h_1, n) \\ \wedge (1 \leq n \leq 3) \wedge \text{Adjacent}(p, h_1, h_2) \wedge \text{Helix}(p, h_2). \end{aligned}$$

This kind of rule could not be learned, or even represented, by an attribute-based mechanism such as we saw in previous chapters. The rule can be translated into English as “Protein p has fold class ‘Four-helical up-and-down-bundle’ if it contains a long helix h_1 at a secondary structure position between 1 and 3 and h_1 is next to a second helix.”

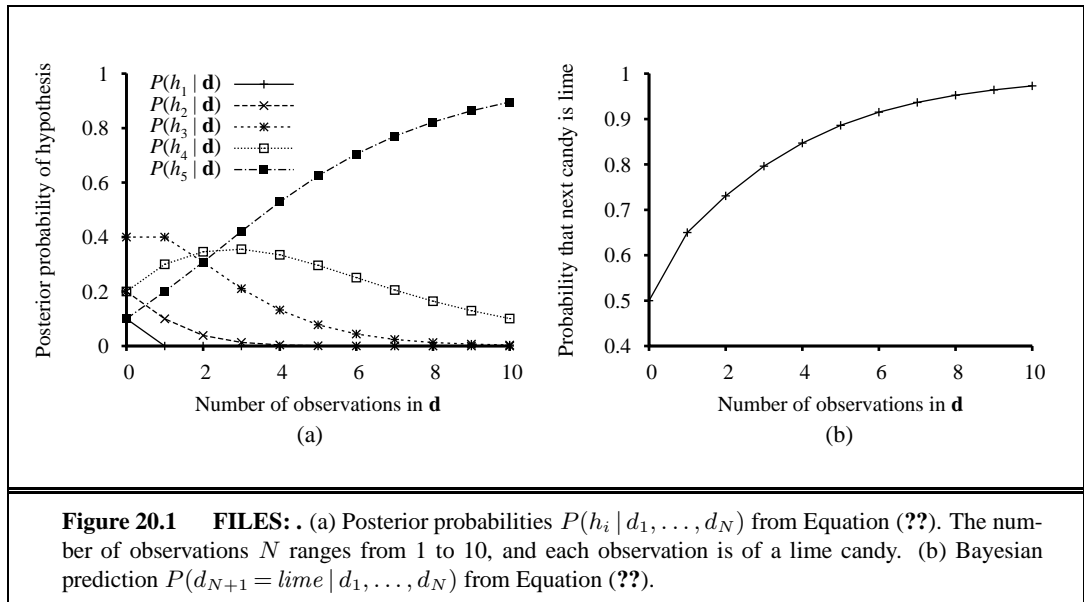






20

LEARNING PROBABILISTIC MODELS



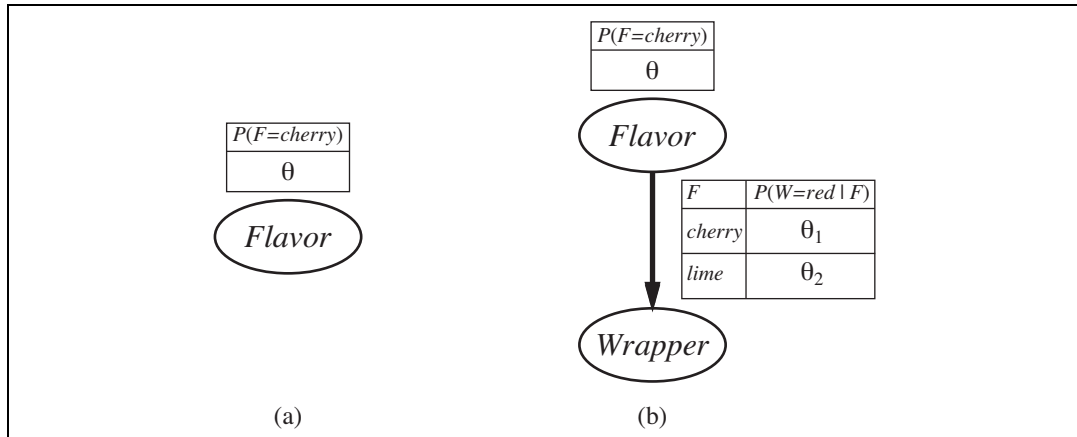
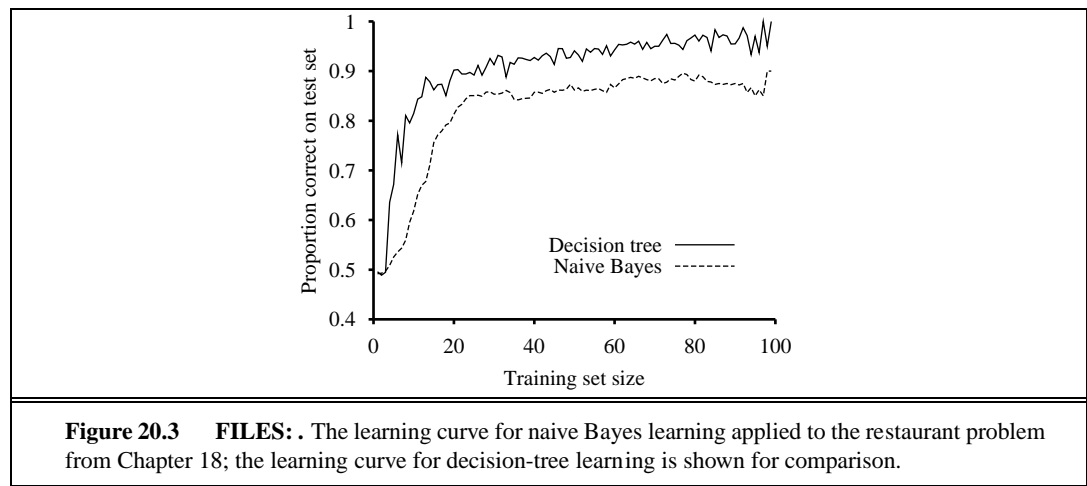


Figure 20.2 FILES: figures/ml-networks.eps (Tue Nov 3 16:23:11 2009). (a) Bayesian network model for the case of candies with an unknown proportion of cherries and limes. (b) Model for the case where the wrapper color depends (probabilistically) on the candy flavor.



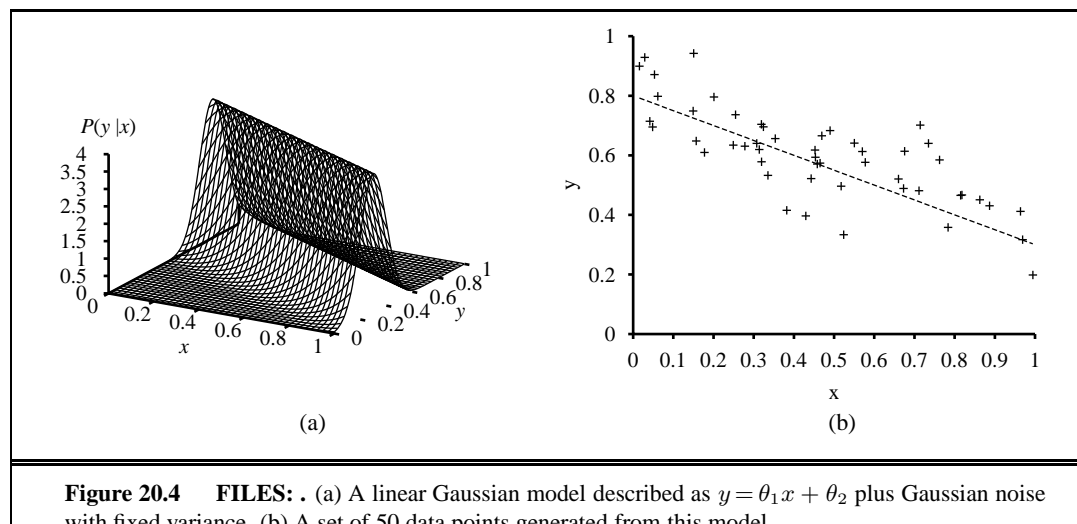
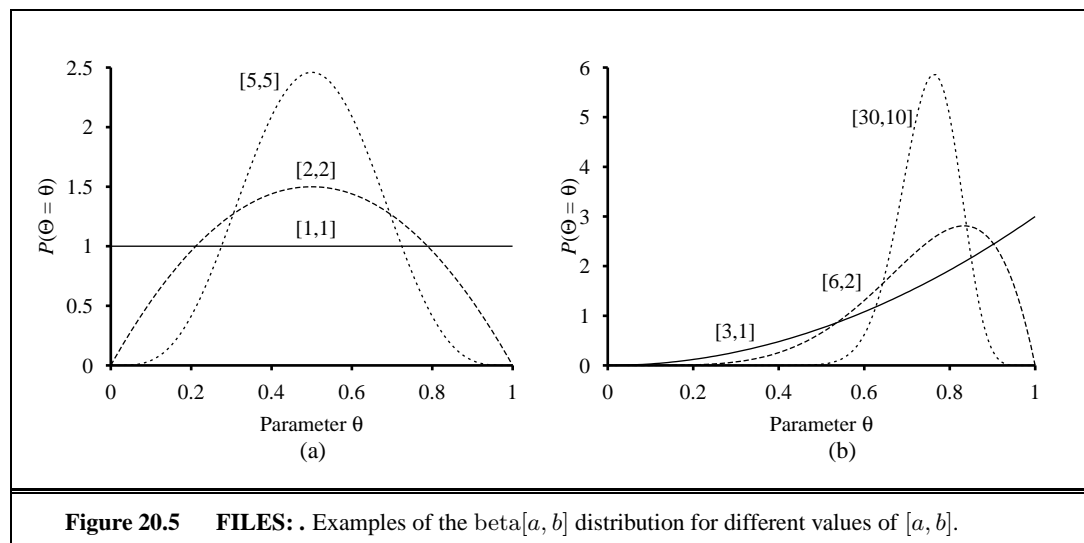
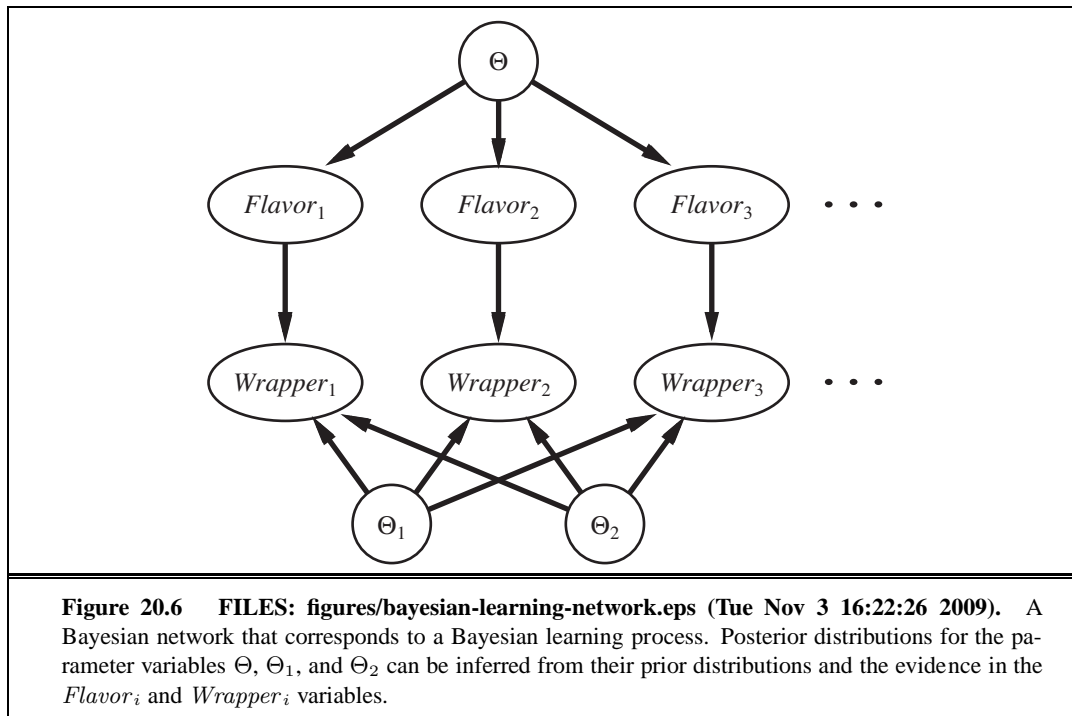


Figure 20.4 FILES: . (a) A linear Gaussian model described as $y = \theta_1 x + \theta_2$ plus Gaussian noise with fixed variance. (b) A set of 50 data points generated from this model.





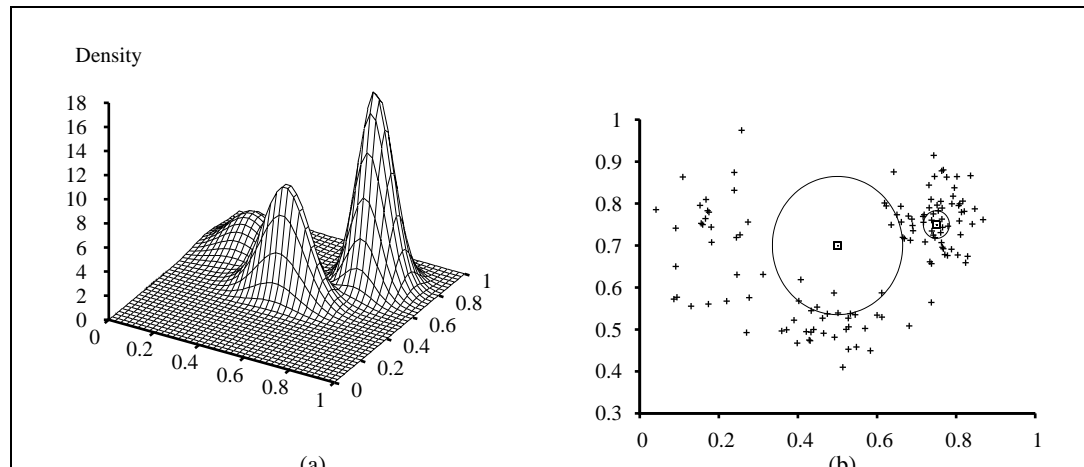
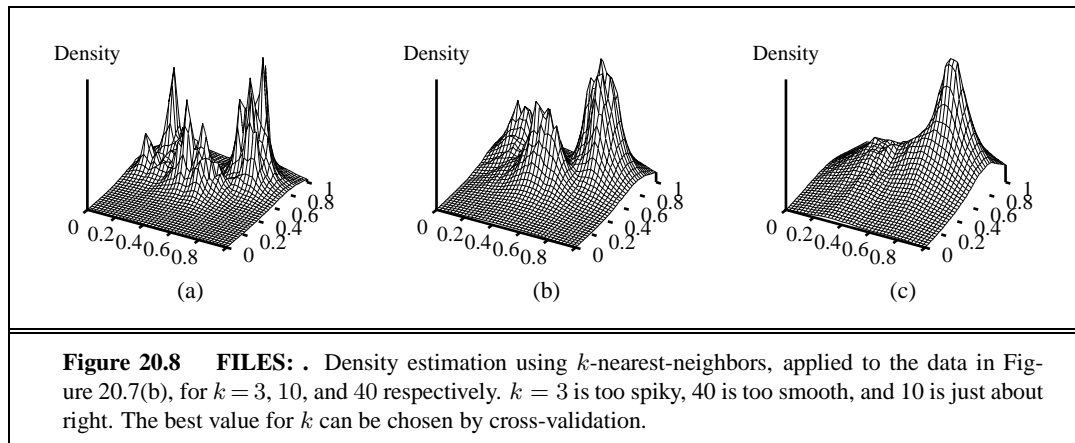
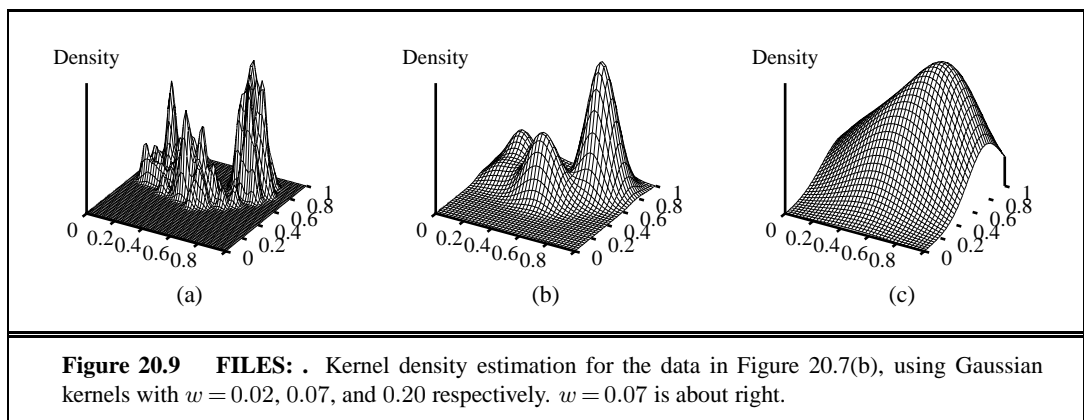
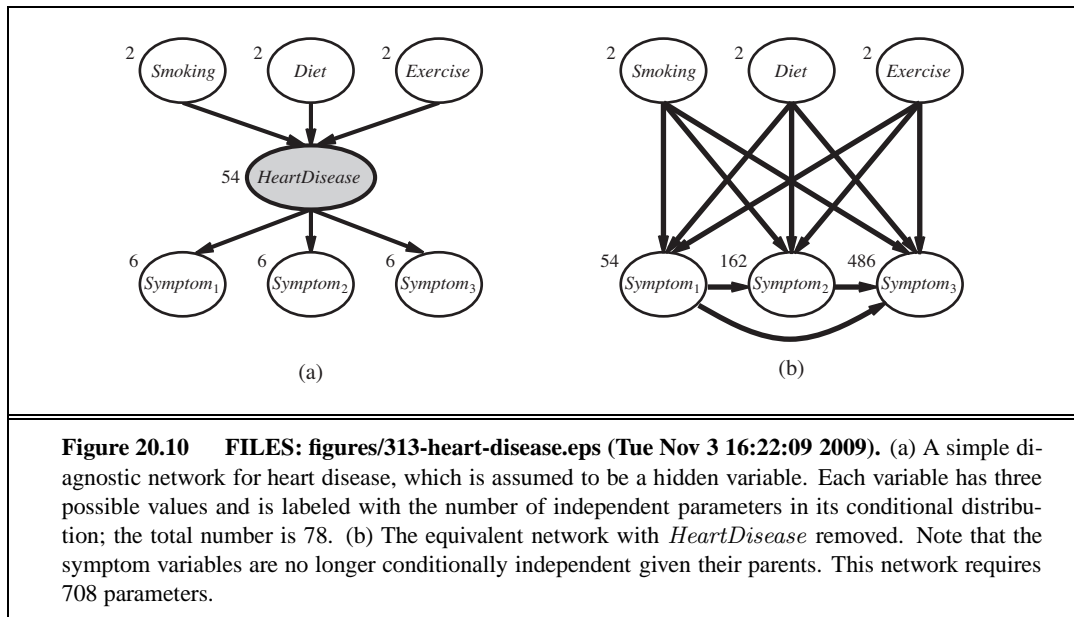


Figure 20.7 FILES: . (a) A 3D plot of the mixture of Gaussians from Figure 20.11(a). (b) A 128-point sample of points from the mixture, together with two query points (small squares) and their 10-nearest-neighborhoods (medium and large circles).







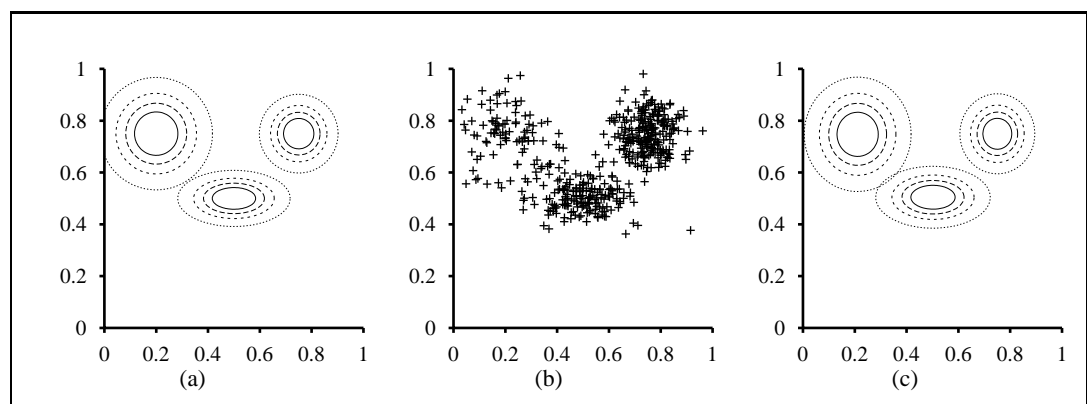


Figure 20.11 FILES: . (a) A Gaussian mixture model with three components; the weights (left-to-right) are 0.2, 0.3, and 0.5. (b) 500 data points sampled from the model in (a). (c) The model reconstructed by EM from the data in (b).

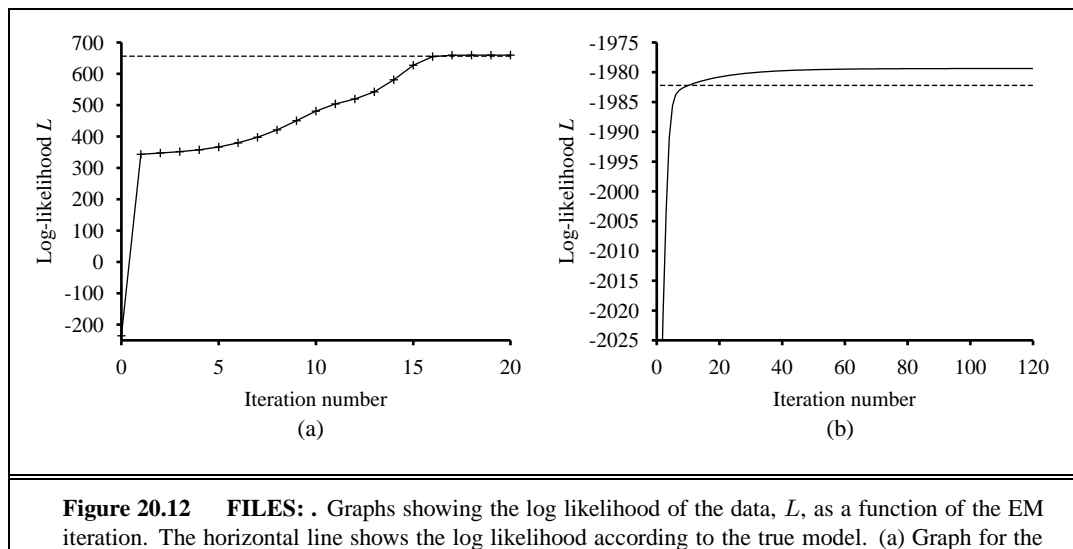
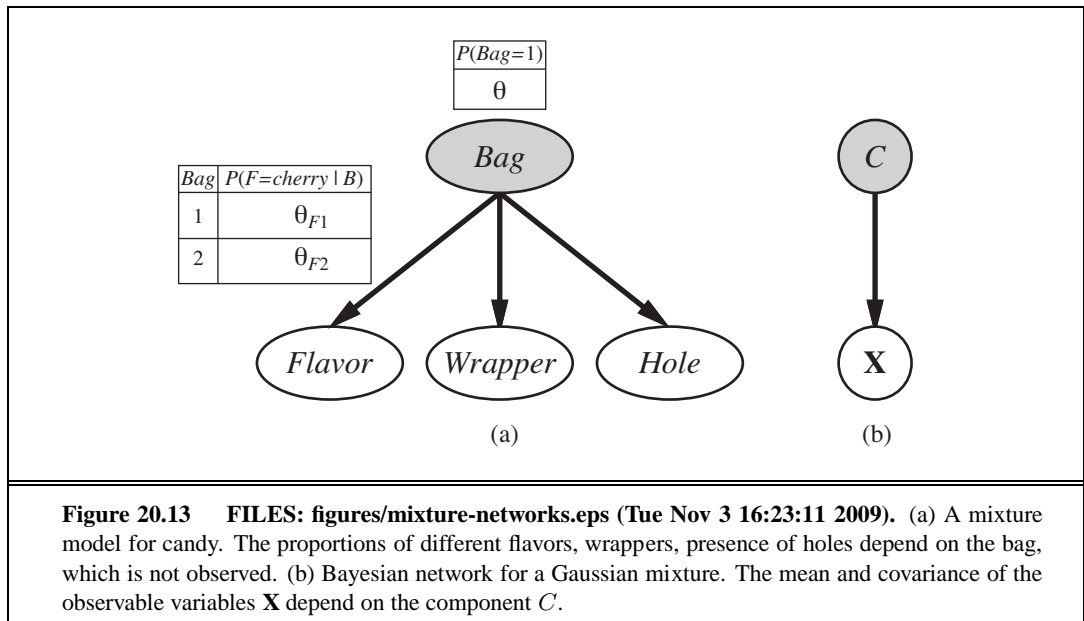
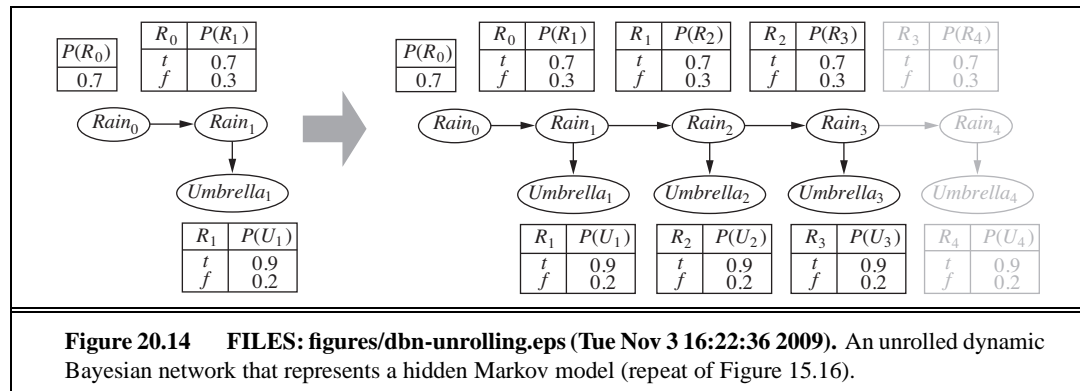
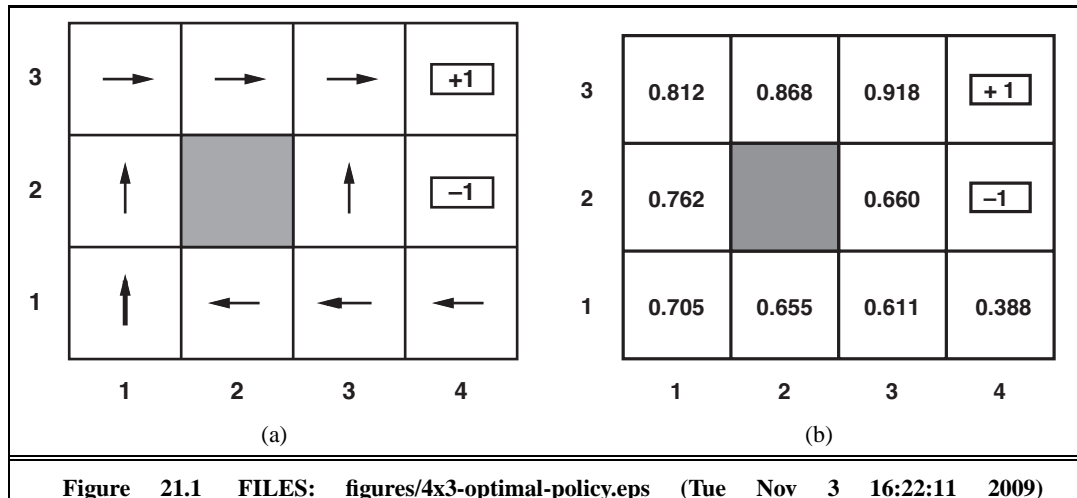


Figure 20.12 FILES: . Graphs showing the log likelihood of the data, L , as a function of the EM iteration. The horizontal line shows the log likelihood according to the true model. (a) Graph for the Gaussian mixture model in Figure 20.11. (b) Graph for the Bayesian network in Figure 20.13(a).





21 REINFORCEMENT LEARNING



**Figure 21.1 FILES: figures/4x3-optimal-policy.eps (Tue Nov 3 16:22:11 2009)
figures/sequential-decision-values.eps (Tue Nov 3 16:23:42 2009).** (a) A policy π for the 4x3 world; this policy happens to be optimal with rewards of $R(s) = -0.04$ in the nonterminal states and no discounting. (b) The utilities of the states in the 4x3 world, given policy π .

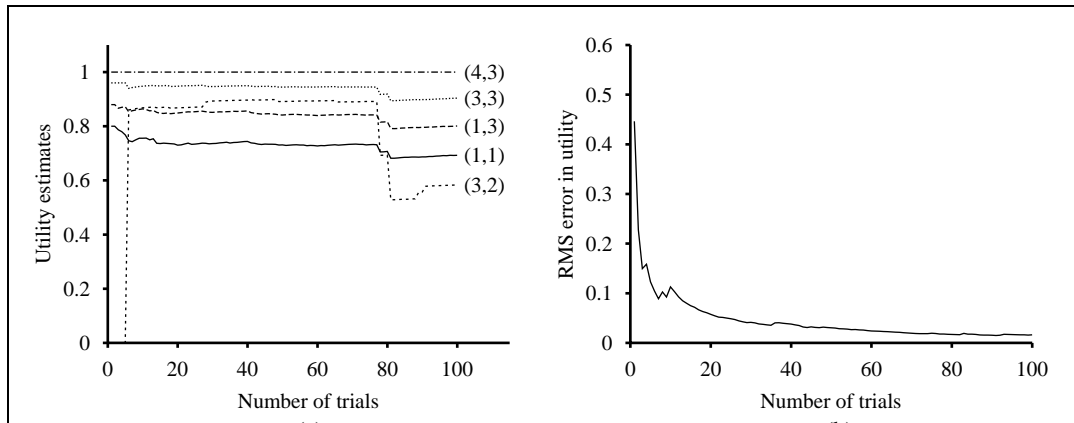


Figure 21.3 FILES: . The passive ADP learning curves for the 4×3 world, given the optimal policy shown in Figure 21.1. (a) The utility estimates for a selected subset of states, as a function of the number of trials. Notice the large changes occurring around the 78th trial—this is the first time that the agent falls into the -1 terminal state at $(4,2)$. (b) The root-mean-square error (see Appendix A) in the estimate for $U(1, 1)$, averaged over 20 runs of 100 trials each.

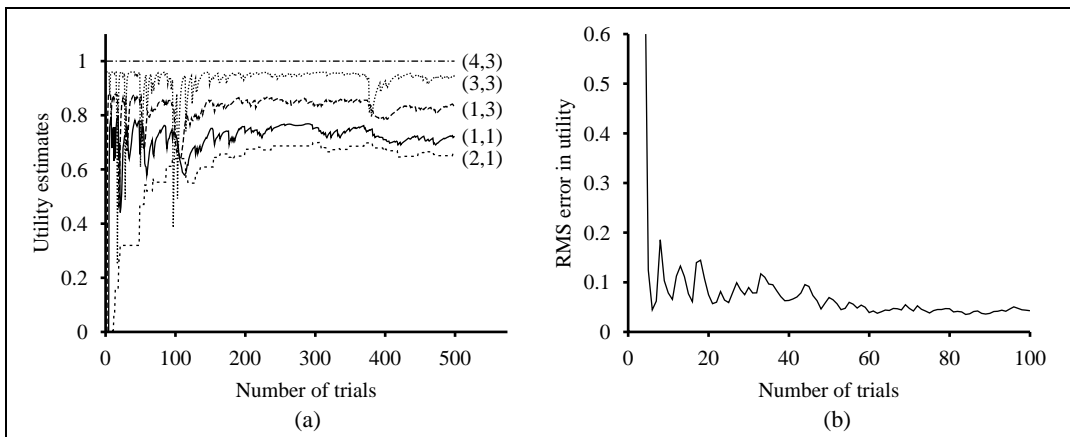


Figure 21.5 FILES: . The TD learning curves for the 4×3 world. (a) The utility estimates for a selected subset of states, as a function of the number of trials. (b) The root-mean-square error in the estimate for $U(1, 1)$, averaged over 20 runs of 500 trials each. Only the first 100 trials are shown to enable comparison with Figure 21.3.

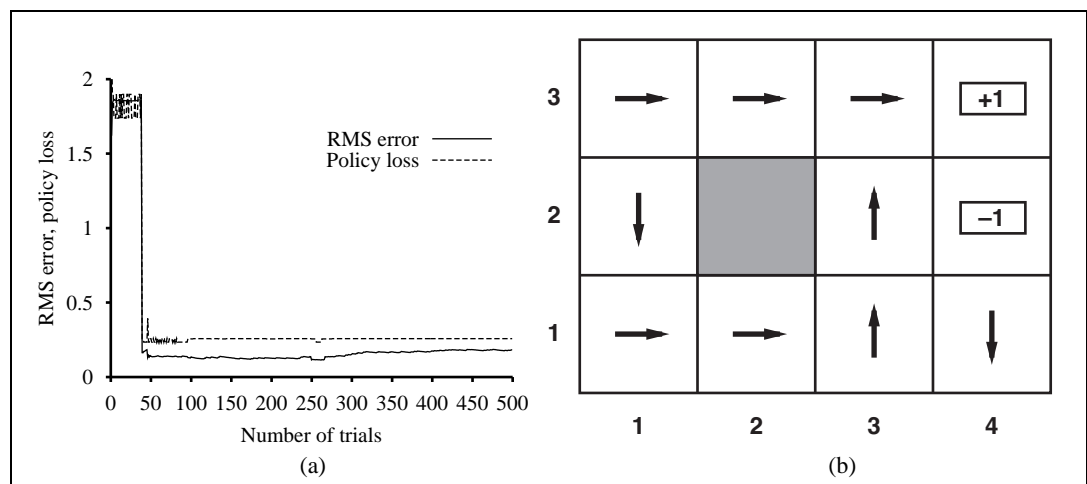


Figure 21.6 FILES: figures/4x3-greedy-adp-policy.eps (Tue Nov 3 16:22:10 2009). Performance of a greedy ADP agent that executes the action recommended by the optimal policy for the learned model. (a) RMS error in the utility estimates averaged over the nine nonterminal squares. (b) The suboptimal policy to which the greedy agent converges in this particular sequence of trials.

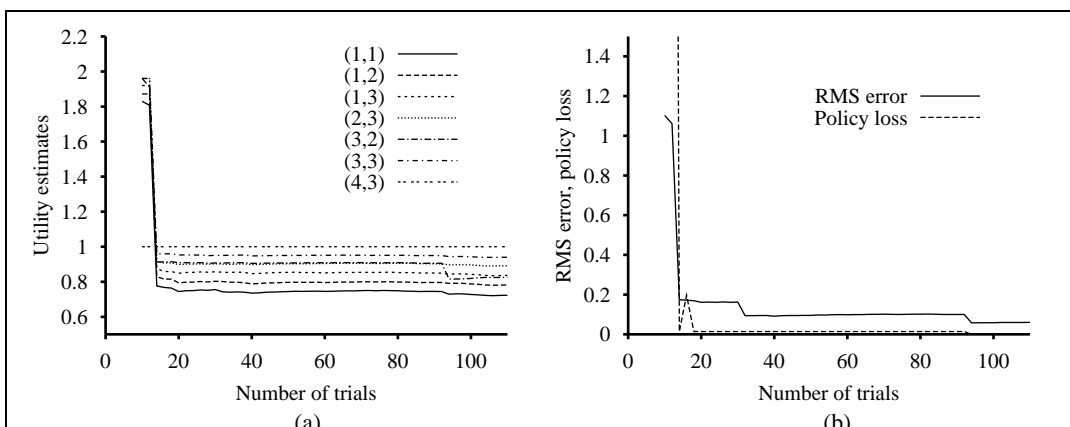


Figure 21.7 FILES: . Performance of the exploratory ADP agent, using $R^+ = 2$ and $N_e = 5$. (a) Utility estimates for selected states over time. (b) The RMS error in utility values and the associated policy loss.

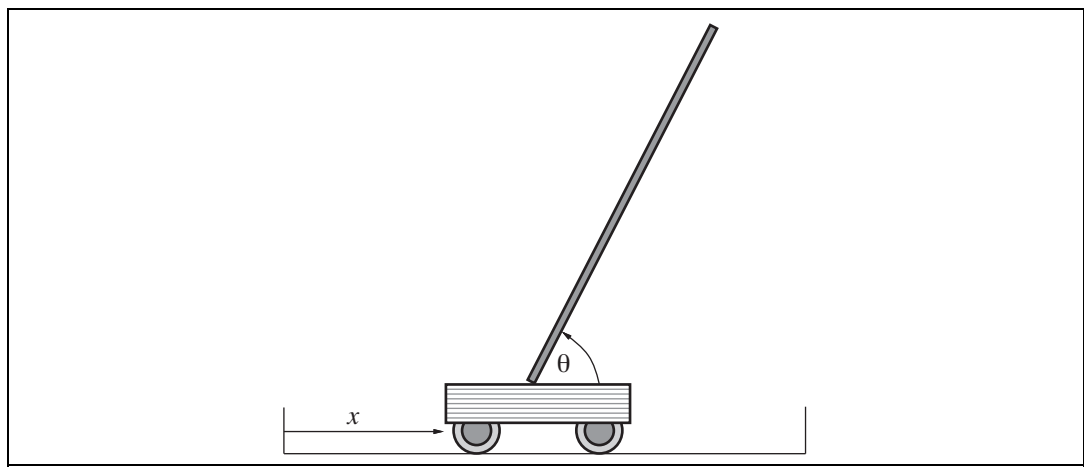


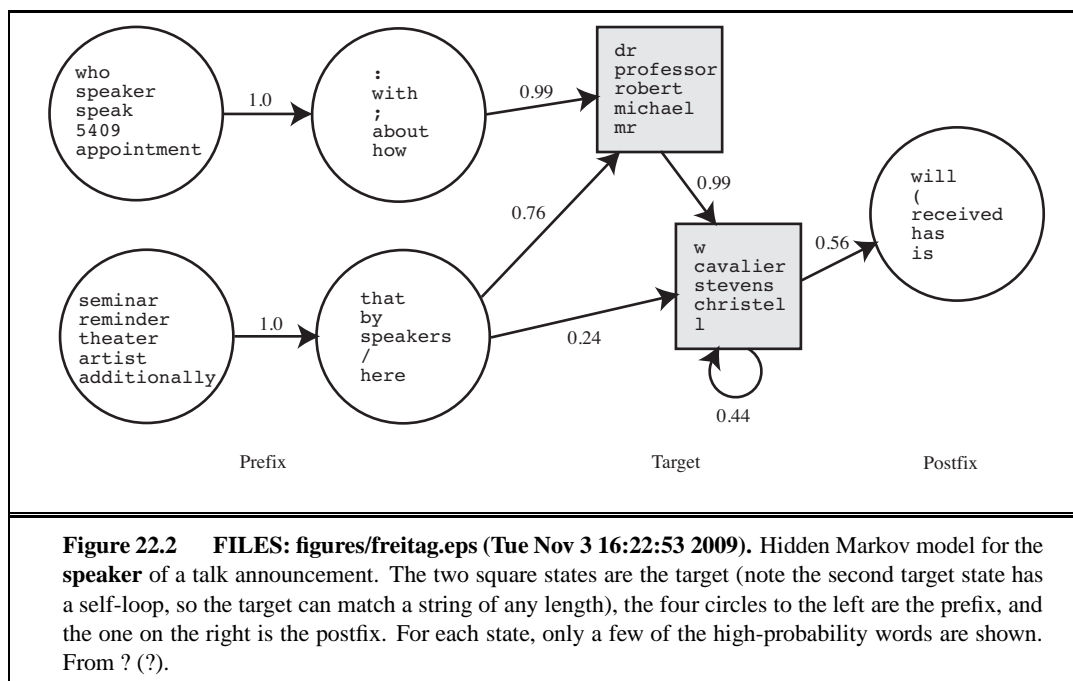
Figure 21.9 FILES: figures/cart-pole.eps (Tue Nov 3 16:22:32 2009). Setup for the problem of balancing a long pole on top of a moving cart. The cart can be jerked left or right by a controller that observes x, θ, \dot{x} , and $\dot{\theta}$.



Figure 21.10 FILES: figures/heliComposite.eps (Tue Nov 3 16:23:02 2009). Superimposed time-lapse images of an autonomous helicopter performing a very difficult “nose-in circle” maneuver. The helicopter is under the control of a policy developed by the PEGASUS policy-search algorithm. A simulator model was developed by observing the effects of various control manipulations on the real helicopter; then the algorithm was run on the simulator model overnight. A variety of controllers were developed for different maneuvers. In all cases, performance far exceeded that of an expert human pilot using remote control. (Image courtesy of Andrew Ng.)

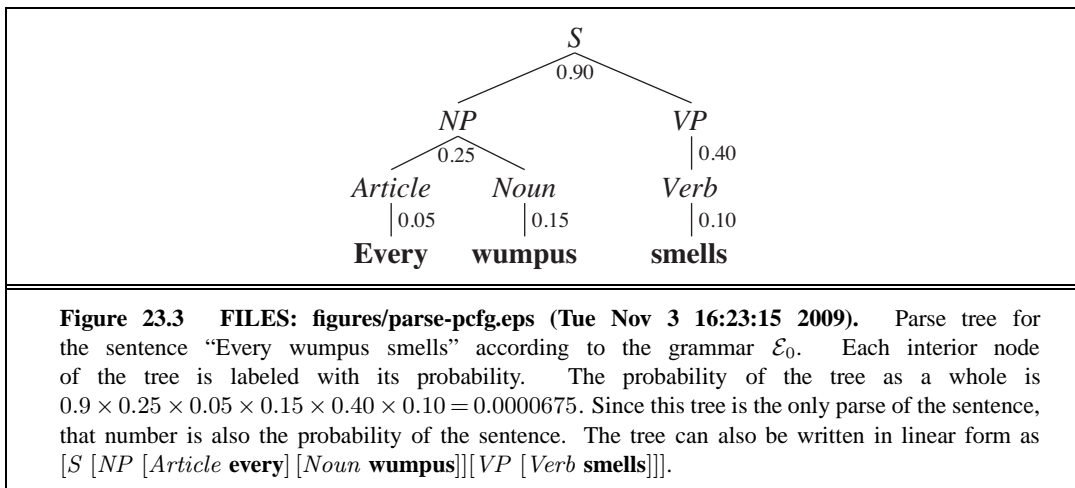
22

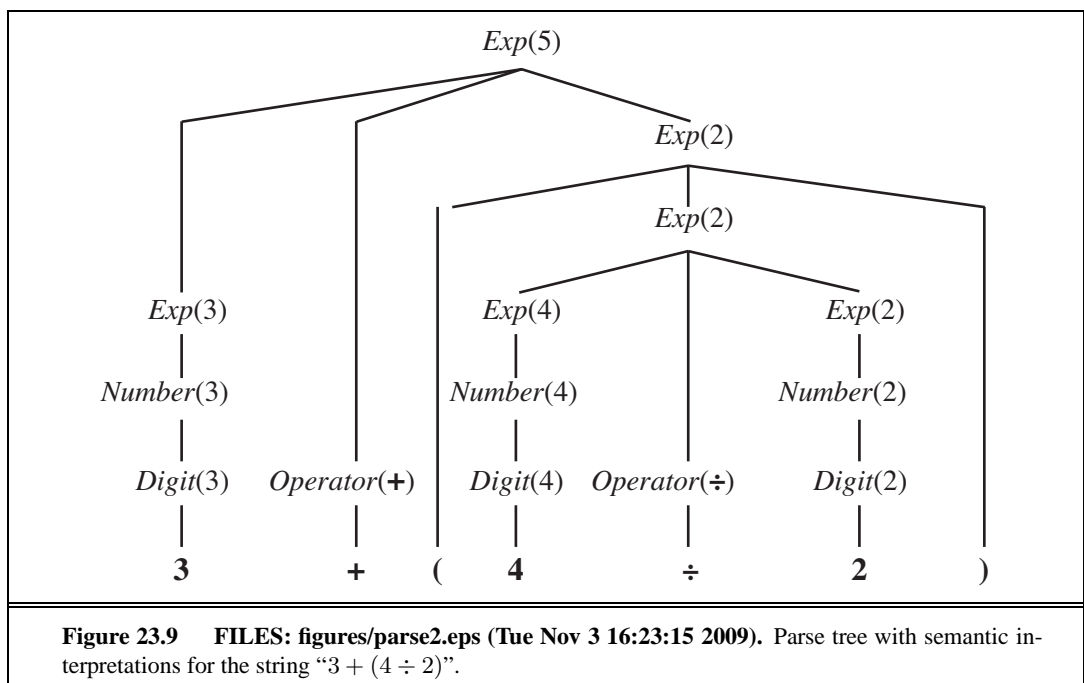
NATURAL LANGUAGE
PROCESSING

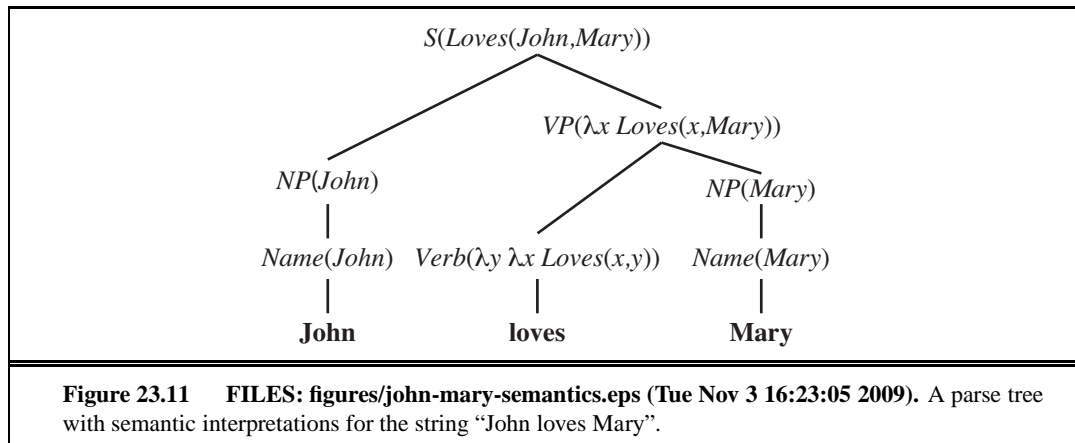


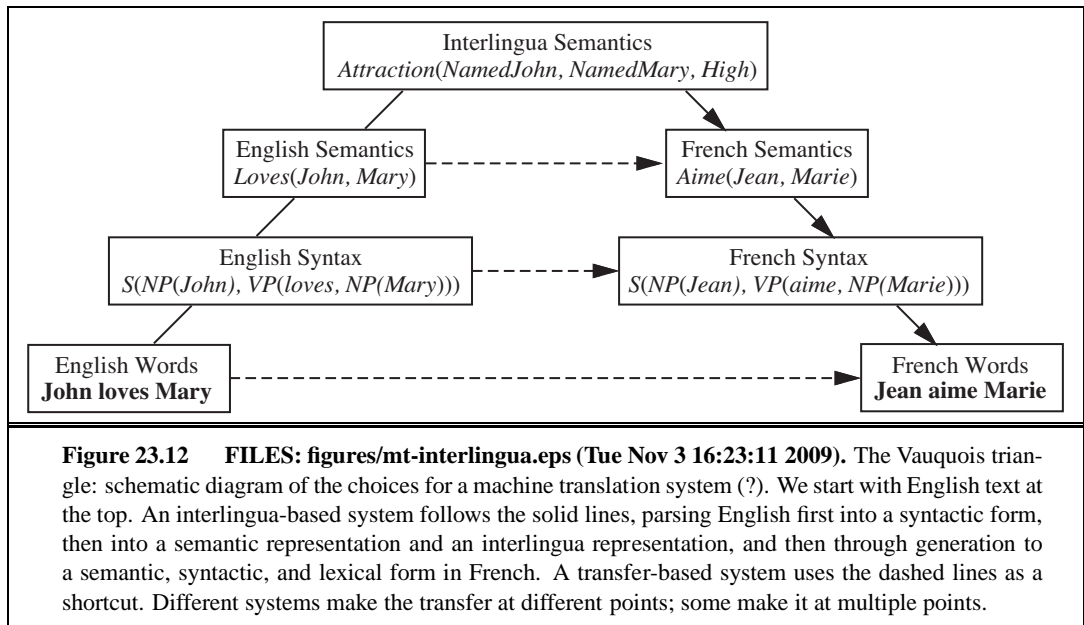
23

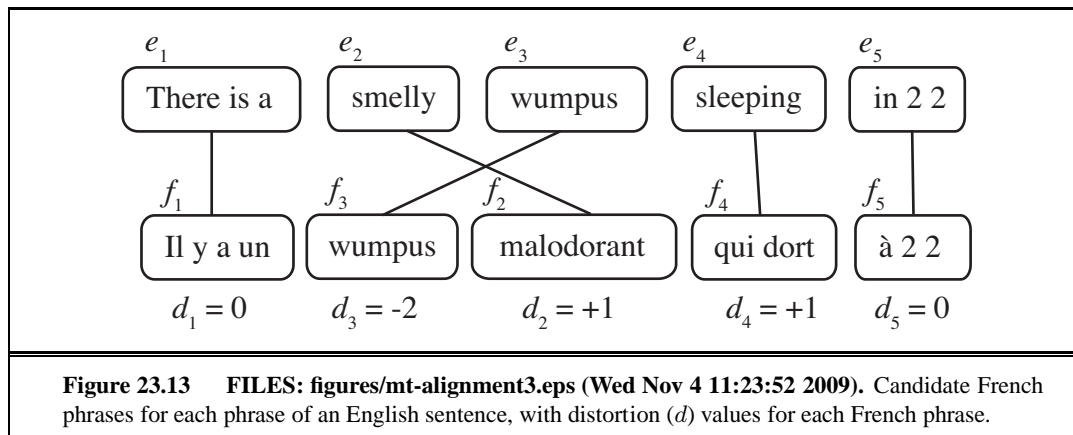
NATURAL LANGUAGE
FOR COMMUNICATION

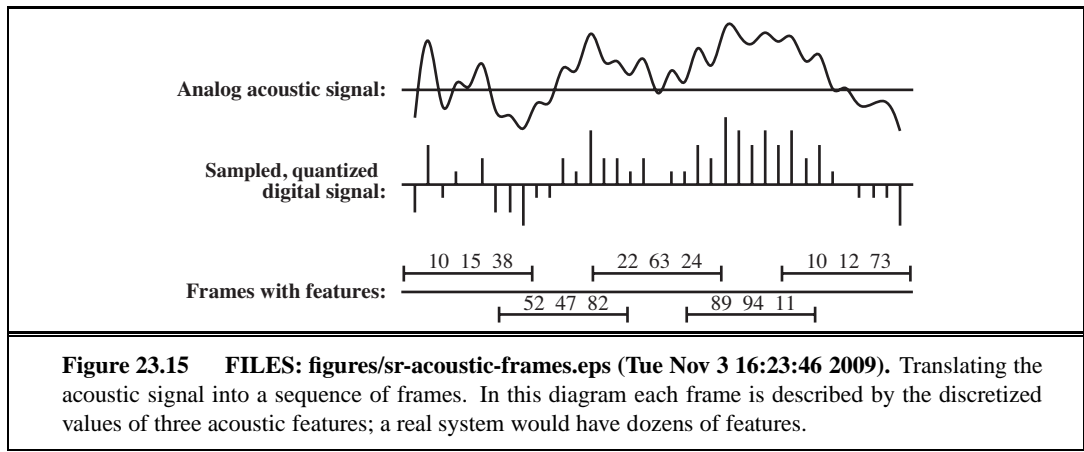


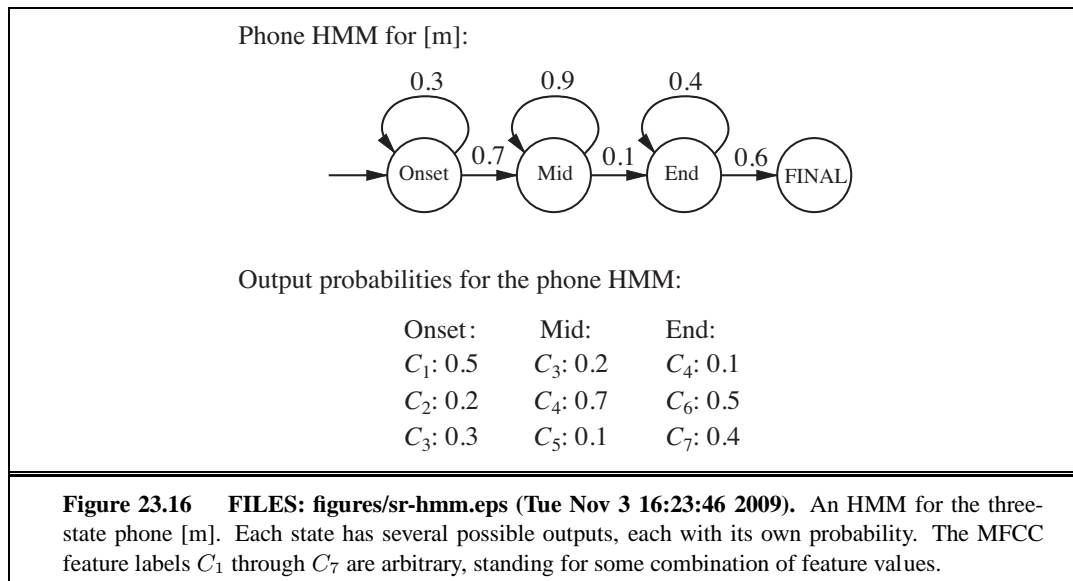


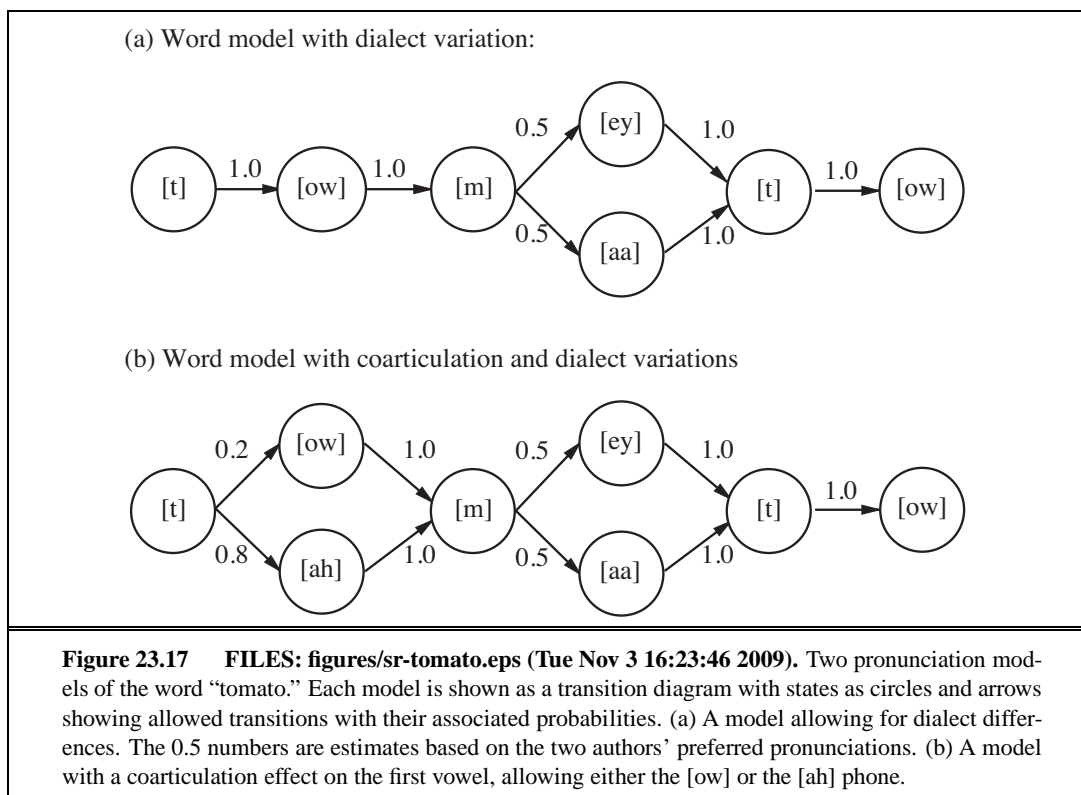












24 PERCEPTION

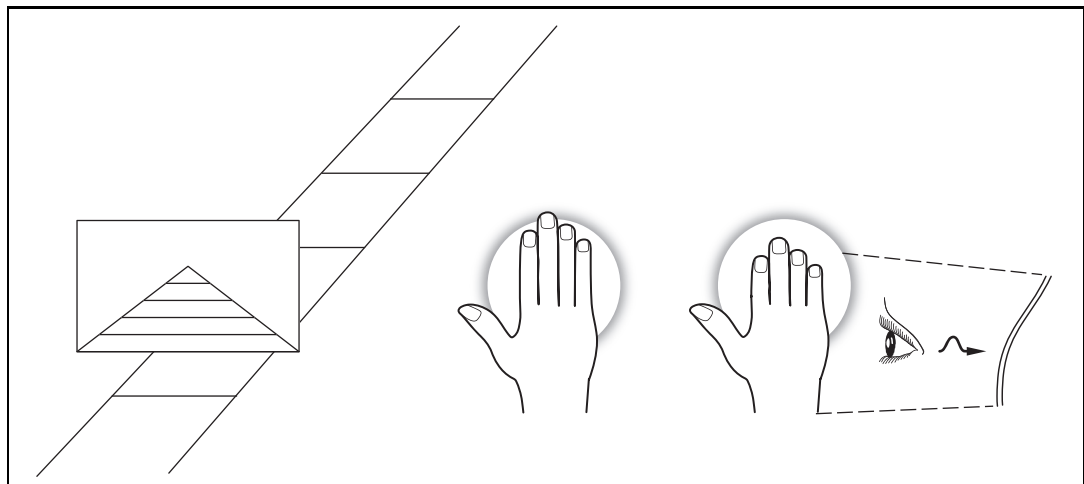


Figure 24.1 FILES: figures/c24f001.eps (Tue Nov 3 16:22:30 2009). Imaging distorts geometry. Parallel lines appear to meet in the distance, as in the image of the railway tracks on the left. In the center, a small hand blocks out most of a large moon. On the right is a foreshortening effect: the hand is tilted away from the eye, making it appear shorter than in the center figure.

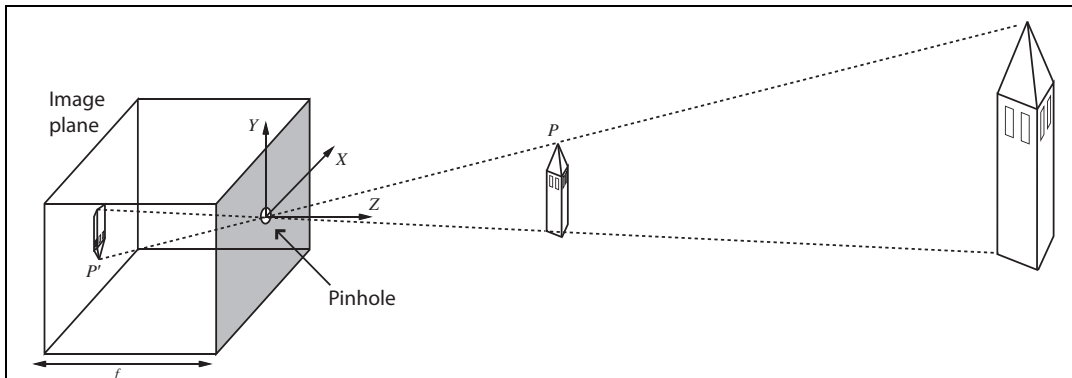


Figure 24.2 FILES: figures/newpinhole.eps (Tue Nov 3 16:23:14 2009). Each light-sensitive element in the image plane at the back of a pinhole camera receives light from a small range of directions that passes through the pinhole. If the pinhole is small enough, the result is a focused image at the back of the pinhole. The process of projection means that large, distant objects look the same as smaller, nearby objects. Note that the image is projected upside down.

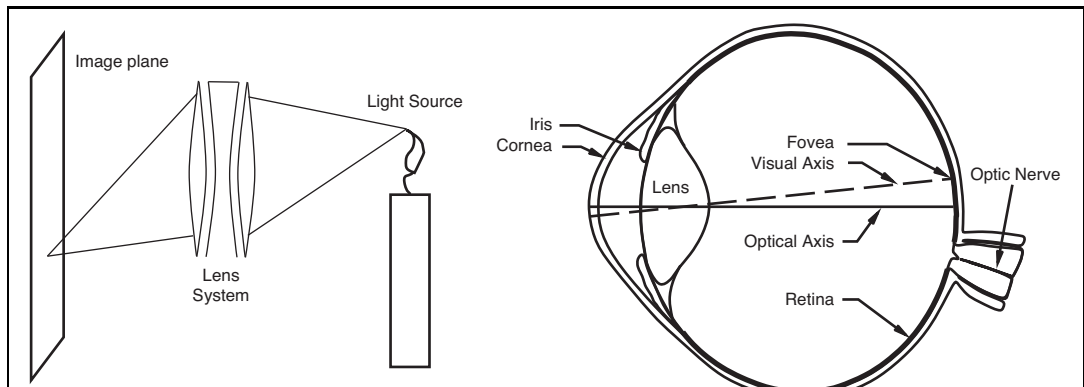
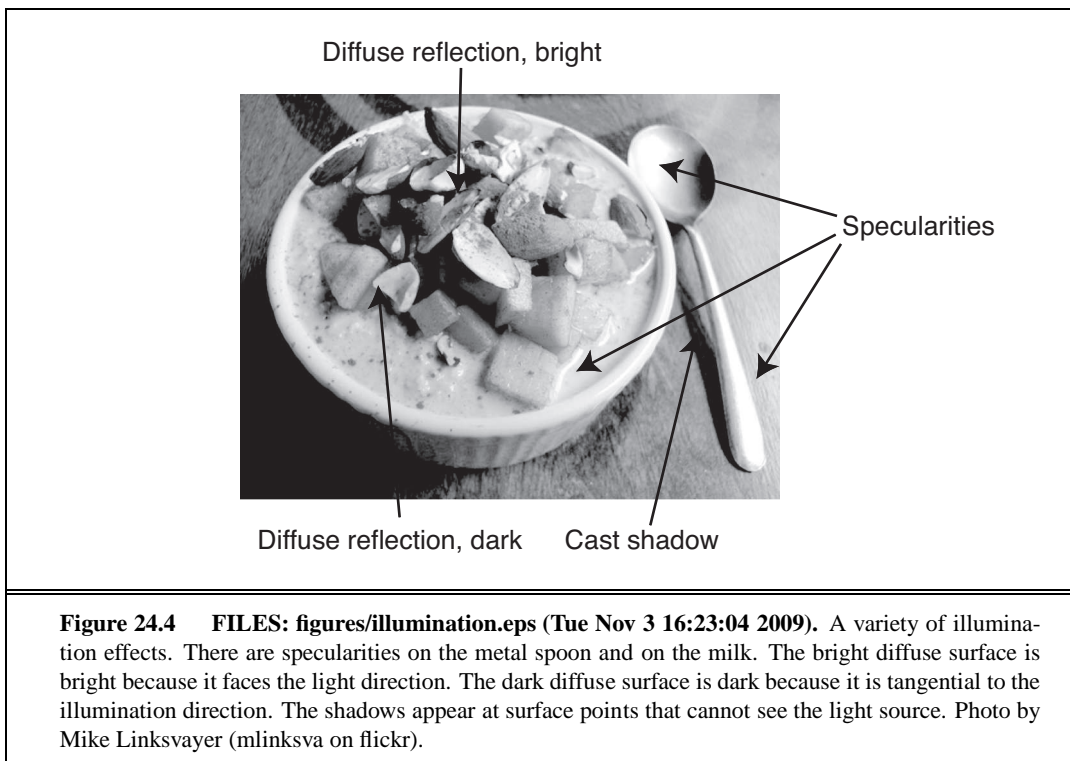


Figure 24.3 FILES: figures/lens-eye.eps (Tue Nov 3 16:23:06 2009). Lenses collect the light leaving a scene point in a range of directions, and steer it all to arrive at a single point on the image plane. Focusing works for points lying close to a focal plane in space; other points will not be focused properly. In cameras, elements of the lens system move to change the focal plane, whereas in the eye, the shape of the lens is changed by specialized muscles.



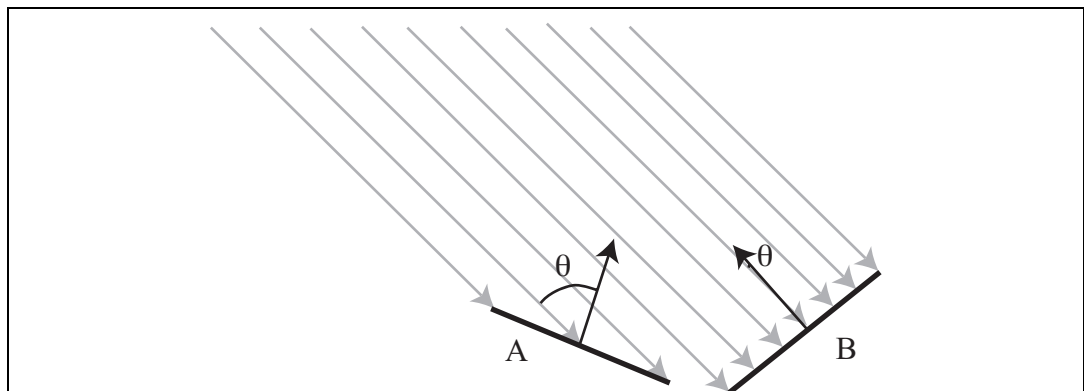


Figure 24.5 FILES: figures/lambert.eps (Tue Nov 3 13:41:38 2009). Two surface patches are illuminated by a distant point source, whose rays are shown as gray arrowheads. Patch A is tilted away from the source (θ is close to 90°) and collects less energy, because it cuts fewer light rays per unit surface area. Patch B, facing the source (θ is close to 0°), collects more energy.

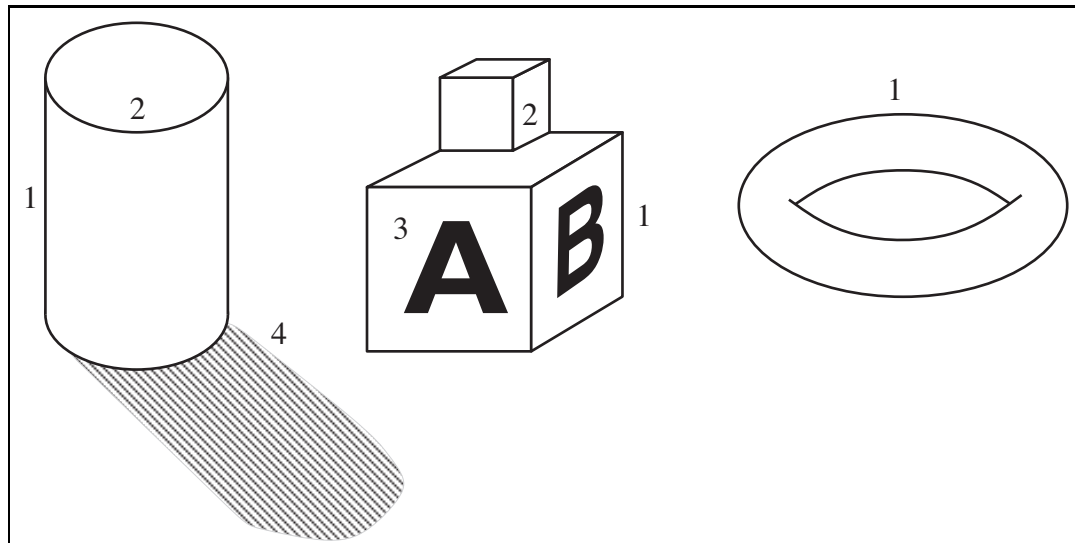


Figure 24.6 FILES: figures/diff-edges.eps (Tue Nov 3 16:22:37 2009). Different kinds of edges:
(1) depth discontinuities; (2) surface orientation discontinuities; (3) reflectance discontinuities; (4) illumination discontinuities (shadows).

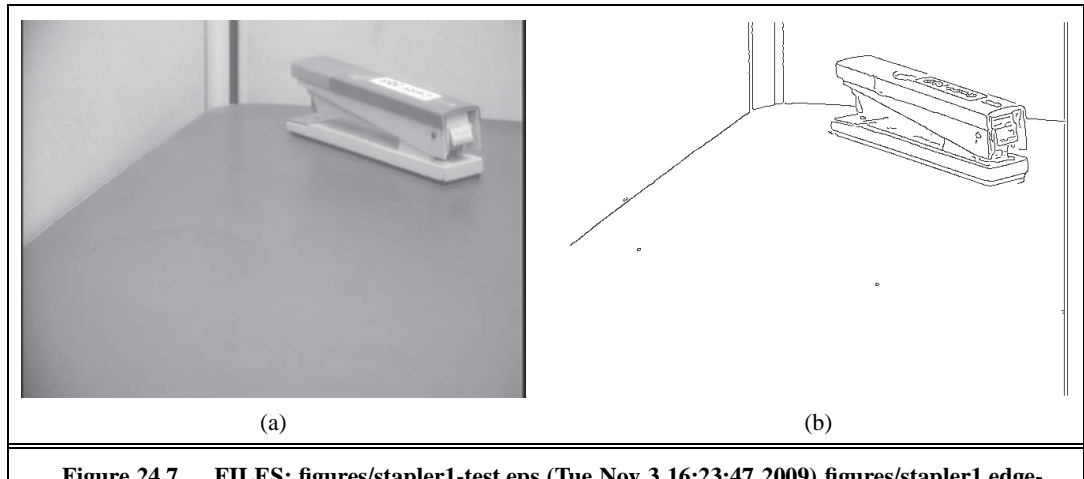
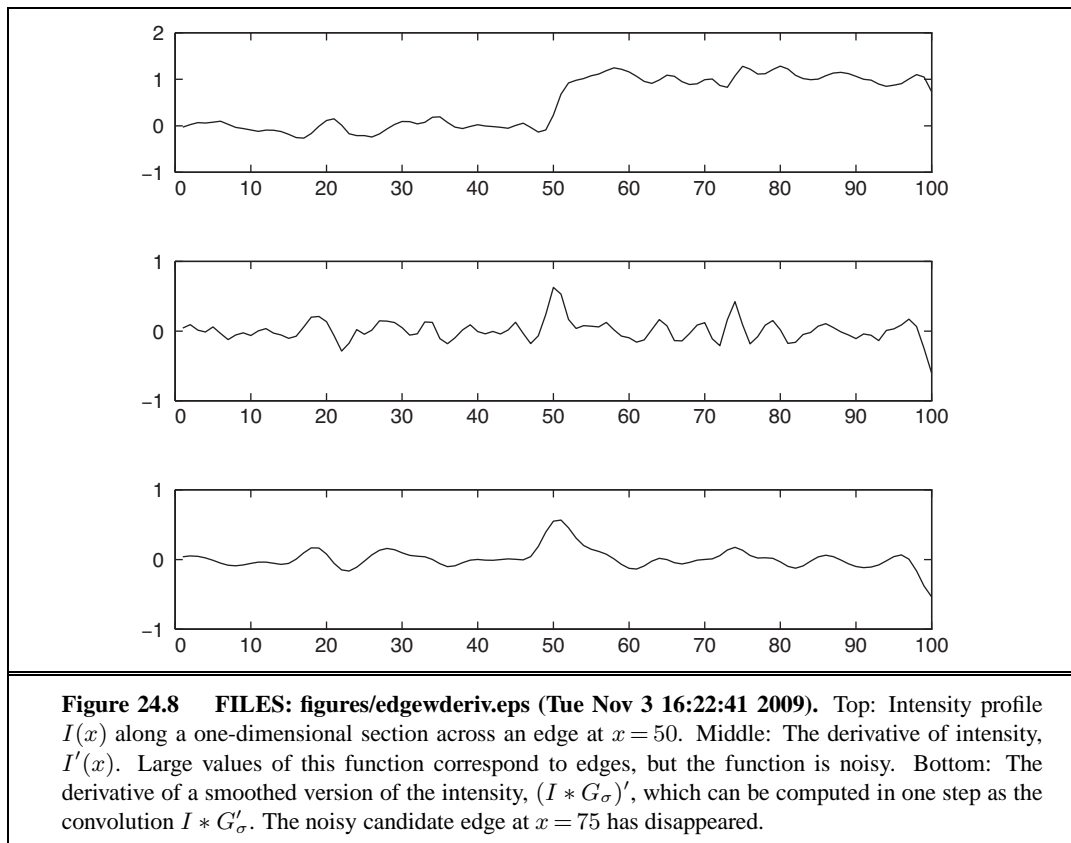


Figure 24.7 FILES: figures/stapler1-test.eps (Tue Nov 3 16:23:47 2009) figures/stapler1.edges-test.eps (Tue Nov 3 16:23:47 2009). (a) Photograph of a stapler. (b) Edges computed from (a).



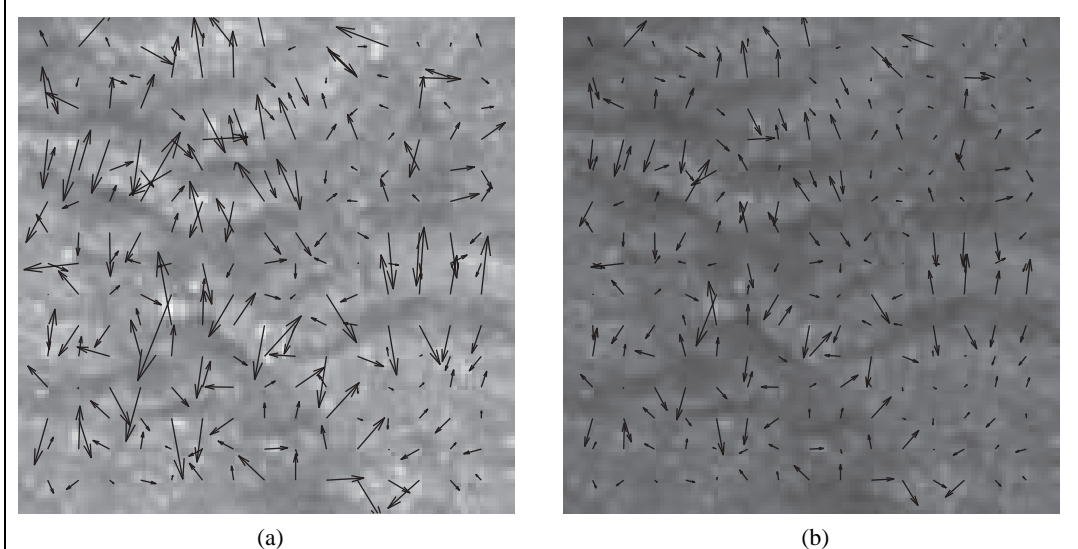


Figure 24.9 FILES: `figures/ligtricegrad.eps` (Wed Nov 4 15:09:20 2009) `figures/darkricegrad.eps` (Wed Nov 4 15:09:26 2009). Two images of the same texture of crumpled rice paper, with different illumination levels. The gradient vector field (at every eighth pixel) is plotted on top of each one. Notice that, as the light gets darker, all the gradient vectors get shorter. The vectors do not rotate, so the gradient orientations do not change.



Figure 24.10 FILES: [figures/broxrevised.eps](#) (Tue Nov 3 16:22:29 2009) [figures/broxIn1.eps](#) (not found) [figures/broxIn2.eps](#) (not found) [figures/broxFlow.eps](#) (not found). Two frames of a video sequence. On the right is the optical flow field corresponding to the displacement from one frame to the other. Note how the movement of the tennis racket and the front leg is captured by the directions of the arrows. (Courtesy of Thomas Brox.)

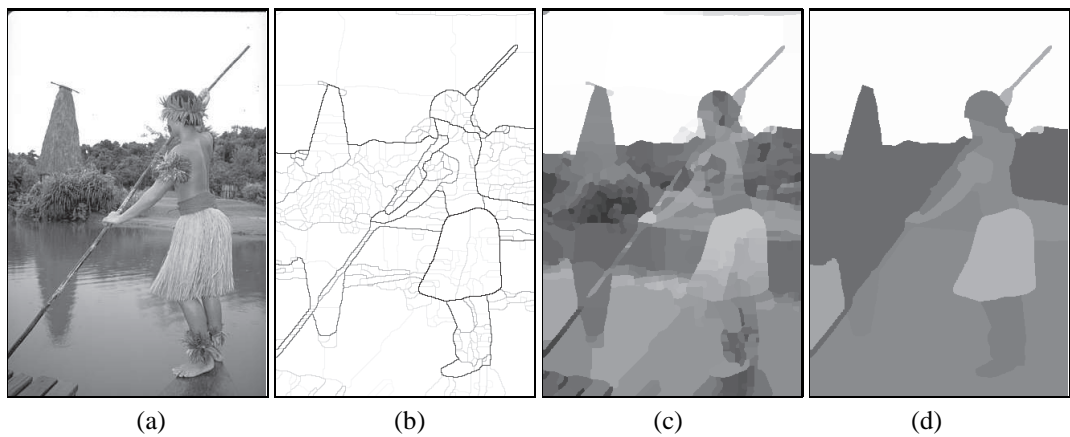


Figure 24.11 FILES: `figures/101087.eps` (Tue Nov 3 16:22:07 2009) `figures/101087-ucm-th0.eps (not found)` `figures/101087-seg-th0.eps (not found)` `figures/101087-seg-th0-5.eps (not found)`. (a) Original image. (b) Boundary contours, where the higher the P_b value, the darker the contour. (c) Segmentation into regions, corresponding to a fine partition of the image. Regions are rendered in their mean colors. (d) Segmentation into regions, corresponding to a coarser partition of the image, resulting in fewer regions. (Courtesy of Pablo Arbelaez, Michael Maire, Charles Fowlkes, and Jitendra Malik)

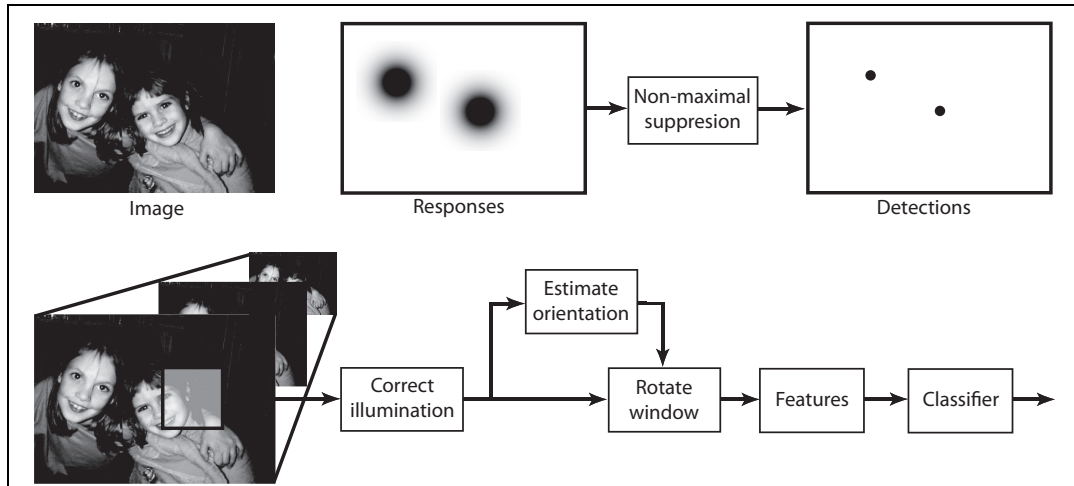


Figure 24.12 FILES: figures/facesys.eps (not found) figures/facesys2.eps (Tue Nov 3 16:22:46 2009). Face finding systems vary, but most follow the architecture illustrated in two parts here. On the top, we go from images to responses, then apply non-maximum suppression to find the strongest local response. The responses are obtained by the process illustrated on the bottom. We sweep a window of fixed size over larger and smaller versions of the image, so as to find smaller or larger faces, respectively. The illumination in the window is corrected, and then a regression engine (quite often, a neural net) predicts the orientation of the face. The window is corrected to this orientation and then presented to a classifier. Classifier outputs are then postprocessed to ensure that only one face is placed at each location in the image.

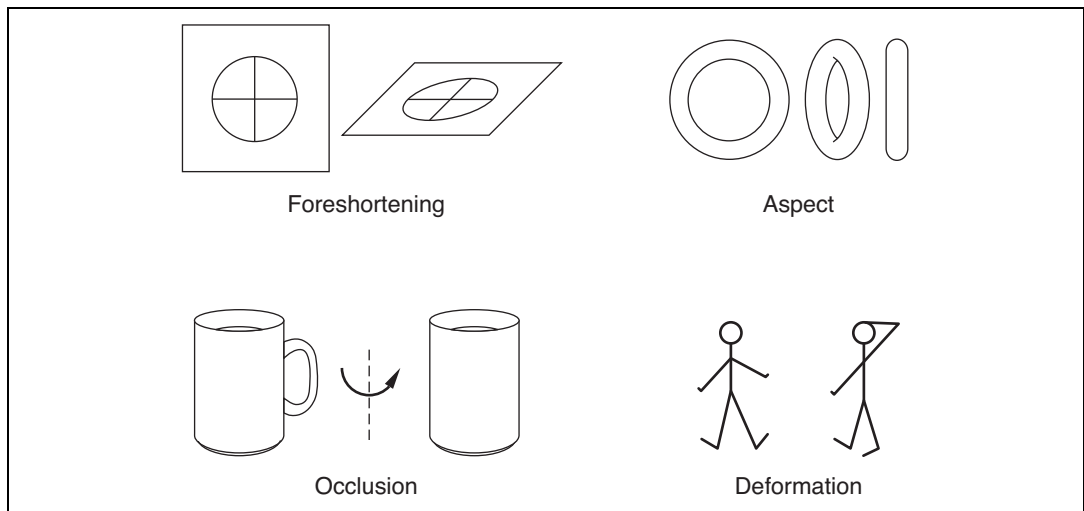
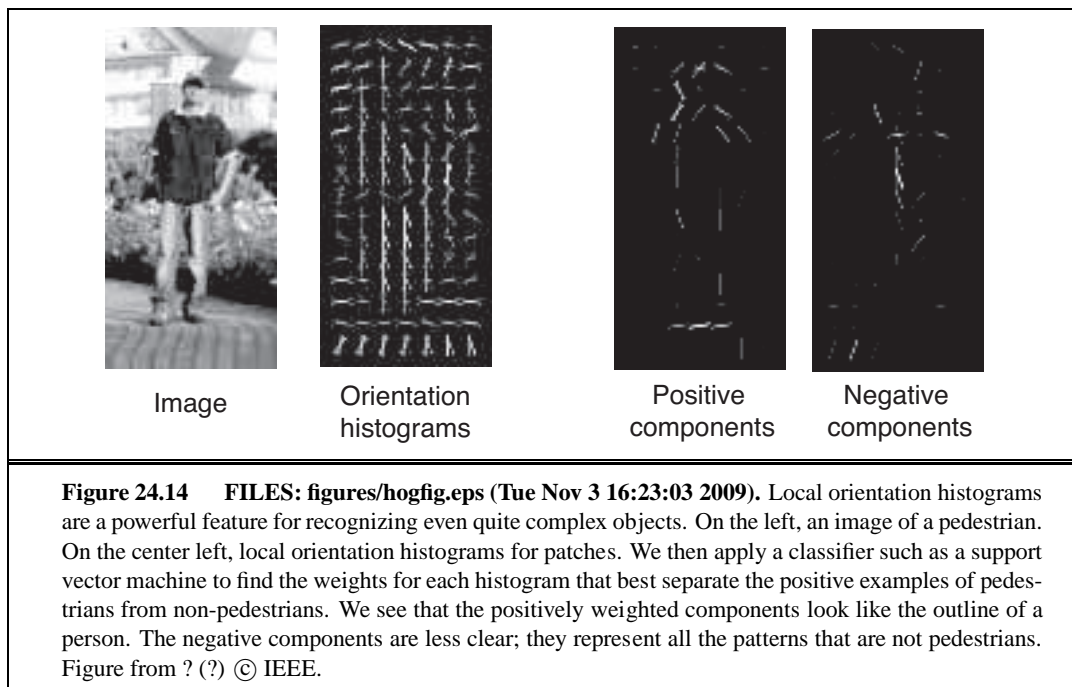
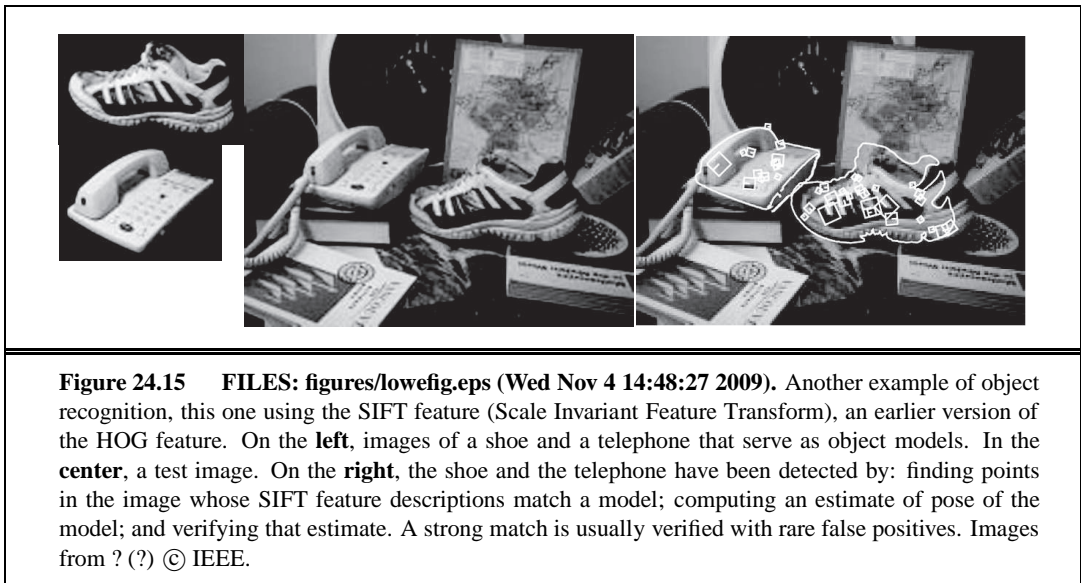
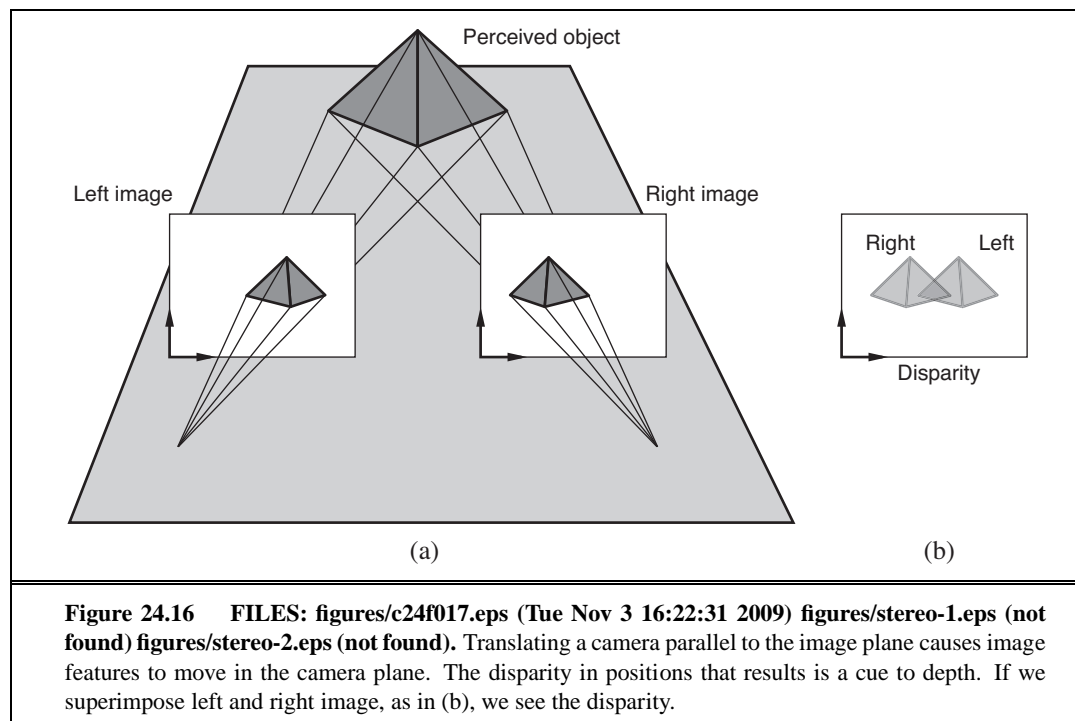


Figure 24.13 FILES: figures/c24f013.eps (Tue Nov 3 16:22:30 2009). Sources of appearance variation. First, elements can foreshorten, like the circular patch on the top left. This patch is viewed at a slant, and so is elliptical in the image. Second, objects viewed from different directions can change shape quite dramatically, a phenomenon known as aspect. On the top right are three different aspects of a doughnut. Occlusion causes the handle of the mug on the bottom left to disappear when the mug is rotated. In this case, because the body and handle belong to the same mug, we have self-occlusion. Finally, on the bottom right, some objects can deform dramatically.







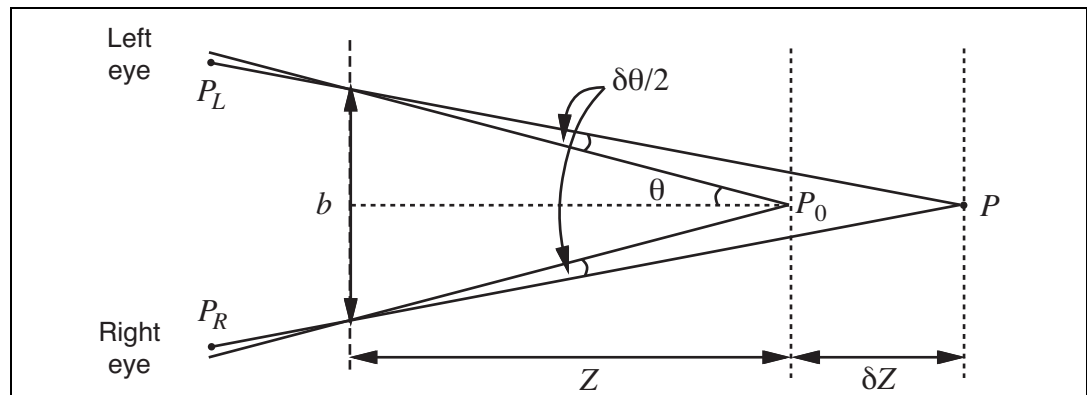


Figure 24.17 FILES: figures/stereopsis.eps (Tue Nov 3 16:23:49 2009). The relation between disparity and depth in stereopsis. The centers of projection of the two eyes are b apart, and the optical axes intersect at the fixation point P_0 . The point P in the scene projects to points P_L and P_R in the two eyes. In angular terms, the disparity between these is $\delta\theta$. See text.

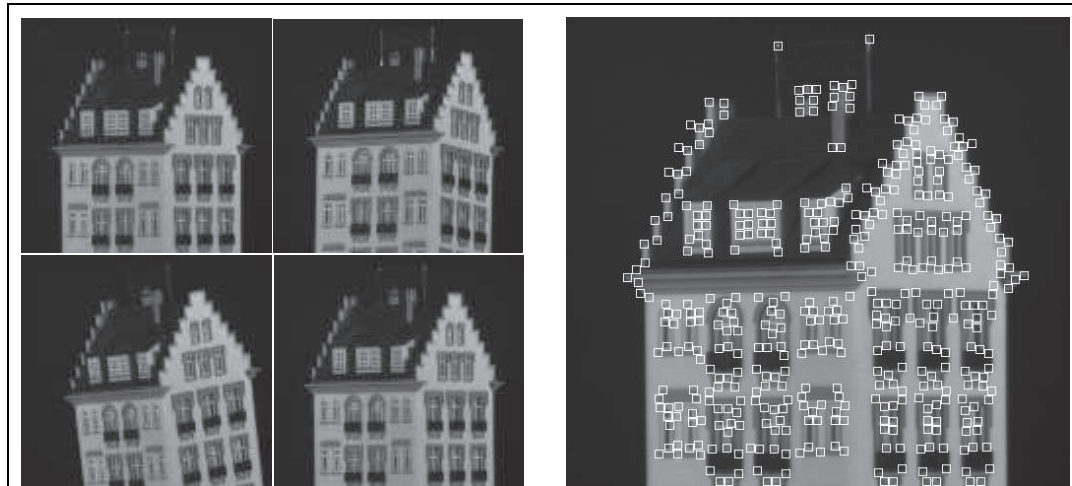


Figure 24.18 FILES: [figures/frame1.eps](#) (Tue Nov 3 16:22:52 2009) [figures/frame60.eps](#) (Tue Nov 3 16:22:53 2009) [figures/frame120.eps](#) (Tue Nov 3 16:22:53 2009) [figures/frame150.eps](#) (Tue Nov 3 16:22:53 2009) [figures/features.eps](#) (Tue Nov 3 16:22:47 2009). (a) Four frames from a video sequence in which the camera is moved and rotated relative to the object. (b) The first frame of the sequence, annotated with small boxes highlighting the features found by the feature detector. (Courtesy of Carlo Tomasi.)

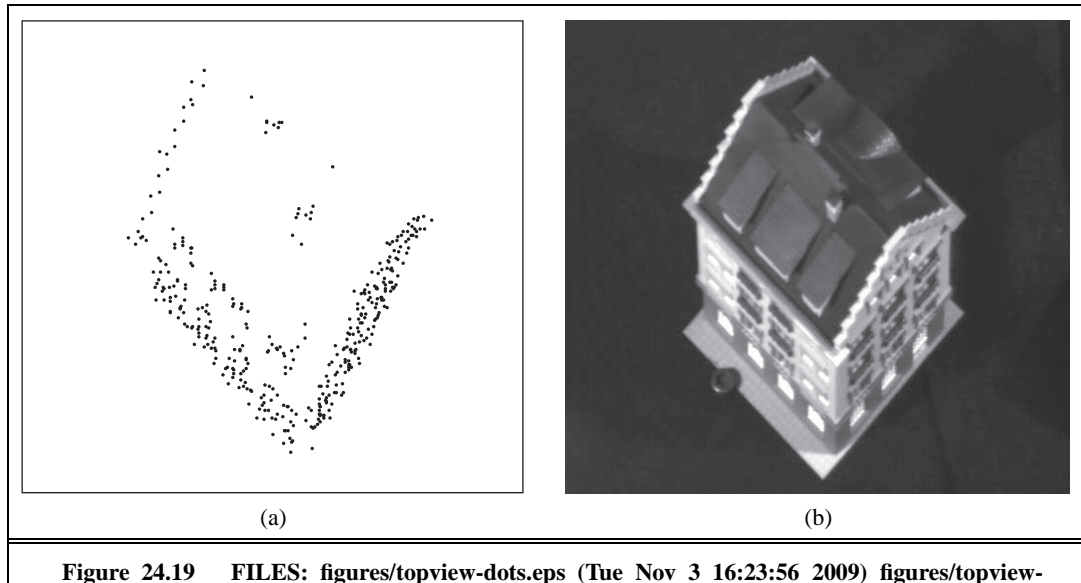


Figure 24.19 FILES: `figures/topview-dots.eps` (Tue Nov 3 16:23:56 2009) `figures/topview-real.eps` (Tue Nov 3 16:23:57 2009). (a) Three-dimensional reconstruction of the locations of the image features in Figure 24.18, shown from above. (b) The real house, taken from the same position.

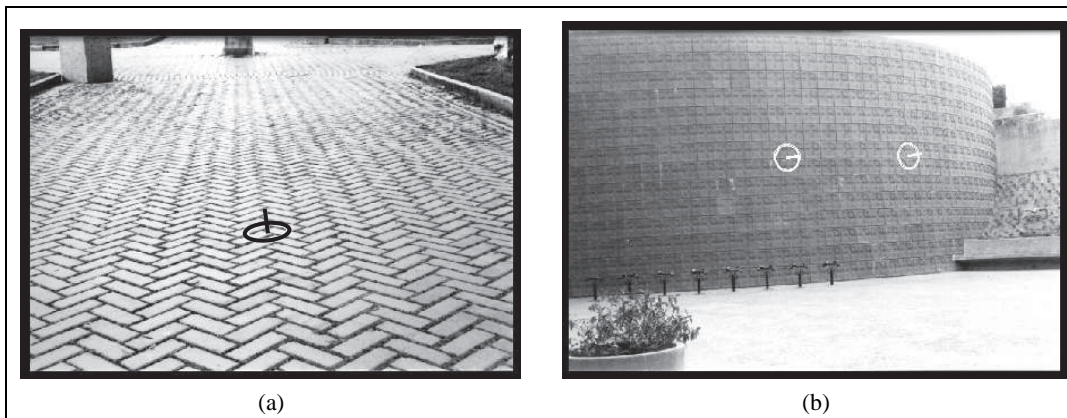


Figure 24.20 FILES: figures/camp-test.eps (Tue Nov 3 16:22:32 2009) figures/chem-test.eps (Tue Nov 3 16:22:32 2009). (a) A textured scene. Assuming that the real texture is uniform allows recovery of the surface orientation. The computed surface orientation is indicated by overlaying a black circle and pointer, transformed as if the circle were painted on the surface at that point. (b) Recovery of shape from texture for a curved surface (white circle and pointer this time). Images courtesy of Jitendra Malik and Ruth Rosenholtz (?).

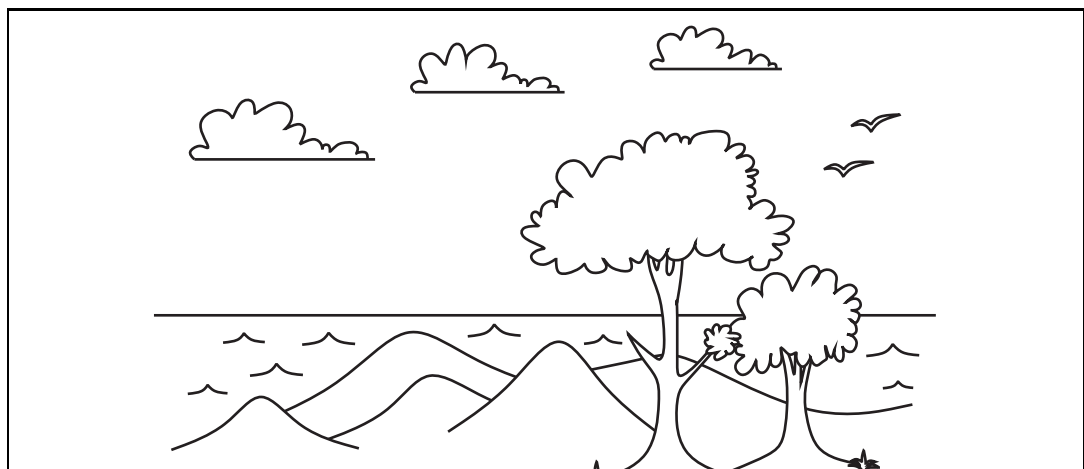


Figure 24.21 FILES: figures/isha.eps (Tue Nov 3 16:23:05 2009). An evocative line drawing.
(Courtesy of Isha Malik.)

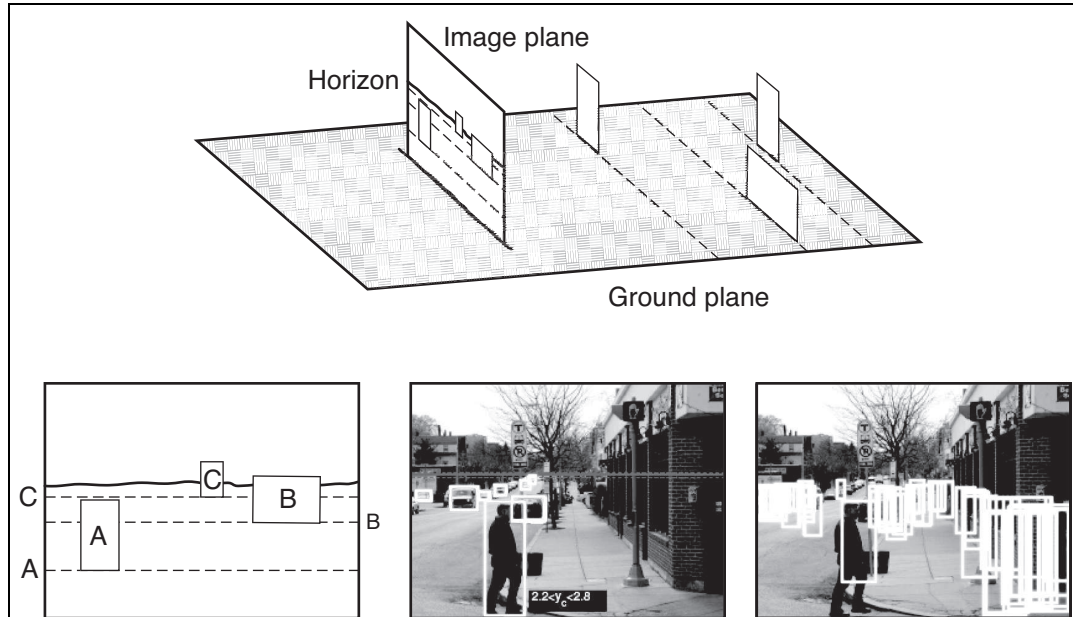


Figure 24.22 FILES: figures/c24f022-a.eps (Tue Nov 3 16:22:31 2009). In an image of people standing on a ground plane, the people whose feet are closer to the horizon in the image must be farther away (top drawing). This means they must look smaller in the image (left lower drawing). This means that the size and location of real pedestrians in an image depend upon one another and on the location of the horizon. To exploit this, we need to identify the ground plane, which is done using shape-from-texture methods. From this information, and from some likely pedestrians, we can recover a horizon as shown in the center image. On the right, acceptable pedestrian boxes given this geometric context. Notice that pedestrians who are higher in the scene must be smaller. If they are not, then they are false positives. Images from ? (?) © IEEE.

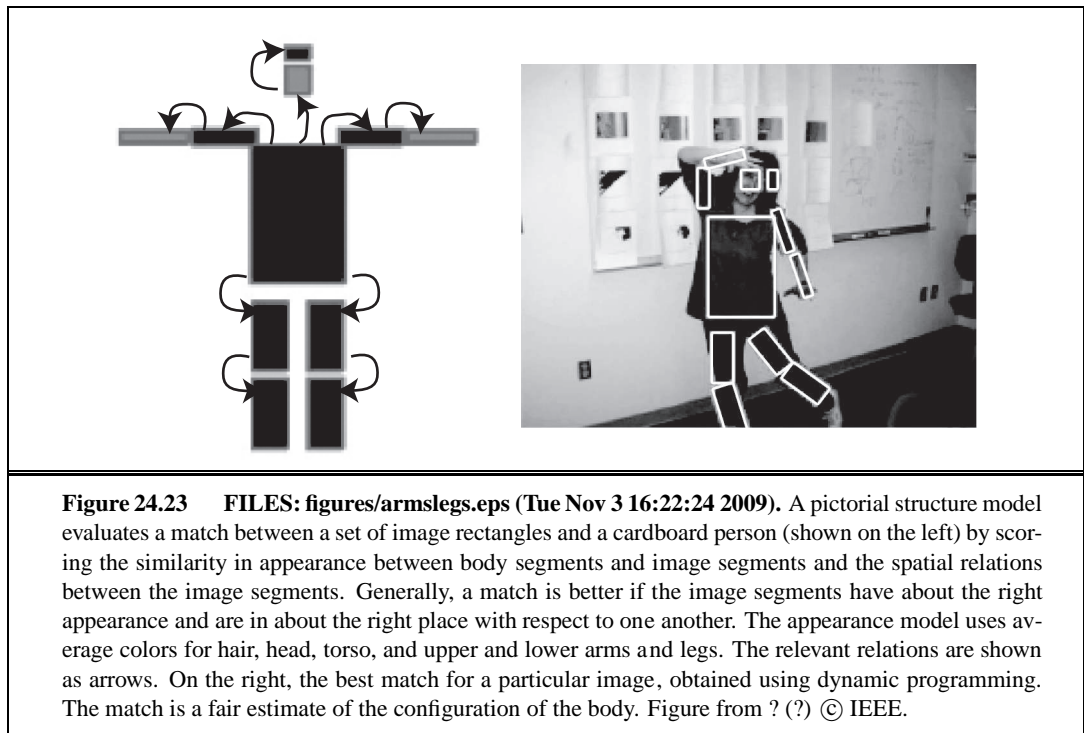


Figure 24.23 FILES: figures/armslags.eps (Tue Nov 3 16:22:24 2009). A pictorial structure model evaluates a match between a set of image rectangles and a cardboard person (shown on the left) by scoring the similarity in appearance between body segments and image segments and the spatial relations between the image segments. Generally, a match is better if the image segments have about the right appearance and are in about the right place with respect to one another. The appearance model uses average colors for hair, head, torso, and upper and lower arms and legs. The relevant relations are shown as arrows. On the right, the best match for a particular image, obtained using dynamic programming. The match is a fair estimate of the configuration of the body. Figure from ? (?) © IEEE.

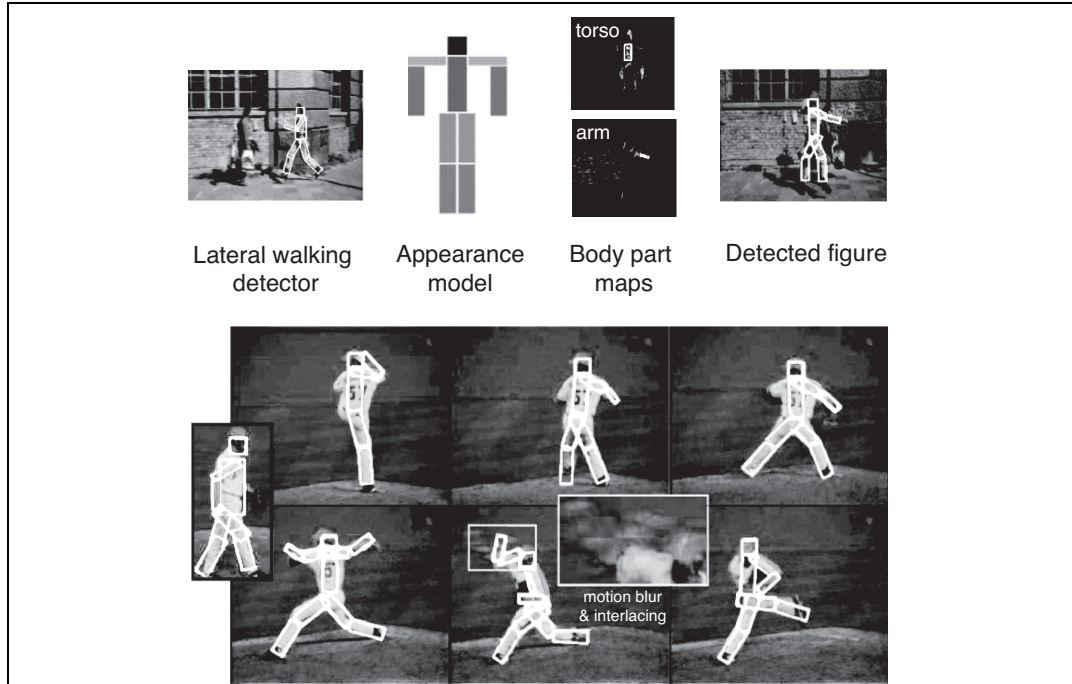
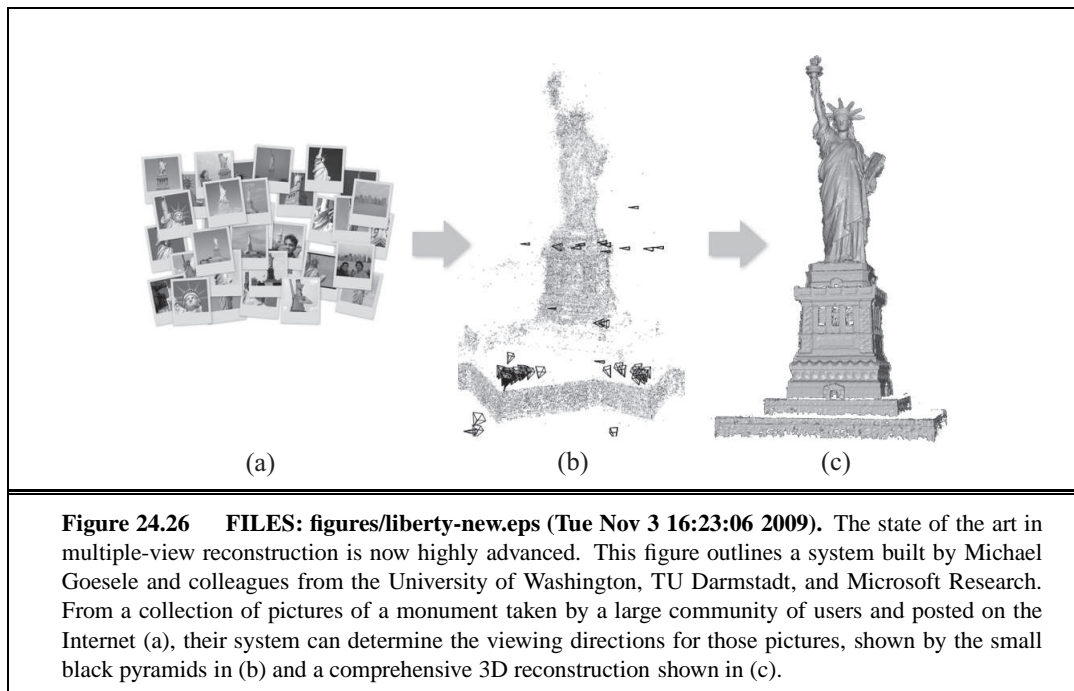


Figure 24.24 FILES: figures/tracker.eps (Tue Nov 3 16:23:57 2009). We can track moving people with a pictorial structure model by first obtaining an appearance model, then applying it. To obtain the appearance model, we scan the image to find a lateral walking pose. The detector does not need to be very accurate, but should produce few false positives. From the detector response, we can read off pixels that lie on each body segment, and others that do not lie on that segment. This makes it possible to build a discriminative model of the appearance of each body part, and these are tied together into a pictorial structure model of the person being tracked. Finally, we can reliably track by detecting this model in each frame. As the frames in the lower part of the image suggest, this procedure can track complicated, fast-changing body configurations, despite degradation of the video signal due to motion blur. Figure from ? (?) © IEEE.



Figure 24.25 FILES: figures/drinking-2.eps (Tue Nov 3 16:22:38 2009). Some complex human actions produce consistent patterns of appearance and motion. For example, drinking involves movements of the hand in front of the face. The first three images are correct detections of drinking; the fourth is a false-positive (the cook is looking into the coffee pot, but not drinking from it). Figure from ? (?) © IEEE.



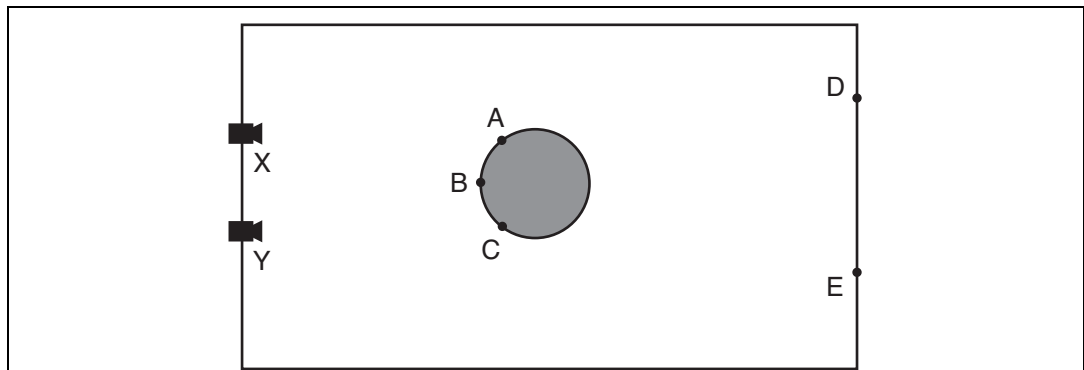
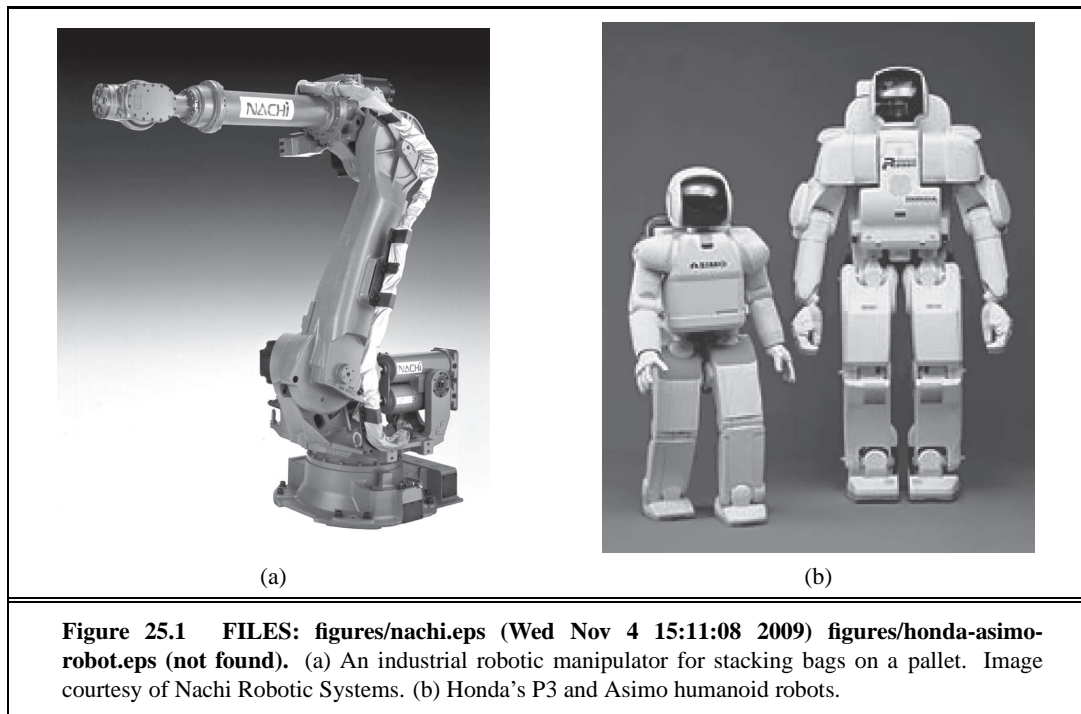


Figure 24.27 FILES: figures/bottle-stereo.eps (Tue Nov 3 16:22:28 2009). Top view of a two-camera vision system observing a bottle with a wall behind it.

25 ROBOTICS



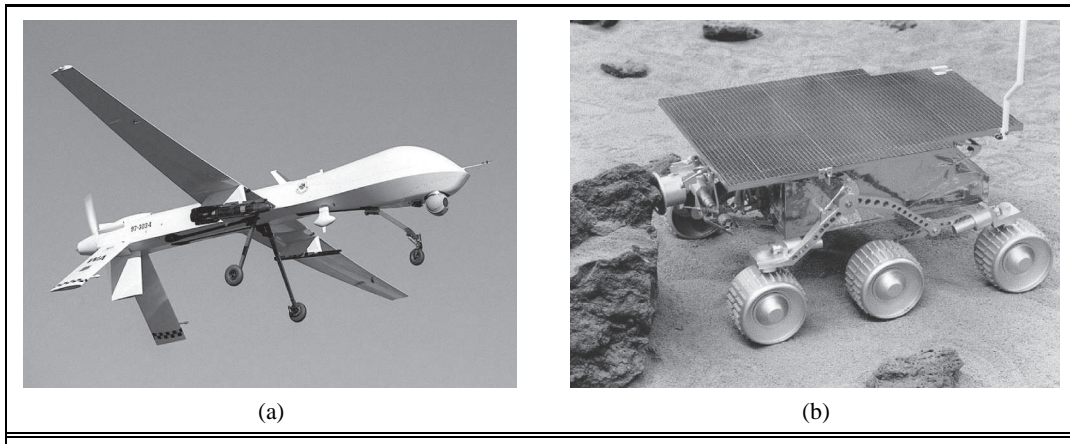


Figure 25.2 FILES: figures/predator.eps (Wed Nov 4 15:12:28 2009) figures/Sojourner.eps (Wed Nov 4 15:12:23 2009). (a) Predator, an unmanned aerial vehicle (UAV) used by the U.S. Military. Image courtesy of General Atomics Aeronautical Systems. (b) NASA's Sojourner, a mobile robot that explored the surface of Mars in July 1997.

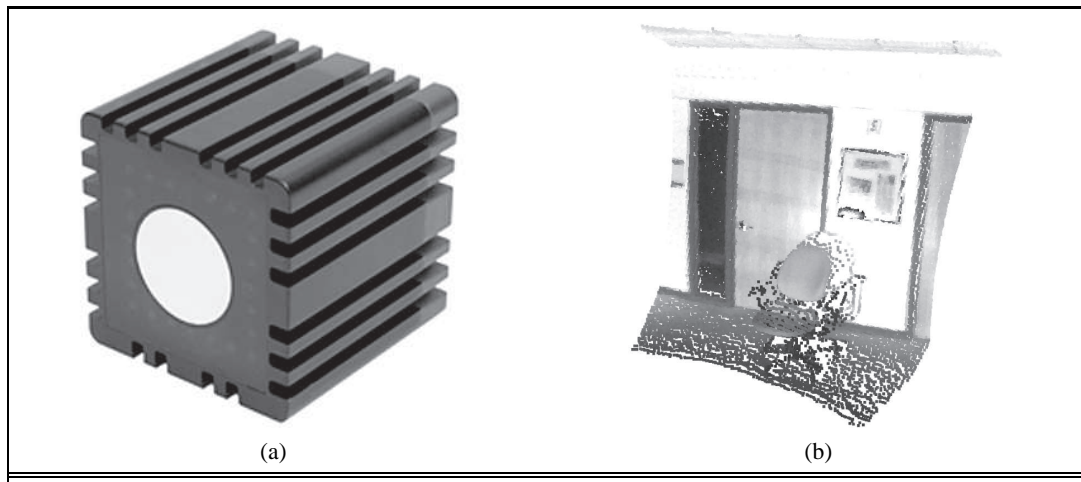


Figure 25.3 FILES: `figures/R317-SR4000-CW.eps` (Wed Nov 4 15:16:09 2009) `figures/wall-chair2.eps` (Wed Nov 4 15:16:06 2009). (a) Time of flight camera; image courtesy of Mesa Imaging GmbH. (b) 3D range image obtained with this camera. The range image makes it possible to detect obstacles and objects in a robot's vicinity.

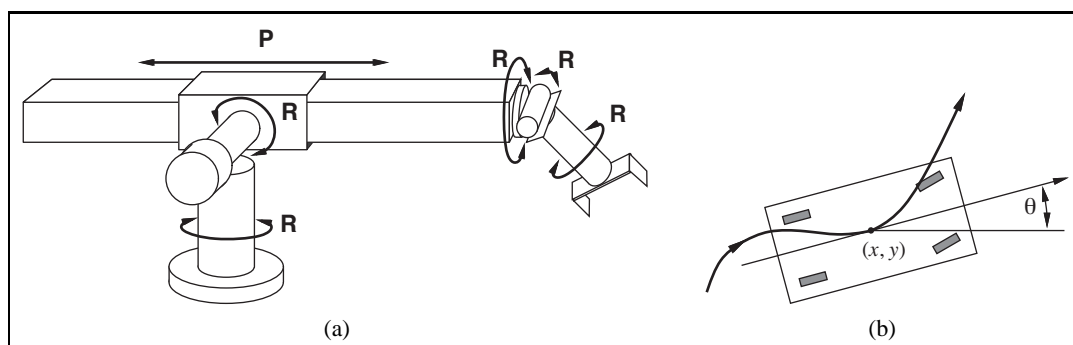


Figure 25.4 FILES: figures/stanford-arm.eps (Tue Nov 3 16:23:46 2009) figures/car-like.eps (Tue Nov 3 16:22:32 2009). (a) The Stanford Manipulator, an early robot arm with five revolute joints (R) and one prismatic joint (P), for a total of six degrees of freedom. (b) Motion of a nonholonomic four-wheeled vehicle with front-wheel steering.

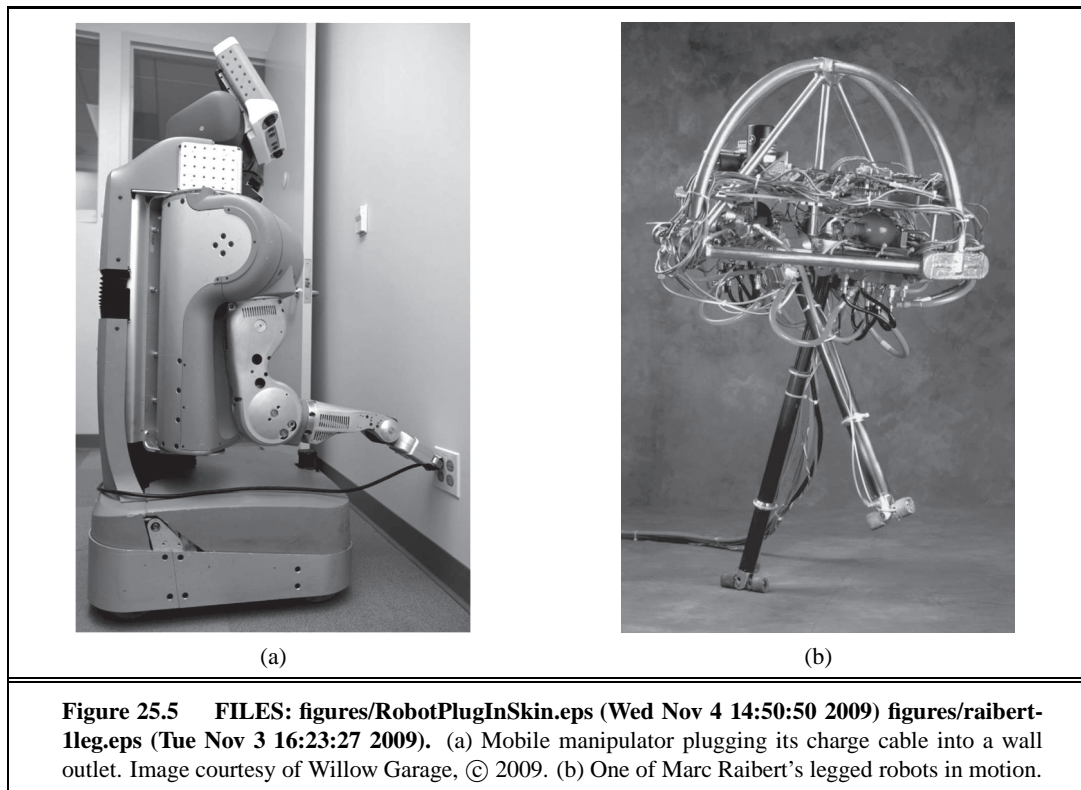


Figure 25.5 FILES: figures/RobotPlugInSkin.eps (Wed Nov 4 14:50:50 2009) figures/raibert-1leg.eps (Tue Nov 3 16:23:27 2009). (a) Mobile manipulator plugging its charge cable into a wall outlet. Image courtesy of Willow Garage, © 2009. (b) One of Marc Raibert's legged robots in motion.

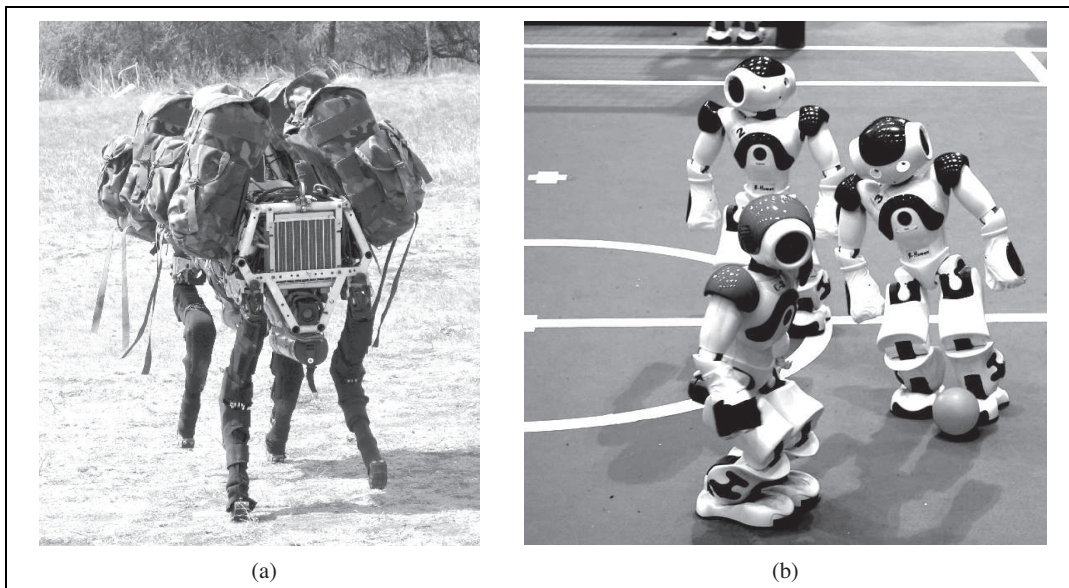
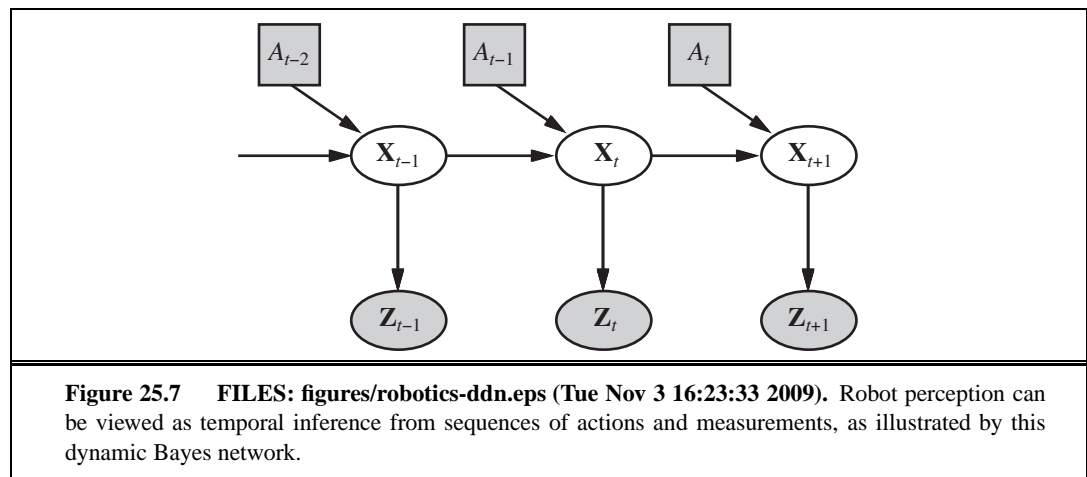


Figure 25.6 FILES: figures/BDI-DKFI.eps (Tue Nov 3 16:22:14 2009). (a) Four-legged dynamically-stable robot “Big Dog.” Image courtesy Boston Dynamics, © 2009. (b) 2009 RoboCup Standard Platform League competition, showing the winning team, B-Human, from the DFKI center at the University of Bremen. Throughout the match, B-Human outscored their opponents 64:1. Their success was built on probabilistic state estimation using particle filters and Kalman filters; on machine-learning models for gait optimization; and on dynamic kicking moves. Image courtesy DFKI, © 2009.



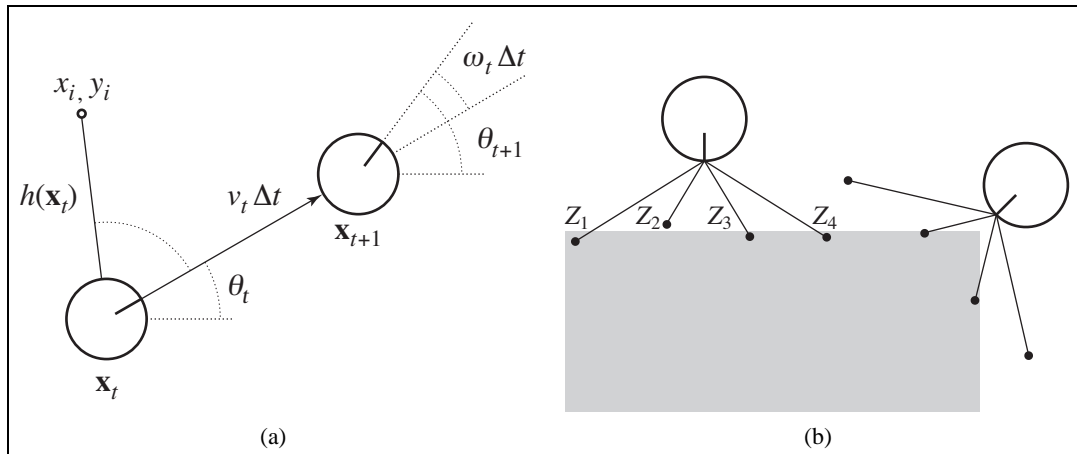


Figure 25.8 FILES: figures/robotics-pic2.eps (Tue Nov 3 16:23:34 2009) figures/range-scan-model.eps (Tue Nov 3 16:23:27 2009). (a) A simplified kinematic model of a mobile robot. The robot is shown as a circle with an interior line marking the forward direction. The state \mathbf{x}_t consists of the (x_t, y_t) position (shown implicitly) and the orientation θ_t . The new state \mathbf{x}_{t+1} is obtained by an update in position of $v_t \Delta t$ and in orientation of $\omega_t \Delta t$. Also shown is a landmark at (x_i, y_i) observed at time t . (b) The range-scan sensor model. Two possible robot poses are shown for a given range scan (z_1, z_2, z_3, z_4) . It is much more likely that the pose on the left generated the range scan than the pose on the right.

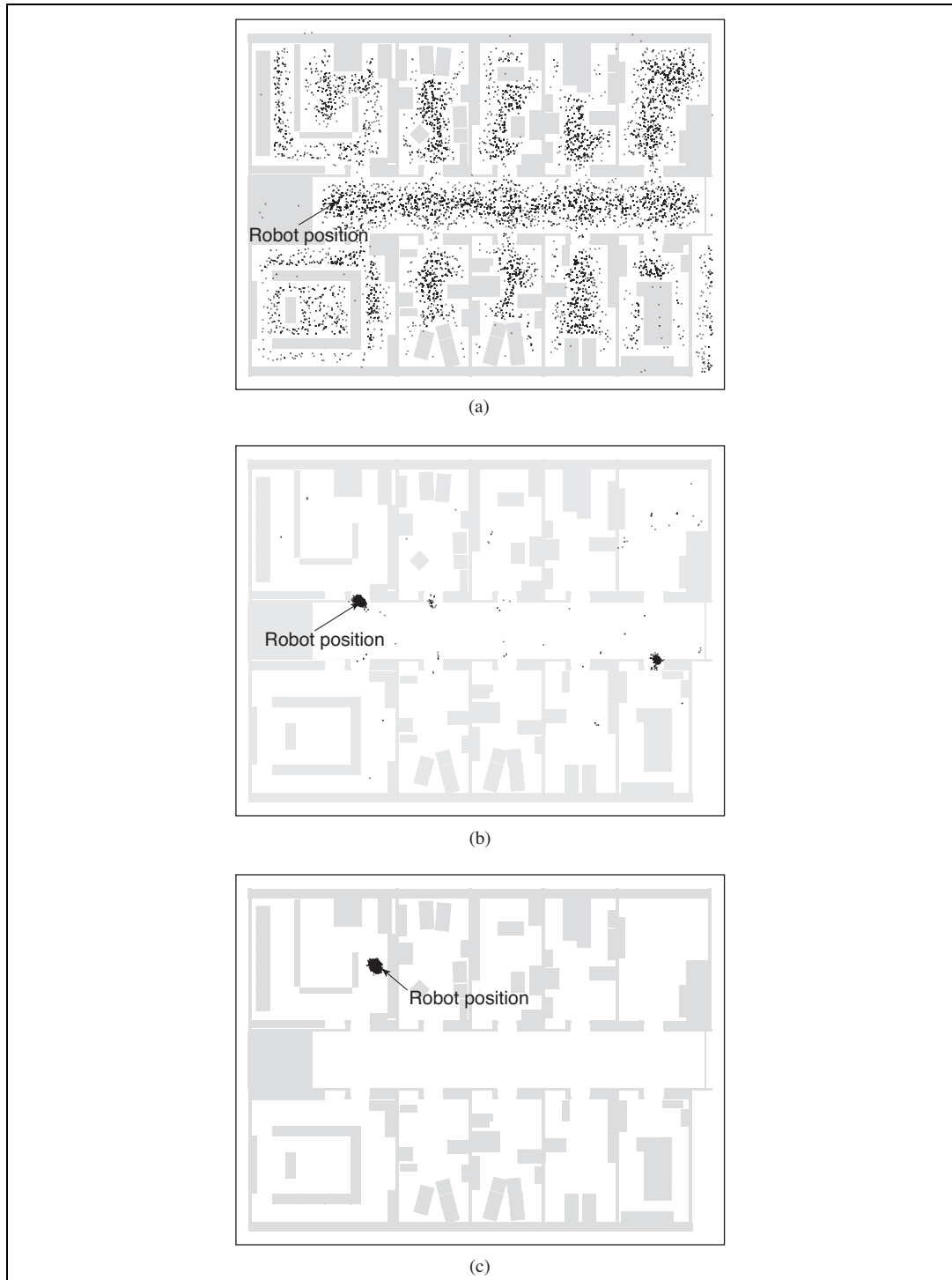


Figure 25.10 FILES: figures/first.eps (Tue Nov 3 16:22:51 2009) figures/second.eps (Tue Nov 3 16:23:41 2009) figures/third.eps (Tue Nov 3 16:23:54 2009). Monte Carlo localization, a particle filtering algorithm for mobile robot localization. (a) Initial, global uncertainty. (b) Approximately bimodal uncertainty after navigating in the (symmetric) corridor. (c) Unimodal uncertainty after entering a room and finding it to be distinctive.

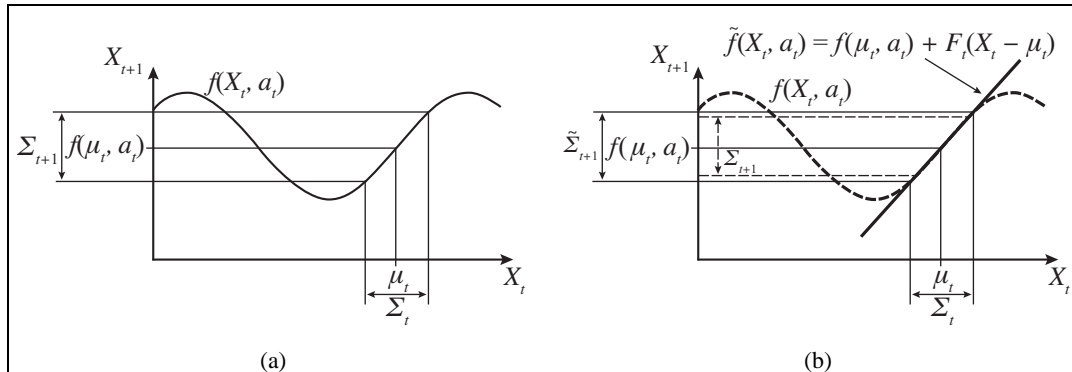
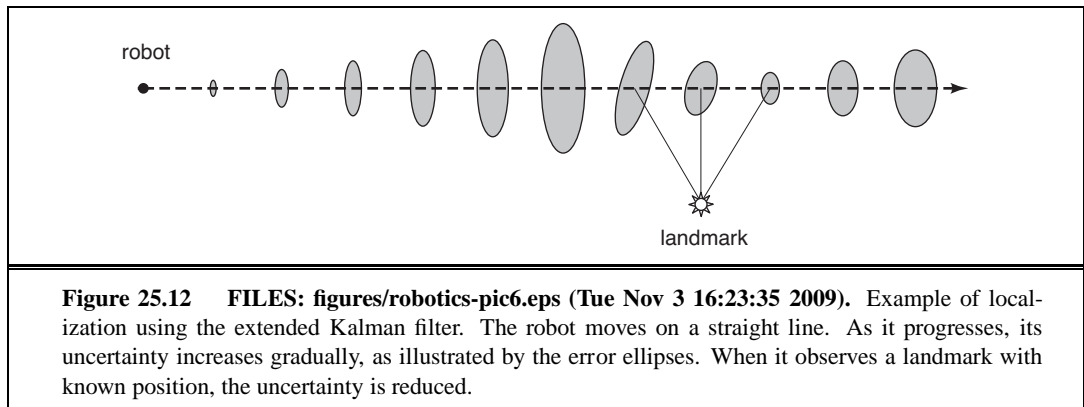
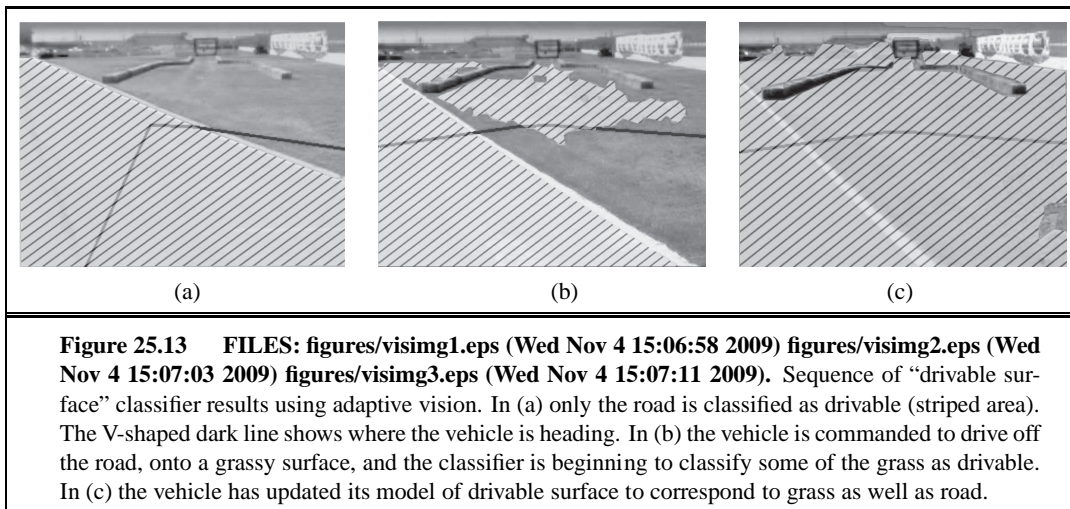


Figure 25.11 FILES: figures/robotics-pic3.eps (Tue Nov 3 16:23:34 2009) figures/robotics-pic4.eps (Tue Nov 3 16:23:34 2009). One-dimensional illustration of a linearized motion model: (a) The function f , and the projection of a mean μ_t and a covariance interval (based on Σ_t) into time $t+1$. (b) The linearized version is the tangent of f at μ_t . The projection of the mean μ_t is correct. However, the projected covariance $\tilde{\Sigma}_{t+1}$ differs from Σ_{t+1} .





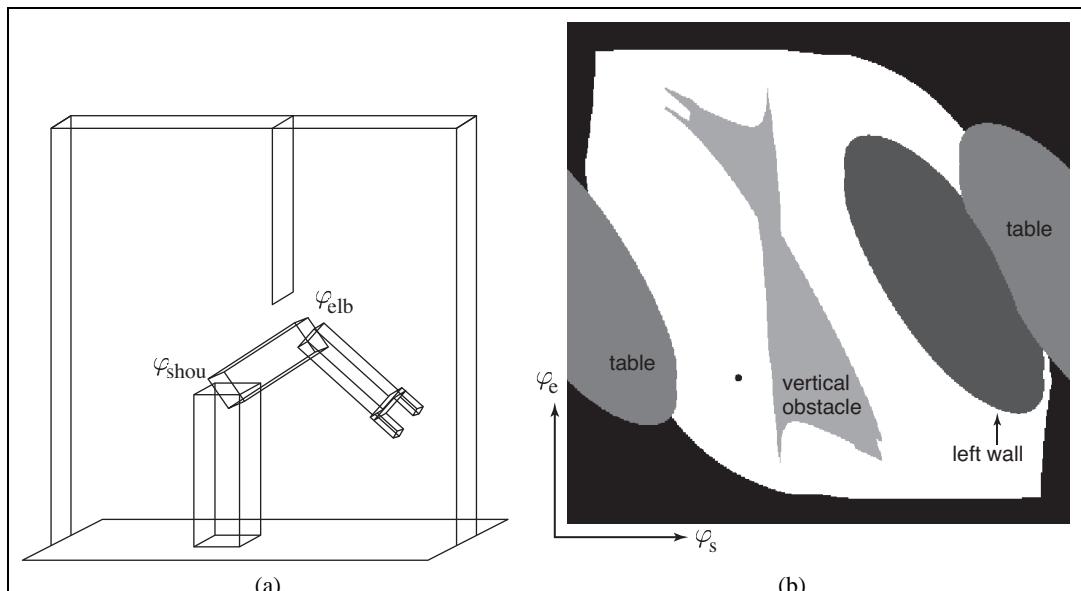
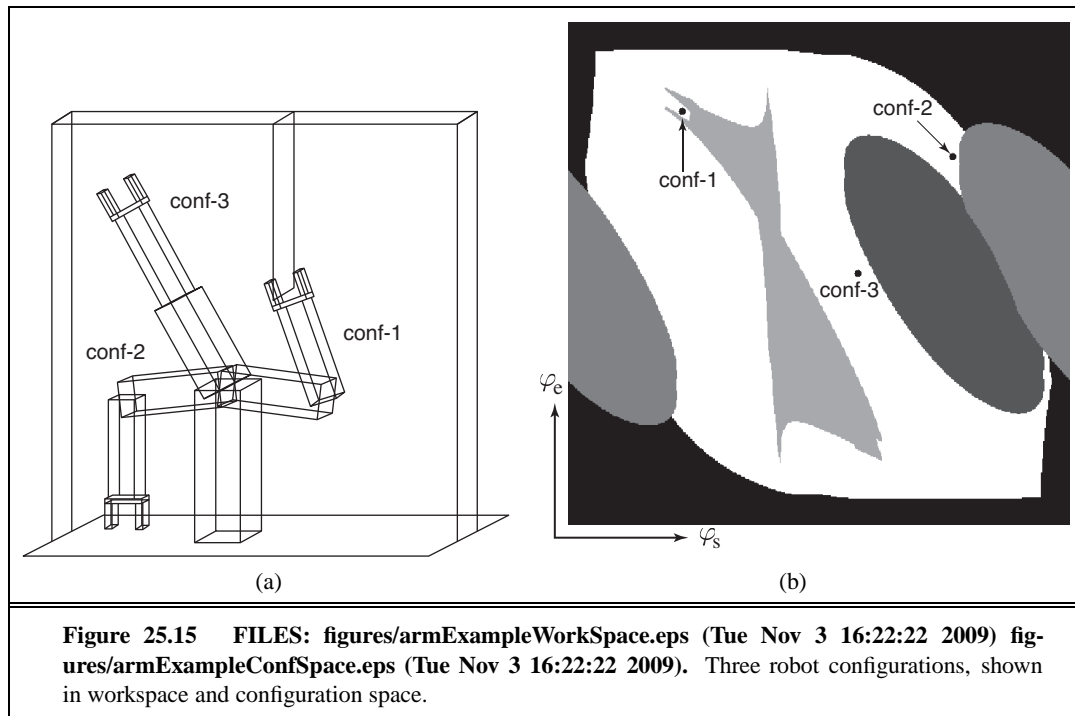


Figure 25.14 FILES: figures/armPlain.eps (Tue Nov 3 16:22:22 2009) figures/armPlainConfSpace.eps (Tue Nov 3 16:22:23 2009). (a) Workspace representation of a robot arm with 2 DOFs. The workspace is a box with a flat obstacle hanging from the ceiling. (b) Configuration space of the same robot. Only white regions in the space are configurations that are free of collisions. The dot in this diagram corresponds to the configuration of the robot shown on the left.



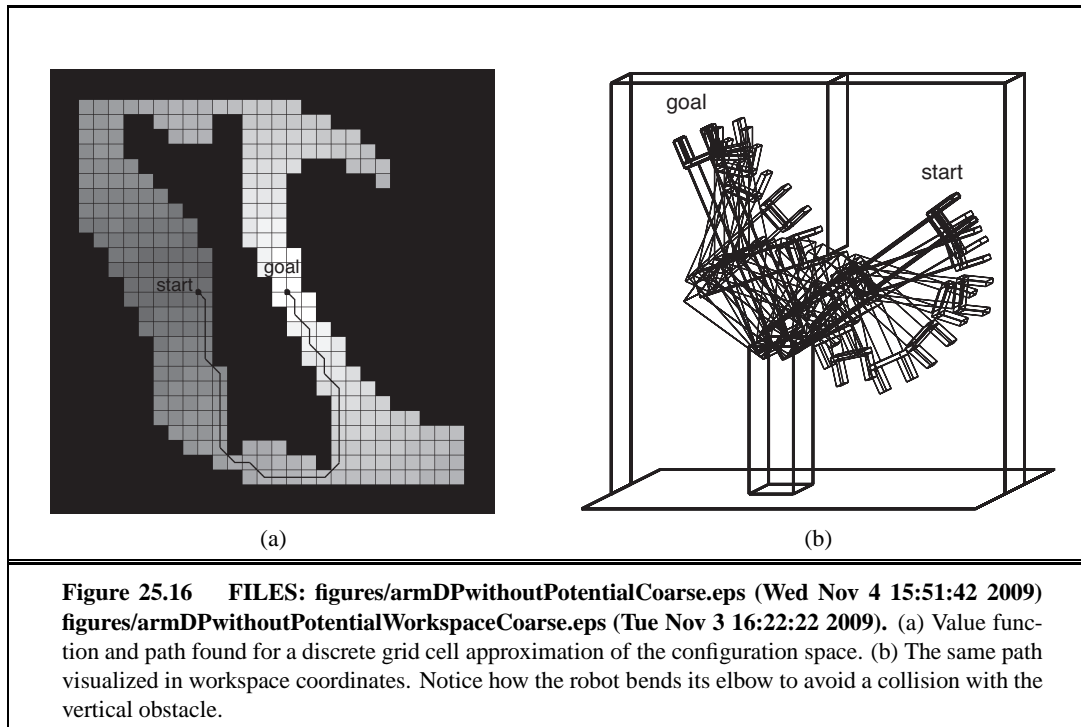


Figure 25.16 FILES: figures/armDPwithoutPotentialCoarse.eps (Wed Nov 4 15:51:42 2009)
figures/armDPwithoutPotentialWorkspaceCoarse.eps (Tue Nov 3 16:22:22 2009). (a) Value function and path found for a discrete grid cell approximation of the configuration space. (b) The same path visualized in workspace coordinates. Notice how the robot bends its elbow to avoid a collision with the vertical obstacle.

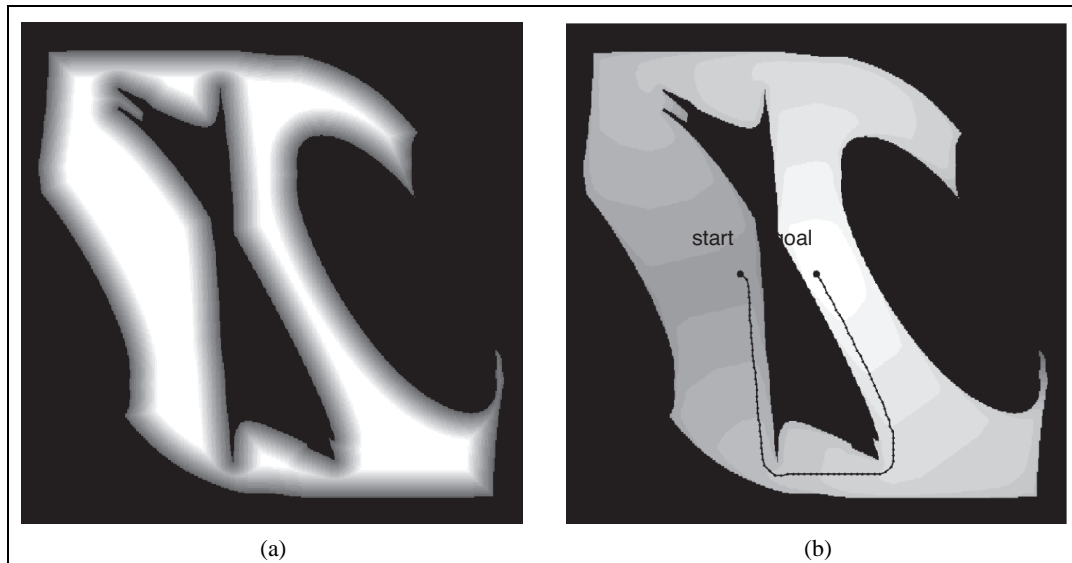


Figure 25.17 FILES: figures/armPotentialField.eps (Tue Nov 3 16:22:23 2009) figures/armDPwithPotential.eps (Tue Nov 3 16:22:21 2009). (a) A repelling potential field pushes the robot away from obstacles. (b) Path found by simultaneously minimizing path length and the potential.

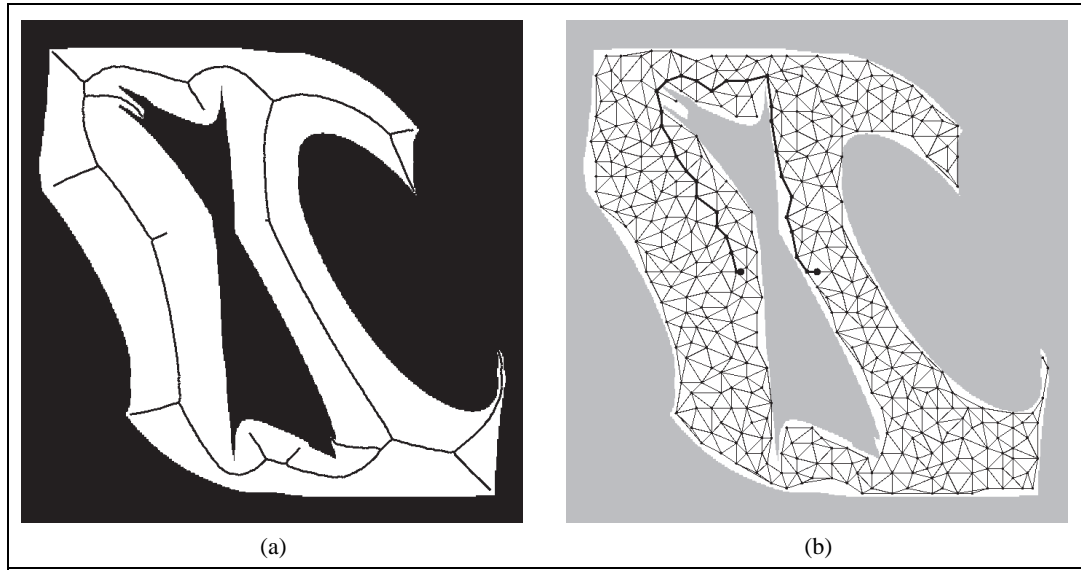
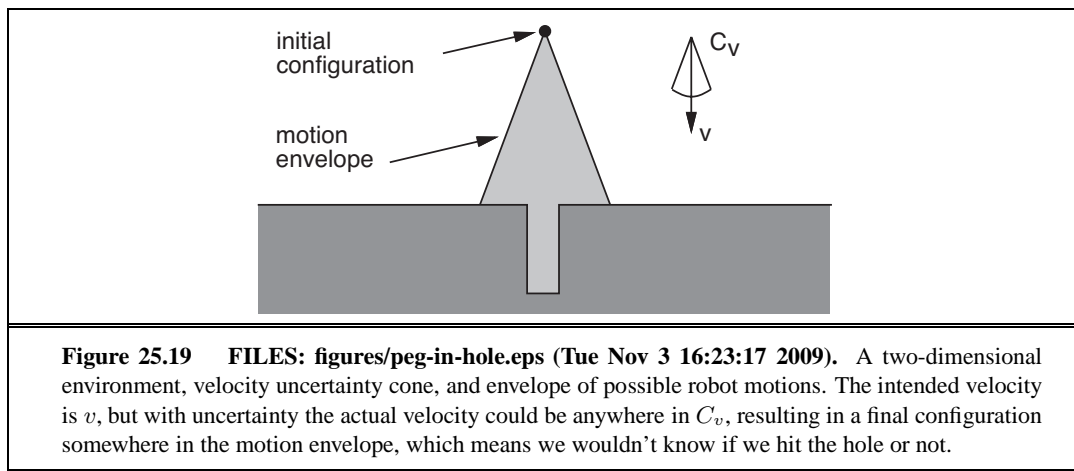
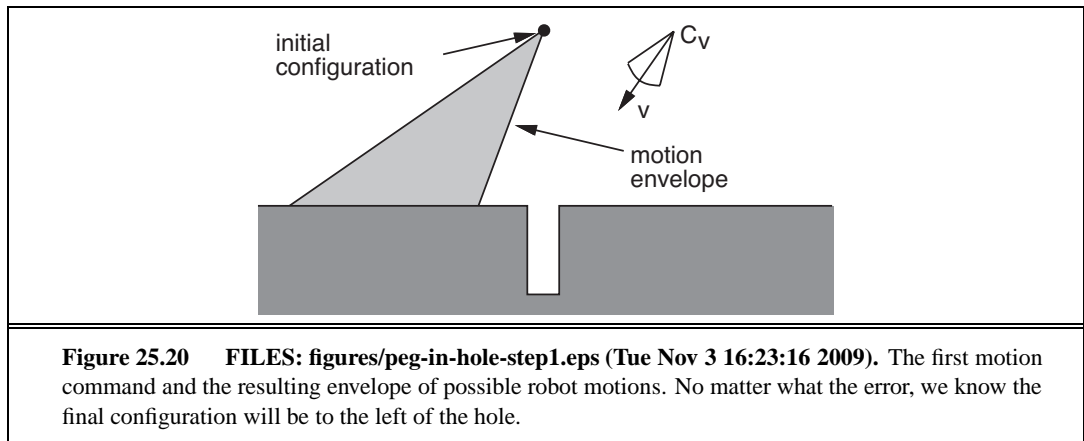
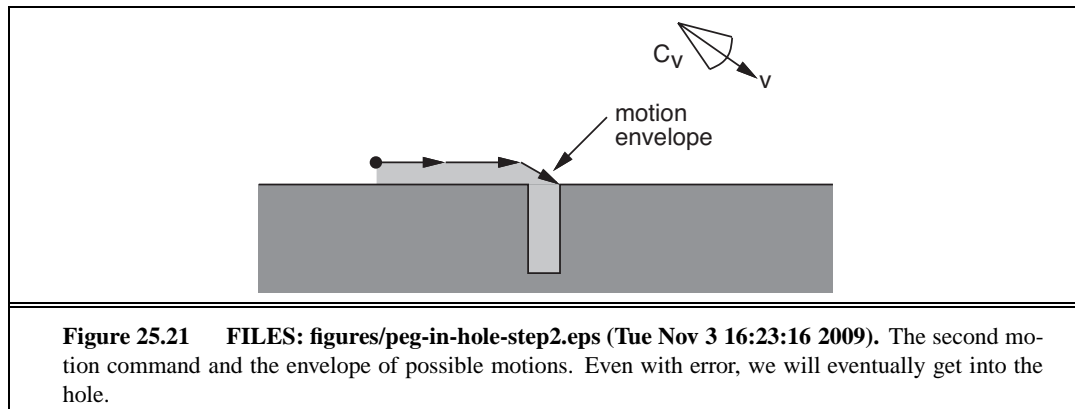


Figure 25.18 FILES: figures/armVoronoi.eps (Tue Nov 3 16:22:23 2009) figures/armRoadmap.eps (Tue Nov 3 16:22:23 2009). (a) The Voronoi graph is the set of points equidistant to two or more obstacles in configuration space. (b) A probabilistic roadmap, composed of 400 randomly chosen points in free space.







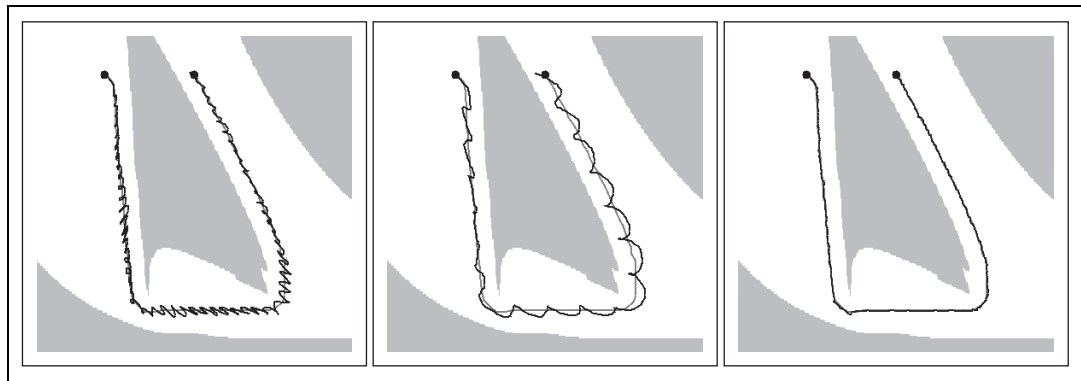


Figure 25.22 FILES: figures/armControlP1.0.eps (Tue Nov 3 16:22:21 2009) figures/armControlP0.1.eps (Tue Nov 3 16:22:21 2009) figures/armControlP0.3D0.8.eps (Tue Nov 3 16:22:21 2009). Robot arm control using (a) proportional control with gain factor 1.0, (b) proportional control with gain factor 0.1, and (c) PD (proportional derivative) control with gain factors 0.3 for the proportional component and 0.8 for the differential component. In all cases the robot arm tries to follow the path shown in gray.

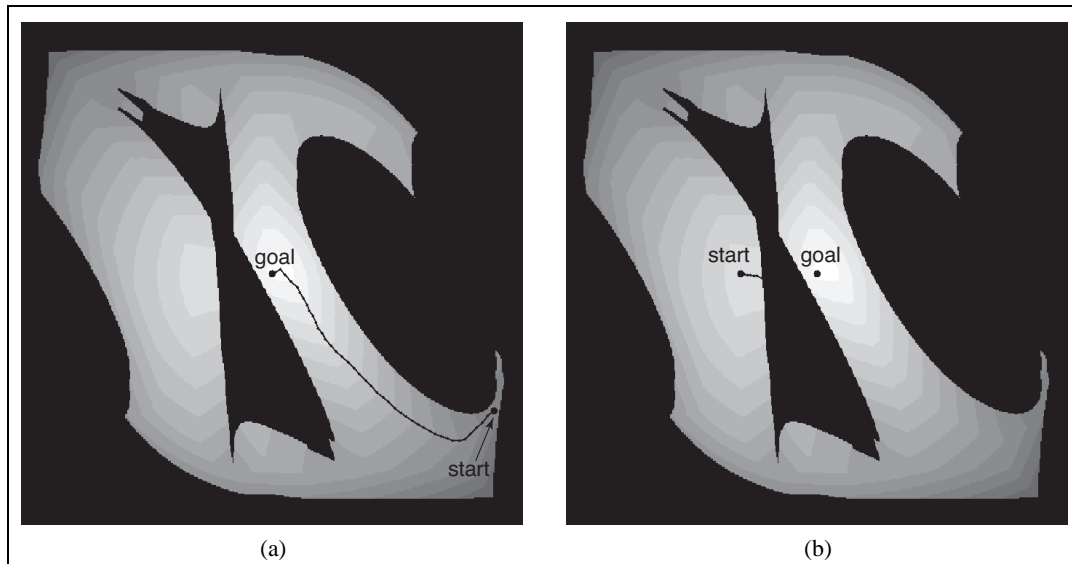


Figure 25.23 FILES: [figures/armSimplePotentialAlt.eps](#) (Tue Nov 3 16:22:23 2009) [figures/armSimplePotential.eps](#) (Tue Nov 3 16:22:23 2009). Potential field control. The robot ascends a potential field composed of repelling forces asserted from the obstacles and an attracting force that corresponds to the goal configuration. (a) Successful path. (b) Local optimum.

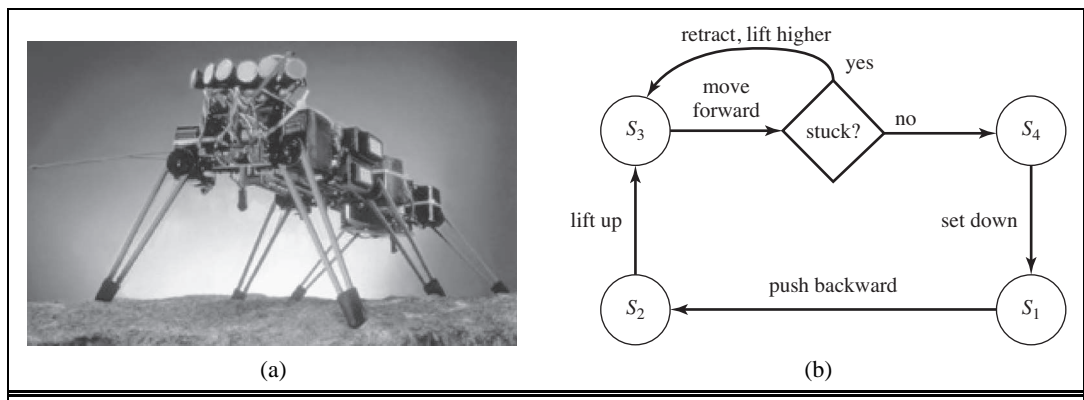


Figure 25.24 FILES: figures/genghis.eps (Tue Nov 3 13:34:49 2009) figures/robotics-pic5.eps (Tue Nov 3 16:23:34 2009). (a) Genghis, a hexapod robot. (b) An augmented finite state machine (AFSM) for the control of a single leg. Notice that this AFSM reacts to sensor feedback: if a leg is stuck during the forward swinging phase, it will be lifted increasingly higher.

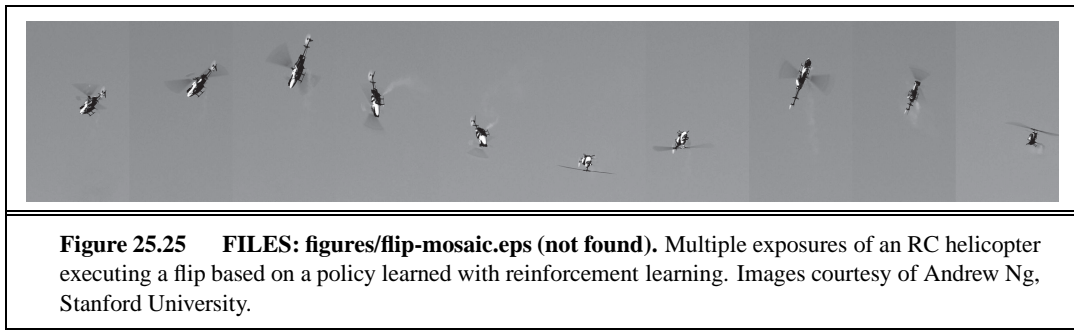
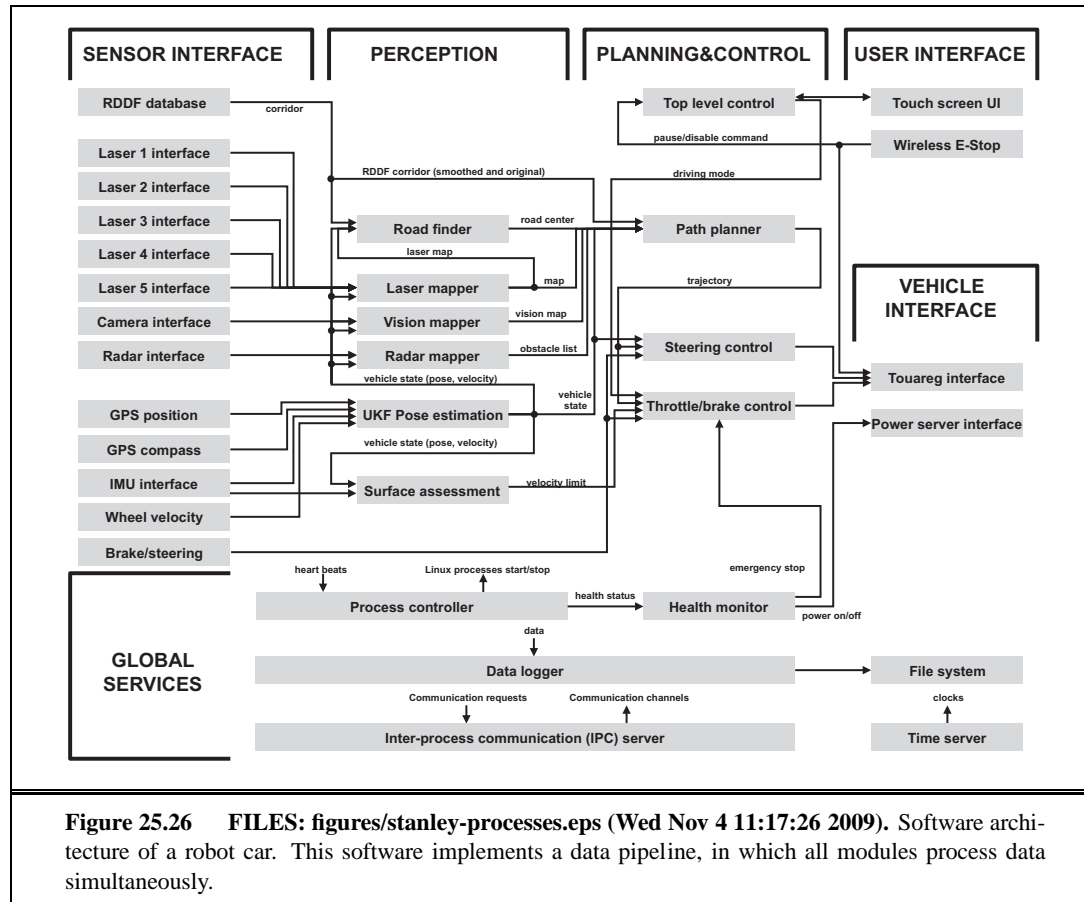


Figure 25.25 FILES: figures/flip-mosaic.eps (not found). Multiple exposures of an RC helicopter executing a flip based on a policy learned with reinforcement learning. Images courtesy of Andrew Ng, Stanford University.



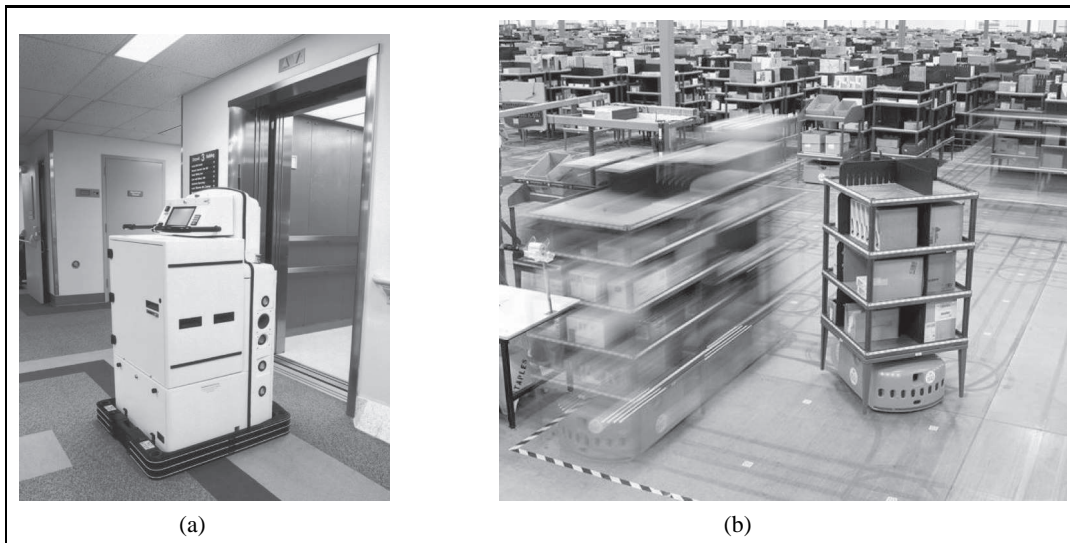


Figure 25.27 FILES: figures/helpmate.eps (Tue Nov 3 15:26:49 2009) figures/DenvierStation.eps (Tue Nov 3 16:22:14 2009). (a) The Helpmate robot transports food and other medical items in dozens of hospitals worldwide. (b) Kiva robots are part of a material-handling system for moving shelves in fulfillment centers. Image courtesy of Kiva Systems.

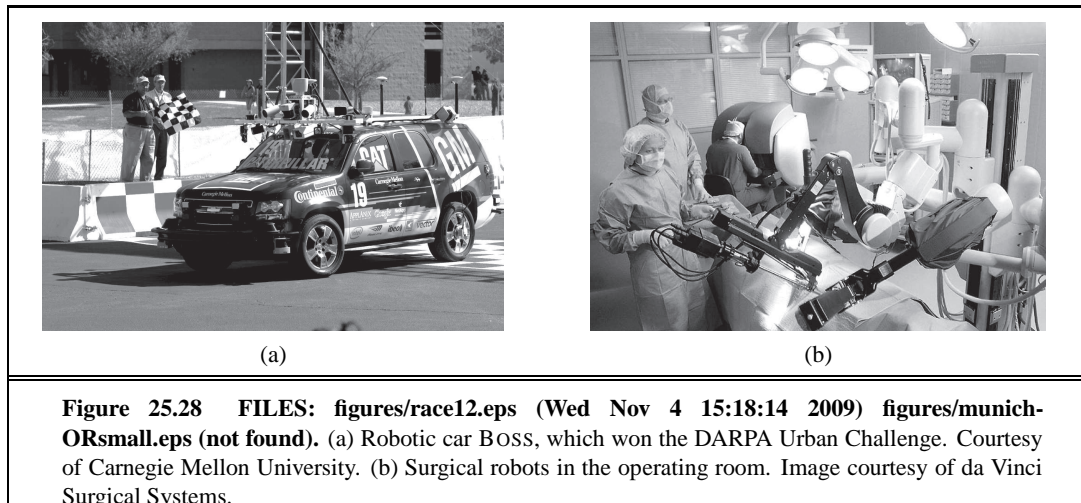


Figure 25.28 FILES: figures/race12.eps (Wed Nov 4 15:18:14 2009) figures/munich-ORsmall.eps (not found). (a) Robotic car BOSS, which won the DARPA Urban Challenge. Courtesy of Carnegie Mellon University. (b) Surgical robots in the operating room. Image courtesy of da Vinci Surgical Systems.

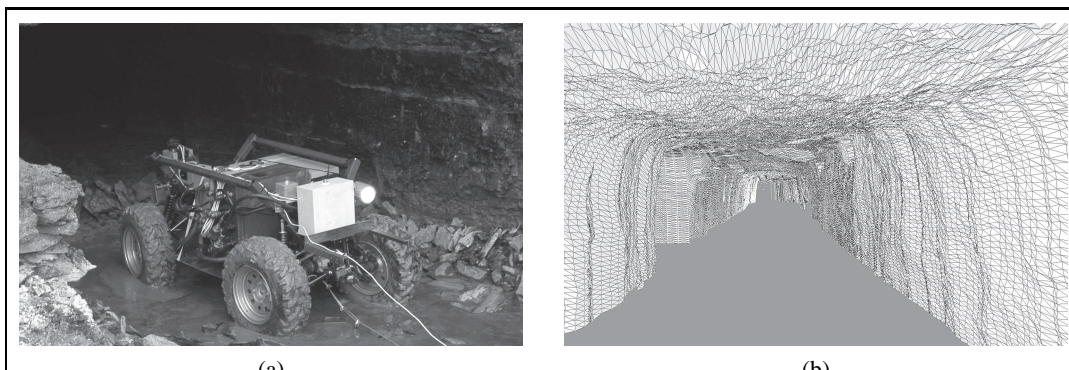
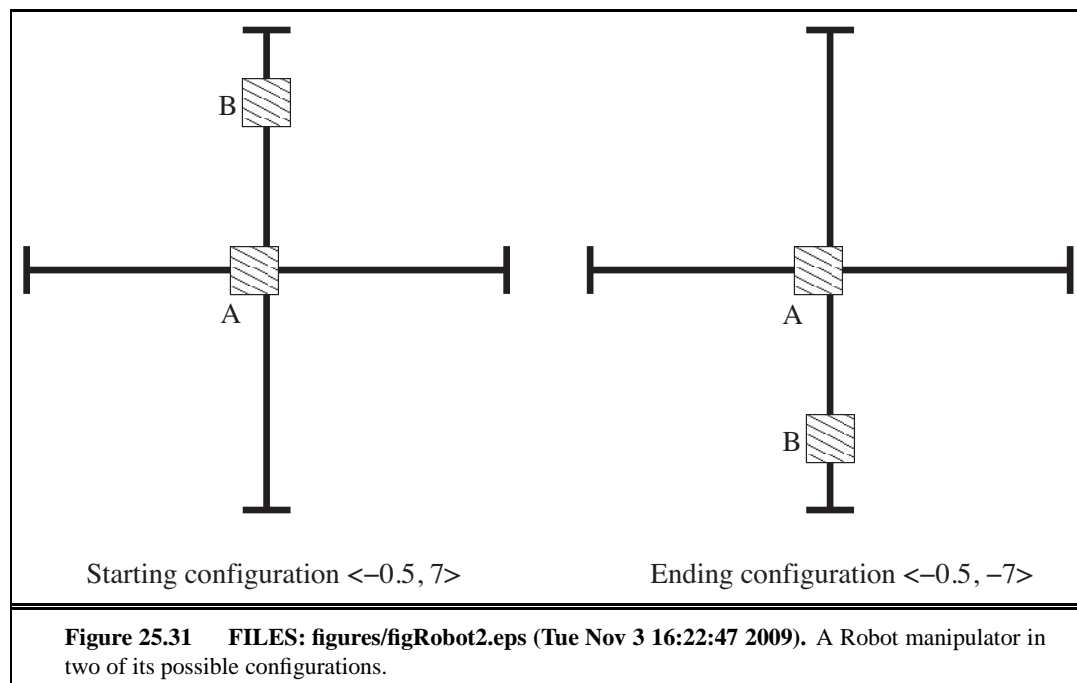


Figure 25.29 FILES: figures/mine-robot.eps (Tue Nov 3 16:23:11 2009) figures/mine-data.eps (Tue Nov 3 16:23:09 2009). (a) A robot mapping an abandoned coal mine. (b) A 3D map of the mine acquired by the robot.



Figure 25.30 FILES: figures/roomba1.eps (Wed Nov 4 15:22:23 2009) figures/icra-cordless-phone-gray3.eps (not found). (a) Roomba, the world's best-selling mobile robot, vacuums floors. Image courtesy of iRobot, © 2009. (b) Robotic hand modeled after human hand. Image courtesy of University of Washington and Carnegie Mellon University.



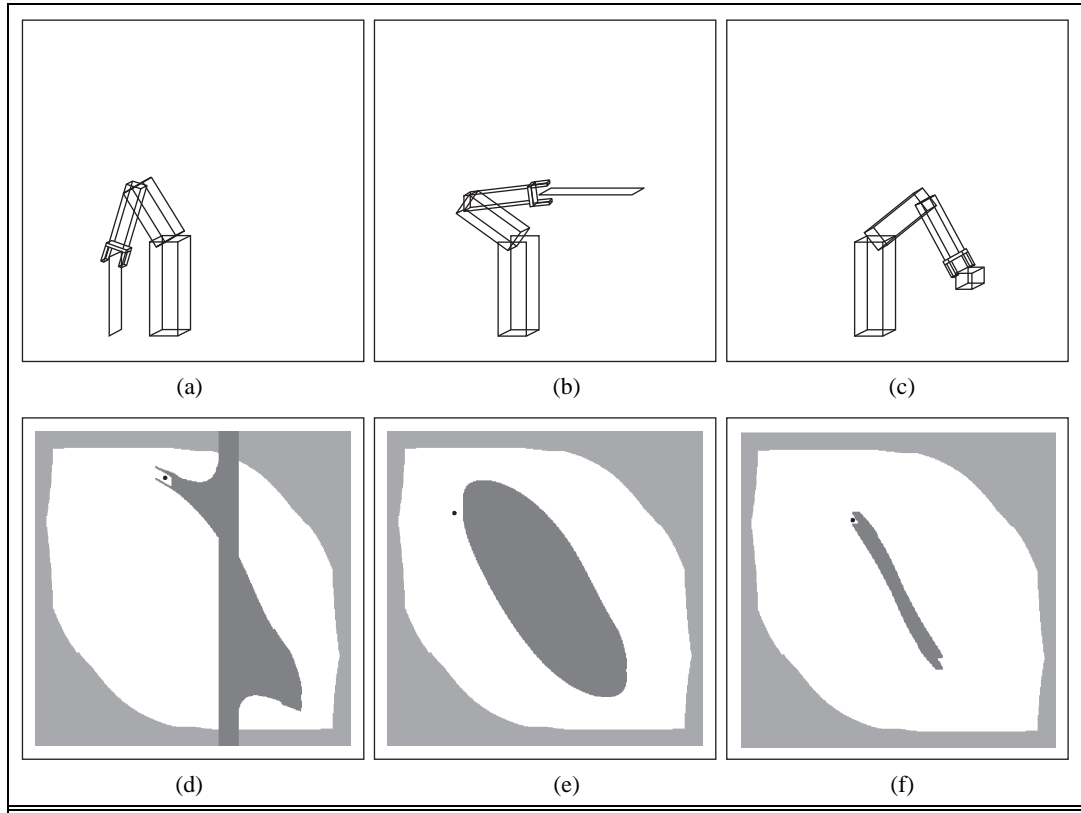
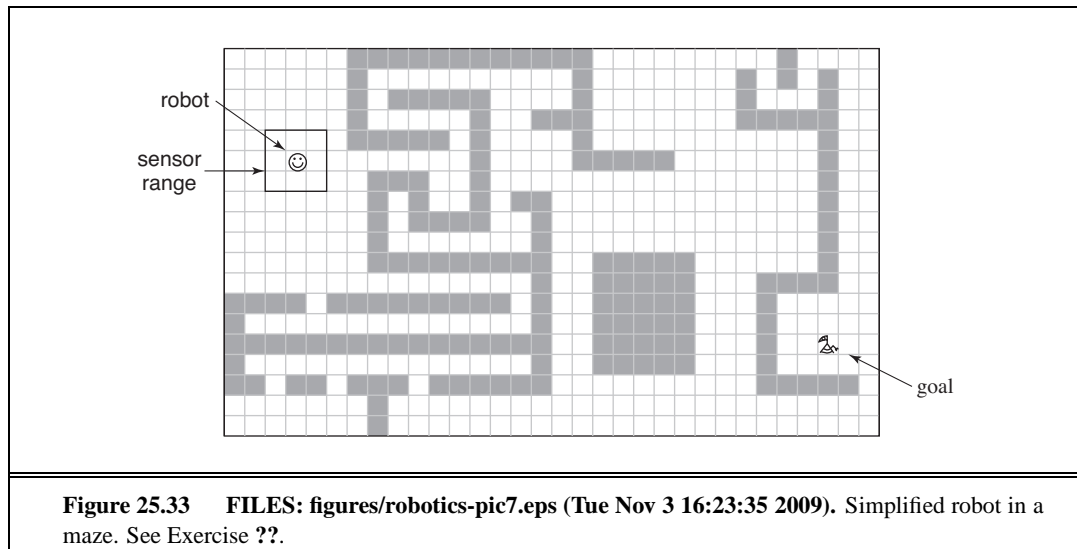
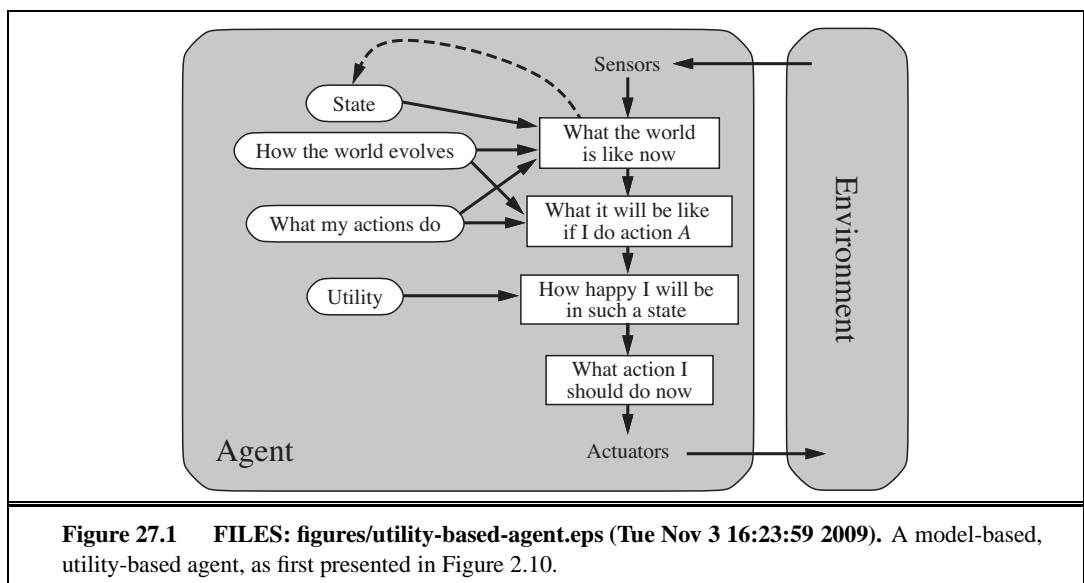


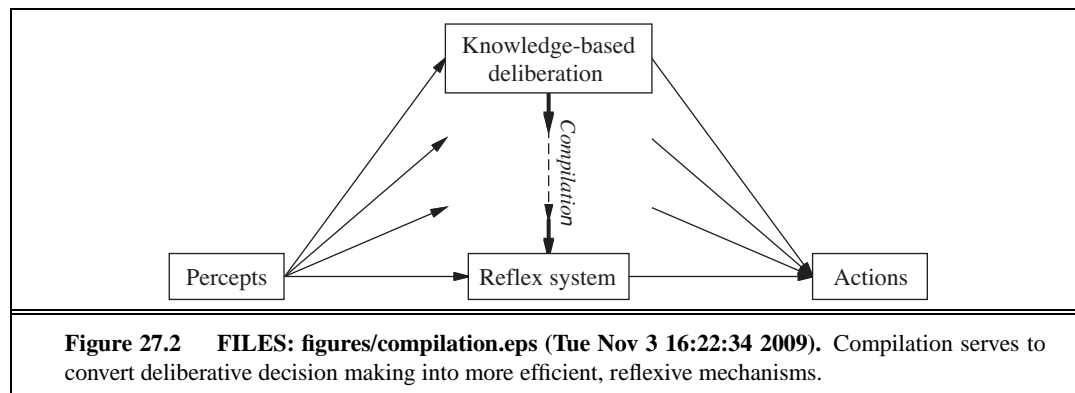
Figure 25.32 FILES: figures/exerciseRobot1.eps (Tue Nov 3 16:22:42 2009) figures/exerciseRobot3.eps (Tue Nov 3 16:22:43 2009) figures/exerciseRobot6.eps (Tue Nov 3 16:22:44 2009) figures/exerciseConf2.eps (Tue Nov 3 16:22:41 2009) figures/exerciseConf4.eps (Tue Nov 3 16:22:42 2009) figures/exerciseConf5.eps (Tue Nov 3 16:22:42 2009). Diagrams for Exercise ??.



26 PHILOSOPHICAL FOUNDATIONS

27 AI: THE PRESENT AND FUTURE





28 MATHEMATICAL BACKGROUND

29 NOTES ON LANGUAGES AND ALGORITHMS